Reservoir-Geomechanics of Underground Coal Gasification (UCG)

by

Hossein Akbarzadeh Kasani

A thesis submitted in partial fulfillment of the requirements for the degree of

Doctor of Philosophy

in

Geotechnical Engineering

Department of Civil and Environmental Engineering

University of Alberta

Abstract

The Underground Coal Gasification (UCG) is still not in a worldwide operation despite inheriting an old idea which is nearly one and a half century old. Aside from effects by other fuel sources on development of the UCG and from a technical perspective, this delay is due to the complex nature of the process. The chemical process of gasification may develop temperature in the order of 1000 ^{o}C, turn the initial solid coal to char and ash, generate pore pressure, create cavities, and develop cracks in the coal seam and rock layers. The later will, in turn, influence the gasification process due to the enhanced porosity and permeability of the strata. Hence, the UCG represents a coupled thermal-hydro-chemical-mechanical process.

Understanding how coal, a fractured organic sedimentary rock, responds to the temperature and pore pressure changes around a gasification chamber is crucial for a successful UCG operation. How pore pressure is influenced by volumetric deformation and the ultra-high temperature around a gasification cavity is of significant importance which has not been well studied. Previous high-temperature experimental studies of coal are scarce yet distributed in multiple disciplines; including chemical, petroleum, and geomechanics. Moreover, previous modeling of the UCG mostly included separate gasification simulations or geomechanical simulations of idealized cavities.

This research encompassed experimental and simulation studies. An inter-disciplinary research of coal was conducted to investigate impact of elevated temperature on weight loss, thermal deformation, microcrack generation, transport properties, as well as strength and stiffness of coals from different ranks. Furthermore, a High-Pressure High-Temperature (HPHT) triaxial set up was upgraded and utilized in this study to accommodate measuring permeability of

Alberta coal to nitrogen gas along with geomechanical test. Several coal specimens were cored from large coal blocks acquired from the Genesee coal mine in Central Alberta. The coal specimens were tested under different confining stresses and temperatures. This experimental program measured thermal deformation, stress-strain, elastic properties, permeability as well as permeability evolution during progressive shearing.

The simulation studies included parametric geomechanical analyses of an idealized UCG cavity to understand fundamentals of the formation response to evolution of a cavity which included high-temperature syngas. Impacts of different operational pressures and coal material properties on thermally-induced pore pressure as well as deformation and stresses around the UCG cavity were investigated. Moreover, a numerical modeling workflow was devised in order to sequentially couple coal gasification capability of a reservoir simulator to a geomechanical software. This coupling workflow facilitated simultaneous observation of gasification process as well as geomechanical effects to the strata. This coupling workflow was applied to a reservoir scale modeling of the Swan Hills, Alberta UCG project implementing the in-situ stress magnitudes and orientations. The gasification modeling was run for a 60-day period utilizing the Controlled Retraction Injection Point (CRIP) operational method and produced syngas compositions which closely matched the field measurements. Simultaneously, deformations, stresses, and mechanical failure in the strata were observed as the gasification front advanced and the tear-drop shape cavities grew in dimensions.

Preface

The research presented in this thesis was completed by Hossein Akbarzadeh Kasani. This thesis is presented in a paper-format style. Five journal articles have been prepared for Chapters 3 to 7. For all papers, I have been responsible for literature review, laboratory experiments, numerical simulations, data analysis, writing the manuscript, as well as being the corresponding author. Professor R.J. Chalaturnyk has been the supervisory co-author and provided editing comments. Chapters 3, 5, and 6 have already been published. Chapters 4 and 7 will be submitted for journal publications. Following is a list of the papers:

Chapter 3	Akbarzadeh, H., & Chalaturnyk, R. J. (2014). Structural changes in coal at elevated temperature pertinent to underground coal gasification: A review. International Journal of Coal Geology, 131, 126-146.
Chapter 4	Akbarzadeh, H., & Chalaturnyk, R. J. (to be submitted). Influence of high pressure and temperature on mechanical behavior and permeability of a fractured coal.
Chapter 5	Akbarzadeh, H., & Chalaturnyk, R. J. (2013). Coupled fluid-thermal-mechanical analyses of a deep underground coal gasification cavity. Journal of Architecture and Civil Engineering, Quest Journals, 1(1), 01-14.
Chapter 6	Akbarzadeh, H., & Chalaturnyk, R. J. (2016). Sequentially coupled flow-geomechanical modeling of underground coal gasification for a three-dimensional problem. Mitigation and Adaptation Strategies for Global Change, 21(4), 577-594.
Chapter 7	Akbarzadeh, H., & Chalaturnyk, R. J. (to be submitted). Coupled reservoir and geomechanical simulation for a deep underground coal gasification project.

Acknowledgements

I would like to express my deepest gratitude to my supervisor Dr. Richard J. Chalaturnyk for the opportunity, support, understanding, and guidance which he provided throughout the course of this research program.

A special thank-you goes to several members of the Reservoir Geomechanics Research Group (RG)^2 and the Geomechanical Reservoir Experimental Facility (GeoREF) of Dr. Chalaturnyk; past and current staff, colleagues, and graduate students within the (RG)^2 and GeoREF who provided assistance and support in many ways; including Ali Azad, Juan Buitrago, Nathan Deisman, Steve Gamble, Mousumi Ghosh, Ehab Hamza, Ekramul Haque, Abel S. Juncal, Mehdi Khajeh, Keivan Khaleghi, Lang Liu, Alireza A. Moghadam, Bauyrzhan Primkulov, Hope Walls, Xinkui Wang, Gilbert Wong, and Gonzalo Zambrano.

My appreciation is extended to Dr. Dave Chan, Associate Chair of the Department of Civil and Environmental Engineering for his support throughout my studies. I would also like to thank past and present graduate students in the same department who provided support and discussions; including Ehsan Abazari, Mohan Acharya, Vahid Dehdari, Renato Macciotta, Daniel Meles, Syed Salman Mobeen, Alireza Roghani, Nadia Shafiezadeh, and Ken Taslagyan.

I am thankful to Dr. Ranjender Gupta and his research group in the Department of Chemical and Materials Engineering, in the early stage of this research; in particular, Ahad Sarraf Shirazi, Shayan Karimipour, M. M. Khan, and Shan Ramasamy. Discussions provided by Saeid Mehdiabadi from the same department are also acknowledged.

Financial support of this research was provided by The Canadian Centre for Clean Coal/Carbon and Mineral Processing Technologies (C5MPT). Thank you C5MPT.

Technical support provided by Yousef Hamedi from the Computer Modelling Group Ltd., Calgary is also appreciated.

I would like to thank my family, parents, and parents in-law, for their companion and continued encouragement. Last but not least, the love, support, and patience provided by my wife Leyla and our children Amirali and Andia are highly acknowledged.

Table of Contents

Abstract ii

Preface iv

Acknowledgements v

Table of Contents vi

List of Figures xii

List of Tables xix

Chapter 1 Introduction 1

1.1. General 1

1.2. Statement of the problem 1

1.3. Objectives 2

1.4. Methodology 2

1.5. Organization of the thesis 4

Chapter 2 Literature Review 6

2.1. Introduction 6

2.2. Geomechanical risks in a UCG project 9

2.3. Previous experimental and field studies of UCG 9

2.4. Review of analytical and numerical modeling of UCG 10

2.4.1. Analytical solutions 10

2.4.2. Gasification simulations 11

2.4.3. Geomechanical simulations 11

2.4.4. Coupled gasification-geomechanical simulations 12

2.5. References 12

Chapter 3 Structural Changes in Coal at Elevated Temperature Pertinent to Underground Coal Gasification ... 19

3.1. Abstract ... 19

3.2. Introduction ... 20

3.3. Structural impacts of UCG on coal and strata; observations from previous trial tests ... 22

3.3.1. Hanna II experiment, Hanna, Wyoming ... 23

3.3.2. Hoe Creek II, Campbell County, Wyoming ... 25

3.3.3. Discussion of geomechanical and hyrogeological risks in a UCG project ... 27

3.4. Coal classification ... 29

3.5. Review of experimental studies related to structural changes in coal at elevated temperature ... 31

3.5.1. Weight loss due to heating ... 36

3.5.2. Thermal deformation ... 38

3.5.3. Crack generation due to heating ... 42

3.5.4. Effect of temperature on pore volume, aperture, porosity, and permeability ... 44

3.5.5. Effect of temperature on strength and stiffness ... 56

3.6. Concluding remarks ... 64

3.6.1. Findings from this study ... 64

3.6.2. Knowledge gaps in HPHT coal experiments ... 65

3.7. Acknowledgements ... 66

3.8. References ... 66

Chapter 4 High-Pressure and High-Temperature Geomechanical Experiments on a Fractured Coal from Alberta ... 74

4.1. Abstract ... 74

4.2. Introduction ... 75

4.3. Experiments ... 76

4.3.1. Apparatus 76
4.3.2. Sample preparation 78
4.3.3. Testing program 80
4.4. Results and discussion 84
4.4.1. Thermal deformation under isotropic compression 84
4.4.2. Internal LVDTs versus external LP; measuring height change during shear 87
4.4.3. Stress-strain and deformation characteristics during shear at room temperature 88
4.4.4. Stress-strain and deformation characteristics during shear at 200 ℃ 92
4.4.5. Comparison between shear strength at room temperature and 200 °C 94
4.4.6. Permeability evolution with temperature and effective stress 96
4.4.7. Permeability evolution during progressive shearing 101
4.5. Conclusions 103
4.6. Acknowledgements 104
4.7. References 104
Chapter 5 Parametric Geomechanical Analyses of an Idealized Underground Coal Gasification Cavity 108
5.1. Abstract 108
5.2. Introduction 109
5.2.1. Advantages of UCG 109
5.2.2. UCG risks 109
5.2.3. Previous studies of UCG 109
5.2.4. Scope and objectives 111
5.3. Description of the simulation model 111
5.3.1. Geometry 111
5.3.2. Initial configurations and material properties 112

5.3.3. Coupled fluid-thermal-mechanical analyses ... 114
5.3.4. Description of five studied scenarios ... 116
5.4. Results and discussions ... 120
5.4.1. Results of scenario 1 ... 120
5.4.2. Impacts of syngas pressure on geomechanical response ... 128
5.4.3. Impacts of temperature-dependent coal elastic modulus on geomechanical response ... 128
5.4.4. Impacts of temperature-dependent coal permeability on geomechanical response .. 129
5.4.5. Displacements of the monitoring points through scenarios 1 to 5 ... 129
5.5. Summary and conclusions ... 130
5.6. Acknowledgements ... 131
5.7. References ... 132
Chapter 6 A Numerical Modeling Workflow for Sequentially Coupled Reservoir and Geomechanical Simulation of Underground Coal Gasification ... 135
6.1. Abstract ... 135
6.2. Introduction ... 136
6.3. Scope and objectives ... 139
6.4. Chemical reactions ... 139
6.5. Governing equations ... 142
6.6. Flow-geomechanical coupling ... 143
6.7. Simulation model ... 146
6.7.1. Geometry ... 146
6.7.2. Material properties ... 147
6.8. Results and discussion ... 151
6.8.1. Syngas production and cavity growth ... 151

6.8.2. Geomechanical changes 154
6.9. Conclusions 158
6.10. Acknowledgements 159
6.11. References 159
Chapter 7 Sequentially Coupled Reservoir and Geomechanical Simulation of Underground Coal Gasification in Alberta 163
7.1. Abstract 163
7.2. Introduction 164
7.3. Scope and objectives 165
7.4. Model descriptions 166
7.4.1. Geology 166
7.4.2. In-situ stresses 169
7.4.3. Coal gasification modeling 170
7.4.4. Geomechanical modeling 177
7.4.5. Sequential gasification and geomechanical coupling approach in UCG 181
7.5. Simulation results and discussion 183
7.5.1. Syngas production and cavity growth 183
7.5.2. Geomechanical effects on the strata 189
7.1. Conclusions 193
7.2. Acknowledgements 194
7.3. References 194
Chapter 8 Conclusions and Recommendations 198
8.1. Summary 198
8.2. Conclusions 199
8.3. Recommendations for future research 201

8.3.1. Experimental research 201

8.3.2. Simulation research 201

References 203

List of Figures

Figure 2.1 Schematics of the UCG processes: a) linked vertical wells (LVW), b) linear CRIP, c) parallel CRIP (Couch, 2009) 8

Figure 3.1 The Hanna II UCG expeiment: a) layout of different phases; b) a cross section showing Phase 1a including injection (well 3) and production (well 1) system along with two monitoring wells (DD and CC) with thermocouples; c) temperature profiles of Phase 1a at different times; d) location of different drill and core wells as well as the injection and production wells for Phases 2 and 3; e) cross sections A-A' of the gasification cavity; and f) cross sections B-B' of the gasification cavity (Brandenburg et al., 1975; Northrop et al., 1977; and Youngberg et al., 1983) 24

Figure 3.2 a) Plan view of exploration boreholes as well as injection and production wells at the Hoe Creek II: b) gasification cavity section A-A'; c) gasification cavity section B-B'; d) gasification cavity section C-C' (Aiman et al., 1980) 26

Figure 3.3 Influence of structural changes in coal on a UCG operation 29

Figure 3.4 Weight loss of the Wyodak coal (subbituminous) during drying and pyrolysis (Thorsness et al., 1978) 37

Figure 3.5 a) Theromogravimetry (TG) curve; and b) derivative theromogravimetric (DTG) of the Yuanbaoshan lignite coal, Inner Mongolia, China (Niu et al., 2014) 38

Figure 3.6 Thermal deformation data of the Hanna Basin subbituminous coal showing the effect of bedding plane (Glass, 1984) 39

Figure 3.7 Thermal deformation data of the Xing-Long-Zhuang mine gas coal: a) heating time along with axial, lateral, and volumetric strains; and b) pyrolysis gas production and volumetric strain against temperature (Feng et al., 2012) 40

Figure 3.8 a) Experimental setup for coal heating; b) temperature variation and AE activity monitored in the process; c) microcrack distribution along the specimen height; and d) average fissure volume along the specimen height for a cubic sample of bituminous coal from the Kushiro mine, Japan, with the bedding plane parallel to the heating surface (Su et al., 2013) 43

Figure 3.9 Permeability and porosity change of the Wyodak subbituminous coal during drying and pyrolysis (Thorsness et al., 1978) 45

Figure 3.10 a) Porosity; and b) air permeability of four bituminous coals from USA (Pittsburgh, Pocahontas No.3, Sewell, Illinois No.6) preheated to 300, 500, 650, and 800 ºC (Singer and Tye, 1979) *Note: Permeability was measured parallel to the bedding plane. 46
Figure 3.11 Porosity variations of bituminous coals from the Markham Main and the Manvers Wath, UK, versus temperature (Balek and de Koranyi, 1990; de Koranyi and Balek, 1985) 47
Figure 3.12 Properties of steam coal from the Xing-Long-Zhuang mine under different N_2-injection pressure after drying and pyrolysis to a particular temperature: a) porosity and average pore aperture; b) nitrogen permeability versus temperature under different injection pressure; and c) nitrogen permeability versus injection pressure under different temperature (Zhao et al., 2010) 49
Figure 3.13 Porosity of lean (semi-anthracite) coal from the Xishan coal field, China, versus temperature (Yu et al., 2012) 50
Figure 3.14 Nitrogen permeability of the Yuanbaoshan lignite coal, Inner Mongolia, China, versus: a) temperature; and b) nitrogen-injection pressure (Niu et al., 2014) 51
Figure 3.15 Normalized permeability of the Wyodak subbituminous coal (Thorsness et al., 1978), the Xing-Long-Zhuang steam coal, China (Zhao et al., 2010), and the Yuanbaoshan lignite coal, Inner Mongolia, China (Niu et al., 2014) to the corresponding values at their ambient temperatures 52
Figure 3.16 Permeability vs. change in porosity during drying and pyrolysis based on the data available for the Wyodak subbituminous coal (Thorsness et al., 1978) and the Xing-Long-Zhuang steam coal (Zhao et al., 2010)... 53
Figure 3.17 Schematic compressive stress-axial strain and shear stress-shear strain curves of coals at different temperatures 57
Figure 3.18 a) Elastic moduli of the Pittsburgh bituminous coal specimens (from the Humphrey No.7 mine, Maidsville, West Virginia) vs. temperature in uniaxial compression; and b) shear moduli of the Pittsburgh coal specimens vs. temperature in a simple shear test (Shoemaker, 1976) 58
Figure 3.19 a) Tensile; and b) compressive strengths of preheated specimens of the Pittsburgh coal (bituminous) showing the effect of carbonization (preheating) and test temperature as well as direction to the bedding plane (Singer and Tye, 1979) 60

Figure 3.20 Mechanical properties of the Hanna Basin coal (subbituminous) as a function of temperature and normal/parallel to the bedding plane: a) elastic and shear moduli; and b) Poisson's ratio (Glass, 1984) 61
Figure 3.21 Relationship between elastic modulus and temperature for the Jincheng anthracite and the Xing-Long-Zhuang gas coals (Wan et al., 2011) 62
Figure 3.22 Normalized moduli of the Pittsburgh bituminous coal from the Humphrey No.7 mine, Maidsville, West Virginia (Shoemaker, 1976) and the Hanna Basin subbituminous coal (Glass, 1984) to the corresponding values at reference temperature (24 ºC for the Pittsburgh coal and 25 ºC for the Hanna Basin coal): a) elastic modulus; and b) shear modulus 63
Figure 4.1 Schematic of the HPHT triaxial apparatus used in this study 77
Figure 4.2 A coal block from the Genesee coal mine in the Central Alberta, Canada 79
Figure 4.3 Specimen S4: a) initial vertical fractures; b) and c) two ends of the specimen showing heterogeneity in initial fracture networks; d) the internal LVDTs and circumferential chain mounted around the specimen; and e) S4 after shear at 203.9 ^{o}C 80
Figure 4.4 Thermal strains recorded by internal axial and circumferential LVDTs during heating from room temperature to about 200 ^{o}C for: a) S2; b) S3; and c) S4 85
Figure 4.5 Two examples showing internal LVDT's measurements during shear compared to an external LP: a) S4 sheared at 203.9 ^{o}C; b) S7 sheared at 23.5 ^{o}C 88
Figure 4.6 Stress-strain curves of specimen S1 at room temperature from different methods..... 90
Figure 4.7 Stress-strain curves of specimen S7 at room temperature from different methods..... 91
Figure 4.8 Stress-strain curves of specimen S3 at 199.3 ^{o}C from different methods 93
Figure 4.9 Stress-strain curves of all specimens: a) room temperature; a) 200 ^{o}C; and c) principal stress ratio vs. axial strain for all specimens 95
Figure 4.10 Laboratory results of a constant-pressure mode N_2 permeability test of S2 at 81.7 ^{o}C 96
Figure 4.11 a) Permeability of S2 versus temperature; b) permeability of S2 versus effective stress; c) permeability of S3 versus temperature; d) permeability of S3 versus effective stress; e) permeability of S4 versus temperature; and f) permeability of S4 versus effective stress 98
Figure 4.12 Variation of permeability of all specimens with: a) temperature; and b) effective stress 100

Figure 4.13 A qualitative representation of gas-permeability vs. thermal deformation of coal inferred from this experiments 101

Figure 4.14 Permeability of S1 and S4 versus axial strain during shearing at room temperature 102

Figure 5.1 3D finite difference grid and the idealized cavity 112

Figure 5.2 Normalized elastic modulus of the Hanna Basin coal versus temperature, normal and parallel to the bedding plane (Glass, 1984) as well as the assumed function used for scenario 3 118

Figure 5.3 Normalized permeability of the Wyodak coal versus temperature (Thorsness et al., 1978) and the assumed function used for scenario 4 119

Figure 5.4 Contours from scenario 1 after 182 days: a) temperature (ºC); b) displacement (m); c) volumetric strain (fraction); and d) plastic zone (yielded state) 121

Figure 5.5 Results from scenario 1: a) change in pore pressure and temperature along middle of the coal seam; b) change in pore pressure and temperature along base of the caprock; c) mean effective stress along middle of the coal seam and base of the caprock; and d) volumetric strain along middle of the coal seam and base of the caprock 123

Figure 5.6 Results from scenario 2: a) change in pore pressure and temperature along middle of the coal seam; b) change in pore pressure and temperature along base of the caprock; c) mean effective stress along middle of the coal seam and base of the caprock; and d) volumetric strain along middle of the coal seam and base of the caprock 124

Figure 5.7 Results from scenario 3: a) change in pore pressure and temperature along middle of the coal seam; b) change in pore pressure and temperature along base of the caprock; c) mean effective stress and elastic modulus along middle of the coal seam as well as mean effective stress along base of the caprock; and d) volumetric strain along middle of the coal seam and base of the caprock 125

Figure 5.8 Results from scenario 4: a) change in pore pressure and temperature along middle of the coal seam; b) change in pore pressure and temperature along base of the caprock; c) mean effective stress and permeability along middle of the coal seam as well as mean effective stress along base of the caprock; and d) volumetric strain along middle of the coal seam and base of the caprock 126

Figure 5.9 Results from scenario 5: a) change in pore pressure and temperature along middle of the coal seam; b) change in pore pressure and temperature along base of the caprock; c) mean effective stress along middle of the coal seam and base of the caprock; and d) volumetric strain along middle of the coal seam and base of the caprock 127
Figure 5.10 Displacements of the four monitoring points in different scenarios: a) point A; b) point B; c) point C; and d) point D 130
Figure 6.1 The UCG sites worldwide (Couch, 2009) 137
Figure 6.2 Schematics of the UCG process: a) linked vertical wells (LVW); and b) Controlled Retraction Injection Point (CRIP) (Couch, 2009) 137
Figure 6.3 Permeability vs. change in fluid porosity during drying and pyrolysis based on data available for the Wyodak coal (Thorsness et al., 1978) and the Xing-Long-Zhuang coal (Zhao et al., 2010) 145
Figure 6.4 Flow-geomechanical sequential coupling algorithms 145
Figure 6.5 Model geometry: a) 3D view; and b) vertical cross section of the gasification model at the plane of injection and production wells including monitoring points A, B, and C in the coal seam 147
Figure 6.6 Relative permeability of the Fruitland formation coal in New Mexico to gas and water (Gash et al., 1992) used in this study 151
Figure 6.7 Flow rates of different gas species in the produced syngas in the first 10 days of the simulation 152
Figure 6.8 Different contours in the horizontal plane containing the injection and production wells after 10 days: a) temperature; b) pore pressure; c) fluid porosity; d) coal concentration; e) char concentration; and f) steam mole fraction 153
Figure 6.9 Geomechanical changes in the model at vertical plane the of injection and production wells after 10 days: a) volumetric strain; b) vertical displacement (m); c) minimum total principal stress (Pa); d) shear stress (Pa); e) failure state; and f) 3D geometry of cavities 155
Figure 6.10 History of temperature, pore pressure, mean effective stress and volumetric strain for monitoring points for 10 days of simulation time: a) point A; b) point B; and c) point C 157
Figure 6.11 a) Geomechanical changes at the caprock bottom: a) mean effective stress profile; and b) vertical displacement profile 158

Figure 7.1 In-situ horizontal stress trajectory map of the WCSB (modified from Bell and Grasby, 2012) and placement of the Swan Hills UCG site 167
Figure 7.2 a) A simplified geology built for the geomechanical model of the Swan Hills UCG site (modified from Swan Hills Synfuels, 2012); b) geometry and mesh size for the coal gasification and geomechanical models; and c) geometry of the gasification model and details of a single linear CRIP 168
Figure 7.3 a) Placement of the Swan Hills UCG site in zone 3 of the Alberta Basin zoning map for lower bound of σhmin (modified from Hawkes et al., 2005); and b) principal stress gradients for the zone 3 170
Figure 7.4 Relative permeability of the Fruitland formation coal of New Mexico to gas and water (Gash et al., 1992) 176
Figure 7.5 A workflow for coupled modeling of the UCG (Akbarzadeh and Chalaturnyk, 2016) 182
Figure 7.6 Syngas composition over a 60-day period: a) syngas and species flow rates; and b) cumulative production of syngas and species as well as cumulative injected gas 184
Figure 7.7 a) Temperature; and b) pore pressure variations in a horizontal plane including the injection points and tip of the producer well 185
Figure 7.8 a) Temperature (^oC); and b) pore pressure contours (kPa) after 60 days in a horizontal plane including the injector and producer wells 186
Figure 7.9 Concentrations of different gas species after 60 days in a horizontal plane including the wellbores: a) CH_4; b) CO; c) CO_2; d) H_2; e) H_2O; and f) O_2 187
Figure 7.10 Outputs from the coal gasification model after 60 days: a) fluid porosity (fraction); b) carbon concentration (gmole/m^3); c) coal concentration (gmole/m^3); at a horizontal plane including the wells; d) fluid porosity (fraction) at a vertical plane including the wells; and e) a 3D view of the four cavities 188
Figure 7.11 a) Maximum shear stress (Pa); and b) volumetric strain increment (fraction); after 60 days in a vertical plane crossing the cavities centerline and containing the wellbores 190
Figure 7.12 Failure zones around the cavities after 60 days: a) in a vertical plane crossing the cavities centerline; and b) in a horizontal plane including the wellbores 191
Figure 7.13 Displacement vectors showing large deformation of coal seam towards the cavities at a vertical plane crossing the cavities centerline and containing the wellbores 192

Figure 7.14 a) Mean effective stress and volumetric strain in bottom of the immediate overburden; and b) z-displacement above the coal seam and top of the model 193

List of Tables

Table 3.1 ASTM D388-12 classification of coals by rank (ASTM, 2012)................................. 30
Table 3.2 Summary of high temperature coal experiment database 33
Table 4.1 Specimens' dimensions and density 79
Table 4.2 Testing program for each specimen 81
Table 4.3 Summary of N_2 gas permeability test results 97
Table 5.1 Geomechanical, thermal, and fluid properties of coal and rock layers....................... 114
Table 5.2 Summary of five numerical simulation scenarios.. 117
Table 6.1 Gasification reactions and kinetic parameters for the UCG in Alberta (Kariznovi et al., 2013) 141
Table 6.2 Proximate analysis of coal of the Alberta UCG (Kariznovi et al., 2013; Swan Hills Synfuels, 2012) 148
Table 6.3 Initial Alberta UCG reservoir properties required for modeling in STARS (Kariznovi et al., 2013; Nourozieh et al., 2010; Seifi et al., 2011) 148
Table 6.4 Coefficients for gas heat capacity correlation in Equation 6.14 (Computer Modelling Group Ltd., 2012) 149
Table 6.5 Geomechanical properties of coal and rock layers assumed in this study 150
Table 7.1 Chemical reactions and their kinetic parameters for the Alberta UCG (Kariznovi et al. 2013; Nourozieh et al., 2010) 172
Table 7.2 Initial properties for the gasification model (Kariznovi et al. 2013; Nourozieh et al. 2010; Seifi et al., 2011).. 177
Table 7.3 Geomechanical properties of different formations 181
Table 7.4 Syngas compositions from this study vs. field measurements by the Swan Hills Synfuels (2012)... 183

Chapter 1 Introduction

1.1. General

The concept of Underground Coal Gasification (UCG) is nearly one and a half centuries old. Numerous trial tests have been conducted worldwide to date; however, the process is still not in worldwide commercial operations. This is partly due to the complex nature of the UCG. This process may develop temperatures in the order of 1000 ^{o}C underground, turn the initial solid coal to char and ash, create a cavity underground, induce water phase change from liquid to steam, and develop cracks and microcracks in the coal seam and rock layers. UCG is a complex, coupled thermal-hydro-chemical-mechanical process.

1.2. Statement of the problem

Understanding how a coal seam and surrounding strata respond to the temperature and pore pressure changes around a gasification chamber is of significant importance for a successful commercial UCG operation. Diffusion of the produced gas (syngas) to the adjacent groundwater may occur if syngas pressure exceeds the reservoir pressure. How pore pressure is influenced by volumetric deformation around the cavity and the gasification temperature is very important, and has not been well studied.

This study revealed that no comprehensive High-Pressure High-Temperature (HPHT) dataset of coal experiments has been published which includes measurement of changes in transport (porosity, permeability), thermal, and mechanical properties of the same coal during heating. Porosity/permeability evolution of coal in the heated zone around the cavity and their relationship with geomechanical response are crucial factors in a coupled gasification-geomechanical simulation. It is more consistent if porosity/permeability measurements of coal are done under the same stress realization and within the same apparatus as the geomechanical experiments.

Published geomechanical modeling of the UCG did not consider a combination of syngas pressure and temperature, and geomechanical impacts, hence, a set of 3D fluid-thermal-mechanical analyses may represent the field behavior more realistically. At the next level of modeling, an appropriate simulation package for UCG should include a coupled reservoir and geomechanical simulation, not a separate gasification model and separate geomechanical model while simplifying the cavity geometry and ignoring the effect of groundwater. Instead, a proper coupled reservoir and geomechanical simulation package should use cavity geometry, temperature, and pore pressure calculated by the gasification model at any time step. Temperature-dependent properties for coal and rock shall be considered in such a model as material properties degrade by temperature in the process. This simulation should also account for chemical reactions, heat conduction and convection, cavity evolution, and multi-phase flow of water and gases. To date, there is no commercial software which offers the capability of fully-coupled gasification and geomechanical simulation of UCG.

1.3. Objectives

The objective of this research was to investigate the geomechanical impacts of the UCG on coal and surrounding formation by means of experimental studies and numerical simulations. The experimental part included studying structural changes in coal at high temperature as well as conducting HPHT triaxial experiments on Alberta coal. The simulation part included parametric geomechanical analyses of an idealized UCG cavity, development of a numerical workflow for coupled reservoir and geomechanical simulation of UCG, and its application for modeling the Alberta UCG project.

1.4. Methodology

To achieve the research objectives, the following steps were carried out:

- It was expected that due to the organic nature of coal, its behavior to elevated temperatures is different from other rock types. To examine this idea, prior to the experimental activities of this research, a comprehensive review of published literature, from different disciplines, was conducted. The impact of elevated temperature on weight loss, thermal deformation, microcrack generation, pore volume, average pore aperture, porosity, permeability, tensile, compressive and shear stress-strain responses, elastic and shear moduli, and Poisson's ratio of coals of different ranks were discussed and compared.

- An HPHT triaxial apparatus up was upgraded and utilized in this study to accommodate measuring permeability of Alberta coal to nitrogen gas along with geomechanical testing. Several coal specimens were cored from large coal blocks acquired from the Genesee coal mine in Central Alberta. The coal specimens were tested under different confining stresses, ranging from 2 to 12 MPa, and temperatures ranging from room temperature to about 200 ^{o}C. Thermal deformation, stress-strain, elastic properties as well as permeability of the specimens were measured under different temperatures and confining stresses. Permeability evolution of some specimens (as analogues for naturally fractured rock) during progressive shearing was also studied.

- Geomechanical simulation of an idealized UCG cavity was performed in order to understand fundamentals of the strata response to evolution of a cubic cavity which included high temperature syngas. This simulation was conducted utilizing FLAC3D of ITASCA by means of a series of three-dimensional (3D) coupled thermal-fluid-mechanical analyses. Impacts of different operational pressures (below, equal, and above the initial reservoir pressure) and coal material properties (constant and temperature-dependent elastic modulus and permeability) on thermally-induced pore pressure around the cavity as well as deformation and stresses were investigated.

- A sequentially coupled reservoir and geomechanical simulation workflow was developed for an example 3D UCG problem. The coal gasification simulation capability of STARS (from the Computer Modelling Group Ltd., CMG) was integrated with geomechanical modeling of FLAC3D. This coupling package was programmed using FORTRAN and a LINUX script program. This coupling workflow facilitates simultaneous observation of the temperature front movement, syngas production, cavity growth, as well as stresses and deformation of the strata (geomechanical responses).

- The developed coupling workflow was applied to reservoir scale modeling of the Alberta UCG project. In-situ stress magnitudes and orientations for this particular site were taken from previous studies on the Alberta sedimentary basin performed by other researchers. Coal properties required for this simulation were estimated based on the observed constitutive behavior of our coal specimens in the experimental program along with other published research papers. This modeling utilized the developed coupling package for simultaneous observation of the syngas production, advancement of the gasification chamber, and the cavity growth as well as stresses and displacements, and zone of failure in the strata.

1.5. Organization of the thesis

This thesis is prepared in a paper format and consists of eight chapters. Five journal articles have been prepared based on the achievements of this research program. Following is a brief outline of each chapter.

- Chapter 1 is the introduction chapter that includes problem statement, objectives and methodologies, as well as organization of the thesis.
- Chapter 2 provides a brief background of the UCG and geomechanical risks involved in a UCG operation. It also presents the state of high-temperature experimental studies of coal, as well as numerical simulations of the UCG.
- Chapter 3 details structural changes in coal at high temperature by conducting an extensive and detailed review of published HPHT experiments of coals of different ranks.
- Chapter 4 presents the HPHT triaxial apparatus, experimental plan, and results of thermal deformation, permeability, and geomechanical tests of the Alberta coal; both at room and high temperatures.
- Chapter 5 includes the parametric geomechanical analyses of an idealized UCG cavity under different syngas pressure and temperature as well as material properties.

- Chapter 6 elaborates on the development of a sequentially coupled reservoir and geomechanical modeling workflow for UCG and its application to a 3D example.
- Chapter 7 demonstrates the application of the sequentially coupled reservoir and geomechanical modeling workflow of chapter 6 to simulation of the UCG project in Swan Hills, Alberta.
- Chapter 8 summarizes the research program, the findings and conclusions of each chapter, and recommendations for further studies.

Chapter 2 Literature Review

2.1. Introduction

Coal is currently the world's second largest source of primary energy (after oil) due to its low-cost, abundance, and global distribution. More than 75 countries have coal deposits. At the moment, coal is accounting for about 40% of global electricity production (World Energy Council, 2013) which is expected to decrease in the coming years; however the actual coal consumption will grow. While countries in Europe and North America are trying to switch to alternative energy sources, the large emerging economies, mainly in Asia, are increasing their coal consumption (World Energy Council, 2013). The 2013 Survey of Energy Resources estimated world coal reserves at about 869 billion tonnes, which is expected to last for about 115 years, longer than those of conventional oil and gas reserves (World Energy Council, 2013).

The great majority of Canadian coal resources are located in Western Canada (National Energy Board, 2013). Coal has constituted a major energy provider for the province of Alberta. The Government of Alberta 2013-2014 Energy Annual Report stated that, in both 2012 and 2013, 52% of Alberta's electricity was supplied by coal (Government of Alberta, 2014). The Alberta Energy Regulator (AER) assessed the remaining coal reserves at 33.2 billion tonnes, the ultimate potential resources at 620 billion tonnes, and the ultimate in-place resources at 2000 billion tonnes (AER, 2014). Alberta's in-place coal resources contain more than three times the energy content of the Alberta's oil sands; however, much of the coal is too deep or too costly to mine by conventional underground methods (Richardson and Singh, 2012).

The major concern about coal-fired power plants is greenhouse gas (GHG) emissions. The 2035 outlook of Canada's energy future predicted a declining role of coal used in power generation (National Energy Board, 2013). The 2035 projection highlighted that under the new federal regulations (Minister of Justice, 2012) requiring coal plants to reduce GHG emissions to below 420 metric tons of CO_2 per GW.h, any coal facilities built after July 11, 2015 should be equipped with carbon capture and storage (CCS) technology in order to be permitted to operate. The province of Alberta is also committed to reduce greenhouse gas (GHG) emission in energy production (Government of Alberta, 2014). One way of exploiting energy out of the vast Alberta coal resources, while meeting the 2035 outlook, could be underground coal gasification (UCG) technology.

Underground coal gasification is a technique to extract energy from coal in-situ. The UCG was first suggested by Sir William Siemens, a German scientist, in 1868, and at about the same time, by Dmitri Mendeleev, a Russian chemist (Couch, 2009). UCG provides access to coal seams which are otherwise un-minable; coal seams which are too deep, too thin, or of poor quality. UCG eliminates presence of coal miners underground, coal transportation and storage, as well as the issue of ash disposal. A UCG plant can be operated using substantially less capital expenses and generates a smaller carbon dioxide (CO_2) footprint compared to the equivalent conventional coal-fired power plants (Burton et al., 2006). The produced gas (synthetic gas or syngas) mainly contains H_2, CH_4, CO, CO_2, and to a lesser extent contaminant by-products. The syngas is used for a number of different applications. It can be directly combusted for power generation; likewise, it can be liquefied to transport fuels. The syngas can also be separated into methane and hydrogen streams for use as petrochemical or fertilizer production (Couch, 2009).

Two main operational techniques have been practiced in UCG trials around the world; Linked Vertical Wells (LVW) and Controlled Retraction Injection Point (CRIP), as shown in Figure 2.1. The LVW method (Figure 2.1.a) requires drilling of vertical injection and production wells and a linkage between them. The linkage can be created in several ways; reverse combustion, electro-linking, hydraulic fracturing, and horizontal directional drilling. After the coal is brought to ignition, pressurized air or an oxygen-based gaseous mix is introduced into the coal seam through the injection well to maintain coal gasification front. Meanwhile, syngas is recovered via the producer well. CRIP is a newer UCG technique which provides more control over where the gasification takes place and allows access to deeper coal seams with far fewer wells being drilled from the surface. CRIP could be performed in two arrangements; linear CRIP, and parallel CRIP. Linear CRIP (Figure 2.1.b) needs one vertical well as the producer and an in-seam horizontal well as the injector. In linear CRIP, ignition is initiated at a point near the producer well. A burner is mounted on the end of a coiled tubing assembly which is passed down to the injection point. A mixture of combustible gases is provided to the burner to ignite the coal. After sufficient amount of coal has been burnt, the injection point is retracted in the upstream direction. In parallel CRIP (Figure 2.1.c), two in-seam horizontal wells are drilled alongside in the lower part of the seam, and then turned to meet at a point. At the interception point, a vertical well is drilled, which is used for ignition of the coal. One of the in-seam wells is used as the injection well and the other one is set as the producer well.

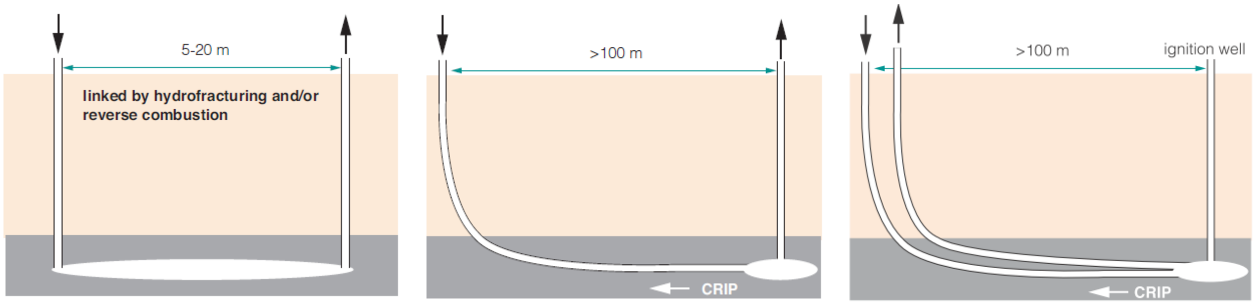

a) b) c)

Figure 2.1 Schematics of the UCG processes: a) linked vertical wells (LVW), b) linear CRIP, c) parallel CRIP (Couch, 2009)

UCG development has been affected by other resources such as oil and gas. Numerous trials have been performed at various depths and in different countries (Burton et al., 2006; Couch, 2009). Yerostigaz, located in Angren, Uzbekistan, is the world's longest running commercial UCG facility which has been in operation for more than 50 years (Linc Energy, 2015). In Canada, a very deep UCG pilot test (depth of 1400 m) was successfully operated in Swan Hills, Alberta (Swan Hills Synfuels, 2012).

2.2. Geomechanical risks in a UCG project

UCG represents a complex process. It covers different areas such as geology, hydrogeology, geomechanics, drilling, chemical, and process engineering. A UCG operation contains, in particular, geomechanical and hydrogeological risks. Coal gasification reactions generate very high temperature, over 1000 ºC, along with evolution of cavities which are partially filled in with ash as well as rock/coal materials spalled into the cavities. The final outcome could be geomechanical damage to the bounding seal system, significant deformation and contamination of groundwater. Gas escape during a UCG operation and leaching of pyrolysis products, both syn- and post-gasification, and leaching of inorganic contaminants from the mineral ash produced by the gasification process are the main sources of concern for groundwater contamination (Burton et al., 2006; Couch, 2009; Sury et al., 2004a; Sury et al., 2004b). The geomechanical component of a UCG operation is a critical element which has two important aspects. Firstly, geomechanical responses of the strata to the coal gasification process can determine level of risk or safety of a UCG project. The linkage between the wells may be blocked due to excessive caprock failure; the project might be asked to shut down due to significant deformation at ground surface or contaminated groundwater. Secondly, failure, cracking, deformation and, in general, geomechanical changes in coal and rock layers around the cavity alters transport properties (porosity and permeability) of coal adjacent to the gasification chamber. The latter will, in turn, influence the chemical process of coal gasification. In conclusion, the UCG represents a coupled hydro-thermal-chemical-mechanical process.

2.3. Previous experimental and field studies of UCG

Performance of a UCG operation depends on a number of factors and can be improved by characterization of coal behavior at elevated temperature, proper on-site monitoring, and process simulation considering the effect of geomechanics. Researchers extensively studied mechanical, thermal, and transport properties (porosity and permeability) of coals of different ranks from various locations (e.g., Balek and de Koranyi, 1990; de Koranyi and Balek, 1985; Feng et al., 2012; Glass, 1984; Liu et al., 2014; Long et al., 2009; Niu et al., 2014; Perera et al., 2012; Qu et al., 2012; Shoemaker, 1976; Singer and Tye, 1979; Su et al., 2013; Thorsness et al., 1978; Wan et al., 2011; Wang et al., 2013; Xu et al., 2014; Yin et al., 2013; Yu et al., 2012; Zhao et al., 2010). Several coal block gasification experiments were also reported (e.g., Daggupati et al., 2010 & 2011; Kostur and Kacur, 2008; Stanczyk et al., 2010 & 2011 & 2012; Wiatowski et al., 2012). The main focus of these coal block gasification experiments were chemical aspects of gasification (i.e., syngas flow rate and composition), as well as temperature front movement and cavity geometry.

Field instrumentation in some previous UCG trials helped to understand the geomechanical and hydrogeological impacts of UCG, both syn- and post-gasification (e.g., Aiman et al., 1980; Bartel et al. 1976; Brandenburg et al., 1975; Cooke and Oliver, 1983; Kotyrba et al., 2015; Luo et al. 2008; Northrop et al., 1977; Swan Hills Synfuels, 2012; Youngberg et al., 1983). Drilling after the Hanna II trial in Wyoming revealed boundaries of the gasification zone. A void space was observed above the rubble zone which indicated spalling of a portion of the caprock into the cavity. Reflectance data on coal samples acquired from the site revealed that the coal was altered by temperatures ranging between 245 ºC and 670 ºC. Rubble of the caprock found within the cavity contained various pyro-metamorphic minerals, indicating that temperatures of at least 1200 ºC were reached during the trials (Brandenburg et al., 1975; Northrop et al., 1977; Youngberg et al., 1983). Post-gasification water analyses of the same trial test site found evidence of groundwater contamination by pyrolysis products and leachate (Cooke and Oliver, 1983). Post-gasification drilling at the Hoe Creek II in Campbell County, Wyoming also helped determine the gasification zone boundaries and revealed a void space above the rubble zone (Aiman et al., 1980). Recently, Kotyrba et al. (2015) utilized microgravity measurements for a shallow UCG test site (a depth of 16 m). They did the survey prior to and after the gasification which helped identify a UCG cavity.

2.4. Review of analytical and numerical modeling of UCG

2.4.1. Analytical solutions

Several researchers developed analytical solutions for cavity growth prediction mainly based on the chemical process of combustion (e.g., Fausett 1984; Jung 1987; Sansgiry 1990).

2.4.2. Gasification simulations

Extensive coal gasification simulation studies of UCG have been published. A series of chemical reactions with the corresponding reaction kinetics were utilized. Two classes of commercial software were used for these modeling works; Computational Fluid Dynamics (CFD) based software such as ANSYS FLUENT (e.g., Sarraf Shirazi et al., 2013; Zogala and Janoszek, 2015), and reservoir engineering software such as STARS (e.g., Nourozieh et al., 2010; Seifi et al., 2011). The output of those modeling works included: syngas flow rate and composition, temperature, change in porosity and permeability of coal, syngas heat value, etc. Khan et al. (2015) recently reviewed underground coal gasification modeling works to date.

2.4.3. Geomechanical simulations

Several geomechanical studies of UCG process have been published. Usually, the UCG cavity geometries were simplified in those works. Some of them even considered the entire formation to be dry and/or ignored any potential influence of the UCG cavity evolution, high temperature of the gasification chamber, and syngas pressure on groundwater. Advani et al. (1976 &1977) applied high temperature and pressure to boundaries of an elliptical cavity using plane strain linear thermo-elastic finite element models to investigate tangential stress changes around the cavity. Tan et al. (2008) applied high temperature to boundaries of a UCG cavity in ANSYS software utilizing a plane strain finite element model. They used temperature-dependent thermal and mechanical properties for coal and rocks and conducted coupled thermal-mechanical analysis in order to study changes in stresses. However, they did not consider groundwater or syngas pressure. Two-dimensional (2D) elastic finite element modeling of a disc-shaped reservoir was carried out by Vorobiev et al. (2008). To simulate a shallow UCG activity, they did element removal and observed stress redistribution and surface subsidence. Pressure and temperature of gasification in the cavity was set to zero. Morris et al. (2009) simulated a simplified three-dimensional (3D) UCG cavity in LDEC (Livermore Distinct Element Code), then removed any coal elements became unstable by the excavation, under gravitational and an in-situ stress fields. They did not consider gasification temperature, nor groundwater or syngas pressure. They also studied the influence of coal cleat orientation and persistence on cavity evolution. Laouafa et al. (2014) performed 2D and 3D geomechanical simulations and studied displacement and fracturing distribution during progressive increase in UCG cavity size.

2.4.4. Coupled gasification-geomechanical simulations

Coupled gasification-geomechanical modeling can better represent this complex process by allowing prediction of geomechanical response of the coal seam and surrounding strata to coal gasification and investigating caprock and bedrock integrity at different times and under various operational conditions. Different coupling approaches used in reservoir-geomechanics explained elsewhere (Settari and Walters, 2001) can be utilized for coal gasification-geomechanics as well. To date, limited coupled coal gasification and geomechanical modeling works have been published. The Lawrence Livermore National Laboratory (LLNL) in California recently developed a new integrated in-house 3D UCG simulator which performs both gasification and geomechanics simulations (Nitao et al., 2011). They validated their cavity geometry and syngas flow rate and species using field trails. Their predictions for 15 days production at the Hoe Creek III test (1979) in Powder River Basin in Wyoming (Camp et al., 2012; Nitao et al., 2011) and 46 days production at the Rocky Mountain I CRIP test (1987-88) in Hanna Basin, Wyoming (Camp et al., 2012) were close to field measurements. How the LLNL's package does the coupling and what type of material properties is used has not yet been disclosed. Moreover, this package is not commercially available.

2.5. References

Advani, S. H., Lin, Y. T., & Shuck, L. Z. (1977). Thermal and structural response evaluation for underground coal gasification. *Society of Petroleum Engineers Journal*, *17*(06), 413-422.

Advani, S. H., Shuck, L. Z., Lin, Y. T., & Chang, H. Y. (1976). Thermomechanics simulations associated with underground coal gasification. In *The 17th US Symposium on Rock Mechanics (USRMS)*. American Rock Mechanics Association.

Aiman, W. R., Ganow, H. C., & Thorsness, C. B. (1980). Hoe Creek II revisited: boundaries of the gasification zone. Combustion Science and Technology, 23(3-4), 125-130.

Alberta Energy Regulator (AER). (2014). ST98-2014: Alberta's Energy Reserves 2013 and Supply/Demand Outlook 2014-2023. (http://www.aer.ca/data-and-publications/statistical-reports/st98, accessed Oct. 08, 2014).

Balek, V., & de Koranyi, A. (1990). Diagnostics of structural alterations in coal: Porosity changes with pyrolysis temperature. *Fuel*, *69*(12), 1502-1506.

Bartel, L. C., Beard, S. G., Beckham, L. W., Reed, R. P., & Seavey, R. W. (1976). Instrumentation results from an in-situ coal gasification experiment. In *SPE Annual Fall Technical Conference and Exhibition*. Society of Petroleum Engineers.

Brandenburg, C. F., Reed, R. P., Boyd, R. M., Northrop, D. A., Jennings, J. W. (1975). Interpretation of chemical and physical measurements from an in situ coal gasification experiment. In *SPE Annual Fall Technical Conference and Exhibition*. Society of Petroleum Engineers.

Burton, E., Friedmann, J., & Upadhye, R. (2006). Best practices in underground coal gasification. Draft. US DOE contract no W-7405-Eng-48. Lawrence Livermore National Laboratory.

Camp, D.W., Nitao, J. J., White, J. A., Burton, G. C., Reid, C., Friedmann, J. (2012). A fully integrated 3-D multi-physics UCG simulator applied to UCG field tests. A presentation at the 2nd IEA Underground Coal Gasification Network Workshop, Banff, Alberta, Canada.

Cooke, S. D., & Oliver, R. L. (1983). Ground water quality at the Hanna underground coal gasification experimental sites, Hanna, Wyoming: data base and summary. *US Department of Energy/Associated Western Universities, Inc. Under cooperative, contract (DE-AC07–76ET10723)*.

Couch, G. R. (2009). Underground coal gasification. IEA Clean Coal Centre. International Energy Agency, London.

Daggupati, S., Mandapati, R. N., Mahajani, S. M., Ganesh, A., Mathur, D. K., Sharma, R. K., & Aghalayam, P. (2010). Laboratory studies on combustion cavity growth in lignite coal blocks in the context of underground coal gasification. *Energy*, *35*(6), 2374-2386.

Daggupati, S., Mandapati, R. N., Mahajani, S. M., Ganesh, A., Sapru, R. K., Sharma, R. K., & Aghalayam, P. (2011). Laboratory studies on cavity growth and product gas composition in the context of underground coal gasification. *Energy*, *36*(3), 1776-1784.

de Koranyi, A., & Balek, V. (1985). Structural changes in coals during pyrolysis. *Thermochimica Acta*, *93*, 737-740.

Feng, Z. J., Zhao, Y. S., & Wan, Z. J. (2012). Experiment study of the thermal deformation of in-situ gas coal. *Rock Mechanics: Achievements and Ambitions-Proceedings of the 2nd ISRM International Young Scholars' Symposium on Rock Mechanics*, 103-108.

Glass, R. E. (1984). The thermal and structural properties of a Hanna basin coal. *Journal of Energy Resources Technology*, *106*(2), 266-271.

Government of Alberta. (2014). Government of Alberta 2013-2014 Energy Annual Report. (http://www.energy.alberta.ca/About_Us/1001.asp, accessed Oct. 08, 2014).

Khan, M. M., Mmbaga, J. P., Shirazi, A. S., Liu, Q., & Gupta, R. (2015). Modelling underground coal gasification-a review. *Energies*, *8*(11), 12603-12668.

Kostur, K., & Kacur, J. (2008). The monitoring and control of underground coal gasification in laboratory conditions. *Acta Montanistica Slovaca*, *13*(1), 111-117.

Kotyrba, A., Kortas, L., & Stańczyk, K. (2015). Imaging the underground coal gasification zone with microgravity surveys. *Acta Geophysica, 63*(3), 634-651.

Laouafa, F., Farret, R., Vidal-Gilbert, S., & Kazmierczak, J. B. (2014). Overview and modeling of mechanical and thermomechanical impact of underground coal gasification exploitation. *Mitigation and Adaptation Strategies for Global Change*, 1-30.

Linc Energy. (2015). (http://www.lincenergy.com, accessed Nov. 26, 2015)

Long, Q.M., Wen, G. C., Zou, Y. H., & Zhao, X. S. (2009). Experimental study on gas permeability by adsorption under 3D-stress. *Journal of Coal Science & Engineering (China) 15*(2), 148-151.

Luo, X., Tan, Q., Luo, C., & Wang, Z. (2008). Microseismic monitoring of burn front in an underground coal gasification experiment. In *The 42nd US Rock Mechanics Symposium (USRMS)*. American Rock Mechanics Association.

Minister of Justice. (2012). Reduction of Carbon Dioxide Emissions from Coal-fired Generation of Electricity Regulations (SOR/2012-167) (http://laws.justice.gc.ca/eng/regulations/SOR-2012-167/, accessed Oct. 14, 2014).

Morris, J. P., Buscheck, T. A., & Hao, Y. (2009). Coupled geomechanical simulations of UCG cavity evolution. In *Proceedings of the 2009 International Pittsburgh Coal Conference, Pittsburgh PA*.

National Energy Board. (2013). Canada's Energy Future 2013 - Energy Supply and Demand Projections to 2035 (http://www.neb-one.gc.ca/clf-nsi/rnrgynfmtn/nrgyrprt/nrgyftr/2013/nrgftr2013-eng.html, accessed Oct. 08, 2014).

Nitao, J. J., Camp, D. W., Buscheck, T. A., White, J. A., Burton, G. C., Wagoner, J. L., & Chen, M. (2011). Progress on a new integrated 3-D UCG simulator and its initial application. In *International Pittsburgh Coal Conference* (pp. 1-13).

Niu, S., Zhao, Y., & Hu, Y. (2014). Experimental investigation of the temperature and pore pressure effect on permeability of lignite under the in situ condition. *Transport in Porous Media*, *101*(1), 137-148.

Northrop, D. A., Beard, S. G., Bartel, L. C., Beckham, L. W., & Hommert, P. J. (1977). Instrumentation for in situ coal gasification: An assessment of techniques evaluated on the Hanna II experiment (No. SAND-77-1072). Sandia Labs., Albuquerque, N. Mex. (USA).

Nourozieh, H., Kariznovi, M., Chen, Z., & Abedi, J. (2010). Simulation study of underground coal gasification in Alberta reservoirs: geological structure and process modeling. *Energy & Fuels*, *24*(6), 3540-3550.

Perera, M. S. A., Ranjith, P. G., Choi, S. K., & Airey, D. (2012). Investigation of temperature effect on permeability of naturally fractured black coal for carbon dioxide movement: An experimental and numerical study. *Fuel*, *94*, 596-605.

Qu, H., Liu, J., Chen, Z., Wang, J., Pan, Z., Connell, L., & Elsworth, D. (2012). Complex evolution of coal permeability during CO_2 injection under variable temperatures. *International Journal of Greenhouse Gas Control*, *9*, 281-293.

Richardson, R. J., & Singh, S. (2012). Prospects for underground coal gasification in Alberta, Canada. *Proceedings of the ICE-Energy, 165*(3), 125-136.

Sarraf Shirazi, A., Karimipour, S., & Gupta, R. (2013). Numerical simulation and evaluation of cavity growth in in situ coal gasification. *Industrial & Engineering Chemistry Research*, *52*(33), 11712-11722.

Seifi, M., Chen, Z., & Abedi, J. (2011). Numerical simulation of underground coal gasification using the CRIP method. *The Canadian Journal of Chemical Engineering*, *89*(6), 1528-1535.

Settari, A., & Walters, D. A. (2001). Advances in coupled geomechanical and reservoir modeling with applications to reservoir compaction. *SPE Journal*, *6*(03), 334-342.

Shoemaker, H. D. (1976). Mechanical properties of the Pittsburgh coal at elevated temperatures. PhD Dissertation, West Virginia University.

Singer, J.M., & Tye, R.P., (1979). Thermal, mechanical, and physical properties of selected bituminous coals and cokes. Bureau of Mines Report RI 8364.

Stanczyk, K., Smolinski, A., Kapusta, K., Wiatowski, M., Swiadrowski, J., Kotyrba, A., & Rogut, J. (2010). Dynamic experimental simulation of hydrogen oriented underground gasification of lignite. *Fuel 89*, 3307-3314.

Stanczyk, K., Howaniec, N., Smolinski, A., Swiadrowski, J., Kapusta, K., Wiatowski, M., Grabowski, J., & Rogut, J. (2011). Gasification of lignite and hard coal with air and oxygen enriched air in a pilot scale ex situ reactor for underground gasification. *Fuel 90*, 1953-1962.

Stanczyk, K., Kapusta, K., Wiatowski, M., Swiądrowski, J., Smolinski, A., Rogut, J., & Kotyrba, A. (2012). Experimental simulation of hard coal underground gasification for hydrogen production. *Fuel*, *91*(1), 40-50.

Su, F., Nakanowataru, T., Itakura, K., Ohga, K., & Deguchi, G. (2013). Evaluation of structural changes in the coal specimen heating process and UCG model experiments for developing efficient UCG systems. *Energies 6*, 2386-2406.

Sury, M., White, M., Kirton, J., Carr, P., Woodbridge, R., Mostade, M., Chappell, R., Hartwell, D., Hunt, D., & Rendell, N. (2004a). Review of environmental issues of underground coal gasification-best practice guide: United Kingdom Department of Trade and Industry Report No. COAL R273. DTI/Pub URN 04/1881.

Sury, M., White, M., Kirton, J., Carr, P., Woodbridge, R., Mostade, M., Chappell, R., Hartwell, D., Hunt, D., & Rendell N. (2004b). Review of environmental issues of underground coal gasification: United Kingdom Department of Trade and Industry. Report No. COAL R272. DTI/Pub URN 04/1880.

Swan Hills Synfuels. (2012). Swan Hills in-situ coal gasification technology development; Final outcomes report. Swan Hills Synfuels, Alberta, Canada.

Tan, Q., Luo, X., & Li, S. (2008). Numerical modeling of thermal stress in a layered rock mass. In *The 42nd US Rock Mechanics Symposium (USRMS)*. American Rock Mechanics Association.

Thorsness, C. B., Grens, E. A., & Sherwood, A. (1978). A one-dimensional model for in situ coal gasification. UCRL-52523, Lawrence Livermore, National Laboratory (LLNL) Report, Berkeley, California.

Vorobiev, O. Y., Morris, J. P., Antoun, T. H., & Friedmann, S. J. (2008). Geomechanical simulations related to UCG activities. In *International Pittsburgh Coal Conference, Pittsburgh, PA*.

Wan, Z., Feng, Z., Zhao, Y., Zhang, Y., Li, G., & Zhou, C., (2011). Elastic modulus's evolution law of coal under high temperature and triaxial stress. *Journal of China Coal Society, 36*(10), 1736-1740.

Wang, C., He, M., Zhang, X., Liu, Z., & Zhao, T. (2013). Temperature influence on macro-mechanics parameter of intact coal sample containing original gas from Baijiao Coal Mine in China. *International Journal of Mining Science and Technology. 23*(4), 597-602.

Wiatowski, M., Stanczyk, K., Swiadrowski, J., Kapusta, K., Cybulski, K., Krause, E., Grabowski, J., Rogut, J., Howaniec, N. & Smoliński, A. (2012). Semi-technical underground coal gasification (UCG) using the shaft method in Experimental Mine "Barbara". *Fuel*, *99*, 170-179.

World Energy Council. (2013). World Energy Resources: 2013 Survey. (https://www.worldenergy.org/publications/2013/world-energy-resources-2013-survey/, accessed Nov. 27, 2015).

Xu, R., Li, H., Guo, C., & Hou, Q. (2014). The mechanisms of gas generation during coal deformation: Preliminary observations. *Fuel 117*, 326-330.

Yin, G., Jiang, C., Wang, J.G., & Xu, J. (2013). Combined effect of stress, pore pressure and temperature on methane permeability in anthracite coal: An experimental study. *Transport in Porous Media 100*(1), 1-16.

Youngberg, A.D., Sinks, D. J., Craig, G. N., Ethridge, F. G., & Burns, L. K. (1983). Postburn evaluation for Hanna II, Phases 2 and 3 underground coal gasification experiments, Hanna, Wyoming. United States Office of Scientific and Technical Information, Technical Information Center. Under cooperative contract (DE-FC21-83FE60177).

Yu, Y., Liang, W., Hu, Y., & Meng, Q. (2012). Study of micro-pores development in lean coal with temperature. *International Journal of Rock Mechanics & Mining Sciences 51*, 91-96.

Zhao, Y., Qu, F., Wan, Z., Zhang, Y., Liang, W., & Meng, Q. (2010). Experimental investigation on correlation between permeability variation and pore structure during coal pyrolysis. *Transport in Porous Media, 82*(2), 401-412.

Zogala, A., & Janoszek, T. (2015). CFD simulations of influence of steam in gasification agent on parameters of UCG process. *Journal of Sustainable Mining*, *14*(1), 2-11.

Chapter 3 Structural Changes in Coal at Elevated Temperature Pertinent to Underground Coal Gasification[1]

3.1. Abstract

Underground coal gasification (UCG) has been identified as an environmentally friendly technique for in-situ gasification of deep un-mineable coal seams. As coal is gasified, a cavity is created which grows with time. Cavity evolution along with high temperature imposes changes to the coal and surrounding strata. Understanding structural changes in the coal during drying/vaporization, pyrolysis, and gasification in UCG is a key factor in studying growth of the gasification zone and helps in optimizing the UCG process in order to minimize syn- and post-gasification risks to the strata and groundwater. The main objective of this study is to elaborate structural impacts of UCG process on coal and to review the current state of knowledge in the area of influence of elevated temperature on transport and mechanical properties of coal in the context of UCG. Published high-pressure high-temperature experimental studies on coals are very scarce; hence, this study reviews and compares behavior of different rank coals from different part of the world in order to develop a pathway for future high-pressure high-temperature geomechanical experiments of coals. Impact of elevated temperature on weight loss, thermal deformation, microcrack generation, pore volume, average pore aperture, porosity, permeability, tensile, compressive and shear stress-strain responses, elastic and shear moduli, and Poisson's ratio of the coals under study are discussed and compared.

Keywords: Underground coal gasification (UCG), Elevated temperature, Cavity, Structural change, Pore structure, Elastic modulus

---

[1] A version of this chapter has been published as:
Akbarzadeh, H., & Chalaturnyk, R. J. (2014). Structural changes in coal at elevated temperature pertinent to underground coal gasification: A review. International Journal of Coal Geology, 131, 126-146.

3.2. Introduction

The 2010 Survey of Energy Resources estimated world coal reserves about 860 Gt. Since 2000, global coal consumption has grown faster than any other fuel at 4.9% per year and is expected to rise by over 60% by 2030 (World Energy Council, 2010). There are greater resources deep underground that can be a supplement to the proved reserves but, based on the current technology, are not economically mineable. Underground coal gasification (UCG) is an alternative technique that can address the extra demands for coal consumption with providing access to coal seams which are not economically mineable (coal seams which are too deep or too thin or of poor quality). A UCG plant can be operated using substantially less capital expenses compared to an equivalent conventional surface gasifier (Burton et al., 2006).

Underground coal gasification was first suggested by Sir William Siemens, a German scientist, in 1868. At about the same time, Dmitri Mendeleev, a Russian chemist, suggested the idea of controlling underground coal fires by means of drilling injection and production wells (Couch, 2009). The UCG has experienced a lot of uncertainty in its development life due to shortage/abundance and fluctuations in price of other resources such as natural gas and oil. The Yerostigaz plant in Angren, Uzbekistan, is the world's only commercial UCG operation. It has been in operation since 1961. It continuously produces one million cubic meters of syngas each day which is transported by pipeline to the nearby Angren Power Station. The coal reserve is sufficient to continue the operation for another 50 years (Linc Energy, 2014). A recent worldwide renewed interest in the UCG technology has been driven in coal-producing regions due to increasing price of other fuels as well as successful and promising UCG trials. Many countries are identifying new sites for UCG or have UCG projects at planning or review stages (UCG Association, 2014). In Canada, the world's deepest UCG pilot test was successfully conducted at 1400 m depth in Swan Hills, Alberta (Swan Hills Synfuels, 2012).

Although the UCG has been attempted in many countries (Burton et al., 2006), because of the nature of the process, which is a coupled thermal-hydro-chemical-mechanical process, there always are risks in a UCG operation. Gasifying coal underground causes mechanical changes to the coal seam and surrounding rock layers. Evolution of a cavity along with high temperature over 1000 ºC, as well as change in pore-fluid phase and pressure may result in fracturing and collapsing of the strata adjacent to the gasification chamber which will create an area of enhanced permeability and porosity around the cavity. Subsidence of the ground surface in shallow UCG and contamination of groundwater are the other risks associated with the UCG projects.

In order to optimize UCG process and mitigate syn- and post-gasification risks, understanding structural changes in the coal seam, especially in the zone around the cavity which is exposed to high temperature, is crucial. Knowledge of structural behavior of coal at elevated temperature can be gained through coal-block gasification, field trials, and high-temperature laboratory testing. Experimental studies of coal-block gasification to date were focused on the chemical aspect of gasification (i.e., syngas flow and composition), as well as temperature front movement and cavity geometry (Daggupati et al., 2010; Daggupati et al., 2011; Kostur and Kacur, 2008; Stanczyk et al., 2010 & 2011 & 2012; Yang, 2004). Numerous UCG trials have been performed worldwide (Couch, 2009; Burton et al., 2006). Findings from some of them were reported and are publically available (Aiman et al., 1980; Bartel et al., 1976; Brandenburg et al., 1975; Cooke and Oliver, 1983; Kapusta et al., 2013; Luo et al., 2008; Northrop et al., 1977; Wang et al., 2009; Youngberg et al., 1983). The outcomes of these trails focused on syngas flow, syngas heating value and composition, temperature front movement with time, microseismic events, groundwater contamination studies, and boundaries of the UCG cavities.

There is scarcity in literature regarding thermo-mechanical response of coal to high temperature. Limited laboratory studies have been carried out in order to understand structural response of coal (of sizes of small laboratory specimens, not in the order of gasification of a coal block) under elevated temperatures approaching the UCG temperature (e.g., Balek and de Koranyi, 1990; de Koranyi and Balek, 1985; Feng et al., 2012; Glass, 1984; Niu et al., 2014; Shoemaker, 1976; Singer and Tye, 1979; Su et al., 2013; Thorsness et al., 1978; Wan et al., 2011; Yu et al., 2012; Zhao et al., 2010). Elevated temperature in this study is considered to be temperature above 200 ºC. There are several works which tested coal samples under lower temperatures (e.g., Long et al., 2009; Perera et al., 2012; Qu et al., 2012; Wang et al., 2013; Xu et al., 2014; Yin et al., 2013) that are not included in this study.

The main objective of this study was to elaborate structural impacts of UCG process on coal seam, and strata, as well as, to review and discuss published experimental studies regarding structural changes in coal at elevated temperature in the context of UCG. It is aimed to give some insights on a number of questions related to structural changes in coal during drying/vaporization, pyrolysis, and gasification as, for example:

- Whether coal swells or shrinks;
- Whether or not thermal deformation characteristics of coal is similar to other porous media;
- Whether or not there is a correlation between gas generation and coal deformation;
- Whether or not there is a typical constitutive model for porosity evolution of all coals;
- Whether or not there is a typical constitutive model for permeability evolution of all coals;
- What is the nature of the porosity and permeability inter-relationship;
- What is the role of injection gas pressure on permeability;
- How are compressive, shear, and tensile strengths of coal affected;
- How are elastic and shear moduli of coal affected;
- Whether or not there is a correlation between coal rank and its response to high temperature;
- What is the role of anisotropy (direction of testing to the bedding plane) on evolution of coal properties; and
- What is the role of specimen size and loading rate on evolution of coal properties?

3.3. Structural impacts of UCG on coal and strata; observations from previous trial tests

Underground coal gasification consists of three main chemical processes; namely drying/vaporization, pyrolysis, and char gasification which result in syngas generation and flow, as well as cavity evolution. Outside the gasification chamber, wherever temperature is above the steam-saturation temperature at the pressure of that particular point, liquid water changes phase to steam. Depending on the pressure difference between the gasification chamber and surroundings, steam may stay in place or move to the gasification chamber and participate in the chemical reactions. Pyrolysis is the process of releasing volatile matter by increasing coal temperature in the absence of oxygen. Main products of pyrolysis include char, methane (CH_4), carbon monoxide (CO), carbon dioxide (CO_2), and hydrogen (H_2) (Anthony and Howard, 1976), and, to a lesser extent, contaminant by-products. Gasification involves reactions between char and other gasses. Syngas produced from the UCG process flows towards the production well thorough the linkage built between injection and production wells. After gasifying some coal, a cavity forms that contains hot syngas, ash, and rubble. Instrumentations in some of the previous field trials, besides monitoring the potential of that particular site for syngas production, also helped to understand the geomechanical and hydrogeological impacts of the UCG (Aiman et al., 1980; Brandenburg et al., 1975; Cooke and Oliver, 1983; Northrop et al., 1977; Youngberg et al., 1983) which are reviewed and discussed in sections 3.3.1 to 3.3.3 of this chapter.

3.3.1. Hanna II experiment, Hanna, Wyoming

The Hanna II experiment was conducted in 1975 and 1976, in three separate phases which included syn- gasification monitoring and post-gasification drilling (Brandenburg et al., 1975; Cooke and Oliver, 1983; Northrop et al., 1977; Youngberg et al., 1983).

Figure 3.1.a shows the Hanna II UCG experiment layout. Cross section of the site including the injection and production wells along with two monitoring well with thermocouples installed at different elevation into coal seam and the shale overburden (caprock) are presented in Figure 3.1.b which were reported by Brandenburg et al. (1975). Initially, reverse combustion linking was done from well 1 to well 3 while the main gasification process proceeded outward from well 3 (injector) towards well 1 (producer). Over the course of gasification, the thermocouples recorded increase in temperature in the coal seam as well as the caprock (Figure 3.1.c). The thermocouples in the well DD (refer to Figure 3.1.b) registered higher temperatures in the shale due to proximity to the injection well.

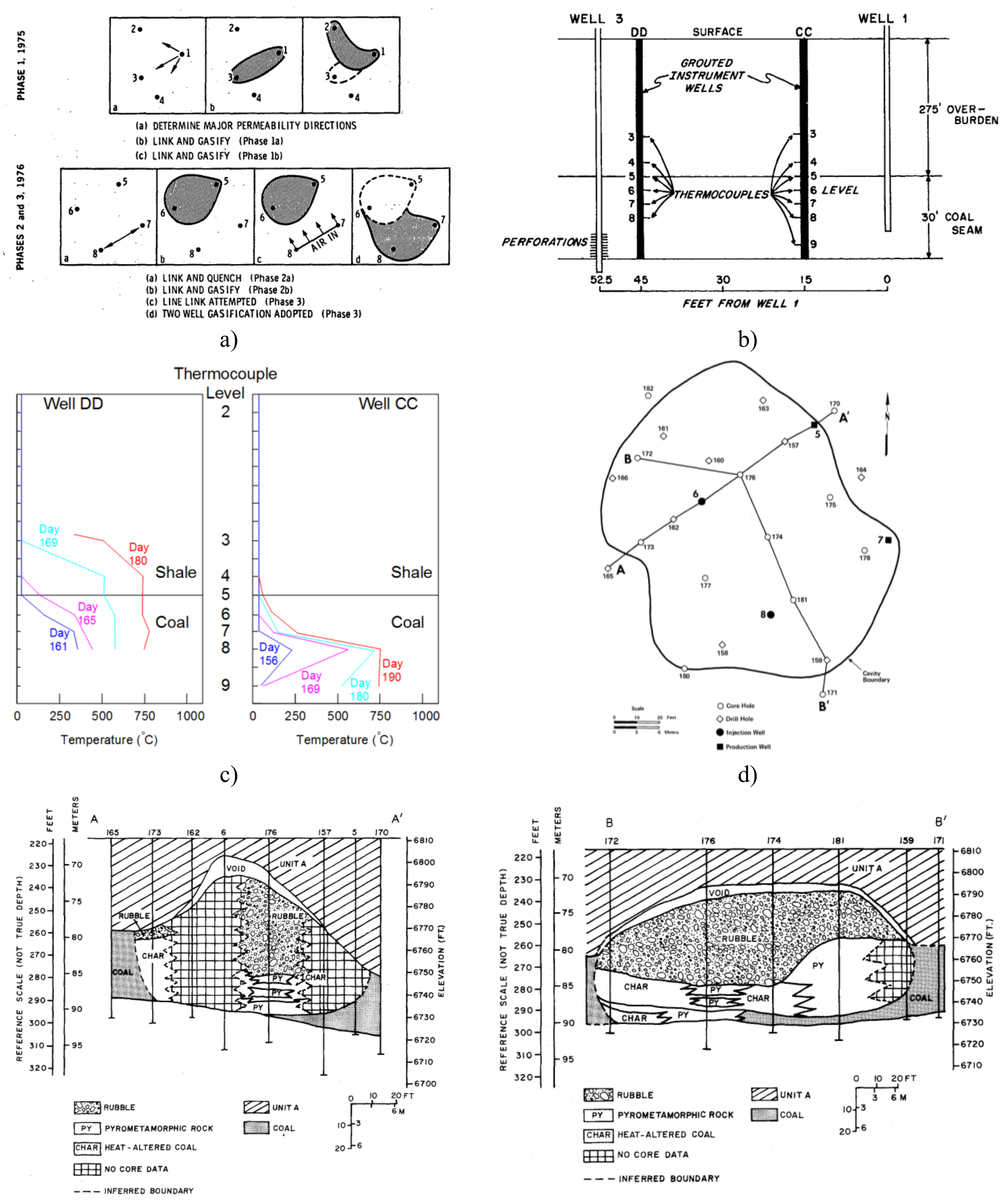

a) b) c) d) e) f)

Figure 3.1 The Hanna II UCG expeiment: a) layout of different phases; b) a cross section showing Phase 1a including injection (well 3) and production (well 1) system along with two monitoring wells (DD and CC) with thermocouples; c) temperature profiles of Phase 1a at different times; d) location of different drill and core wells as well as the injection and production wells for Phases 2 and 3; e) cross sections A-A' of the gasification cavity; and f) cross sections B-B' of the gasification cavity (Brandenburg et al., 1975; Northrop et al., 1977; and Youngberg et al., 1983)

During 1980 and 1981, a post-burn study was conducted at the Hanna II, Phases 2 and 3 underground coal gasification (UCG) site, Hanna, Wyoming (Youngberg et al., 1983). One of the outcomes of this study was determination of boundaries of the gasification zone. Figure 3.1.d shows location of different drill and core wells as well as the injection and production wells. Lithological and geophysical well log data from 22 drill holes, combined with seismic data determined a steep-sided, approximately elliptical cavity with a long axis of 42.7 m long, a short axis of 35.1 m, and a maximum height of 21.3 high (from the floor of the coal seam) that was partly filled in with rubble, char, and thermally-altered rock. Reflectance tests on coal samples acquired from within the cavity and cavity wall revealed that the coal was altered by temperatures ranging from 245 ºC to 670 ºC. Rubbles of the caprock found within the cavity contained various pyro-metamorphic minerals, indicating that temperatures of at least 1200 ºC were reached during the trials. Figure 3.1.e and f show cross sections A-A’ and B-B’ of the gasification cavity, respectively. Both cross sections indicated a void space above the rubble zone which implied spalling of a portion of the caprock to the gasification cavity.

Post-gasification water analyses of the same site was done from 1978 through 1982 on water samples from several wells which concluded evidence of water contamination in boreholes drilled into the coal and overburden aquifers (Cooke and Oliver, 1983).

3.3.2. Hoe Creek II, Campbell County, Wyoming

Post-gasification boring was done in the Hoe Creek II test site, nine months after ending the gasification as reported by Aiman et al. (1980). As depicted in Figure 3.2.a, well A was the injection well while wells B and C were production wells (well C was plugged). Post-burn boreholes (PB-1 through PB-8) and the wells A, B, and C were γ-logged. Some coring was also done to determine the gasification zone boundaries. Figure 3.2.b, c, and d show the gasification cavity sections A-A’, B-B’, and C-C’, respectively.

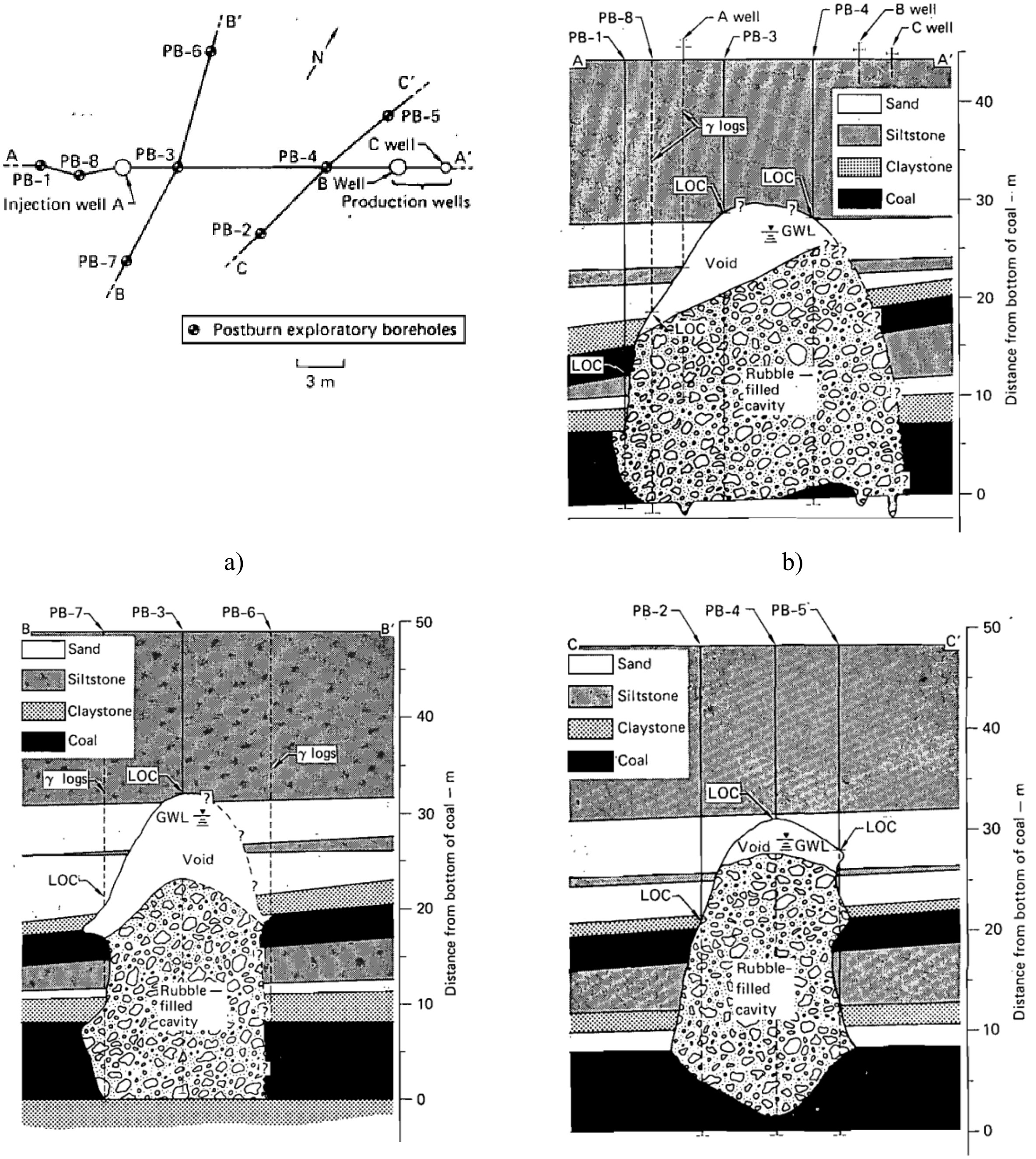

a)

b)

c)

d)

Figure 3.2 a) Plan view of exploration boreholes as well as injection and production wells at the Hoe Creek II: b) gasification cavity section A-A’; c) gasification cavity section B-B’; d) gasification cavity section C-C’ (Aiman et al., 1980)

*Note: LOC indicates the location at which loss of circulation occurred during drilling. GWL indicates ground-water level. "'?" indicates that the boundary is conjectural.

The two coal seams (the 7.6 m-thick lower coal seam, and the 3 m-thick upper coal seam) with intervenning layers of sand, siltstone, and claystone were all influenced by the gasification process. It was reported that the gasification zone never reached either wells B or C because oxygen breakthrough did not occur. Near the production wells, unreacted coal was found on the bottom of the seam. The gasification zone was estimated to be 12 to 16 m wide which extended at least 7.6 m behind the injection well and 18 m toward the production well. In all the three cross sections, a void space was observed in the upper part of the sections which indicated spalling and collapse of the roof rocks to the gasification zone. The section C-C' showed some underburden rock failure as the wells PB-2, PB-4, and PB-5 were filled with some rubble material, at the levels below the floor of the lower coal seam.

3.3.3. Discussion of geomechanical and hyrogeological risks in a UCG project

Potential geomechanical and hyrogeological damages/risks to coal, strata, and groundwater during and after a UCG process can be listed as follows (Aiman et al., 1980; Brandenburg et al., 1975; Burton et al., 2006; Cooke and Oliver, 1983; Couch, 2009; Kapusta et al., 2013; Northrop et al., 1977; Sury et al., 2004a; Sury et al., 2004b; Youngberg et al., 1983):

- Fracturing and collapse of caprock into the cavity;
- Fracturing of underburden rock;
- Subsidence (in shallow UCG);
- Microcrack generation in the heated area of coal and rock;
- Change in flow and mechanical properties of coal and rock due to heating as well as fracturing;
- Change in water phase from liquid to steam in the heated area (based on values of pressure and temperature in any particular point); and
- Syngas loss to the strata or leaching of pyrolysis products.

The primary concern during a UCG operation is gas escape. Installation of monitoring wells in permeable strata above the gasification chamber or in fault areas and a groundwater sampling program will provide an early warning of gas escape (Sury et al., 2004a). The potential causes for groundwater contamination are leaching of pyrolysis products, both syn- and post-gasification, and leaching of inorganic contaminants from the mineral ash produced by the gasification process (Sury et al., 2004b). Previous UCG trials have confirmed that the risk of groundwater contamination is more significant for shallow reactors (Sury et al., 2004b).

Level of the UCG damage/risk depends on site-specific chemical, thermal, hydrogeological, and geomechanical properties of the strata. The risk can be minimized through selection of an appropriate site, optimum operating and monitoring conditions, as well as a proper site-closure plan (Burton et al., 2006). Over time, the temperature front advances to fresh coal and the cavity increases in size. Some portion of the caprock and underburden rocks as well as surrounding coal in the drying/vaporization, pyrolysis, and gasification zones are exposed to high temperature along with mechanical perturbation caused by cavity evolution. The outcome of this complex process is generation of cracks, increase in porosity and permeability, and decline of strength and stiffness of the coal in the zone of influence which will, in turn, impact the chemical process of gasification. The thermal and chemical properties of coal in the zone of influence are also altered, but this is beyond the scope of this chapter. One of the complexities of the UCG is that occurrence of any of these structural changes may accelerate another one or all may happen at the same time along with chemical reactions of the UCG. Depending on the thickness of the coal seam and time of the operation, the zone of influence of a UCG may be contained in the coal seam (beginning of the operation) or may extend to the caprock and underburden rock (which will happen at a later time in the process). Evaluation of structural changes in coal in the zone of influence is important for performing an efficient UCG and maintaining the geomechanical and hydrogeological risks at an acceptable level. Figure 3.3 explains how these structural changes can impact cavity growth, the surrounding coal, and syngas production.

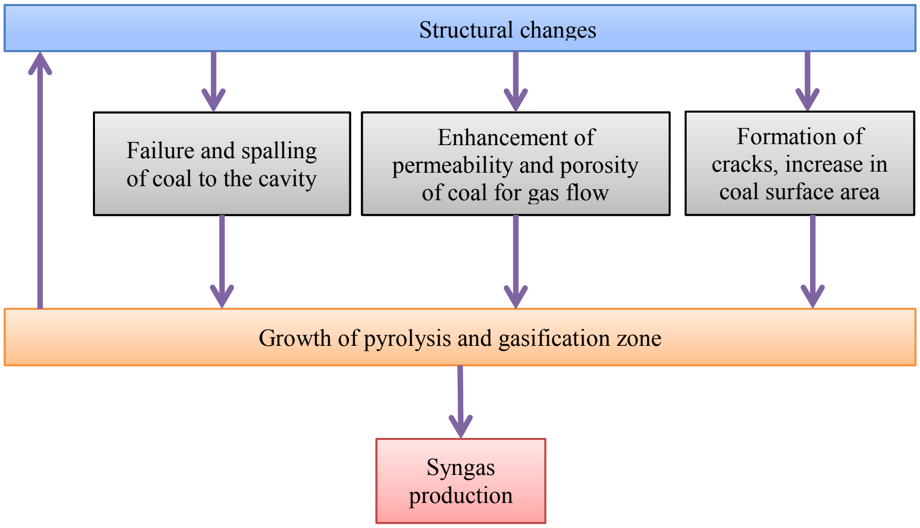

Figure 3.3 Influence of structural changes in coal on a UCG operation

3.4. Coal classification

Coal is an organic sedimentary rock that contains varying amounts of carbon, hydrogen, nitrogen, oxygen, and sulfur as well as small amounts of other elements, including mineral matter (Speight, 2005). Variation in chemical, physical, thermal, and mechanical properties of coals arises from differences in the original plant material from which the coal is derived, the amount of decay that occurred before the eventual burial, the amount of contamination by inorganic material during deposition, and the temperature and pressure during its geological history (Couch, 2009).

Globally, there are different coal classification systems. ASTM D388-12 (American Society for Testing and Materials, 2012) classifies coals by rank as depicted in Table 3.1. This classification is based on the amount of fixed carbon on a dry, mineral-matter-free basis for higher-rank coals, and gross calorific value on a moist, mineral-matter-free basis for lower-rank coals. The agglomerating character of coal is used as a basis to differentiate between certain groups of coals (ASTM D388-12; Speight, 2005). ASTM D388-12 is applicable to coals that are composed primarily of vitrinite. Coals mainly containing inertinite or liptinite, or both, cannot be properly classified because, in those macerals, the properties that determine rank (calorific value, volatile matter, and agglomerating character) are mainly different from those of vitrinite in the same coal. Such coals can be better classified by megascopic examination (ASTM D388-12).

Table 3.1 ASTM D388-12 classification of coals by rank[a] (ASTM, 2012)

Class		Fixed carbon limits (dry, mineral matter-free basis), %		Volatile matter limits (dry, mineral-matter-free basis), %		Gross calorific value limits (moist, [b] mineral-matter-free basis), MJ/kg [c]		Agglomerating character
		Equal or greater than	Less than	Greater than	Equal or less than	Equal or greater than	Less than	
Anthracite	Meta-anthracite	98		. . .	2	. . .	. . .	Nonagglomerating
	Anthracite	92	98	2	8	. . .	. . .	
	Semianthracite[d]	86	92	8	14	. . .	. . .	
Bituminous	Low volatile bituminous coal	78	86	14	22	. . .	. . .	Commonly Agglomerating[e]
	Medium volatile bituminous coal	69	78	22	31	. . .	. . .	
	High volatile A bituminous coal		69	31		32.557[f]		
	High volatile B bituminous coal	. . .	. . .	. . .	. . .	30.232[f]	32.557	
	High volatile C bituminous coal	. . .	. . .	. . .	. . .	26.743	30.232	
		. . .	. . .	. . .	. . .	24.418	26.743	Agglomerating
Subbituminous	Subbituminous A coal	. . .	. . .	. . .	. . .	24.418	24.418	Nonagglomerating
	Subbituminous B coal	. . .	. . .	. . .	. . .	22.09	24.418	
	Subbituminous C coal	. . .	. . .	. . .	. . .	19.30	22.09	
Lignitic	Lignite A	. . .	. . .	. . .	. . .	14.65	19.30	
	Lignite B	. . .	. . .	. . .	. . .	. . .	14.65	

[a] This classification does not apply to certain coals, as discussed in Section 3 of this chapter.

[b] Moist refers to coal containing its natural inherent moisture but not including visible water on the surface of the coal.

[c] Megajoules per kilogram.

[d] If agglomerating, classify in low volatile group of the bituminous class.

[e] It is recognized that there may be nonagglomerating varieties in these groups of the bituminous class, and that there are notable exceptions in the high volatile C bituminous group.

[f] Coals having 69 % or more fixed carbon on the dry, mineral-matter-free basis shall be classified according to fixed carbon, regardless of gross calorific value.

ASTM D388-12 identifies several ranks of coal; from hard coal (anthracite) to low-rank coal (lignite). Anthracite coal is hard and brittle, with black luster. It contains a high percentage of fixed carbon whereas a low percentage of volatile matter. Fresh-mined anthracite has usually less than 15% (by weight) moisture content. Bituminous coal is dense, usually black or dark brown and with distinct strips of bright and dull segments. Moisture content of bituminous coal is usually less than 20% by weight. Subbituminous coal properties range from those of lignite to those of bituminous coal. It might be dull, dark brown to black, and soft and fragile at the lignite side, to bright, black, and hard at the bituminous end of the range. Moisture content of subbituminous coal varies from 20% to 30% by weight. Lignite is the lowest rank of coal, often referred to as brown coal which has brownish black color and high moisture content, sometimes as high as 45% by weight (Speight, 2005).

3.5. Review of experimental studies related to structural changes in coal at elevated temperature

Table 3.2 summarizes published information regarding experimental studies of coal under elevated temperature. The studies summarized in this table cover almost all coal ranks from different parts of the world. Studies in the 1970's performed measurements on preheated (carbonized) specimens (Shoemaker, 1976; Singer and Tye, 1979), while recent studies used High-Pressure High-Temperature (HPHT) triaxial apparatus (Feng et al., 2012; Niu et al., 2014; Wan et al., 2011; Zhao et al., 2010) and some used a 3D CT scan system (Su et al., 2013).

Followings are the structural properties of coal under elevated temperature investigated in these studies:

- Weight loss
- Linear thermal deformation
- Axial, lateral, and volumetric strains
- Microcrack distribution
- Pore volume, average aperture, porosity, and permeability
- Tensile, compressive, and shear stress-strain responses, as well as elastic and shear moduli

It should be emphasized that this study only reviews the observed structural changes in coal specimens in the laboratory due to high temperature and does not deal with the mechanical perturbation due to the creation of the UCG cavity or combined effect of cavity and elevated temperature.

This review discusses the case studies of Table 3.2 in several sections. The sections are grouped based on different subjects such as weight loss due to heating, thermal deformation, and so on. The organization of this review is in a way that, in each section, initially, brief background information is provided, and then, the experimental cases from different parts of the world are reviewed in a chronological order with all the possible analyses and interpretations. At the end of each section, further discussion and comparisons amongst the studied coals is provided.

Table 3.2 Summary of high temperature coal experiment database

Reference	**Coal seam**	**Coal rank**	**Apparatus**	**Specimen size**	**Direction to bedding**	**Thermal treatment**	**Properties measured**	t_{prehea} (ºC)	t_{test} (ºC)	P_i (MPa)	σ_1/σ_3 (MPa)
Shoemaker (1976)	Pittsburgh coal, Humphrey No.7 mine, Maidsville, West Virginia, USA	Bituminous	Uniaxial & simple shear	Cubic; 1.27 × 1.27 × 2.54 cm 2.54 × 2.54 × 5.08 cm 5.08 × 5.08 × 10.16 cm 10.16 × 10.16 × 20.32 cm 1.27 × 5.08 × 5.08 cm	⊥ and //	Specimens were preheated in a furnace to the target temperature, then placed in the apparatus. The specimen area in the apparatus were heated to the same temperature	Stress-strain, Elastic & Shear moduli at different loading rate	Up to 343	Equal to preheat	-	-
Thorsness et al. (1978)	Wyodak coal, Wyoming, USA	Sub-bituminous[a]	-	-	-	-	Permeability, porosity, weight loss	Up to 650[b]	-	-	-
Singer and Tye (1979)	Pitsburgh[c], Pocahontas No.3, Sewell, Illinois No.6, USA	Bituminous	-	Cylindrical; 1.91 / 2.54 cm (diam)	-	Tests on specimens preheated (carbonized) up to, 800 ºC	Porosity[d] (to water/helium), Permeability (to air)	Up to 800	Ambient	-	σ_3=1.03 (helium porosity), 0.669 (air perm)
				Dumbbell; 7.6 × 1.3 × 0.3 cm			Tensile strength		23, 200	-	-
				Cylindrical; 1.3 × 2.5cm			Compressive strength		23, 200	-	-

$t_{preheat}$: Preheating temperature

t_{test}: Test temperature

P_i : Injection pressure

σ_1/σ_3: Axial/confining stress

[a] The ASTM rank was not mentioned in the article; the rank was assumed to be the same as for the Wyodak Coal Mine, Wyoming (http://en.wikipedia.org/wiki/Wyodak_Mine).

[b] Not clarified in the article that whether this is preheat temperature or test temperature.

[c] The location of the coal seam, from which the Pittsburgh samples were taken, was not mentioned in the article.

[d] Not clarified in the article that whether, for carbonized specimens, porosities were measured using water or helium.

Table 3.2 (Continued) Summary of high temperature coal experiment database

Reference	**Coal seam**	**Coal rank**	**Apparatus**	**Specimen size**	**Direction to bedding**	**Thermal treatment**	**Properties measured**	t_{prehea} **(ºC)**	t_{test} **(ºC)**	P_i **(MPa)**	σ_1/σ_3 **(MPa)**
Glass (1984)	Hanna Basin coal, USA	Sub-bituminous[e]	Triaxial & uniaxial	-	⊥ and //	-	Elastic modulus, Poisson's ratio, stress-strain, linear thermal expansion	Up to 450		1	-/2
de Koranyi and Balek (1985), Balek and de Koranyi (1990)	Manvers Wath, and Markham Main, UK	Bituminous	-	-	-	Heating in argon at 5 ºC/min to 300, 500, 600, 800, and 900 ºC	Porosity (to helium/ mercury)	Up to 900	-	-	-
Zhao et al. (2010)	Xing-Long-Zhuang coal mine, Shandong, China	Steam coal[f,i]	HPHT triaxial	Cylindrical; 20 × 40 cm	-	Heating the specimen, keeping it for 5hrs at the target temp and measuring pyrolysis products, then Injecting N2	Permeability (to nitrogen)	-	Up to 600	1, 2, 3, 4	-
			Mercury porometer	Cubic; 1.5 × 1.5 × 2 cm	-	Heating the specimen in an electrical furnace, for 5hrs and connecting the furnace to vacuum system during heating	Porosity (to mercury), pore volume	Up to 600[g]	-	-	-
			Micro-structural analysis				Average aperture				
Wan et al. (2011)	Jincheng coal field, China	Anthracite	HPHT triaxial	Cylindrical; 20 × 40 cm	-	Applying triaxial loading, heating the specimen at the rate of 10 ºC /h, maintaining the target temperature for 4 hrs, record lateral and axial strains	Elastic modulus	-	Up to 600	-	12.5/15
	Xing-Long-Zhuang coal mine, Shandong, China	Gas coal[h,i]	HPHT triaxial	Cylindrical; 20 × 40 cm	-						

[e] Location of the coal seam and the ASTM rank was not mentioned in the article; the rank was assumed to be the same as in another article about the Hanna Basin coal by Schrider and Jennings (1974).

HPHT: High-Pressure High-Temperature

[f] The ASTM rank was not mentioned in the article. "Steam coal" is a grade between bituminous and anthracite coals, once widely used as a fuel for steam locomotives (http://en.wikipedia.org/wiki/Coal#Types).

[g] Not clarified in the article that if porosity was measured while maintaining high temperature or not.

[h] The ASTM rank was not mentioned in the article.

[i] It's not clear to the authors of this review paper if both steam coal and gas coal are referring to the same ASTM rank as the coal seam locations in these two articles were identical.

Table 3.2 (Continued) Summary of high temperature coal experiment database

Reference	**Coal seam**	**Coal rank**	**Apparatus**	**Specimen size**	**Direction to bedding**	**Thermal treatment**	**Properties measured**	t_{prehea} **(°C)**	t_{test} **(°C)**	P_i **(MPa)**	σ_1/σ_3 **(MPa)**
Yu et al. (2012)	Xishan coalfield, China	Lean coal[j]	Micro CT scan	Cylindrical; 0.1 × 1 cm	-	Keeping every specimen at target temperature for 15 min, then scanning	Porosity (using Micro CT Scan)	Up to 600	-	-	-
Feng et al. (2012)	Xing-Long-Zhuang coal mine, Shandong, China	Gas coal[k,i]	HPHT triaxial	Cylindrical; 20 × 40 cm	-	Heating from 20 °C to 600 °C. The temp of 300 °C and 600 °C were kept longer until all gas was released to investigate the effect creep on the deformation	Axial, lateral and volumetric strains, volume of produced gas	-	Up to 600	-	12.5/15
Su et al. (2013)	Kushiro coal mine, Japan	Bitumin-ous[l]	A set up containing a heating plate & AE & X-ray 3D CT scan	Cubic; 4 × 2 × 0.5 cm	⊥ and //	Coal specimens were covered with plaster to prevent disintegration	Microcrack distribution	-	Up to 500	-	-
	specimens from a deep coal seam (1400 m), Alberta, Canada	-[k]		Cylindrical; 2 × 1 cm	//		Microcrack distribution	-	Up to 500	-	-
Niu et al. (2014)	Yuanbaosh-an, Inner Mongolia, China	Lignite	HPHT triaxial	Cylindrical; 5 × 10 cm	-	Heating from 25 °C to 650 °C with rate of 10 °C /min. Each temp was kept for 4 hours, then measuring permeability under different N_2 pressure	Permeability (to nitrogen)	-	Up to 650	0.5, 1, 1.5	7.5/9
			DTU-2B weight loss analysis instrument	-	-	Temperature increasing rate of 10 °C /min	weight loss	-	Up to 1000	-	-

[j] Lean coal= semi-anthracite coal as mentioned by Lu and Laman (xxxx). The ASTM classification was not mentioned in the article.

[k] The ASTM rank was not mentioned in the article.

[l] The ASTM rank was not mentioned in the article. The rank was assumed to be the same as in the article by Ohtomo et al. (2013)

CT: Computed Tomography

AE: Acoustic Emission

3.5.1. Weight loss due to heating

Heating coal may cause drying/vaporization and pyrolysis. After temperature exceeds a certain limit, the chemical process of pyrolysis happens and volatile matter is released which will, in turn, intensify microcrack formation and increase the porosity and permeability of the coal. Also, the coal surface area will be increased which helps in growth of the pyrolysis and gasification zone. Pyrolysis is defined as thermochemical decomposition of coal at elevated temperature in the absence of oxygen which results in production of gaseous compounds (volatile matter), tar, and solid residue (char). Coal pyrolysis includes three steps (Arenillas et al., 2003):

- Desorption of water and adsorbed gases that takes place at temperatures lower than 150 ºC. The main reactions in the first stage are disruption of hydrogen bonds, vaporization, and transport of non-covalently bonded guest molecules.
- Between 150 and 500 ºC, degradation of the coal matrix happens with production of CO_2, pyrolysis water, and aliphatic compounds.
- Formation of aromatic tar and gases with the subsequent condensation of aromatic structures to char occurs between 500 and 800 ºC, which is associated with the formation of mainly CO, H_2, and CH_4.

One of the consequences of such changes is weight loss of the coal. Weight loss is investigated by mean of thermal analysis. Thermal Gravimetry (TG) on crushed powder has been the focus of numerous studies (Arenillas et al., 1999; Avid et al., 2002; Balek and de Koranyi, 1990; de Koranyi and Balek, 1985; de la Puente et al., 1998; Elbeyli et al., 2004; Hill et al., 1989; Krzesinska et al., 2009; Niu et al., 2014; Podder et al., 1995; Rotaru, 2012; Seo et al., 2011; Sonibare et al., 2005; Wang et al., 2010; Yu et al., 2012).

3.5.1.1. Subbituminous coal, USA

Thermal analysis of the Wyodak subbituminous coal was done by Thorsness et al. (1978) (Figure 3.4). As depicted in Figure 3.4, the amount of weight loss increased with temperature; at 650 ºC, the coal lost 45% of its original weight.

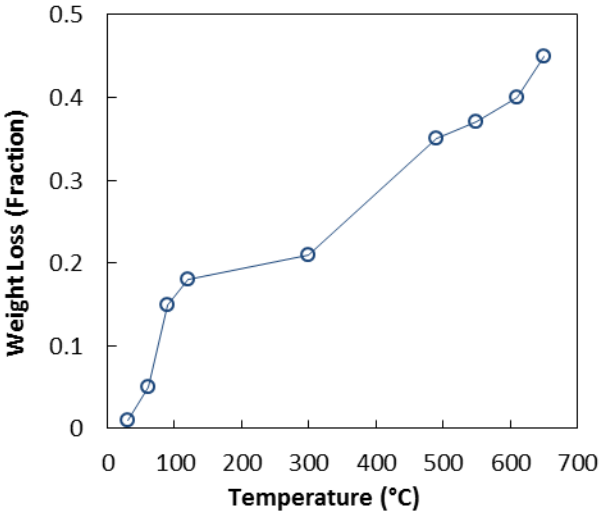

Figure 3.4 Weight loss of the Wyodak coal (subbituminous) during drying and pyrolysis (Thorsness et al., 1978)

3.5.1.2. Lignite coal, China

Niu et al. (2014) examined the Yuanbaoshan lignite coal, from Inner Mongolia, China (Figure 3.5). Instantaneous weight of the specimen at any temperature is shown as a percentage of its original weight in Figure 3.5.a. Derivative of the weight loss curve with respect to temperature is depicted in Figure 3.5.b. The latter shows rate of weight loss during heating, allowing identification of temperatures where significant changes occurred during pyrolysis. There are two significant temperatures in Figure 3.5.b attributed to notable weight loss rates; one is around 100 ºC and the other one is about 470 ºC.

3.5.1.3. Implications for UCG

Thermal gravimetric analysis is an experimental method which traces reduction in a physical property of coal (i.e., weight (mass)) as an indication of progress of chemical phenomena of drying, pyrolysis, and gasification. Although it is not possible to directly monitor weight loss during UCG, monitoring temperature profile is an indirect confirmation of weight loss in-situ. After some weight loss happened, the coal matrix becomes more porous/permeable and, structurally, weaker. As discussed in the introductory part of the section 3.5.1, minor weight loss corresponds to coal pyrolysis which mainly happens in the coal gasification cavity wall;

however, major weight loss is related to coal gasification which is the major factor in the evolution of the gasification cavity.

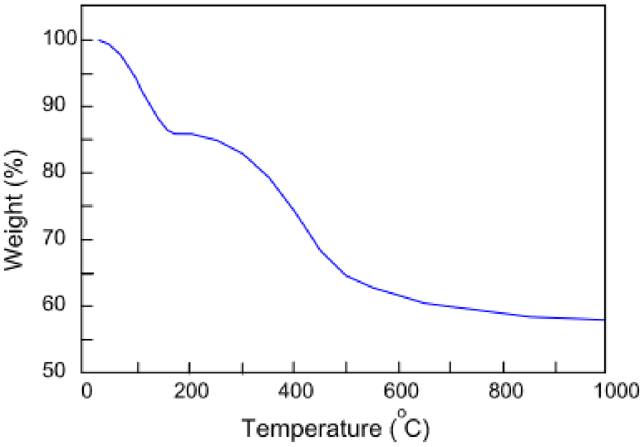

a) b)

Figure 3.5 a) Theromogravimetry (TG) curve; and b) derivative theromogravimetric (DTG) of the Yuanbaoshan lignite coal, Inner Mongolia, China (Niu et al., 2014)

3.5.2. Thermal deformation

Coal undergoes thermal deformation and stress while heating which may generate microcracks in coal (Su et al., 2013); however, coal's response to heating is more complicated than other rocks. Initially, coal expands in response to heating. After pyrolysis (and later on, gasification) begins, coal tends to shrink and exhibits compressional deformation (Glass, 1984; Feng et al., 2012).

3.5.2.1. Subbituminous coal, USA

Linear thermal deformation of subbituminous coal from the Hanna Basin was investigated by Glass (1984). It was observed that this coal initially underwent expansion (less than 1%) and then, at a temperature of about 150 ºC, it started to shrink (Figure 3.6). Between temperature of 150 and 400 ºC, the amount of shrinkage with temperature was low (less than 2%); however, beyond 400 ºC, shrinkage increased dramatically to such an extent that at temperature of 500 ºC, the shrinkage was about 10%. Figure 3.6 also presents the effect of anisotropy on thermal deformation. Similar trends were observed parallel and perpendicular to the bedding plane; however, magnitudes of deformation were different.

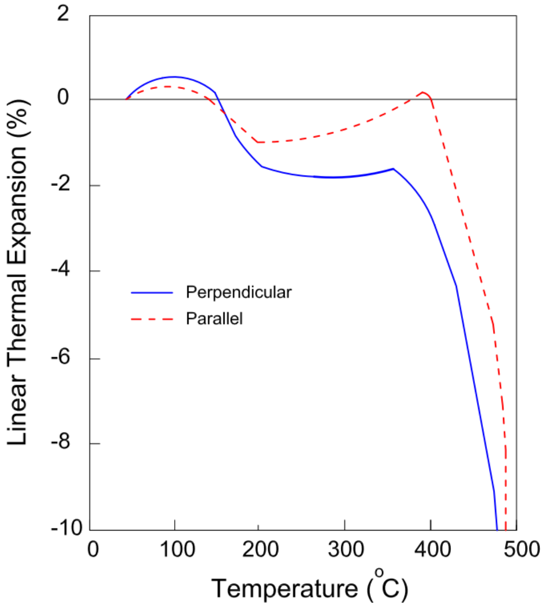

Figure 3.6 Thermal deformation data of the Hanna Basin subbituminous coal showing the effect of bedding plane (Glass, 1984)
*Note: Expansion is shown positive.

3.5.2.2. Gas coal, China

Thermal deformation of gas coal specimens from the Xing-Long-Zhuang coal mine in Shandong, China, was studied in a HPHT triaxial apparatus under stresses equivalent to a burial depth of 500 m by Feng et al. (2012). While the coal specimens were being heated up to temperature of 600 ºC, axial, lateral, and volumetric strains as well as produced gas volume were measured. The entire heating process from room temperature (about 20 ºC) to 600 ºC was performed in about 140 hours. The transition from room temperature to 300 ºC was done in about 70 hours. Then the sample was kept at 300 ºC for about 40 hours to investigate impact of creep. It took about 20 hours to raise temperature from 300 to 600 ºC. The temperature of 600 ºC was also maintained for a longer time to observe how creep will influence the specimen at this temperature (Figure 3.7.a). Thermal expansion was the main deformation mechanism at temperatures below 250 ºC; however, the gas began to come out of the specimen at around 150 ºC. Feng et al. (2012)

concluded that under 250 ºC, the gas release had little effect on the coal structure. Thermal expansion started to decline as a result of increased gas production at about 200 ºC and transformed to compressional deformation (shrinkage) at 250 ºC. Volumetric strain at 200 ºC was 0.65% (expansion). The major compressional deformation was induced by the sharp increase of pyrolysis gas production at about 250 ºC. The two creep phases caused more gas production and sharp increases in strains (Figure 3.7.a and b). At 300 ºC, volumetric strain before and after the creep was recorded as 0.7% and 17%, respectively. Final volumetric strain before and after the creep at 600 ºC was about 35% (Figure 3.7.b) and 65%, respectively.

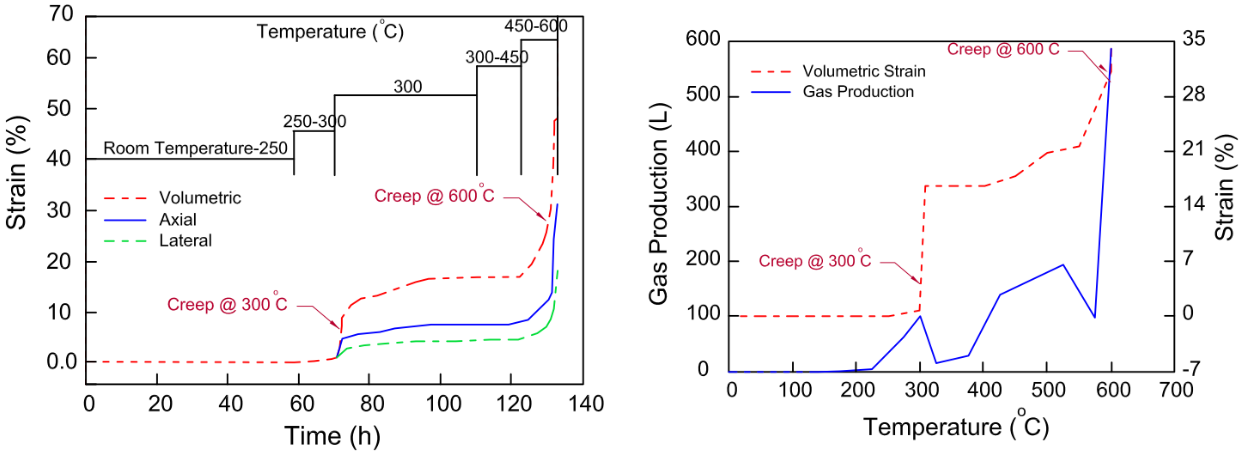

a)

b)

Figure 3.7 Thermal deformation data of the Xing-Long-Zhuang mine gas coal: a) heating time along with axial, lateral, and volumetric strains; and b) pyrolysis gas production and volumetric strain against temperature (Feng et al., 2012)
*Note: Compressional volumetric strain is shown positive. The figure also shows effect of creep at 300 and 600 ºC on deformation and gas production.

3.5.2.3. Discussion of the unique thermal deformation characteristic of coals

Both the Hanna Basin coal and the gas coal specimens from the Xing-Long-Zhuang coal mine reviewed in this section initially showed minor expansion which was attributed to positive thermal expansion coefficient. However, further heating of coal resulted in compressional deformation which corresponded to a negative thermal expansion coefficient. This is in accordance with an earlier study by Bangham and Franklin (1946) who reported thermal shrinkage of three coals, one anthracite coal and two bituminous coals, between room temperature and about 300 ºC. This distinctive behavior of coal differentiates it from other rock types. Inorganic rocks exhibit continuous expansion and, hence, positive thermal expansion coefficient under elevated temperature. This observation was reported in several studies as, for example, by Richter and Simmons (1974) on igneous rocks over a temperature range of 25-550 ºC, by Heuze (1983) on granitic rocks at temperatures below 550 ºC, and by Luo and Wang (2011) on mudstone over a temperature range of 20-700 ºC.

The thermal expansion coefficient of a homogeneous and isotropic porous material constituted by one single solid phase is not function of porosity variations and is simply equal to thermal expansion coefficient of its solid phase (Ghabezloo, 2013). The unusual thermal deformation response of coal is because of the fact that coal is a heterogeneous organic-inorganic porous rock containing moisture and volatile matter, often with an inherent cleat network. Different constituents of coal respond differently to heating because of the differences in their mineral types and coefficients of thermal expansion. Moisture and volatile matter are released during heating. Inorganic minerals of coal expand during heating. The organic part of coal i.e. carbon expands at low temperature whereas further heating will cause the organic constituent to take part in the chemical reactions of pyrolysis/gasification and be partially consumed. The partial consumption of the carbon lowers structural stiffness of the coal, hence, results in internal collapse of some of the unstable solid matrix which manifests in the form of compression (shrinkage) of the coal rock.

3.5.2.4. Implications for UCG

Thermal deformation behavior of coal affects in-situ response of coal seam to temperature. Areas with mild high temperature (i.e. less than about 200 ºC as it is seen in Figure 3.6 and Figure 3.7.b) tend to expand while heating. These are the areas near the wall of a gasification cavity and beyond. It can be interpreted that the areas very next to a gasification cavity deform towards the cavity; however, those which are farther will experience thermal stress as they are bounded by the surrounding formation which prevent free displacement. Where temperature is above 200 ºC, coal shrinks as depicted in Figure 3.6 and Figure 3.7.b. This shrinkage happens in the zone of pyrolysis and gasification.

3.5.3. Crack generation due to heating

Heating a coal specimen causes microcracks which can be a combination of thermally induced cracks related to deformation of coal (swelling or shrinkage) or cracks created due to the chemical process of pyrolysis and gasification, depending on temperature level and coal properties.

3.5.3.1. Bituminous coal, Japan

In an experimental effort, crack generation of coal specimens due to heating was studied using an Acoustic Emission (AE) and CT scan technology (Su et al., 2013). As shown in Figure 3.8.a and summarized in Table 3.2, the specimen was mounted on the heating plate of the setup. The AE event, microcrack distribution, and average fissure volume along the specimen height were studied on cubic bituminous coal specimens taken from the Kushiro mine, Japan, and cylindrical coal specimens from a deep coal seam (about 1400 m) in Alberta, Canada. Figure 3.8.b illustrates the AE count rate and surface temperature with time for a cubic specimen from the Kushiro mine, having a bedding plane normal to the heating plate and for a heating time of 127 minutes. As the surface temperature of the specimen increased, AE activities considerably increased, indicating creation of microcracks. The majority of the microcracks occurred in the bottom 8 mm of the height of the specimen (Figure 3.8.c and d); however, for a similar specimen but under a greater temperature gradient, fractures were distributed throughout the whole specimen height. For the specimen having the bedding plane parallel to the heating plate, crack extension occurred along the horizontal directions in the specimen.

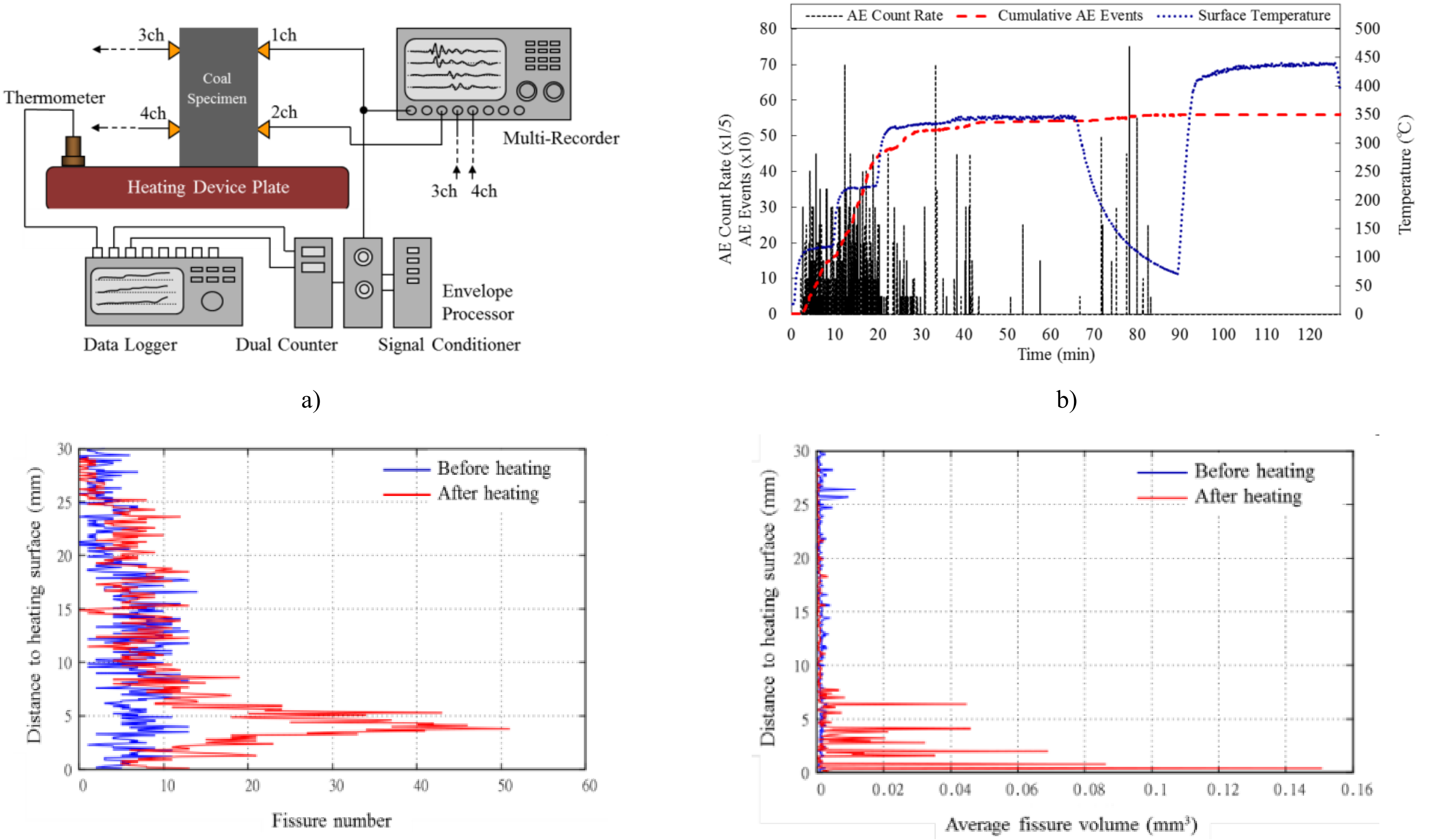

a)

b)

c)

d)

Figure 3.8 a) Experimental setup for coal heating; b) temperature variation and AE activity monitored in the process; c) microcrack distribution along the specimen height; and d) average fissure volume along the specimen height for a cubic sample of bituminous coal from the Kushiro mine, Japan, with the bedding plane parallel to the heating surface (Su et al., 2013)

3.5.3.2. Implications for UCG

Although the study by Su et al. (2013) was performed under no mechanical restraints on the coal specimens, it can be concluded that temperature of the heating source and temperature gradient as well as inherent fracture network and direction of the stratification in the coal seam play important roles in response of a coal to heating process. Moreover, in a UCG site, heating direction might have any inclination to the stratification and heating gradient may vary with location and time which can result in a complicated microcrack generation in the coal around the gasification chamber in combination with mechanical fracturing related to the cavity evolution.

3.5.4. Effect of temperature on pore volume, aperture, porosity, and permeability

Thermal deformation and microcracks as well as release of volatile matter during heating alter pore volume and permeability of a coal. Published literature utilized helium gas, mercury intrusion, water saturation, or micro CT scan technique to predict porosity of preheated coal specimens (see Table 3.2). Permeability measurements were conducted either on preheated specimens using flow of air or in a HPHT triaxial cell against flow of nitrogen gas (see Table 3.2).

3.5.4.1. Subbituminous coal, USA

Thorsness et al. (1978) measured permeability and change in porosity of the Wyodak subbituminous coal as a function of temperature. As presented in Figure 3.9, permeability and porosity of this coal increased with temperature. Porosity experienced a gradual increase throughout the studied temperature range. The amount of observed change in porosity at 650 ºC was 0.49 (decimal). Initial permeability of this coal at 30 ºC was 10 mD which increased with temperature. Permeability gradually increased as temperature increased; however, drastic increase of permeability occurred at temperature of 490 ºC onwards. The magnitudes of permeability at 490 and 650 ºC were measured as 1200 and 16000 mD, respectively. An exponential porosity-permeability correlation was proposed by Thorsness et al. (1978) based on the experiments on the Wyodak coal as presented in Equation 3.1.

$$ln\left(\frac{K}{K_0}\right) = \alpha\,(\emptyset - \emptyset_0) \qquad or \qquad \frac{K}{K_0} = e^{\alpha\,(\emptyset-\emptyset_0)} \tag{3.1}$$

where K_0 and $\emptyset_0$ are initial permeability and porosity of the Wyodak coal and α has a value of approximately 12.

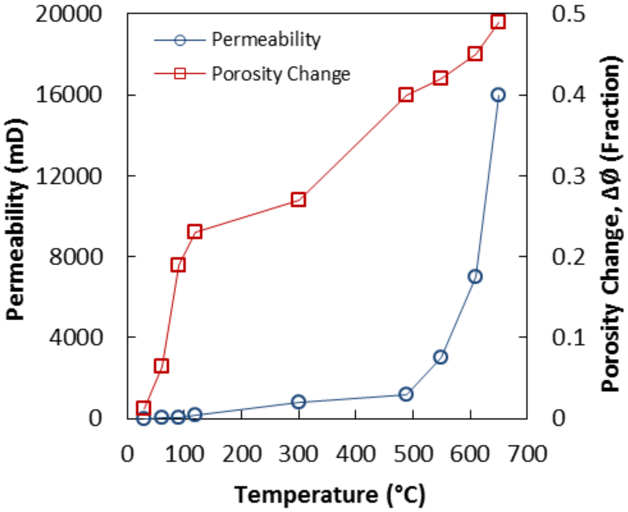

Figure 3.9 Permeability and porosity change of the Wyodak subbituminous coal during drying and pyrolysis (Thorsness et al., 1978)

3.5.4.2. Bituminous coals, USA

Singer and Tye (1979) studied porosity and permeability of specimens of four bituminous coals from USA (Pittsburgh, Pocahontas No.3, Sewell, Illinois No.6) preheated up to 800 ºC. It is not clear whether the porosities of these carbonized specimens were measured using helium or water. Variation of porosity and air permeability of these coals to carbonization (preheating) temperature are shown in Figure 3.10.a and b. Average of the measurements (one or two or, in some cases, three measurements at a temperature) from a data table in the reference document was plotted. According to Figure 3.10.a, porosities increased with carbonization temperature until a peak was reached at 650 ºC for the Pittsburgh and Illinois No.6 coals and at 500 ºC for Sewell coal. Thereafter, there was slight decrease in porosities as carbonization progressed to the next temperature levels. The Pocahontas No.3 coal exhibited continuous increase in porosity while carbonization temperature increased. The other observation in this study was that porosities decreased as coal rank increased, i.e., volatile matter decreased throughout these four coals (volatile matter for the Pittsburgh, Pocahontas No.3, Sewell, and Illinois No.6 coals were 36.6, 17.4, 29.1, and 33.7 %, respectively; the basis for these measurements was not specified in the reference.). Since the Pocahontas No.3 coal had the highest rank (the lowest volatile matter) amongst these coals, its porosity at different elevated temperature was the lowest amongst these coals. It could be interpreted from the Pocahontas No.3 porosity-temperature plot that in a higher-rank coal, compared to a lower rank coal, the coal is structurally stronger hence less pyrolysis and volatile matter release happen, which leads to less porosity evolution at elevated temperatures.

Although permeability curves in Figure 3.10.b show great scatter and variability, it was observed that permeability depended on carbonization temperature of each coal. Singer and Tye (1979) extended the beginning of the Pittsburgh and Pocahontas No.3 curves to porosities at ambient temperature cited by Thimons and Kissell (1973). Singer and Tye (1979) also stressed that properties measured in the temperature range of 350-550 ºC were very uncertain, as the coal specimens were showing some activities even after 4 to 5 hours of heating. Equation 3.2 was developed by Singer and Tye (1979) for permeability-porosity of the Pittsburgh coal.

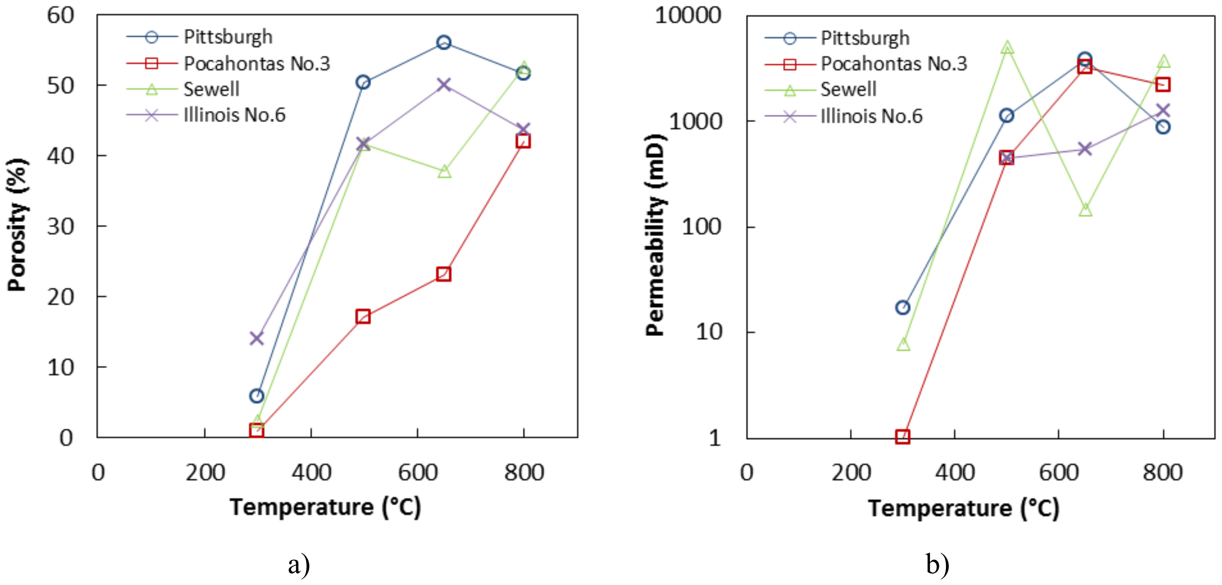

Figure 3.10 a) Porosity; and b) air permeability of four bituminous coals from USA (Pittsburgh, Pocahontas No.3, Sewell, Illinois No.6) preheated to 300, 500, 650, and 800 ºC (Singer and Tye, 1979) *Note: Permeability was measured parallel to the bedding plane.

$$K = 8.3364\, e^{(0.09913\, \emptyset)} \tag{3.2}$$

where K and $\emptyset$ are permeability (in mD) and porosity (in percent) of the Pittsburgh coal preheated to a temperature in the range of 50 to 800 ºC.

3.5.4.3. Two bituminous coals, UK

Porosity variations of two bituminous British coals were studied by de Koranyi and Balek (1985) and Balek and de Koranyi (1990). As shown in Figure 3.11, initial porosities of the Manvers Wath coal was 26% which dropped to 14% at temperature of 300 ºC and then reached a peak of 42% at 700 ºC and decreased to 31% at 900 ºC. For the Markham Main coal, the initial porosity was 22% which dropped to 17% at 300 ºC and reached the maximum of 53% at 600 ºC and slightly decreased to 47% at 900 ºC (for the purpose of plotting, initial measurements at ambient temperature were assumed to be at 20 ºC).

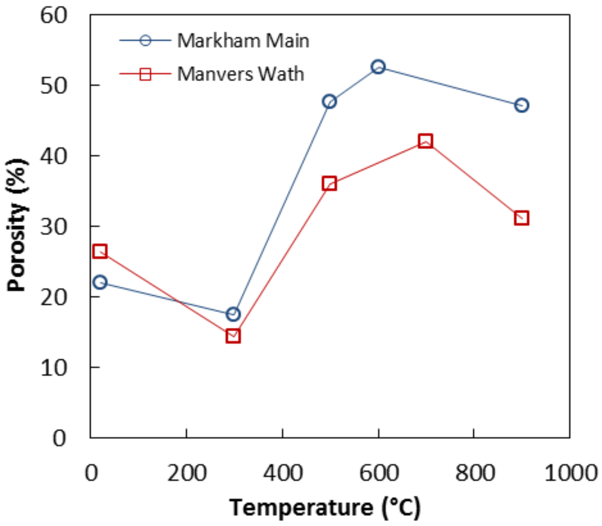

Figure 3.11 Porosity variations of bituminous coals from the Markham Main and the Manvers Wath, UK, versus temperature (Balek and de Koranyi, 1990; de Koranyi and Balek, 1985)

3.5.4.4. Steam coal, China

Zhao et al. (2010) measured mercury porosity and pore volumes of steam coal specimens from the Xing-Long-Zhuang coal mine in Shandong, China, preheated to different temperatures. Initial porosity of the coal at 20 ºC was 7.5% which slightly decreased to 6.1% at temperature of 300 ºC (Figure 3.12.a). Then, porosity drastically increased to 36.7% at 600 ºC. Also measured in this study was the average aperture of the coal after drying and pyrolysis at a particular temperature (Figure 3.12.a). Pore aperture showed similar trend to that of porosity. Initial aperture at 20 ºC was measured 0.037 μm which slightly dropped to 0.023 μm at 300 ºC and rose to 0.144 μm at 600 ºC.

Change in permeability of coal specimens from the same mine was measured under different nitrogen (N_2) injection pressure in a HPHT triaxial cell. The initial permeability of the coal specimens at temperature of 20 ºC under N_2-injection pressure in the range of 1 to 4 MPa was between 1.5 and 2.7 mD which increased with temperature (Figure 3.12.b).

Zhao et al. (2010) divided the permeability-temperature relationship into three stages. The first stage is the low-temperature range from 20 to 300 ºC within which permeability slightly fluctuated with temperature. They attributed this behavior to variation in size and connectivity of the pores and fractures in the specimen due to heating and water vaporization. The second stage is the medium temperature range from 300 to 400 ºC within which permeability increased exponentially with temperature. The third stage is the high temperature range from 400 to 600 ºC within which permeability remarkably increased with temperature to such an extent that for nitrogen injection pressure of 1 and 2 MPa, the measured values of permeability were 1922 and 1926 mD, respectively. They concluded that under the high temperature, pyrolysis happened and large amounts of gas and tars were generated which consequently increased the pore and fracture volume in the specimens and led to the rapid increase of permeability with temperature.

Plots of permeability versus N_2-injection pressure at different temperature is presented in Figure 3.12.c. Unlike the permeability-temperature plots, at different temperatures, permeability showed varying trends with an increase in injection pressure. Since Zhao et al. (2010) did not report the axial and confining stresses during this experiment, it is not possible to make any interpretation about this response, whether it is because of the effect of shearing load while heating or it is natural to this coal.

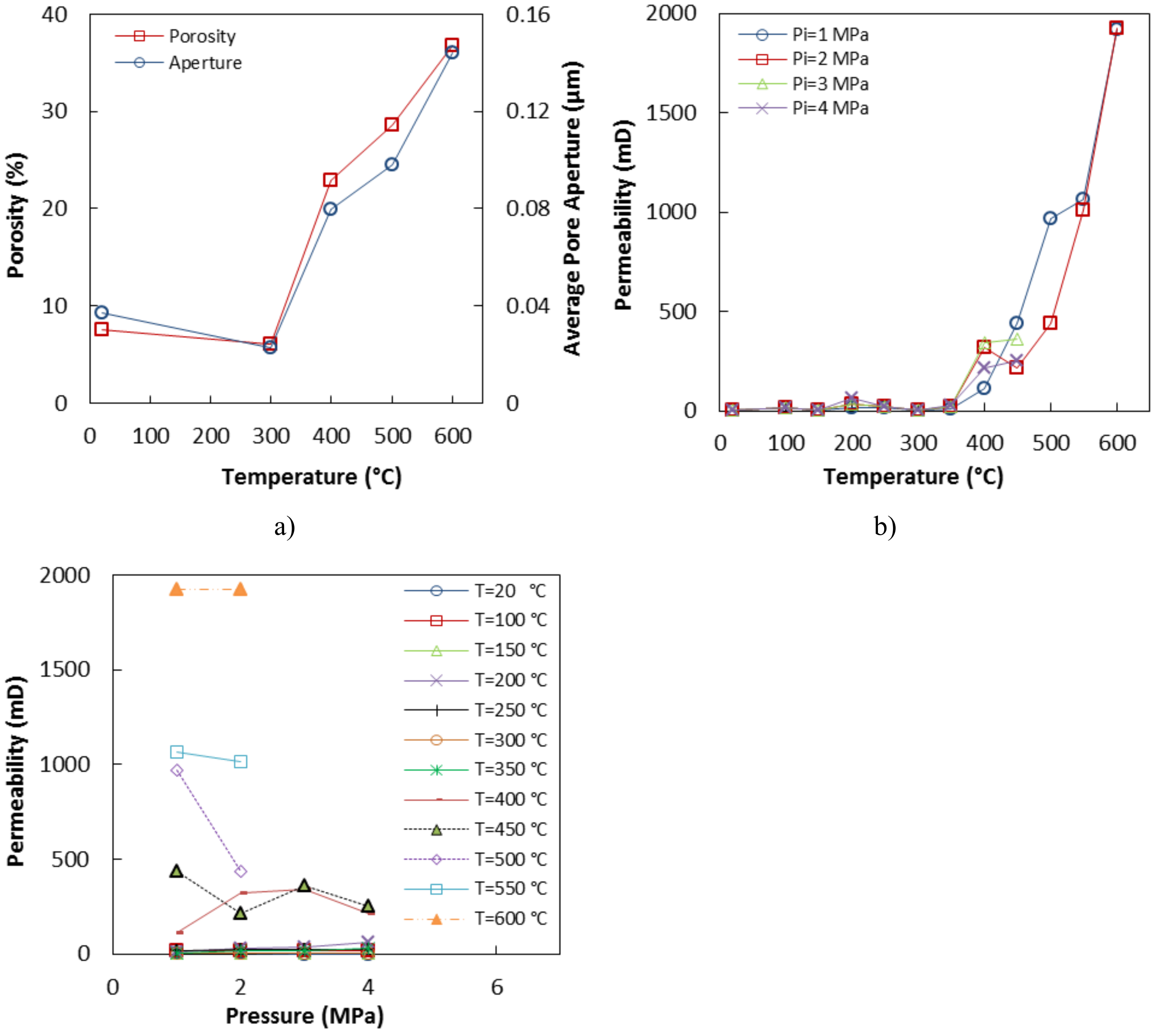

a)

b)

c)

Figure 3.12 Properties of steam coal from the Xing-Long-Zhuang mine under different N_2-injection pressure after drying and pyrolysis to a particular temperature: a) porosity and average pore aperture; b) nitrogen permeability versus temperature under different injection pressure; and c) nitrogen permeability versus injection pressure under different temperature (Zhao et al., 2010)

3.5.4.5. Lean (semi-anthracite) coal, China

Variations of porosity of lean (semi-anthracite) coal from the Xishan coalfield, China, during heating was studied by Yu et al. (2012). The specimen was heated in the absence of oxygen from room temperature of 18 up to 600 ºC. Pore analysis was done using a micro CT scan device. As shown in Figure 3.13, it was observed that as temperature increased from 18 to 200 ºC, porosity of the lean coal slightly decreased as a result of dehydration, devitalization, and thermal expansion of the solid matrix. From 200 to 400 ºC, porosity increased greatly due to a coupling effect of the physical reactivity and pyrolysis. They observed gradual decrease of porosity at above 400 ºC.

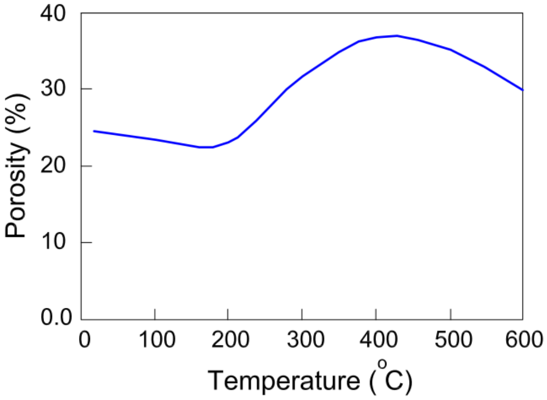

Figure 3.13 Porosity of lean (semi-anthracite) coal from the Xishan coal field, China, versus temperature (Yu et al., 2012)

3.5.4.6. Lignite coal, China

Effect of temperature and pore pressure on nitrogen permeability of lignite coal from the Yuanbaoshan area, Inner Mongolia, China, was studied in a HPHT triaxial cell by Niu et al. (2014) (Figure 3.14). Temperature effect on permeability was much more complicated than the injection pressure effect. Generally, permeability showed ascending trends with temperature; however, it fluctuated as shown in Figure 3.14.a, but three peak values of permeability under each injection pressure, located at about 250, 400, and 600 ºC, were observed. On the other hand, pore pressure effect on permeability was consistent throughout all temperatures. Based on Niu et al. (2014), permeability decreased as N_2-injection pressure increased (Figure 3.14.b).

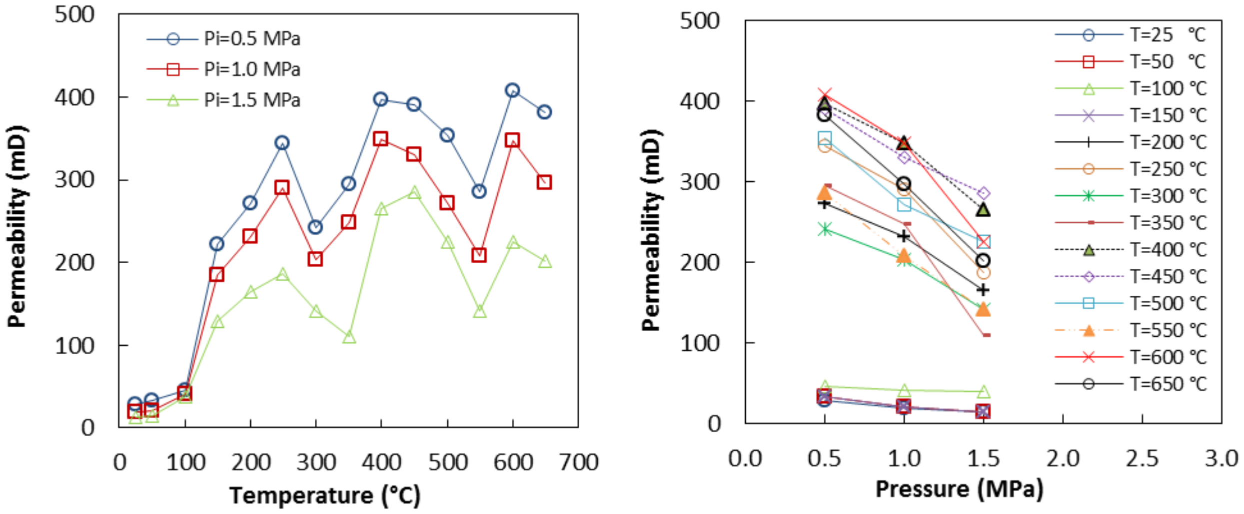

a) b)

Figure 3.14 Nitrogen permeability of the Yuanbaoshan lignite coal, Inner Mongolia, China, versus: a) temperature; and b) nitrogen-injection pressure (Niu et al., 2014)

Niu et al. (2014) did not provide a good explanation on why permeability decreased as injection gas pressures increased. Our interpretation is that this permeability-injection pressure response is related to change in stress condition of the coal specimens. The coal specimens were under triaxial stress condition, not isotropic stress, as the axial and confining stresses were not equal (see Table 3.2). In the triaxial test, the mean effective stress and the deviator stress are defined as in Equations 3.3 and 3.4, respectively.

$$p' = \frac{\sigma_1 + \sigma_3}{2} - P_i \tag{3.3}$$

$$q = \frac{\sigma_1 - \sigma_3}{2} \tag{3.4}$$

where p', q, and P_i are mean effective stress, deviator stress, and nitrogen-injection pressure, respectively.

The parameter $\frac{q}{p'}$ is a measure of shear. Increase of this parameter indicates shearing is progressing in the specimen. The increase of nitrogen-injection pressure (P_i) decreased the mean effective stress and, consequently, increased $\frac{q}{p'}$. Therefore, as the nitrogen-injection pressure increased in these experiments, more shearing occurred which, in turn, caused more shear deformation, hence, closure of some of the pores and drop in the coal permeability.

3.5.4.7. Dimensionless permeability versus temperature

Ratios of permeability of the Wyodak, the Xing-Long-Zhuang, and the Yuanbaoshan coals at elevated temperatures to the corresponding values at their ambient temperatures (which was 30 ºC for the Wyodak coal experiment, 20 ºC for the Xing-Long-Zhuang coal, and 25 ºC for the Yuanbaoshan coal) were plotted against temperature, as shown in Figure 3.15. It is apparent that the dimensionless permeability of these three coals shows general increasing orders with temperature; however, the data points are very scattered and more experimental data is required to define a typical trend for such a plot.

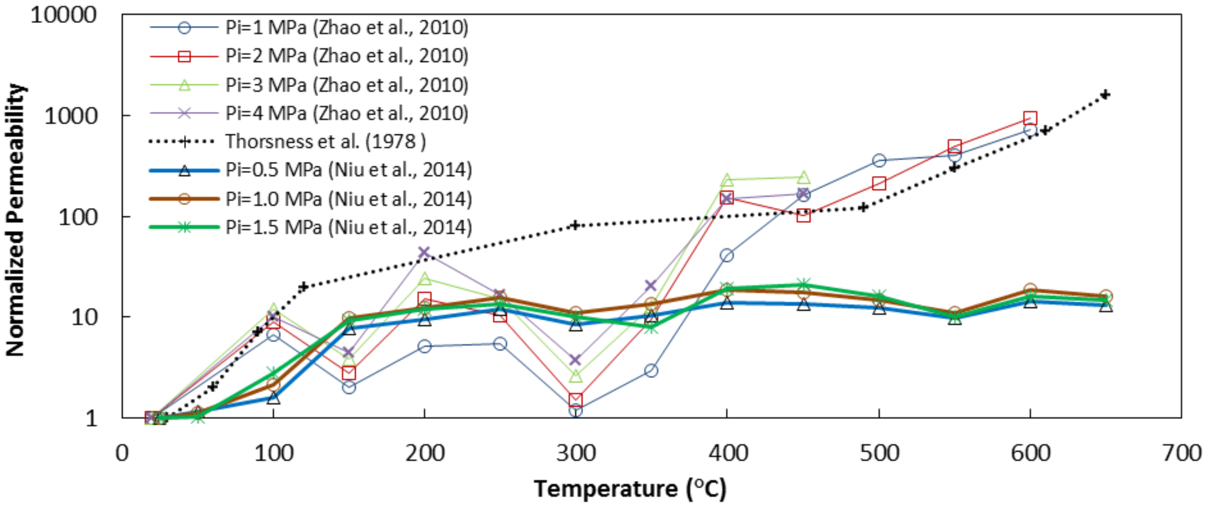

Figure 3.15 Normalized permeability of the Wyodak subbituminous coal (Thorsness et al., 1978), the Xing-Long-Zhuang steam coal, China (Zhao et al., 2010), and the Yuanbaoshan lignite coal, Inner Mongolia, China (Niu et al., 2014) to the corresponding values at their ambient temperatures

3.5.4.8. Correlation between permeability and porosity

Correlation between permeability and porosity is an important factor, especially for numerical simulation of UCG where permeability is usually updated as a function of porosity at any time-step. There is a scarcity of literature in regards to simultaneous measurement of permeability and porosity of coal under elevated temperature. Some of the reviewed studies measured permeability under high stress (equivalent to their in-situ stresses) and high temperature while in other studies porosity measurement was done differently using a mercury/helium porosimeter which cannot maintain high stress on the specimens. Knowing the mentioned deficiency and in order to update permeability-porosity correlation of Equation 3.1, data of the study by Zhao et al. (2010) was added to the Thorsness et al. (1978) data and the logarithm of permeability was plotted versus the change in porosity. A function similar to Equation 3.1 was fitted to all data points (Figure 3.16) and the parameter α of Equation 3.1 was estimated to be 16.7, which was derived based on the data available for these two types of coals and for the following conditions.

- Porosity change: $\Delta\emptyset \leq 0.5$
- Temperature: $t \leq 650$ ℃
- Final permeability after heating: $K \leq 16\ D$arcy

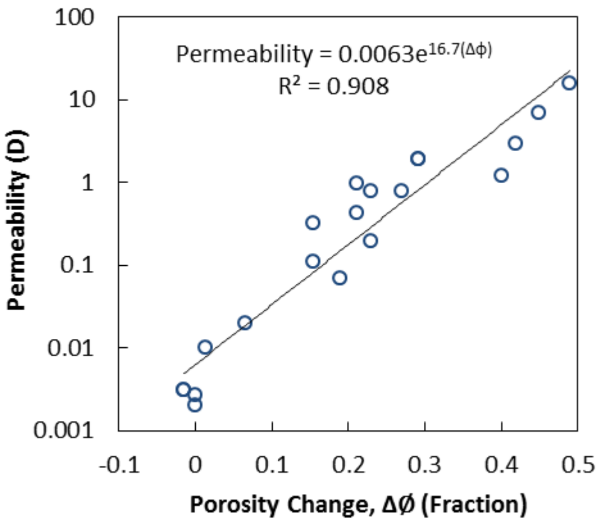

Figure 3.16 Permeability vs. change in porosity during drying and pyrolysis based on the data available for the Wyodak subbituminous coal (Thorsness et al., 1978) and the Xing-Long-Zhuang steam coal (Zhao et al., 2010)

The other permeability-porosity relationship is Equation 3.2 which was suggested for the Pittsburgh coal. It should be noted that Equation 3.1 relates permeability to change in porosity due to heating while Equation 3.2 defines permeability as a function of absolute porosity.

3.5.4.9. Discussion of porosity variation with temperature

It was observed during this review that almost all coals showed similar porosity response to the elevated temperatures. Initially, coals porosity decreased while heating from room temperature up to some temperature between 200 and 300 ºC and then rose as temperature further increased. The porosity curves experienced peaks at some temperature in the range of 400 to 700 ºC, and then slightly decreased with an increase in temperature. The initial drop in the porosity can be attributed to the non-uniform expansion of different compounds of coal (ash, and organic matter) which is a physical change; however, the decrease in porosity after passing the peak porosity could be due to the chemical process of pyrolysis and gasification.

The porosity measurement methods were not consistent throughout the database reviewed in this paper. Yu et al. (2012) used a CT-scan to estimate porosity. Some researchers used the mercury porosimetry (e.g., Balek and de Koranyi, 1990; de Koranyi and Balek, 1985; Zhao et al., 2010) while others used the helium porosimetry (Balek and de Koranyi, 1990; de Koranyi and Balek, 1985; Singer and Tye, 1979). Differences in porosity measuring methods on identical coal samples, no matter treated to an elevated temperature or not, would result in different values for porosity. Since helium has the smallest molecule, it seems to provide more accurate porosimetry than mercury, as helium can penetrate into very small pores in coal. The studies by Singer and Tye (1979) and Yao et al. (2009) supported this idea that different porosimetry methods may result in different values for porosity. Singer and Tye (1979) reported helium porosities and porosity by water-saturated porosimetry method for nineteen virgin (non-carbonized) samples of the Pittsburgh coal taken from different directions (normal to the bedding plane, parallel to butt cleat, and parallel to face cleat). For these nineteen samples, the helium porosities were between 1.9 to 13.1 times of the water-saturated porosities. Similar observations were reported by other researchers, other than those included in the HPHT database of Table 3.2. Yao et al. (2009) measured helium porosity, porosity by water-saturated porosimetry, and porosity by the X-ray computed tomography method on specimens of fourteen Chinese coals including lignite, bituminous, semi-anthracite, anthracite, and meta-anthracite. Although their measurement was not related to elevated temperatures, their results provide a valuable comparison between porosities measured by different methods. The helium porosities measured by Yao et al. (2009) were larger than the water porosities for all specimens; however, the average porosities of their CT-scan method (average of the porosities corresponding to consecutive slices) were larger than the helium porosities for all specimens. The larger CT-scan porosities could be because of this fact that the CT-scan method detects both the inter-connected and closed pores, whereas, the porosities measured using intrusion of fluid (water, mercury, and helium) only represents the inter-connected pores. It should be mentioned that there are some concerns regarding over-estimation of the CT-scan porosimetry as the area occupied with very low-density materials may contribute to the CT-scan porosity (Yao et al., 2009). Zou et al. (2013) also observed larger helium porosities than water porosities on nine coal samples taken from different mines in China. Yao and Liu (2012) reported results of helium and mercury porosimetry on four samples out of the fifteen coal samples published by Yao et al. (2009). For a lignite sample, mercury porosity was almost twice of that of the helium porosity while, for the other three samples (which were bituminous, semi-anthracite, and anthracite), helium porosities were a bit larger than mercury porosities (Yao and Liu, 2012).

3.5.4.10. Discussion of permeability variation with temperature

Permeability of the coals under study showed general ascending order as temperature increased; however, no unique trend was observed throughout the studied cases in this review. This scatter can be attributed to several factors; e.g. differences in the coals' petrology and rank, differences in type of the fluid being injected through the specimen (air or nitrogen), differences in size of the specimens (unlike small specimens, larger specimens may include cleat network which may affect the permeability measurements.), anisotropy, and different stress states on the samples.

3.5.4.11. Implications for UCG

In a UCG project, as temperature front advances, more drying/vaporization, pyrolysis, and gasification occur which enhance transport properties (i.e., porosity and permeability) of coal in the zone of influence of the UCG. The enhanced transport properties will ease syngas flow to the production well. The other contribution of high temperature to UCG is escalating heterogeneity in coal transport properties in the drying/vaporization, pyrolysis, and gasification zone. Initially, despite the inherent cleat network in coal, the solid matrix of the coal rock may have nearly uniform porosity and permeability; however, after the coal has been exposed to high temperature, volatile matters are released, and carbon is partially consumed. The latter would impose changes to the pore structure of the coal hence; alter its porosity and permeability.

3.5.5. Effect of temperature on strength and stiffness

Effect of temperature on coal strength and stiffness is critical as it influences the geomechanical response of the coal adjacent to a UCG gasification chamber. Geomechanical simulation of a UCG cavity considering temperature influence on stiffness and shear strength parameters of the coal and rock can better represent impacts of UCG on the strata as well as groundwater. This impact is different than the response from a simulation using constant material properties (Akbarzadeh and Chalaturnyk, 2013).

At higher temperature, coal specimens generally fail under smaller compressive (or shear) stress while exhibiting larger axial (or shear) strain (Shoemaker, 1976; Glass, 1984). Figure 3.17 shows a schematic of stress-strain responses of coals under different temperature.

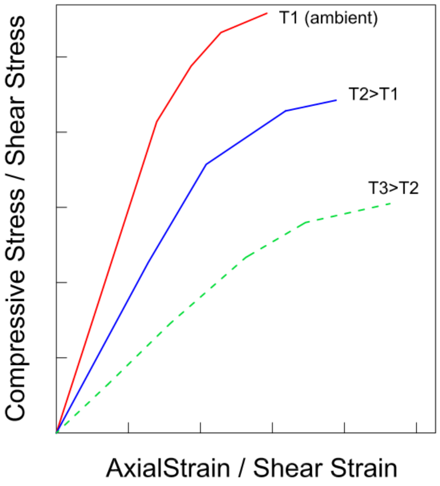

Figure 3.17 Schematic compressive stress-axial strain and shear stress-shear strain curves of coals at different temperatures
*Note: the curves are not to scale and only meant to show the comparative behaviors at different temperatures.

3.5.5.1. Bituminous coals, USA

Shoemaker (1976) studied the impact of heating on mechanical properties of pre-heated specimens of the Pittsburgh bituminous coal for demonstrating underground gasification of the eastern US coals. The specimens were taken from the Humphrey No.7 mine in Maidsville, West Virginia when the mine working face was near the Mount Morris, Pennsylvania, and at about 146 m depth. Specimens of different sizes were tested under different loading rates in uniaxial compression tests (Table 3.2). Remarkable influences on Uniaxial Compressive Strength (UCS) and elastic and shear moduli due to heating were observed. The behavior was somewhat similar to those in Figure 3.17. Specimens subjected to higher temperature exhibited smaller UCS but larger axial strain, except the specimen tested at 93.3 ºC which showed the largest UCS. These experiments showed that loading direction with regard to the bedding plane also affects coal strength and moduli. Shoemaker (1976) concluded that, when loading a coal specimen normal to the bedding plane, the strength is more than twice that obtained when loading normal to the face or butt cleats. Similar trends to that of Figure 3.17 were observed in shear tests in the bedding plane. Under higher temperatures, maximum shear stresses decreased but the amount of shear strains increased, except the specimen tested at 93.3 ºC which showed the largest peak shear strength.

Shoemaker (1976) also determined elastic modulus of the Pittsburgh coal specimens of different sizes with temperature in uniaxial compression in different directions (normal to the bedding plane, normal to the face cleats, and normal to the butt cleats) and under different loading rates (Figure 3.18.a). Elastic modulus, the slope of stress-train curve under a particular temperature in its initial elastic region, showed increase up to temperture of about 93.3 ºC and then decreased as temperature increased (Figure 3.18.a). Based on Figure 3.18.a, the initial part of the elastic modulus-temperature plots showed either no decline or a gain in elastic modulus and after temperature of about 300 ºC, elastic moduli approached the abscissa.

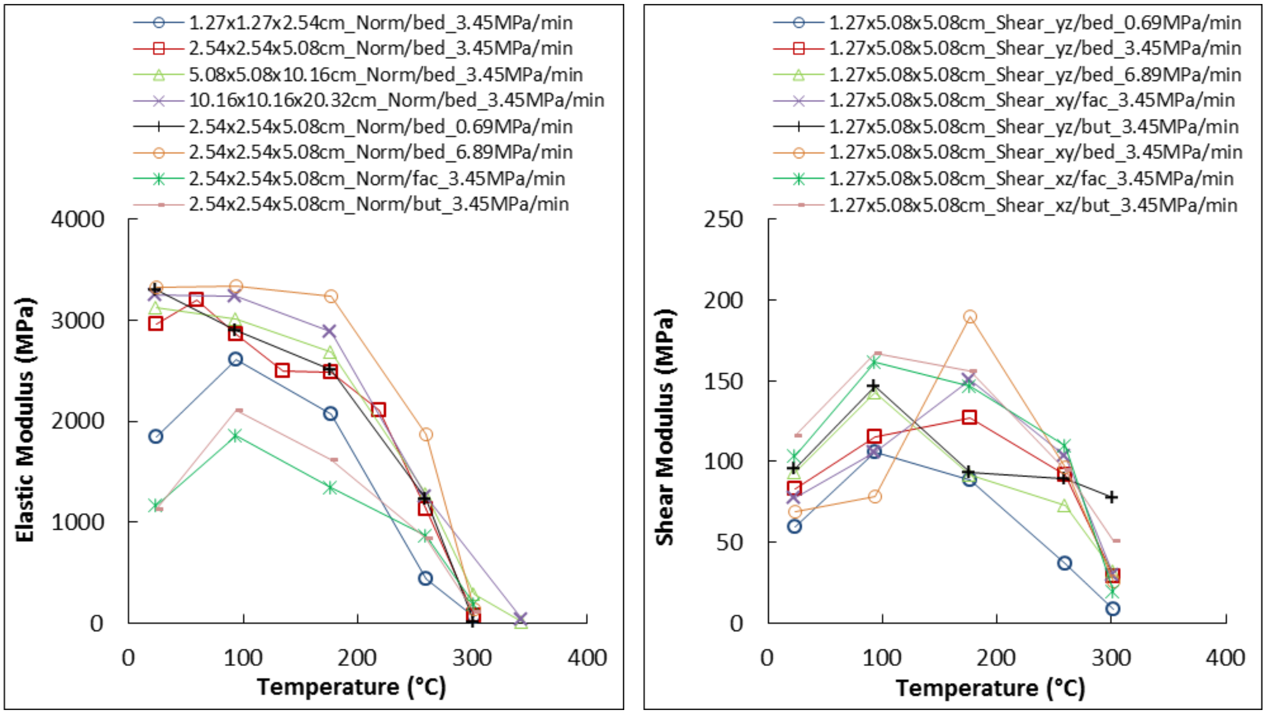

a) b)

Figure 3.18 a) Elastic moduli of the Pittsburgh bituminous coal specimens (from the Humphrey No.7 mine, Maidsville, West Virginia) vs. temperature in uniaxial compression; and b) shear moduli of the Pittsburgh coal specimens vs. temperature in a simple shear test (Shoemaker, 1976)

*Note: 1.27x1.27x2.54cm: specimen dimensions; Norm/bed: normal to the bedding plane; 3.45 MPa/min: loading rate; Shear_xy/fac: shear in xy plane in the direction of face cleats; Shear_xz/but: shear in xz plane in the direction of but cleats

Figure 3.18.b presents shear moduli of the Pittsburgh coal specimens in simple shear test in the bedding plane, the face cleats, and the butt cleats directions under different loading rates.

Initial part of the shear modulus-temperature plots showed a gain in stiffness. At temperature of about 300 ºC, there were significant drops in shear moduli. Also, it was observed that an increase in shear loading rate resulted in larger shear modulus.

Figure 3.18 also provides some insights on the effects of specimen size, loading rate, and anisotropy on elastic and shear moduli of the Pittsburgh coal. Generally, larger specimen size resulted in greater elastic modulus; likewise, greater loading rate led to greater elastic modulus. Elastic moduli for loading normal to the face and butt cleats were smaller than that of normal to the bedding plane.

Singer and Tye (1979) studied tensile and compressive strength of preheated specimens from the Pittsburgh bituminous coal. As mentioned in Table 3.2, the location where these samples were taken from was not mentioned in the article by Singer and Tye (1979); hence, it is not clear if they used samples from the same coal seam as Shoemaker (1976) or not. The tensile strength specimens were preheated to 350, 650, and 850 ºC whereas for the compressive strength specimens, preheating temperatures were 350, 475, 650, and 850 ºC. Both groups of specimens were tested at 23 ºC and 200 ºC. Variation of tensile and compressive strengths with carbonization and test temperature is shown in Figure 3.19. Both types of strengths decreased with an increase in test temperature. The tensile and compressive strengths significantly decreased as preheating temperature increased to 350 ºC. Specimens preheated to 650 and 850 ºC exhibited larger tensile and compressive strengths than those preheated to 350 ºC. Singer and Tye (1979) pointed out that this uncertain range (between 350 and 650 ºC) might be related to inconsistency in carbonization, or disturbance during storage or placement of the specimens in the strength measuring apparatus. Figure 3.19 also shows the effect of strength anisotropy of the Pittsburgh coal. The samples taken perpendicular to the bedding plane exhibited larger strength compared to the specimens taken parallel to the bedding plane.

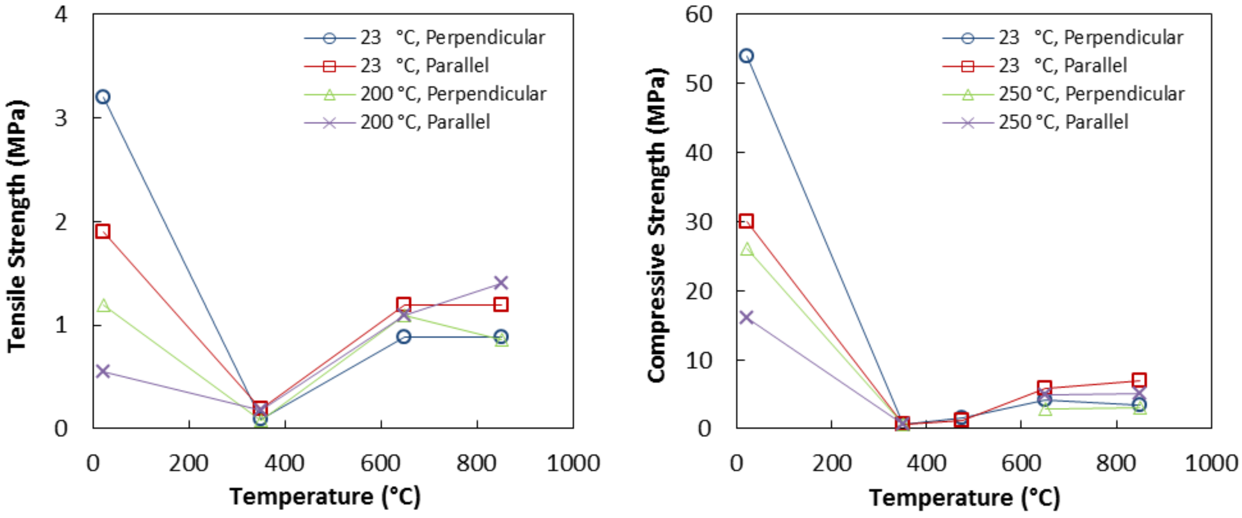

a) b)

Figure 3.19 a) Tensile; and b) compressive strengths of preheated specimens of the Pittsburgh coal (bituminous) showing the effect of carbonization (preheating) and test temperature as well as direction to the bedding plane (Singer and Tye, 1979)

3.5.5.2. Subbituminous coal, USA

Glass (1984) carried out triaxial experiments up to 250 ºC on subbituminous coal specimens from the Hanna Basin, perpendicular and parallel to the bedding plane. Specimens with maximum principal stress in the direction of the stratification resisted smaller deviator stress and had smaller elastic modulus. Similar trends to those presented in Figure 3.17 were observed for deviator stress plots versus axial and lateral strains normal and parallel to the bedding plane. There was a significant decrease in maximum deviator stress under elevated temperature, e.g., the coal sample parallel to the bedding plane at 250 ºC, resisted less than half of the deviator stress of the 25 ºC test. The elastic moduli of this coal from triaxial tests parallel and perpendicular to the bedding plane are shown in Figure 3.20.a. Elastic modulus curves were extended to higher temperatures using results of uniaxial tests, conducted in air at 350 ºC and 450 ºC. In the direction parallel to the bedding plane, initially a gain in elastic modulus was observed while for the other direction, continuous degradation of elastic modulus occurred (Figure 3.20.a). Also derived from the triaxial experiments was shear modulus for the same temperature in the direction normal to the stratification. Shear modulus changed from 960 to 140 MPa as temperature increased from 25 to 250 ºC (Figure 3.20.a). Poisson's ratio (from the triaxial tests) fluctuated between 0.38 and 0.23 under heating up to temperature of 250 ºC for the direction normal to the stratification whereas for the other direction, the corresponding values were 0.43 and 0.11(Figure 3.20.b).

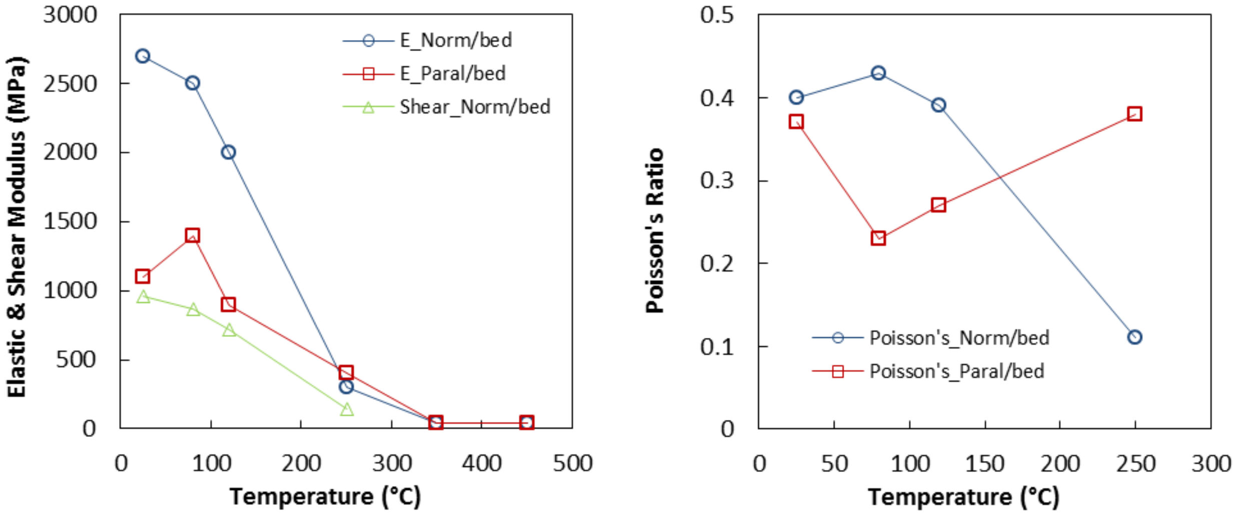

a) b)

Figure 3.20 Mechanical properties of the Hanna Basin coal (subbituminous) as a function of temperature and normal/parallel to the bedding plane: a) elastic and shear moduli; and b) Poisson's ratio (Glass, 1984)
*Note: "E" and "G" refer to elastic and shear modulus, respectively.

3.5.5.3. Anthracite and gas coals, China

Wan et al. (2011) reported elastic modulus degradation with temperature for specimens of anthracite and gas coals from high-pressure high-temperature triaxial tests which is presented in Figure 3.21. They used Equation 3.5, which is based on the theory of elasticity, to calculate elastic modulus from measured axial and lateral strains under axial and lateral stresses. Based on Figure 3.21, the elastic modulus of the anthracite coal approached the abscissa at a temperature of about 400 ºC, while the corresponding temperature for the gas coal was about 600 ºC. The trends shown in Figure 3.21 are somewhat similar to that of the Pittsburgh (Figure 3.18.a) and the Hanna Basin (Figure 3.20.a) coals.

$$E = \frac{(\sigma_1 - \sigma_2)(\sigma_1 + 2\sigma_2)}{(\sigma_1 + \sigma_2)\varepsilon_1 - 2\sigma_2\varepsilon_2} \tag{3.5}$$

where E is elastic modulus, σ_1 and σ_2 are axial and confining stresses, and $\varepsilon_1$and ε_2 are axial and lateral strains.

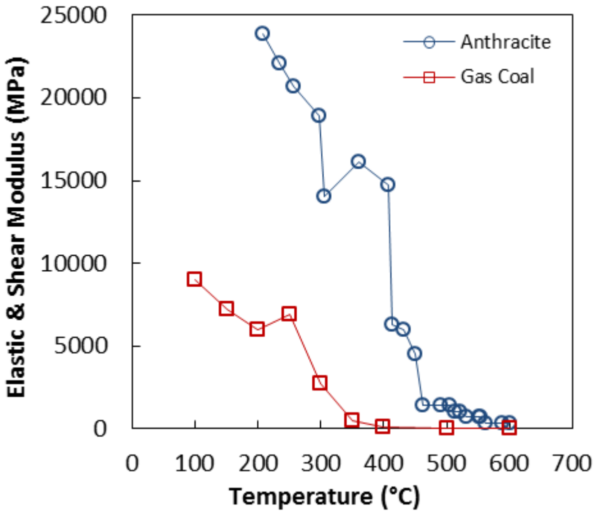

Figure 3.21 Relationship between elastic modulus and temperature for the Jincheng anthracite and the Xing-Long-Zhuang gas coals (Wan et al., 2011)

3.5.5.4. Dimensionless elastic and shear moduli versus temperature

Normalized elastic and shear moduli of the Pittsburgh coal (from Figure 3.18.a) and the Hanna Basin coal (from Figure 3.20.b) are plotted in Figure 3.22.a. The data from the Jincheng anthracite and the Xing-Long-Zhuang gas coal were not included in this figure as the original document did not report moduli values at ambient temperature (which was 24 ºC for the Pittsburgh coal and 25 ºC for the Hanna Basin coal). Based on Figure 3.22.a, one can define a range for normalized elastic modulus versus temperature. This range has a peak at about 100 ºC and approaches the abscissa at about 350 ºC. The peak value for normalized elastic modulus is about 1.85.

Normalized shear modulus-temperature range shows somewhat similar trend to that of elastic modulus-temperature (Figure 3.22.b). As shown in Figure 3.22.b, the maximum value for normalized shear modulus was 2.75 at temperature of 177 ºC from shear of a Pittsburgh coal specimen in the bedding plane under a loading rate of 3.45 MPa/min.

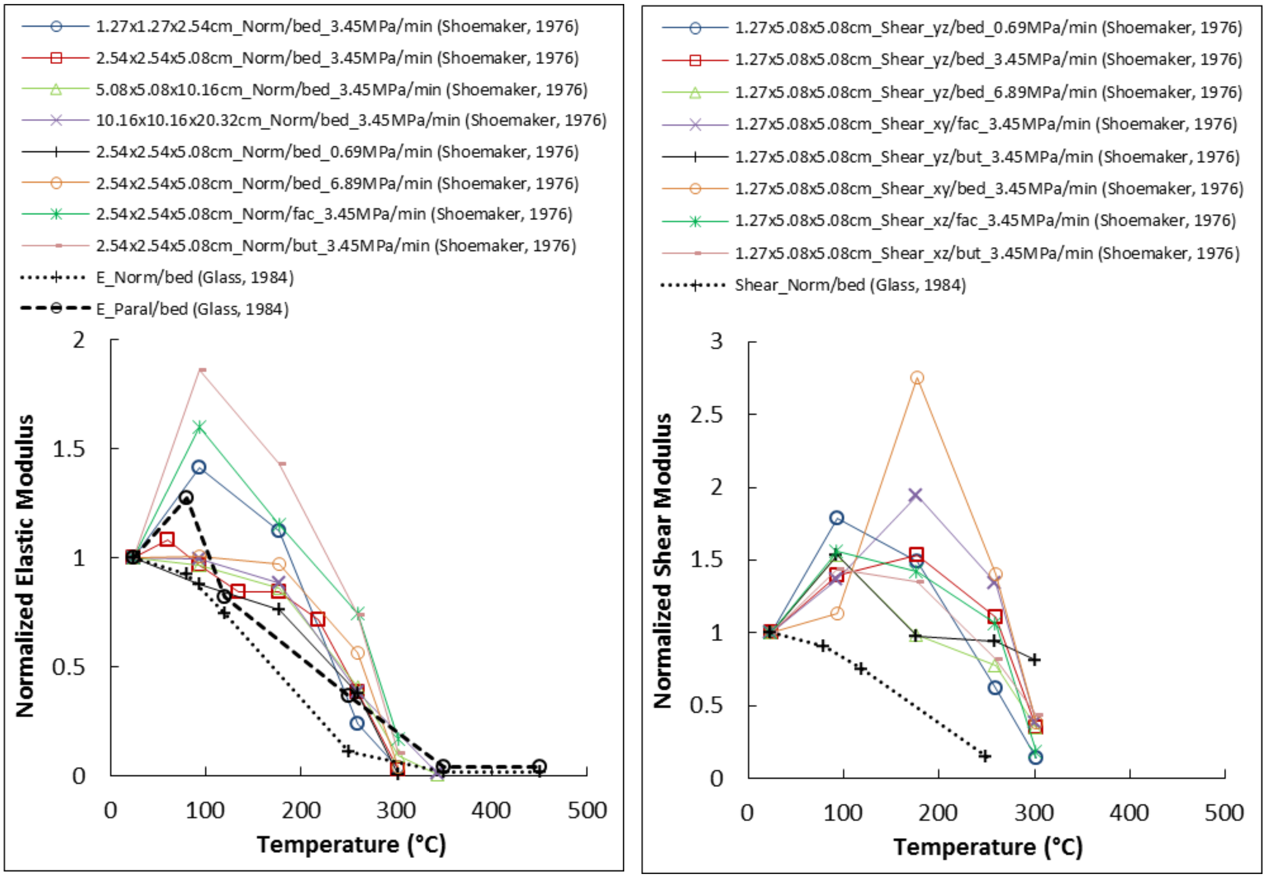

a)

b)

Figure 3.22 Normalized moduli of the Pittsburgh bituminous coal from the Humphrey No.7 mine, Maidsville, West Virginia (Shoemaker, 1976) and the Hanna Basin subbituminous coal (Glass, 1984) to the corresponding values at reference temperature (24 ºC for the Pittsburgh coal and 25 ºC for the Hanna Basin coal): a) elastic modulus; and b) shear modulus

3.5.5.5. Effect of anisotropy on strength and moduli degradation with temperature

The orientation of a coal specimen with regard to its bedding plane influences its strength and stiffness. As shown in Figure 3.18, Figure 3.20 and Figure 3.22, testing in the direction normal to the bedding plane resulted in greater strength and elastic modulus than parallel to the bedding plane. However, as temperature approached 300 ºC, the effect of anisotropy vanished because the massive thermo-chemical changes in a coal at higher temperature eliminate other effects such as anisotropy and inherent cleat network.

3.5.5.6. Implications for UCG

Mechanical properties of coal play important roles on the stability of the gasification cavity and integrity of caprock and underburden rock in a UCG project. The areas adjacent to the gasification cavity are exposed to high temperature and their strength and stiffness decline. The strength and stiffness degradation at elevated temperatures influence thermal deformation and stress of the strata. This response is in compliance with the published numerical simulations (Akbarzadeh and Chalaturnyk, 2013) which observed that using temperature-weakening elastic modulus for coal resulted in larger deformation and volumetric strain in the coal; however, smaller mean effective stress in both coal seam and caprock was observed.

3.6. Concluding remarks

3.6.1. Findings from this study

In this paper, impacts of UCG on structural properties of coal and their contributions to the growth of the gasification zone and/or cavity size were explained. A database including published experimental research studies regarding structural changes in coals at elevated temperature in the context of UCG were reviewed and discussed. Based on this study, following observations and conclusions can be drawn:

- Published HPHT experimental studies on coals are very scarce; hence, by reviewing and comparing behavior of different rank coals from different parts of world, this study tried to develop a pathway for future HPHT geomechanical experiments of coals.
- In the research studies done in 1970's, the performed mechanical tests were on preheated (carbonized) specimens. In these cases, preheating temperature showed a significant influence on the mechanical properties.
- Recent research studies are moving in the direction of using HPHT triaxial apparatus.
- High temperature causes drying/vaporization and pyrolysis in coal surrounding the gasification chamber of a UCG plant.
- Coal loses its weight under elevated temperature which is due to drying/vaporization and pyrolysis.

- While heating, coal exhibits a unique thermal deformation characteristic. Initially coal expands, at a certain temperature pyrolysis initiates and coal loses volatile matter and some of the macerals; hence, coal undergoes compressional volumetric strain.
- Heating causes microcracks in coal. The governing factors in the degree of cracking are temperature of the heating source and temperature gradient as well as the inherent fracture network and direction of heating with regard to the stratification in the coal.
- Maintaining a constant temperature on coal causes more pyrolysis gas production and rapid increase in compressional volumetric strain (creep phenomenon).
- In general, pore volume, aperture, porosity, and permeability of coal increase with temperature. The trend of changes is function of the coal type and its properties. This study compared porosity and permeability development of different coals.
- Generally, tensile, compressive, and shear strengths of coal decline with temperature.
- Elastic and shear moduli of coal under heating may initially stay unchanged or increase, but after exceeding a threshold temperature, they degrade drastically. Both moduli exhibited dependence on loading direction with regard to the bedding plane, loading rate, and the specimen size.
- Poisson's ratio of coal fluctuates with temperature.
- The orientation of a coal specimen with regard to its bedding plane influences its strength and stiffness. However the effect of anisotropy vanishes at elevated temperature.

3.6.2. Knowledge gaps in HPHT coal experiments

Structural response of a coal specimen to elevated temperature is function of several factors ranging from specimen geometry to measurement methodologies. Unlike other materials, there is no standard test method for geomechanical experiments on coal. The following are some of the knowledge gaps in this regard which asks for further development:

- What is the right size for measuring transport and geomechanical properties of coal in a HPHT triaxial test device? Although it is hard to answer this question because of the inherent cleat network in coals, the potential standard may specify the appropriate size as a function of the cleat network.

- What is the effect of restraints (confining and axial stresses) on porosity and permeability measurements at HPHT?
- What is the effect of heating rate on crack generation, and porosity and permeability evolution?
- Which gas should be used for porosity and permeability measurements? Should both measurements be done using the same gas? Does N_2 provide access to all small pores in coal specimen treated at HPHT?
- An appropriate constitutive geomechanical model for coal under elevated temperature, which also includes the thermo-chemical changes, is missing.

3.7. Acknowledgements

The authors are grateful to The Canadian Centre for Clean Coal/Carbon and Mineral Processing Technologies (C^5MPT) for providing the financial support to this research program.

3.8. References

Aiman, W. R., Ganow, H. C., & Thorsness, C. B. (1980). Hoe Creek II revisited: Boundaries of the gasification zone. *Combustion Science and Technology*, *23*(3-4), 125-130.

Akbarzadeh, H., & Chalaturnyk, R. J. (2013). Coupled fluid-thermal-mechanical analyses of a deep underground coal gasification cavity. *Journal of Architecture and Civil Engineering, Quest Journals 1*(1), 01-14.

American Society for Testing and Materials. (2012). ASTM D388-12 Standard Classification of Coals by Rank. ASTM, USA.

Anthony, D. B., & Howard, J. B. (1976). Coal devolatilization and hydrogastification. *AIChE Journal*, *22*(4), 625-656.

Arenillas, A., Rubiera, F., & Pis, J. J. (1999). Simultaneous thermogravimetric–mass spectrometric study on the pyrolysis behaviour of different rank coals. *Journal of Analytical and Applied Pyrolysis*, *50*(1), 31-46.

Arenillas, A., Rubiera, F., Pis, J. J., Cuesta, M. J., Iglesias, M. J., Jimenez, A., & Suarez-Ruiz, I. (2003). Thermal behaviour during the pyrolysis of low rank perhydrous coals. *Journal of Analytical and Applied Pyrolysis*, *68*, 371-385.

Avid, B., Purevsuren, B., Born, M., Dugarjav, J., Davaajav, Y., & Tuvshinjargal, A. (2002). Pyrolysis and TG analysis of Shivee Ovoo coal from Mongolia. *Journal of Thermal Analysis and Calorimetry*, *68*(3), 877-885.

Balek, V., & de Koranyi, A. (1990). Diagnostics of structural alterations in coal: Porosity changes with pyrolysis temperature. *Fuel*, *69*(12), 1502-1506.

Bangham, D., & Franklin, R.E. (1946). Thermal expansion of coals and carbonised coals. *Transactions of the Faraday Society, 42*, B289-294.

Bartel, L. C., Beard, S. G., Beckham, L. W., Reed, R. P., & Seavey, R. W. (1976). Instrumentation results from an in-situ coal gasification experiment. In *SPE Annual Fall Technical Conference and Exhibition*. Society of Petroleum Engineers.

Brandenburg, C. F., Reed, R. P., Boyd, R. M., Northrop, D. A., & Jennings, J. W. (1975). Interpretation of chemical and physical measurements from an in situ coal gasification experiment. In *SPE Annual Fall Technical Conference and Exhibition*. Society of Petroleum Engineers.

Burton, E., Friedmann, J., & Upadhye, R. (2006). Best practices in underground coal gasification. Draft. US DOE contract no W-7405-Eng-48. Lawrence Livermore National Laboratory, 119 pages.

Cooke, S. D., & Oliver, R. L. (1983). Ground water quality at the Hanna underground coal gasification experimental sites, Hanna, Wyoming: data base and summary. *US Department of Energy/Associated Western Universities, Inc. Under cooperative, contract (DE-AC07–76ET10723).*

Couch, G. R. (2009). Underground coal gasification. IEA Clean Coal Centre. International Energy Agency, London.

Daggupati, S., Mandapati, R. N., Mahajani, S. M., Ganesh, A., Mathur, D. K., Sharma, R. K., & Aghalayam, P. (2010). Laboratory studies on combustion cavity growth in lignite coal blocks in the context of underground coal gasification. *Energy*, *35*(6), 2374-2386.

Daggupati, S., Mandapati, R. N., Mahajani, S. M., Ganesh, A., Sapru, R. K., Sharma, R. K., & Aghalayam, P. (2011). Laboratory studies on cavity growth and product gas composition in the context of underground coal gasification. *Energy*, *36*(3), 1776-1784.

de Koranyi, A., & Balek, V. (1985). Structural changes in coals during pyrolysis. *Thermochimica Acta*, *93*, 737-740.

De la Puente, G., Iglesias, M. J., Fuente, E., & Pis, J. J. (1998). Changes in the structure of coals of different rank due to oxidation-effects on pyrolysis behaviour. *Journal of Analytical and Applied Pyrolysis*, *47*(1), 33-42.

Elbeyli, I., Piskin, S., & Sutcu, H. (2004). Pyrolysis kinetics of Turkish bituminous coals by thermal analysis. *Turkish Journal of Engineering* and *Environmental Sciences, 28*, 233-239.

Feng, Z. J., Zhao, Y. S., & Wan, Z. J. (2012). Experiment study of the thermal deformation of in-situ gas coal. *Rock Mechanics: Achievements and Ambitions-Proceedings of the 2nd ISRM International Young Scholars' Symposium on Rock Mechanics*, 103-108.

Ghabezloo, S. (2013). Effect of porosity on the thermal expansion coefficient of porous materials. *In Poromechanics V@ ASCE 2013. Proceedings of the Fifth Biot Conference on Poromechanics*, 1857-1866.

Glass, R. E. (1984). The thermal and structural properties of a Hanna basin coal. *Journal of Energy Resources Technology*, *106*(2), 266-271.

Hill, J. O., Ma, S., & Heng, S. (1989). Thermal analysis of Australian coals-a short review. *Journal of Thermal Analysis*, *35*(6), 2009-2024.

Heuze, F. E. (1983). High-temperature mechanical, physical and thermal properties of granitic rocks-a review. *International Journal of Rock Mechanics and Mining Sciences & Geomechanics Abstracts 20*(1), 3-10.

http://en.wikipedia.org/wiki/Coal#Types (accessed May 02, 2014) http://en.wikipedia.org/wiki/Wyodak_Mine (accessed May 02, 2014)

Kapusta, K., Stanczyk, K., Wiatowski, M., & Checko, J. (2013). Environmental aspects of a field-scale underground coal gasification trial in a shallow coal seam at the Experimental Mine Barbara in Poland. *Fuel 113*, 196-208.

Kostur, K., & Kacur, J. (2008). The monitoring and control of underground coal gasification in laboratory conditions. *Acta Montanistica Slovaca*, *13*(1), 111-117.

Krzesinska, M., Szeluga, U., Czajkowska, S., Muszynski, J., Zachariasz, J., Pusz, S., Kwiecinska, B., Koszorek, A., & Pilawa, B. (2009). The thermal decomposition studies of three Polish bituminous coking coals and their blends. *International Journal of Coal Geology 77*(3), 350-355.

Linc Energy. (2014). http://www.lincenergy.com (accessed May 02, 2014)

Long, Q. M., Wen, G. C., Zou, Y. H., & Zhao, X. S. (2009). Experimental study on gas permeability by adsorption under 3D-stress. *Journal of Coal Science & Engineering (China) 15*(2), 148-151.

Lu, T., Laman, G., xxxx. A preliminary comparison of coal Classification and processing between Canada and China (http://www.tetratech.com/pdfs/66/Coal_Classification_CMP2012_Ting_Lu.pdf, accessed May 02, 2014*)*

Luo, J. A., & Wang, L. (2011). High-temperature mechanical properties of mudstone in the process of underground coal gasification. *Rock Mechanics and Rock Engineering 44*(6), 749-754.

Luo, X., Tan, Q., Luo, C., & Wang, Z. (2008). Microseismic monitoring of burn front in an underground coal gasification experiment. In *The 42nd US Rock Mechanics Symposium (USRMS)*. American Rock Mechanics Association.

Niu, S., Zhao, Y., & Hu, Y. (2014). Experimental investigation of the temperature and pore pressure effect on permeability of lignite under the in situ condition. *Transport in Porous Media*, *101*(1), 137-148.

Northrop, D. A., Beard, S. G., Bartel, L. C., Beckham, L. W., & Hommert, P. J. (1977). Instrumentation for in situ coal gasification: An assessment of techniques evaluated on the Hanna II experiment (No. SAND-77-1072). Sandia Labs., Albuquerque, N. Mex. (USA).

Ohtomo, Y., Ijiri, A., Ikegawa, Y., Tsutsumi, M., Imachi, H., Uramoto, G. I., ... & Inagaki, F. (2013). Biological CO_2 conversion to acetate in subsurface coal-sand formation using a high-pressure reactor system. *Frontiers in Microbiology, 4*, 1-17.

Perera, M. S. A., Ranjith, P. G., Choi, S. K., & Airey, D. (2012). Investigation of temperature effect on permeability of naturally fractured black coal for carbon dioxide movement: An experimental and numerical study. *Fuel*, *94*, 596-605.

Podder, J., Hossain, T., & Mannan, K. M. (1995). An investigation into the thermal behaviour of Bangladeshi coals. *Thermochimica Acta*, *255*, 221-226.

Qu, H., Liu, J., Chen, Z., Wang, J., Pan, Z., Connell, L., & Elsworth, D. (2012). Complex evolution of coal permeability during CO_2 injection under variable temperatures. *International Journal of Greenhouse Gas Control*, *9*, 281-293.

Richter, D., & Simmons, G. (1974). Thermal expansion behavior of igneous rocks. *International Journal of Rock Mechanics and Mining Sciences & Geomechanics Abstracts, 11*(10), 403-411.

Rotaru, A. (2012). Thermal analysis and kinetic study of Petroşani bituminous coal from Romania in comparison with a sample of Ural bituminous coal. *Journal of Thermal Analysis and Calorimetry, 110*(3), 1283-1291.

Schrider, L. A., & Jennings, J. W. (1974). An underground coal gasification experiment, Hanna, Wyoming. In *Fall Meeting of the Society of Petroleum Engineers of AIME*. Society of Petroleum Engineers.

Seo, D. K., Park, S. S., Kim, Y. T., Hwang, J., & Yu, T. U. (2011). Study of coal pyrolysis by thermo-gravimetric analysis (TGA) and concentration measurements of the evolved species. *Journal of Analytical and Applied Pyrolysis*, *92*(1), 209-216.

Shoemaker, H. D. (1976). Mechanical properties of the Pittsburgh coal at elevated temperatures. PhD Dissertation, West Virginia University.

Singer, J. M., & Tye, R. P., (1979). Thermal, mechanical, and physical properties of selected bituminous coals and cokes. Bureau of Mines Report RI 8364.

Sonibare, O. O., Ehinola, O. A., Egashira, R., & KeanGiap, L. (2005). An investigation into the thermal decomposition of Nigerian coal. *Journal of Applied Sciences 5*, 104-107.

Speight, J. G. (2005). Handbook of Coal Analysis. John Wiley & Sons.

Stanczyk, K., Smolinski, A., Kapusta, K., Wiatowski, M., Swiadrowski, J., Kotyrba, A., & Rogut, J. (2010). Dynamic experimental simulation of hydrogen oriented underground gasification of lignite. *Fuel 89*, 3307-3314.

Stanczyk, K., Howaniec, N., Smolinski, A., Swiadrowski, J., Kapusta, K., Wiatowski, M., Grabowski, J., & Rogut, J. (2011). Gasification of lignite and hard coal with air and oxygen enriched air in a pilot scale ex situ reactor for underground gasification. *Fuel 90*, 1953-1962.

Stanczyk, K., Kapusta, K., Wiatowski, M., Swiądrowski, J., Smolinski, A., Rogut, J., & Kotyrba, A. (2012). Experimental simulation of hard coal underground gasification for hydrogen production. *Fuel*, *91*(1), 40-50.

Su, F., Nakanowataru, T., Itakura, K., Ohga, K., & Deguchi, G. (2013). Evaluation of structural changes in the coal specimen heating process and UCG model experiments for developing efficient UCG systems. *Energies 6*, 2386-2406.

Sury, M., White, M., Kirton, J., Carr, P., Woodbridge, R., Mostade, M., Chappell, R., Hartwell, D., Hunt, D., & Rendell, N. (2004a). Review of environmental issues of underground coal gasification-best practice guide: United Kingdom Department of Trade and Industry Report No. COAL R273. DTI/Pub URN 04/1881.

Sury, M., White, M., Kirton, J., Carr, P., Woodbridge, R., Mostade, M., Chappell, R., Hartwell, D., Hunt, D., & Rendell N. (2004b). Review of environmental issues of underground coal gasification: United Kingdom Department of Trade and Industry. Report No. COAL R272. DTI/Pub URN 04/1880.

Swan Hills Synfuels. (2012). Swan Hills in-situ coal gasification technology development; Final outcomes report. Swan Hills Synfuels, Alberta, Canada.

Thimons, E. D., & Kissell, F. N. (1973). Diffusion of methane through coal. *Fuel*, *52*(4), 274-280.

Thorsness, C. B., Grens, E. A., & Sherwood, A. (1978). A one-dimensional model for in situ coal gasification. UCRL-52523, Lawrence Livermore, National Laboratory (LLNL) Report, Berkeley, California.

UCG Association. (2014). http://www.ucgassociation.org (accessed May 02, 2014)

Wan, Z., Feng, Z., Zhao, Y., Zhang, Y., Li, G., & Zhou, C., (2011). Elastic modulus's evolution law of coal under high temperature and triaxial stress. *Journal of China Coal Society, 36*(10), 1736-1740.

Wang, C., He, M., Zhang, X., Liu, Z., & Zhao, T. (2013). Temperature influence on macro-mechanics parameter of intact coal sample containing original gas from Baijiao Coal Mine in China. *International Journal of Mining Science and Technology. 23*(4), 597-602.

Wang, J., Du, J., Chang, L., & Xie, K. (2010). Study on the structure and pyrolysis characteristics of Chinese western coals. *Fuel Processing Technology 91*(4), 430-433.

Wang, G. X., Wang, Z. T., Feng, B., Rudolph, V., & Liao, J. L. (2009). Semi-industrial tests on enhanced underground coal gasification at Zhong-Liang-Shan coal mine. *Asia-Pacific Journal of Chemical Engineering 4*(5), 771-779.

World Energy Council. (2010). 2010 survey of energy resources. World Energy Council, London, UK.

Xu, R., Li, H., Guo, C., & Hou, Q. (2014). The mechanisms of gas generation during coal deformation: Preliminary observations. *Fuel 117*, 326-330.

Yang, L. (2004). Study on the model experiment and numerical simulation for underground coal gasification. *Fuel*, *83*(4), 573-584.

Yao, Y., & Liu, D. (2012). Comparison of low-field NMR and mercury intrusion porosimetry in characterizing pore size distributions of coals. *Fuel 95*, 152-158.

Yao, Y., Liu, D., Che, Y., Tang, D., Tang, S., & Huang, W. (2009). Non-destructive characterization of coal samples from China using microfocus X-ray computed tomography. *International Journal of Coal Geology, 80*(2), 113-123.

Yin, G., Jiang, C., Wang, J. G., & Xu, J. (2013). Combined effect of stress, pore pressure and temperature on methane permeability in anthracite coal: An experimental study. *Transport in Porous Media 100*(1), 1-16.

Youngberg, A.D., Sinks, D. J., Craig, G. N., Ethridge, F. G., & Burns, L. K. (1983). Postburn evaluation for Hanna II, Phases 2 and 3 underground coal gasification experiments, Hanna, Wyoming. United States Office of Scientific and Technical Information, Technical Information Center. Under cooperative contract (DE-FC21-83FE60177).

Yu, Y., Liang, W., Hu, Y., & Meng, Q. (2012). Study of micro-pores development in lean coal with temperature. *International Journal of Rock Mechanics & Mining Sciences 51*, 91-96.

Zhao, Y., Qu, F., Wan, Z., Zhang, Y., Liang, W., & Meng, Q., (2010). Experimental investigation on correlation between permeability variation and pore structure during coal pyrolysis. *Transport in Porous Media, 82*(2), 401-412.

Zou, M., Wei, C., Zhang, M., Shen, J., Chen, Y., & Qi, Y. (2013). Classifying coal pores and estimating reservoir parameters by nuclear magnetic resonance and mercury intrusion porosimetry. *Energy & Fuels 27*(7), 3699-3708.

Chapter 4 High-Pressure and High-Temperature Geomechanical Experiments on a Fractured Coal from Alberta[1]

4.1. Abstract

Understanding mechanical behavior and permeability of coal, a fractured organic rock, at ambient and high temperature is key in optimizing a high-temperature in-situ process such as underground coal gasification. The main objectives of this study were to characterize the thermal deformation, stress-strain behavior as well as gas permeability of coal samples acquired from the Genesee coal mine in the Central Alberta, Canada, at temperatures varying from about 25 to 200 ^{o}C and under confining stresses ranging from 4 to 12 MPa. These measurements were conducted in a high-pressure high-temperature triaxial apparatus that had a maximum operating temperature of 200 ^{o}C. Initial thermal expansion was observed during heating which was followed by contraction in both axial and lateral directions at about 140 ^{o}C. This temperature corresponds to occurrence of thermo-chemical process of pyrolysis. Specimens sheared at 200 ^{o}C showed higher peak strengths and larger axial strains compared to those tested at room temperature. This coal exhibited a compressional volumetric strain response up to peak stress, both at room temperature and 200 ^{o}C; however, a reversal point was observed in the volumetric strain curves in post-peak region. Permeability of this coal was studied under various temperatures; room temperature, 80, 140, and 200 ^{o}C. Fluctuations of permeability were observed with both effective confining stress and temperature. At 80 ^{o}C, permeability was the lowest which was due to thermal expansion of the matrix and closure of the initial fractures. Permeability increased at 140 and 200 ^{o}C which was a combined response of thermal expansion and pyrolysis effects. Permeability dropped with progressive shearing in the beginning of stress-strain curve.

Keywords: Coal, Permeability, Volumetric strain, Elastic modulus, Temperature, Triaxial

---

[1] A version of this chapter will be submitted for journal publication as:
Akbarzadeh, H., & Chalaturnyk, R.J. (201x). Influence of high pressure and temperature on mechanical behavior and permeability of a fractured coal.

4.2. Introduction

Coal is an organic sedimentary rock which is of economic interest. Coal contains varying amounts of carbon, hydrogen, nitrogen, oxygen, and sulfur as well as small amounts of other elements, including mineral matter (Speight, 2005). The organic nature of this rock along with natural fracture networks makes its behavior distinctive from other rocks.

Understanding coal behavior is crucial in successful operation of an in-situ process such as Underground Coal Gasification (UCG). In UCG, after building a system of injector and producer wells, coal is ignited. Thereafter, the gasification process is maintained by providing an oxygen-based mixture. The gasification generates temperatures well over 1000 ^{o}C. After some coal has been burnt away, a cavity is formed. Temperature front advances beyond this cavity, but with less intensity. This zone is where a complex coupled thermal-hydro-chemical-mechanical process happens. Devolatilization, change in water phase, thermal stress and strain, change in porosity and permeability, and stiffness degradation simultaneously occur. Understanding behavior of coal seam in this zone helps optimize UCG process and mitigate syn- and post-gasification risks.

Extensive experimental researches were carried out to understand coal mechanical behavior under ambient temperature (e.g., Buzzi et al., 2014; Gentzis et al., 2007; Medhurst and Brown, 1998). Permeability of coal to water, air, and gas at room temperature was previously studied (e.g., Dabbous et al., 1974; Gensterblum et al., 2014; Li et al., 2014; Somerton et al., 1975). Change in permeability of coal during progressive shearing was also investigated (Wang et al., 2013). The challenging part of coal research is conducting experiments under high temperature. Akbarzadeh and Chalaturnyk (2014) reviewed structural changes in coal during heating including, but not limited to; micro crack generation, thermal deformation, porosity and permeability, and strength and stiffness. Experimental studies conducted in 1970's, utilized preheated specimens (Glass, 1984; Shoemaker, 1976; Singer and Tye, 1979; Thorsness et al., 1978). Coal samples were preheated (carbonized) in a furnace then moved to a geomechanical apparatus (direct shear, simple shear, uniaxial, triaxial) for measuring their strength and stiffness. Similar approach was followed for permeability measurements. Recent studies used High-Pressure High-Temperature (HPHT) triaxial apparatus to measure permeability at various temperatures up to some 600 ^{o}C (Feng et al., 2012; Liu et al., 2014; Niu et al., 2014; Wan et al., 2011; Zhao et al., 2010). Feng et al. (2012) measured thermal deformation using a raster sensor; however, other researchers did not specify how they measured thermal deformation and which cross section area (original or instantaneous) they used for permeability and stress calculations.

Since coal undergoes a significant thermal deformation, using initial cross section area, especially in the case of very high temperatures, would not be accurate. In high temperature triaxial experiments on rocks, unlike traditional soil mechanics testing, cell liquid volume change is not accurate and cannot be utilized to estimate the specimen volume change. Cell liquid expands remarkably due to heating. Instead, internal LVDTs facilitate measuring deformation during heating and shearing. To date, no high-temperature study on Alberta coal has been reported. The objectives of this study were to investigate thermal deformation characteristics, stress-strain characteristics as well as gas permeability of some Alberta coal samples both at room temperature and high temperature. It was intended to perform all these measurements in a single apparatus, namely a HPHT triaxial device.

4.3. Experiments

4.3.1. Apparatus

The HPHT triaxial machine (Figure 4.1) was equipped with nitrogen cylinders to facilitate gas-permeability measurements. The apparatus included a high-capacity triaxial cell that was accompanied with multiple ISCO pumps and instruments. Working temperature for this apparatus is 200 ^{o}C.

The cell pressure pump exerted confining stress on the specimen utilizing high-temperature white oil. A high pressure transducer recorded oil pressure (cell pressure) adjacent to the cell. Heating of the specimen was done by means of heating rods embedded in the wall of the triaxial cell which were connected to the temperature controller panel. Heat generated by the heating rods was transmitted from the cell to the confining fluid and eventually to the specimen. One thermocouple was placed inside the confining fluid to help control and maintain constant temperature throughout the experiment.

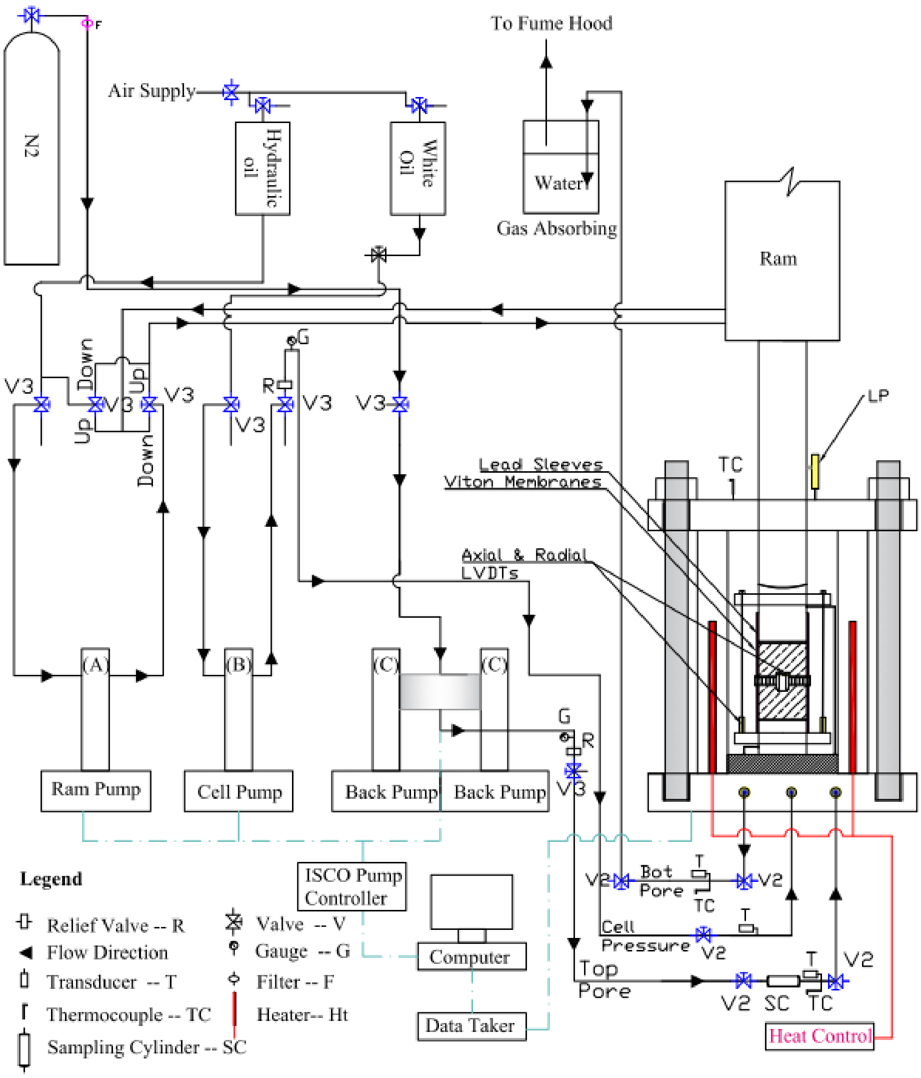

Figure 4.1 Schematic of the HPHT triaxial apparatus used in this study

Back pumps received nitrogen gas from nitrogen cylinders and supplied pore pressure to the specimen. These pumps were used to measure permeability of the specimen. Two high-pressure transducers were mounted on the pore lines, adjacent to the cell, to record pore pressure in the upstream and downstream.

The ram pump pushed a hydraulic ram to provide axial force required for shearing the specimen. Axial load was recorded by means of a load cell.

An external linear potentiometer (LP) measured axial deformation of the specimen. The specimen was jacketed with an in-house made lead sleeve and then enclosed with a Viton membrane. The lead sleeve was utilized to prevent gas diffusion through the Viton membrane at elevated temperatures. Two internal linear variable displacement transducers (LVDT) were mounted around the specimen that recorded axial deformation of the specimen. Another LVDT was placed in a circumferential chain to measure circumferential deformation. The axial LVDTs were used as a complimentary measure of axial deformation during shear. However all the axial strain calculations during shear presented in the stress-strain curves was done based on the external LP readings. Though, the internal LVDTs were the only tools for measuring deformation during heating.

The far end of the downstream pore line was submerged in water to allow nitrogen and pyrolysis gas (if any) absorbed into water. Any remaining gas was directed to a fume hood. The entire ISCO pump controllers and electronics were connected to data logging systems which utilize two PCs.

4.3.2. Sample preparation

Cylindrical coal specimens with diameter of about 6.1 cm (2.5 inches) were cored from coal blocks acquired from the Genesee coal mine in the Central Alberta, Canada. One of the coal blocks is shown in Figure 4.2. The blocks had visually detectable face and but cleats as well as discontinuities along the bedding plane. The face cleats' spacing varied from about 0.6 to 3.8 cm (0.25 to 1.5 inches); however, the but cleats were not as consistent as the face cleats. The specimens were drilled perpendicular to the bedding plane. Bedding plane discontinuities made it very challenging for coring. Wet drilling with water was not successful. Therefore, drilling was done dry while containing the drill bit area in order to enclose the dusts. Most of cores broke along bedding plane discontinuities; hence none of the specimens were twice as long as their diameters. The specimens were end-trimmed using a lathe machine. No specific measurements regarding any potential gas desorption was included in the coring process.

Specimen S4, as an example, is shown in Figure 4.3. Vertical fractures, bedding plane fissures, as well as dissimilar natural fracture networks in two end surfaces of the specimen are depicted in Figure 4.3.a, b, and c, respectively. This heterogeneity was also observed in other specimens. Figure 4.3.d shows how the two internal axial LVDTs and the circumferential chain were mounted inside the triaxial cell.

Ten specimens were obtained which were between 5.6 and 10.6 cm long. Table 4.1 summarizes dimensions of five specimens successfully tested in this study.

Figure 4.2 A coal block from the Genesee coal mine in the Central Alberta, Canada
*Note: The measuring tape's divisions are in inches.

Table 4.1 Specimens' dimensions and density

Specimen ID	Diameter (cm)	Length (cm)	Length to diameter ratio (L/D)	Density (g/cm^3)
S1	6.1	10.6	1.7	1.3
S2	6.1	8.7	1.4	1.3
S3	6.1	8.0	1.3	1.3
S4	6.1	7.7	1.3	1.3
S7	6.1	6.5	1.1	1.3

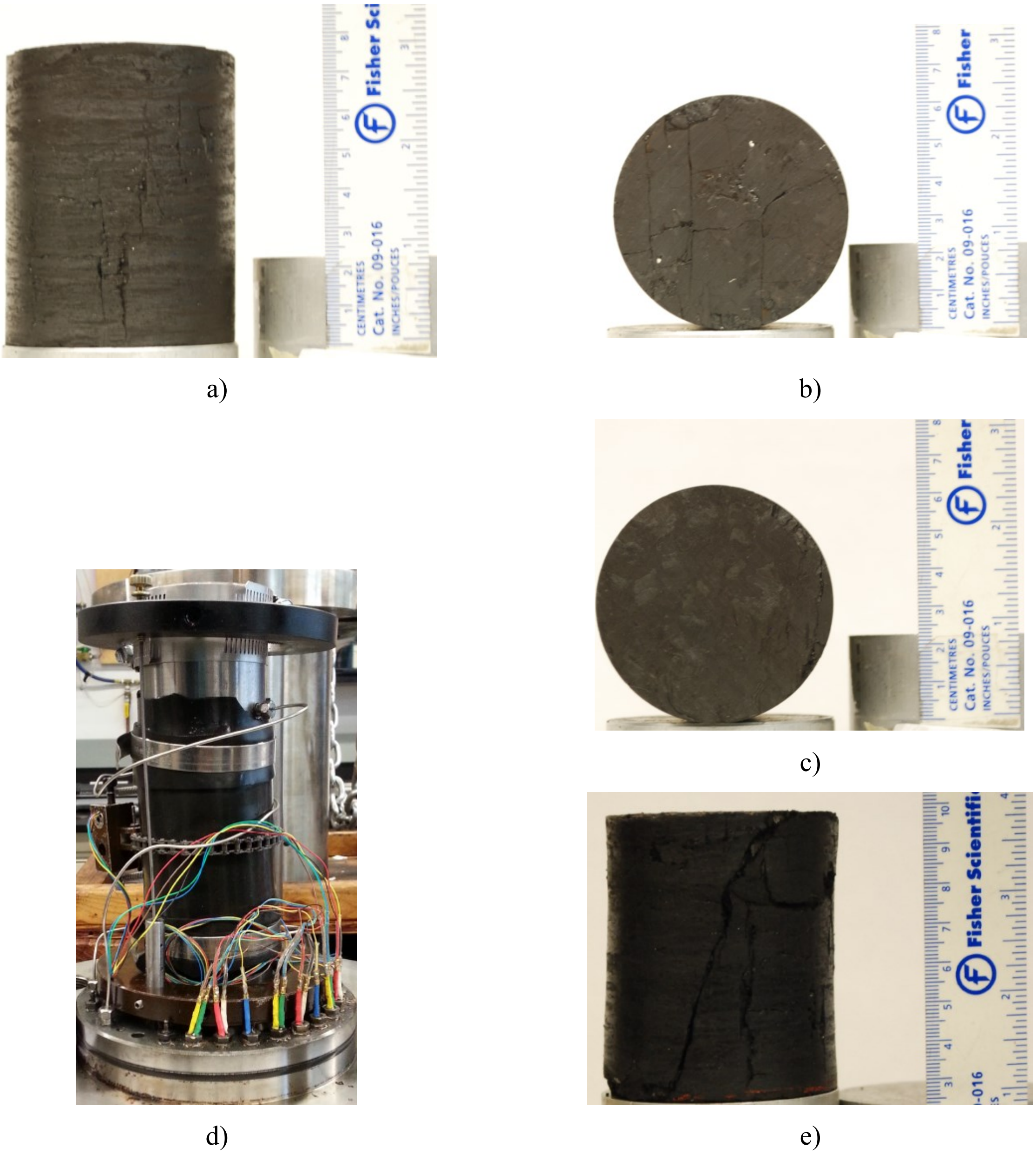

a)

b)

c)

d)

e)

Figure 4.3 Specimen S4: a) initial vertical fractures; b) and c) two ends of the specimen showing heterogeneity in initial fracture networks; d) the internal LVDTs and circumferential chain mounted around the specimen; and e) S4 after shear at 203.9 ^{o}C

*Note: The measuring tape's divisions are in cm.

4.3.3. Testing program

The testing plan for this study is explained in Table 4.2. Two specimens (S1 and S7) were selected for testing at room temperature but under different confining stresses. Specimen S1 was tested at room temperature under a cell pressure equal to 12 MPa. Nitrogen permeability of S1 was measured prior and during shearing. Specimen S7 was also tested at room temperature but under 4 MPa confining stress.

Table 4.2 Testing program for each specimen

Specimen ID	Maximum temperature (^{o}C)	Cell pressure (MPa)	Experimental steps [a]
S7	Room	4	– Perform shear at room temperature and at a rate of 2% axial strain/day
S1	Room	12	– Measure N_2 permeability at room temperature and under various differential pressures, – Perform shear at room temperature and at a rate of 5% axial strain/day, – Pause shearing at various time and measure N_2 permeability
S2	200	6.5	– Measure N_2 permeability at room temperature and under various differential pressures, – Apply about 2 MPa deviator stress at a rate of 5% axial strain/day, measure permeability, remove the 2 MPa deviator stress (only S4), – Heat up specimen to about 80 ^{o}C and at a rate of 10 ^{o}C /hour, – Maintain specimen at 80 ^{o}C overnight (at least 12 hours), – Measure N_2 permeability at 80 ^{o}C and under various differential pressures, – Heat up specimen to about 140 ^{o}C and at a rate of 10 ^{o}C/hour, – Maintain specimen at 140 ^{o}C overnight (at least 12 hours), – Measure N_2 permeability at 140 ^{o}C and under various differential pressures, – Heat up specimen to about 200 ^{o}C and at a rate of 10 ^{o}C /hour, – Maintain specimen at 200 ^{o}C overnight (at least 12 hours), – Measure N_2 permeability at 200 ^{o}C and under various differential pressures, – Perform final shear at 200 ^{o}C and at a rate of 5% axial strain/day
S3	200	9	
S4	200	4	

[a] All final shear tests were performed in drained compression mode while maintaining constant confining stress.

Specimens S2, S3, and S4 were chosen to be tested at higher temperatures. Initially the corresponding confining stress was applied to each specimen which was 6.5, 9, and 4 MPa, respectively. Heating was done at a rate of 10 ^{o}C/hr. Thermal deformation of each specimen during heating was recorded by the internal LVDTs. The LVDTs were rated for 200 ^{o}C by manufacture. Each target temperature, i.e. about 80, 140, and 200 ^{o}C, was maintained over one night (at least 12 hours). Permeability was measured at room temperature, and then at each target temperature. Two or three permeability measurements were performed at each temperature but under differential pressures. Finally, Specimens S2, S3, and S4 were sheared at 200 ^{o}C.

Thermal volumetric strain was calculated as a ratio of thermal volume change divided by the initial volume of the specimen (Equation 4.1), while assuming contraction as positive.

$$\varepsilon_v = 100 \times \left(\frac{V_o - V}{V_o}\right) = 100 \times \left(\frac{r_o^2 h_o - (r_o + \Delta r)^2 (h_o + \Delta h)}{r_o^2 h_o}\right) \tag{4.1}$$

where:

ε_v: volumetric strain (%),

V_o: initial volume of specimen, m^3,

V: volume of specimen after deformation, m^3,

r_o: initial radius of specimen, m,

Δr: change in radius of specimen, m,

h_o: initial height of specimen, m, and

Δh: change in height of specimen, m.

In this study, the top end of the sample was exposed to nitrogen gas pressure while bottom end was open to the atmosphere. Permeability measurements were mostly done in a constant pressure mode, where a constant differential pressure was maintained between top and bottom of the specimen. After an equilibrium gas flow rate was attained, the flow rate was measured and permeability was calculated. Flow rate stabilization took from one hour to more than one day, depending on how fractured or pervious the specimen was. During this time, data logging was done at one minute interval (in some cases even shorter intervals). A few constant flow mode tests were also performed in which nitrogen gas with a constant rate was flowed through the specimen, and equilibrium upstream pressure was measured. For each specimen and under each temperature, multiple permeability measurements under various differential pressures or flow rates were done. Pressure transducers continuously recorded upstream and downstream pressures. Flow rate was calculated from ISCO pump volume change. Since gas flow rate (q) varies with pressure and temperature, therefore the value of q at ISCO pump was converted (using the ideal-gas law) to a flow rate at the average pressure and temperature in the specimen. The latter was input to Equation 4.2 for permeability calculation. Equation 4.2 applies to the low (laminar/viscous) flow rate region (Ahmed, 2006) where Darcy's equation is valid. To date, there is no ASTM standard for gas permeability tests of rocks in a triaxial apparatus to specify a laminar flow in terms of flow rate. ASTM D4525-8 (ASTM, 2008), which standardizes permeability of rocks by flowing air in a specimen holder, states that a flow rate less than 2 cm^3/s per one cm^2 of the specimen end face area found to be below a turbulent flow threshold. It was made sure that this flow rate was never exceeded in the this study.

$$k = \left[2\left(\frac{T_{Specimen}}{T_{ISCO}}\right).q_{ISCO}.P_{ISCO}.\mu.L\right]/[(P_{up}^2 - P_{down}^2).A] \tag{4.2}$$

where:

k: coefficient of apparent permeability, m^2,

$T_{Specimen}$: temperature of specimen, K,

T_{ISCO}: temperature of nitrogen at ISCO pump, K,

q_{ISCO}: flow rate of nitrogen at ISCO pump, m^3/s,

P_{ISCO}: absolute pressure of nitrogen at ISCO pump, Pa,

L: length of specimen, m,

P_{up}: absolute pressure of nitrogen at upstream of specimen, Pa,

P_{down}: absolute pressure of nitrogen at downstream of specimen, Pa,

μ: viscosity of nitrogen at specimen temperature and average pressure ($\frac{P_{up}+P_{down}}{2}$), Pa.s, and

A: cross section area of specimen, m^2.

4.4. Results and discussion

4.4.1. Thermal deformation under isotropic compression

Utilizing internal LVDTs is one way to measure deformation of a rock specimen in a drained triaxial test or a triaxial test with gas as the pore fluid. In the latter case, pore pressure pump volume change cannot be used as a measure of specimen volume change due to gas compressibility. Using oil as a cell fluid under high temperature poses a real challenge to utilize strain gauges in a triaxial cell. In this experiments, high-temperature internal LVDTs were used which facilitated capturing deformation behavior of specimens S4, S2, and S3 during heating under isotropic confining stress.

Figure 4.4 presents axial, lateral, and volumetric strains in these specimens during heating from room temperature to about 200 ^{o}C. The curves in Figure 4.4 only include deformation measurements during heating time until the end of sitting time at any target temperature (80, 140, and 200 ^{o}C) which was over one night. The LVDTs' recordings during permeability tests or shearing times were excluded from these curves.

Specimen S2 did not show a significant deformation in axial and lateral directions up to a temperature of about 100 ^{o}C. Further heating resulted in decrease in height. At 100 ^{o}C, compression in the axial direction was accelerated. At 140 ^{o}C, the specimen suddenly collapsed in the axial direction and exhibited more than 4% axial contraction. By further heating from 140 to 200 ^{o}C, the specimen exhibited contraction in the axial direction such that axial compressional strain was more than 5% at 200 ^{o}C (Figure 4.4.a).The circumferential LVDT started to record contraction at about 140 ^{o}C, but it moved outside of its limit.

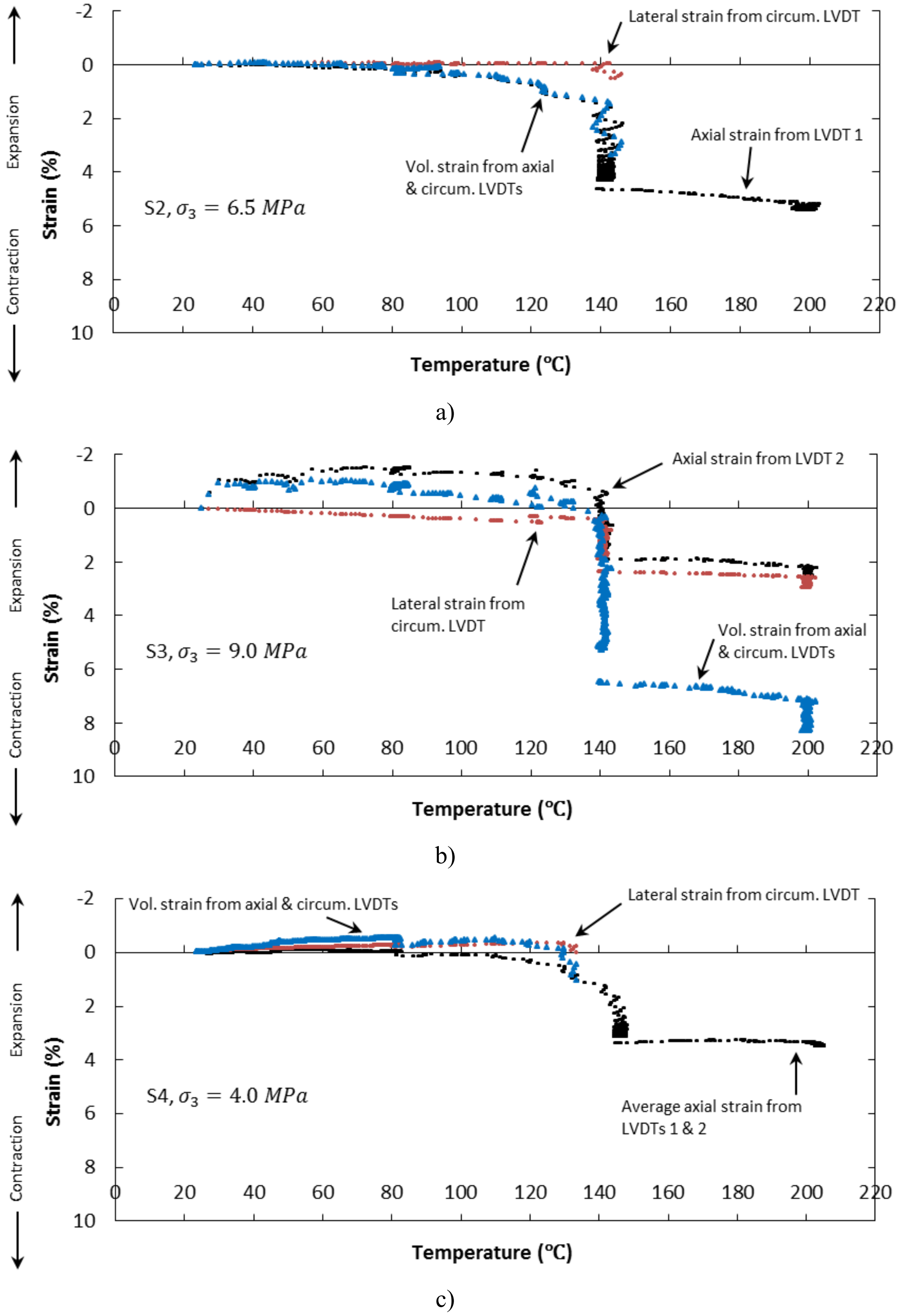

Figure 4.4 Thermal strains recorded by internal axial and circumferential LVDTs during heating from room temperature to about 200 °C for: a) S2; b) S3; and c) S4

The height of specimen S3 rapidly increased by more than 1% as temperature increased from room temperature to about 30 ^{o}C. Further heating caused slight reduction in height. At 140 °C, axial strain suddenly dropped to nearly 1.9% (contraction) which further gradually dropped to about 2.6% compressional strain at 200 ^{o}C. Heating caused gradual lateral contraction. Lateral strain was about 0.5% contraction at 140 °C which was followed by a sudden collapse to about 2.4% contraction at 140 °C. Increasing temperature gradually escalated radial contraction to more than 2.9% at 200 ^{o}C (Figure 4.4.b). The volumetric strain curve had a similar trend to those of the axial and lateral strains. Maximum volumetric expansion was about 1%; however, at 140 ^{o}C, it suddenly dropped to about 6.5% contraction. Thereafter volumetric contraction gradually increased to 8.2% at 200 ^{o}C.

Starting heating up from room temperature, specimen S4 exhibited slight expansion both in axial and radial directions. As temperature approached 80 ^{o}C, the axial LVDT recorded compressional deformation which was accelerated at 135 ^{o}C and was followed by a sudden collapse in the axial direction to more than 3% contraction at 145 ^{o}C. The circumferential LVDT also started to show sudden decrease in the circumference (contraction) at 135 ^{o}C; however, it moved outside of its limit. From 140 to 200 ^{o}C, not a significant change in the height was observed (Figure 4.4.c).

From the study of these three specimens, it can be concluded that the temperature of about 140 ^{o}C seems to be a characteristic temperature where thermal deformation held a transition from expansion to contraction. This point corresponds to the temperature where pyrolysis started. Pyrolysis is defined as thermo-chemical decomposition of coal due to heating in the absence of oxygen. It produces gases (volatile matter), tar, and char. As stated by Arenillas et al. (2003), below 150 ºC, desorption of water and adsorbed gases occur. Further heating from 150 to 500 ºC, degrades coal matrix which generates CO_2, pyrolysis water, and aliphatic compounds. Main products of heating between 500 and 800 ºC include CO, H_2, and CH_4. Other researchers observed similar behavior in other coals. Feng et al. (2012) studied gas coal specimens from the Xing-Long-Zhuang coal mine in Shandong, China, up to temperature of 600 ^{o}C in a HPHT triaxial apparatus. They measured pyrolysis gas production along with deformation measurements. In their experiments, major compressional deformation was induced by a sharp increase of pyrolysis gas production at about 250 ^{o}C. They reported volumetric expansion of 0.65% at 200 °C which rapidly dropped to 7% compression at 280 °C. Glass (1984) reported that specimens of the Hanna Basin coal initially expanded due to heating (less than 1% expansion). Axial contraction started at about 150 °C and reached about 10% at about 500 °C (see Figure 3.6). By comparing the observation on Alberta coal with the ones from Feng et al. (2012) and Glass (1984), it can be concluded that the temperature of 140 °C, corresponds to pyrolysis initiation in our specimens. Increasing confining stress from 4 to 9 MPa for the three specimens did not seem to influence this characteristic temperature. The magnitudes of thermal deformation for the specimens shown in Figure 4.4 were not identical. This could be because of material variability, dissimilarity in fracture network in the specimens, and different confining stresses. It is worth noting that the results in Figure 4.4 might include creep effects at any target temperature, where permeability tests were done over time periods longer than the heating times. The creep effects were not excluded from the data in Figure 4.4. A non-stop heating test, from room temperature to 200 °C, on another specimen(s) could prevent the creep effect. Such a test was not conducted in this work.

Unlike inorganic rocks which continuously expand with temperature (e.g., Elliot and Brown, 1988; Heuze, 1983; Luo and Wang, 2011; Richter and Simmons, 1974), coal exhibits initial expansion followed by contraction after the characteristic temperature. This distinctive thermal deformation behavior of coal is because of its heterogeneous structure. Coal contains organic and inorganic solids, moisture and volatile matter, and cleat (fracture) network. Thermal deformation of coal is a resultant response of multiple constituents of the coal to heat as discussed by Akbarzadeh and Chalaturnyk (2014).

4.4.2. Internal LVDTs versus external LP; measuring height change during shear

It is very common and convenient to use two axial LVDTs along with one circumferential LVDT in a triaxial testing. Unlike an external LP which provides an average height change, internal axial LVDTs, depending on their positions and proximity to any developing shear plane, might be very closely following the external LP or maybe somewhat offset from it. Taking an average between two LVDTs may result in a better estimation of axial deformation. This idea can be examined by comparing the internal LVDTs against the external LP during final shearing. Figure 4.5 shows two measurements of axial LVDTs during shearing of S4 at 203.9 °C and S7 at room temperature. Average of the LVDTs 1 and 2 provided a better estimation of change in height of S4 during shear; however, for S7, the observation was different. For the latter, LVDT 1 was closely following the LP whereas average of the LVDTs 1 and 2 resulted in a less precise estimation of S7 height change.

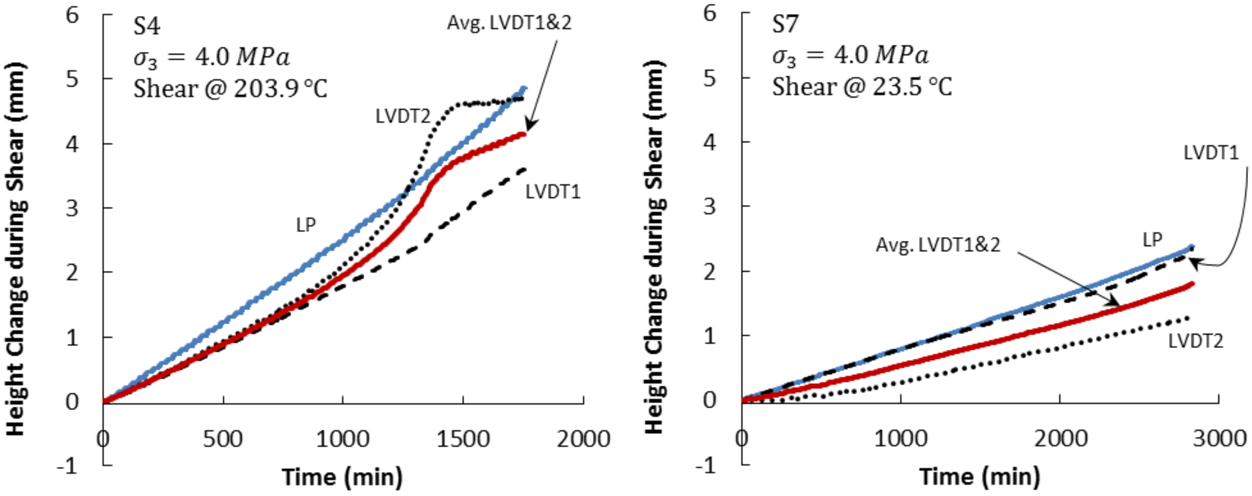

a) b)

Figure 4.5 Two examples showing internal LVDT's measurements during shear compared to an external LP: a) S4 sheared at 203.9 °C; b) S7 sheared at 23.5 °C

4.4.3. Stress-strain and deformation characteristics during shear at room temperature

Specimen S1 exhibited a fairly linear behavior in the beginning of shear, which was followed by a curvilinear section prior to peak stress, and a softening behavior post-peak (Figure 4.6). Maximum strength was observed at an axial strain of 4.38%. Stress-strain curve of this specimen was calculated using three different values for its cross section area; a constant area equal to the original cross section area, instantaneous cross section area calculated based on the circumferential LVDT recordings, and instantaneous cross section area determined based on the cell pump volume change and the external LP readings. Data logging was done at an interval of one minute during the entire shear. The three deviator stress-axial strain curves of specimen S1 are presented in Figure 4.6. It was observed that there was not a significant difference between the three curves, particularly in the pre-peak portion. Compressive strength from the circumferential LVDT readings was 53.1 MPa; however, from cell pump/LP and original are were 53.2 MPa and 54.1 MPa, respectively. The latter would result in 0.27% and 1.84% error, respectively, in estimating the compressive strength compared to using the circumferential LVDT.

Figure 4.6 also shows lateral strain plots for S1 using the circumferential LVDT as well as cell pump/LP. Lateral strain at peak was extensional which were determined equal to 0.91% and 0.78% from the circumferential LVDT and the cell pump/LP, respectively.

Axial and lateral strain curves were used for deducing values of Young's modulus, E, and Poisson's ratio, ν, compliant to the methods explained in ASTRM D7012-13 (American Society for Testing and Materials, 2013). In this study, E was measured as an average modulus of the linear portion of the axial stress-strain curve using a linear regression curve-fitting. Young's modulus was 1468 MPa using stress-strain curve acquired from the circumferential LVDT; however, based on the cell pump readings, E was determined equal to 1473 MPa. Slope of the lateral curve was determined in the same manner as for the axial curve. Poisson's ratio is equal to the negative of the ratio between slope of axial and lateral strain curves in Figure 4.6. The circumferential LVDT and cell pump/LP resulted in Poisson's ratios of 0.22 and 0.21, respectively.

Volumetric strain of S1 was calculated using the cell pump as well as the circumferential LVDT/external LP. In using the cell pump volume change, calibration was done for the volume of the loading ram entering cell fluid area and expelling cell fluid back to the pump. Equation 4.1 was used in the calculation of volumetric strain from the circumferential LVDT/external LP. Contraction was taken as positive. Volumetric strain curves of S1 from the two methods mentioned above are presented in Figure 4.6. As shown in the figure, S1 exhibited contraction even after peak stress. The reversal points were indeed observed in the post-peak region from either method. The maximum volumetric strain was determined to be 3.43% and 2.98% from the circumferential LVDT/external LP and the cell pump, respectively.

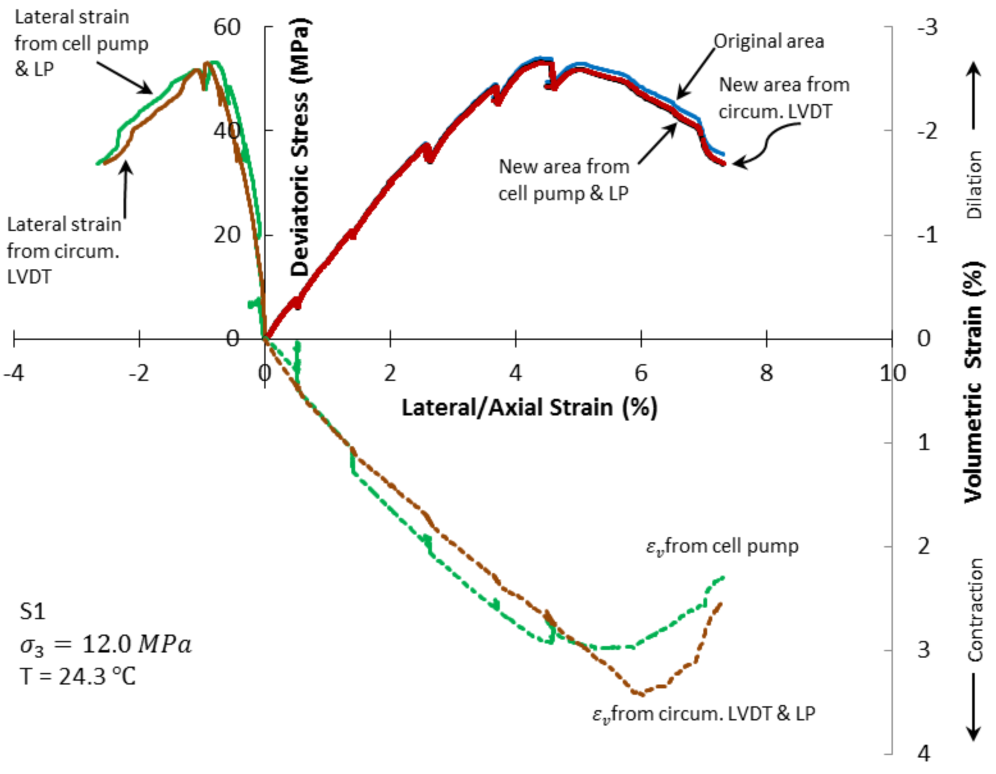

Figure 4.6 Stress-strain curves of specimen S1 at room temperature from different methods
*Note: The jumps in the curves correspond to the trials for permeability measurements during shear.

Two classes of volumetric strain curves have been reported by Palchik (2013) studying carbonate rocks. In type 1, total volumetric strain curve has a reversal point, the location where the maximum volumetric strain occurred. This point represents the onset of unstable crack growth in the specimen. This notion was first suggested by Martin and Chandler (1994) while performing uniaxial/triaxial compression tests on the Lac du Bonnet granite. Martin and Chandler (1994) called the corresponding axial stress for this point as crack damage stress which, for the Lac du Bonnet granite tested in a triaxial compression test, it occurred between 70 and 85% of the peak strength. Another characteristic feature of type 1 is that, at maximum axial/deviator stress, total volumetric strain switches from compression to dilatation. Type 2 volumetric strain curve (Palchik, 2013) does not have a reversal point in total volumetric strain in the pre-peak region. For type 2, he concluded that crack damage stress is equal to the peak stress and total volumetric strain at peak is still compressional; however, he did not mention about occurrence of a reversal point in the post-peak region. It can be seen from Figure 4.6 that S1 exhibited a volumetric strain response which falls in the type 2 of Palchik (2013)'s classification.

Specimen S7 was tested under a smaller confining stress (4 MPa). There was no circumferential LVDT available for this sample; however, lateral and volumetric strains were calculated from the cell pump volume change and an external LP (Figure 4.7). Similar to S1, using original cross section area and the deformed area (concluded from the cell pump and LP) did not result in a significant deviation in stress-strain curve in pre-peak region. Peak deviator stresses using the original and deformed area were equal to 36.33 and 36.10 MPa, respectively. The corresponding peak axial strain was 3.51 %. Figure 4.7 also shows lateral strain curve of S7. Lateral strain initially was compressional which later changed to extensional. Although the initial portion of the lateral strain curve seems uncertain, it is used here. One possible reason for this uncertain region could be fluctuations of room temperature; therefore, the cell pump compliance. Lateral strain at peak was determined equal to 0.32% (extension).

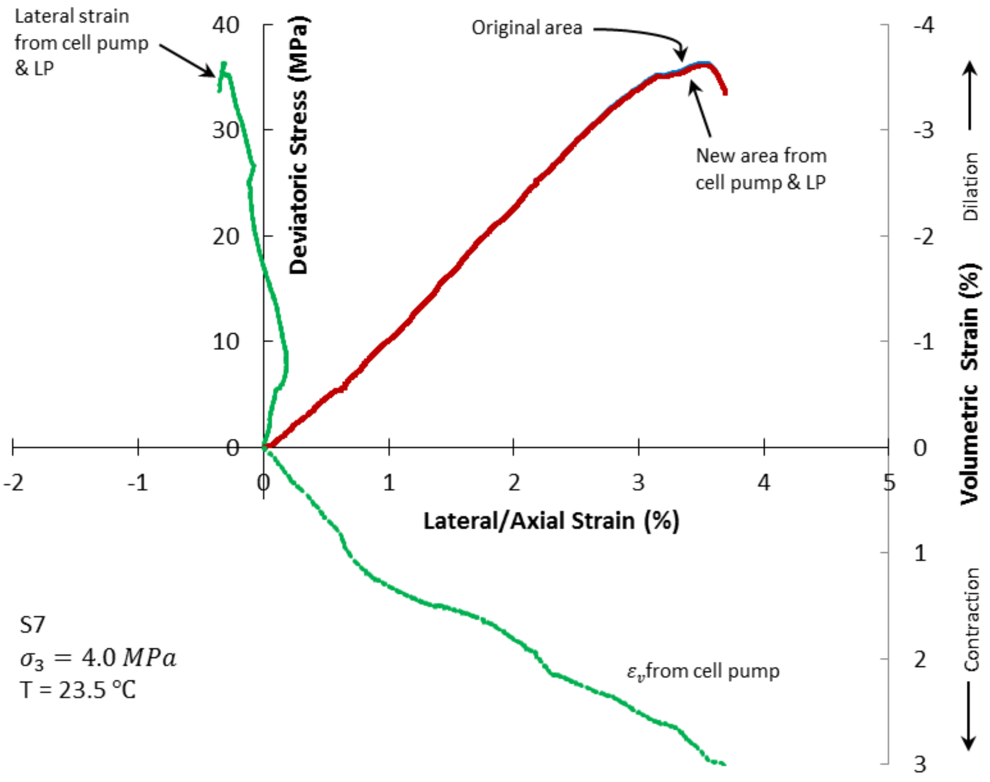

Figure 4.7 Stress-strain curves of specimen S7 at room temperature from different methods

If one trusts the deformation calculation of this specimen, following the same approach as for S1, Young's modulus and Poisson's ratio would be equal to 1253 MPa and 0.25, respectively. Volumetric strain of S7 was analyzed in a similar manner to S1 and the corresponding curves are presented in Figure 4.7. Volumetric strain curves for S7 also sits in the type 2 volumetric strain as per Palchik (2013)'s classification. No clear reversal point was observed in the volumetric strain curve in the pre-peak region.

4.4.4. Stress-strain and deformation characteristics during shear at 200 ℃

Specimen S3 was sheared at about 200 ^{o}C (the actual average temperature during shearing was 199.3 ^{o}C) and under a confining stress of 9 MPa. It should be noted that, due to thermal expansion of the cell fluid, using cell pump volume change for deformation calculation is irrational. Hence, deformation measurement in a HPHT triaxial test remains a challenge unless one uses high-temperature circumferential LVDTs or another method. Based on the thermal deformation response reported in Figure 4.4.c, diameter and height of the specimen at 199.3 ^{o}C and prior to shearing at that temperature was calculated. Those dimensions were used as initial dimensions for shearing at 199.3 ^{o}C.

Lateral deformation of S3 during shear was recorded using the circumferential LVDT. As depicted in Figure 4.8, using original cross section area resulted in a noticeable deviation of the stress-strain curve from the curve concluded by lateral strain measurements. The peak deviator stress in case of using the original area was 72.1 MPa (compared to 76.4 MPa from the circumferential LVDT) which was 5.6% smaller than using the lateral strain results. The specimen underwent 7.37% axial strain at peak which was larger than the specimens tested at room temperature; S1 and S7.

As plotted in Figure 4.8, it was observed that the circumferential LVDT did not capture a notable deformation until it reached the peak strength where there was a sudden change in the lateral deformation reading. This could be related to forming a failure plane in the specimen.

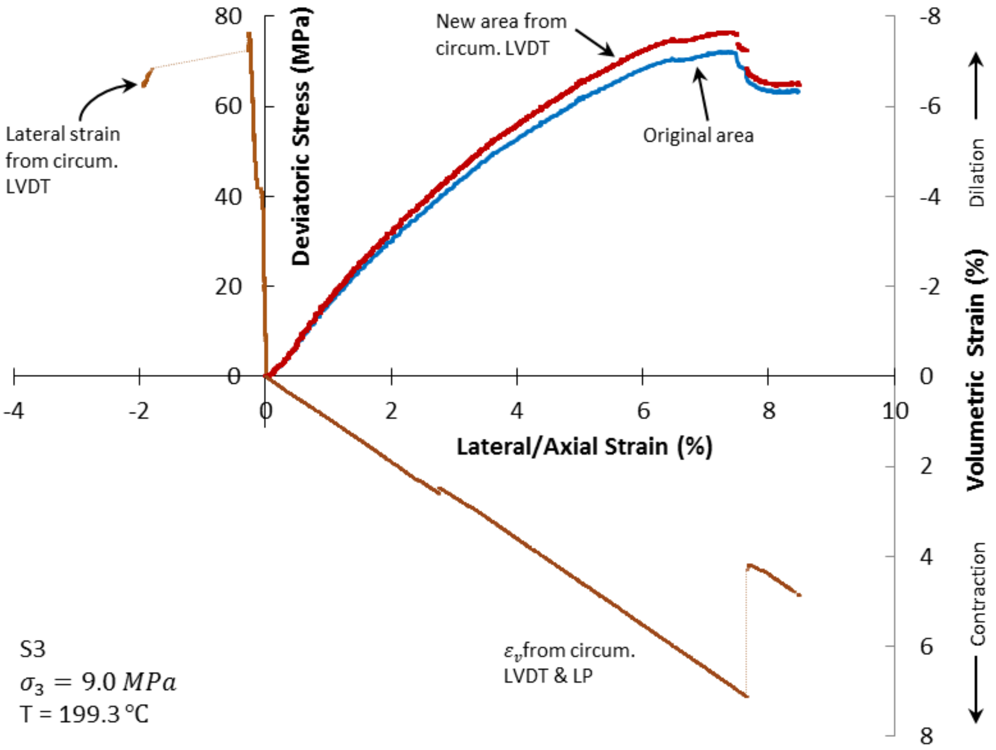

Figure 4.8 Stress-strain curves of specimen S3 at 199.3 ^{o}C from different methods

Young's modulus and Poisson's ration for this specimen were determined as 1809 MPa and 0.03, respectively. Despite the curvilinear stress-strain plot, slope of the straight-line portion of the curve was calculated as Young's modulus. Since this is the only measurement of Poisson's ratio for this coal at high temperature, it is not possible to make any statement in regards to its accuracy. Fluctuation of coal Poisson's ratio with temperature was reported by Glass (1984) where a value as small as 0.11 was measured at 250 ^{o}C.

The volumetric strain curve showed a compressional behavior (Figure 4.8); however, there was no reversal point prior to peak strength which is an indication of type 2 volumetric strain response as per Palchik (2013)'s classification.

For the other two specimens tested at about 200 ^{o}C, i.e., S2 and S4, the circumferential LVDT was out of its limit during final shear. Because of that, for those specimens, initial cross section areas were used in the analyses. Their results are presented in the following sections.

Number of specimens available for this study was not sufficient to conclude any trend for elastic modulus versus temperature. Young's modulus variations with temperature for other coals were reported elsewhere (Glass, 1984; Shoemaker, 1976; Wan et al., 2011).

4.4.5. Comparison between shear strength at room temperature and 200 °C

All experiments, room or high temperature, exhibited brittle behavior while forming through-going failure planes along with multiple other fractures. An example of such brittle failure is shown in Figure 4.3.e depicts specimen S4 after shear at 203.9 °C. Figure 4.9.a and b show stress-strain curves of room temperature and 200 °C tests, respectively.

For room temperature, increasing confining stress from 4 MPa (S7) to 12 MPa (S1) resulted in an increase in peak deviator stress from 36.1 MPa (S7) to 53.1 MPa (S1). Moreover, peak axial strain increased from 3.51% (S7) to 4.38% (S1). Similar trends were observed for 200 °C tests. Peak stress as well as peak axial strain became greater as confining stress increased. Maximum deviator stresses in the cases of confining stresses of 4 (S4), 6.5 (S2), and 9 MPa (S3) were 38.0, 64.3, and 76.4 MPa, respectively. The corresponding values for peak axial strains were, 4.38%, 6.20%, and 7.37%, respectively. Generally, specimens showed greater peak stresses and axial strains at 200 °C compared to room temperature. A possible interpretation for that could be volume contraction due to the thermo-chemical response beyond the characteristic temperature (refer to Figure 4.4). In addition, coal material at 200 °C is different for the initial coal at room temperature.

It should be mentioned that the curves presented in Figure 4.9 embrace two potential sources that might have caused variabilities in the results; shear rate and L/D effects. The data in this figure were not corrected for these effects. Specimen S7 was sheared at a slower rate (2% axial strain per day) compared to the other specimens (which was 5% axial strain per day). S7 could exhibit a higher strength if it was sheared at 5% rate. None of the specimens tested in this study satisfied the length-to-diameter ratio requirement by ASTM D7012-13 (ASTM, 2013). According to ASTM (2013), L/D needs to be between 2.0:1 and 2.5:1 and specimens with L/D less than 2.0:1 are unacceptable. According to other researchers (e.g., Thuro et al., 2001; Tuncay and Hasancebi, 2009), specimens with L/D less than 2.0:1 exhibit larger strength compared to specimens with L/D equal to 2.0:1. None of the specimens' L/D complied with ASTM (2013); however, they were utilized for this study since taller specimens could not be obtained. ASTM (2013) does not suggest any correction factor for the L/D effect; hence, no correction was done in this regard.

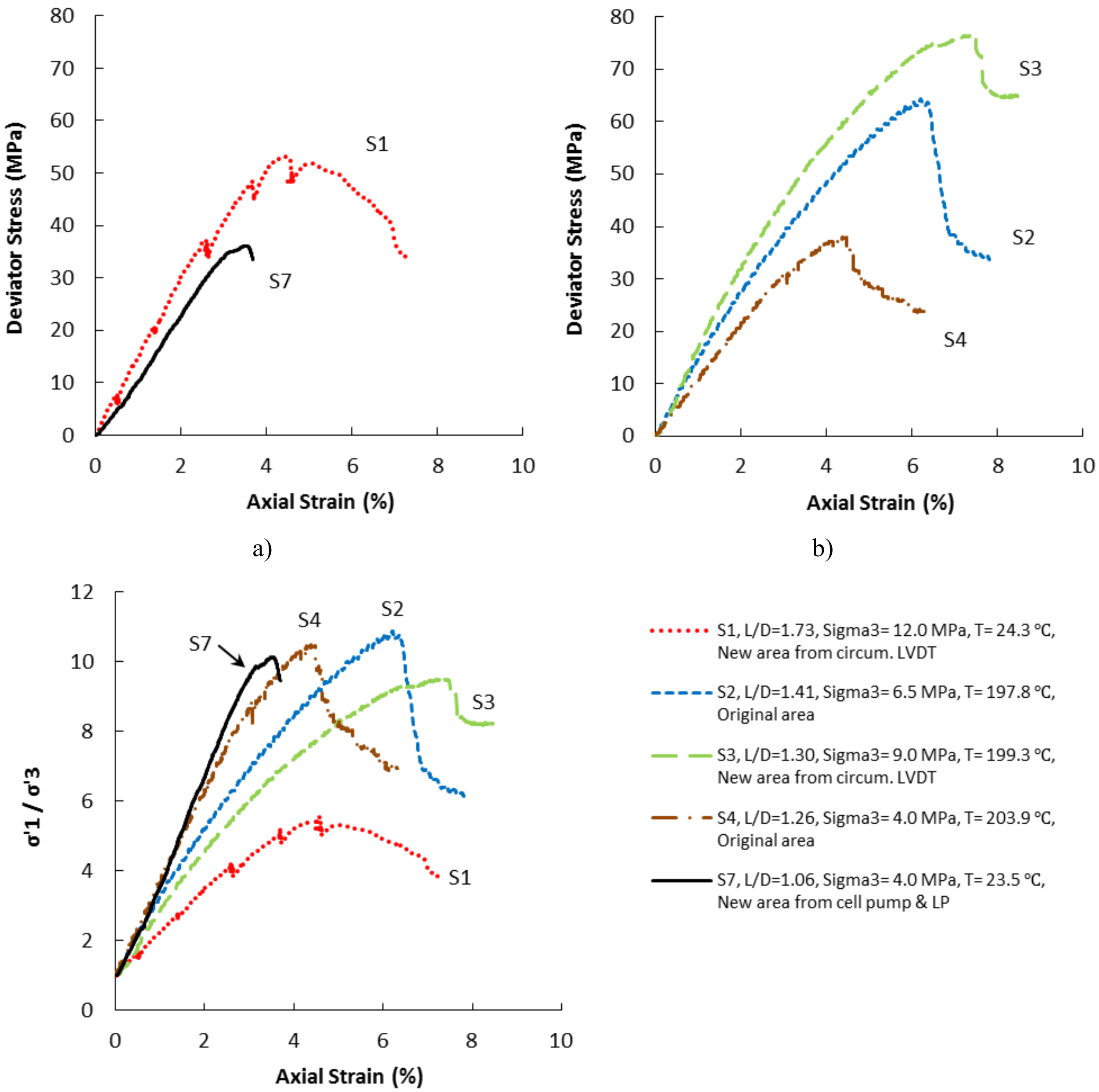

a)

b)

c)

Figure 4.9 Stress-strain curves of all specimens: a) room temperature; a) 200 ^{o}C; and c) principal stress ratio vs. axial strain for all specimens

Principal stress ratio is plotted against axial strain in Figure 4.9.c. From both room temperature and 200 °C, it was concluded that increase in confining stress generally resulted in smaller principal stress ratio.

4.4.6. Permeability evolution with temperature and effective stress

Figure 4.10, as an example, presents upstream/downstream pressure as well as cumulative flow rate curves for permeability measurement on S2 at 81.7 °C. After about 420 minutes, equilibrium flow rate at the ISCO pump was attained. Similar curves were generated for each specimen, at any temperature and differential pore pressure. Experimental measurements along with the corresponding viscosity (as a function of temperature and average pressure in the specimen, taken from NIST (2016)) were input into Equation 4.2 to determine permeability. Table 4.3 summarizes information regarding permeability tests for each specimen. Effective stress in this study followed Terzaghi's definition, that is, total stress minus average pore gas pressure.

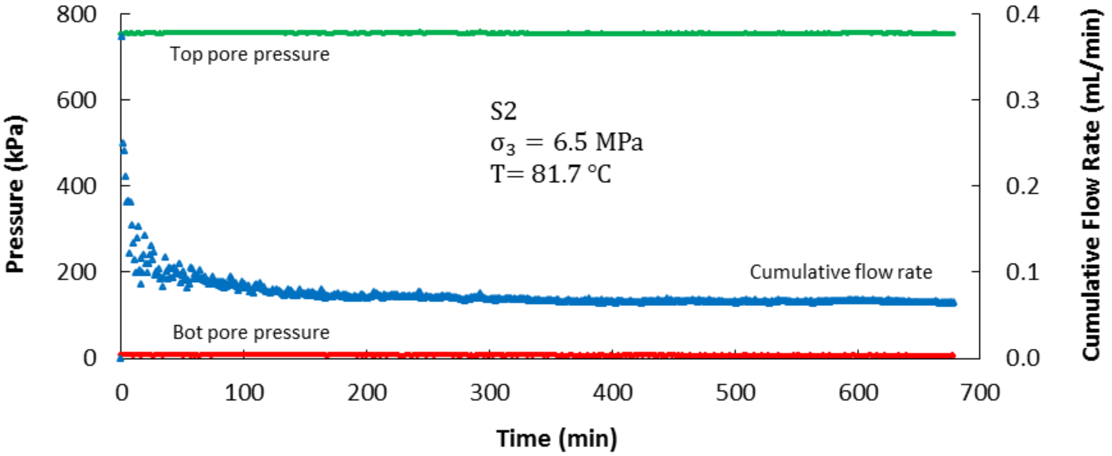

Figure 4.10 Laboratory results of a constant-pressure mode N_2 permeability test of S2 at 81.7 °C

Table 4.3 Summary of N_2 gas permeability test results

Specimen ID	Confining stress (MPa)	Temperature (^{o}C)	Upstream pore pressure range (MPa)
S1	12.0	24.3	0.172
		24.3 (during shear)	0.973-0.994
S2	6.5	23.5	0.240-0.462
		81.7	0.597-0.849
		140.9	0.128-0.155
		197.8	0.150-0.295
S3	9.0	23.9	0.290-0.414
		80.0	1.002-1.382
		141.2	0.318-0.419
		198.9	0.436-0.783
S4	4.0	23.5	0.121-0.204
		23.5 (after 2 MPa shear)	0.113-0.305
		81.3	0.387-0.786
		145.4	0.013-0.019
		203.1	0.016-0.028

Effective permeability of specimens S2, S3, and S4 are plotted in Figure 4.11. As depicted in Figure 4.11.a, c, and e, tests at 80 ^{o}C, despite applying higher differential pressures (that is, lower effective confining stresses), usually resulted in smaller permeability values. These phenomena could be due to thermal expansion of the matrix, hence closure of natural fractures. Further heating of the specimens caused increase in permeability at 140 and 200 ^{o}C. This increase in permeability is related to the thermo-chemical process of pyrolysis as discussed earlier. Variations of permeability with effective stress for these specimens are presented in Figure 4.11.b, d, and f. Generally, increase in effective stress led to reduction of permeability of the specimens.

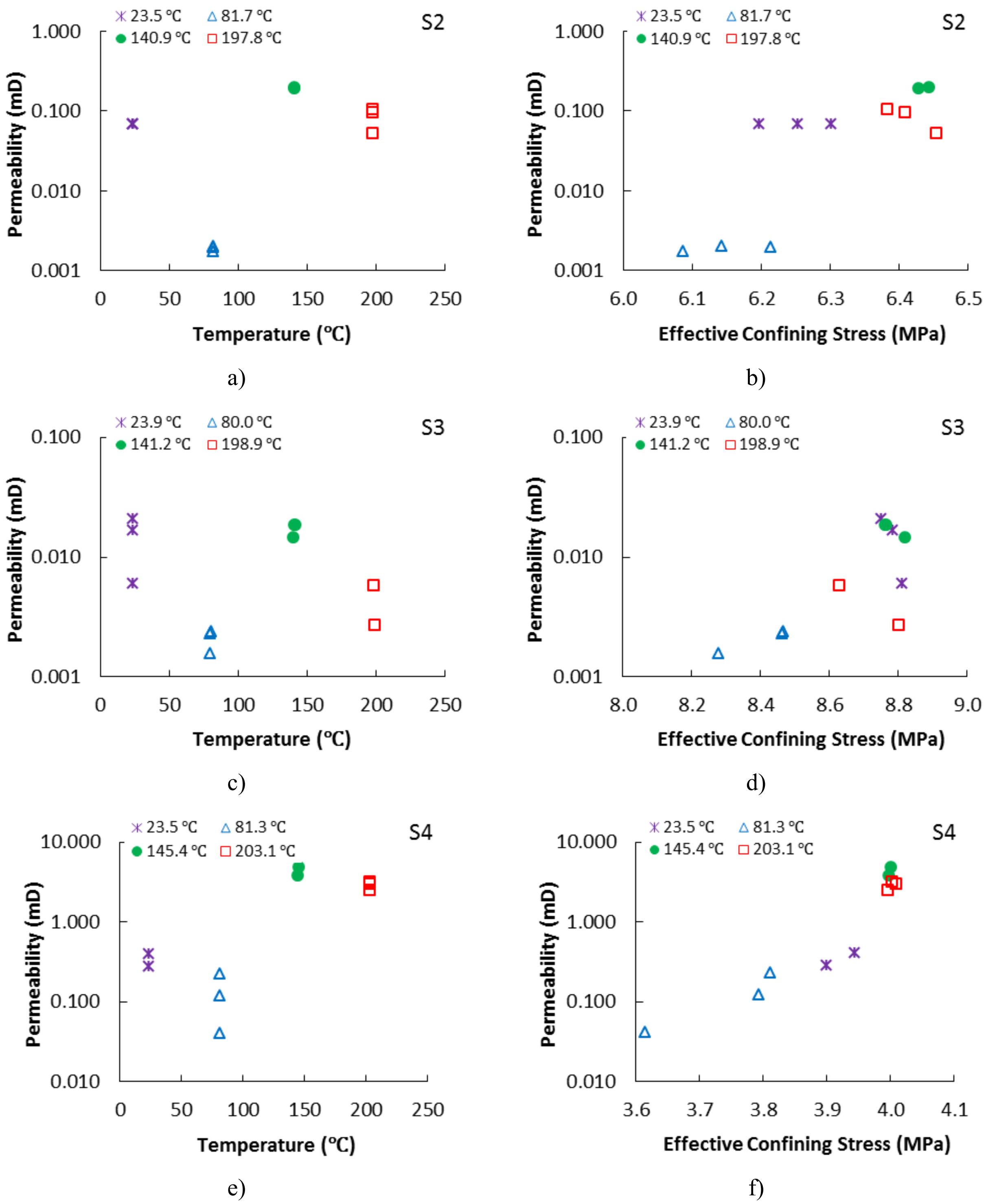

a)

b)

c)

d)

e)

f)

Figure 4.11 a) Permeability of S2 versus temperature; b) permeability of S2 versus effective stress; c) permeability of S3 versus temperature; d) permeability of S3 versus effective stress; e) permeability of S4 versus temperature; and f) permeability of S4 versus effective stress

Figure 4.12.a summarizes all permeability results versus temperature. Initial permeability at room temperature varied between 0.006 and 0.399 mD. The results show fluctuations. All samples belonged to one coal seam; however, they had different cleat networks. Moreover, they were tested under various differential pressures, effective stresses, and temperatures.

Variations of permeability with effective confining stress for these specimens are plotted in Figure 4.12.b. In this figure, each family of data points at each effective confining stress belongs to a specific specimen but under different temperature. Based on this figure, permeability generally decreased as effective confining stress increased.

Fluctuations of coal permeability with temperature and effective confining stress were reported by other researchers (Liu et al., 2014; Niu et al., 2014; Singer and Tye, 1979; Thorsness et al., 1978; Zhao et al., 2010). The general trend of permeability with temperature was ascending in those works. Especially at ultra-high temperatures such as 500 or 600 ^oC, significant increase in permeability was observed. Nonetheless, at lower temperatures such as 100 or 200 ^oC, fluctuations in permeability were noted (e.g., Niu et al., 2014; Zhao et al., 2010). Based on experimental results of this study, a conceptual model was inferred for N_2-permeability vs. thermal deformation of the Alberta coal which is depicted in Figure 4.12 Three zones could be interpreted from Figure 4.13 with different mechanisms of permeability evolution. The first zone existed from room temperature (about 25 ^oC) to a temperature between 80 and 140 ^oC. In this zone, the governing mechanism is gradual expansion of the matrix under heating which closed initial fractures; hence, reduced permeability. The second zone existed thereafter to a temperature just after 140 ^oC. The characteristic feature of the second zone was significant contraction of the specimen and simultaneous development of internal pores due to pyrolysis initiation; hence, increase in permeability. Beyond the second zone, there was a region with gradual contraction up to 200 ^oC (Zone 3). In this zone permeability may drop or increase, depending on development of new pores as a result of pyrolysis or collapse of some of the existing pores. One could justify this conceptual model by measuring porosity under similar temperatures and average effective confining stresses to permeability tests. Such porosity measurements need to be done within the same triaxial apparatus, perhaps utilizing the Boyle-Mariotte law.

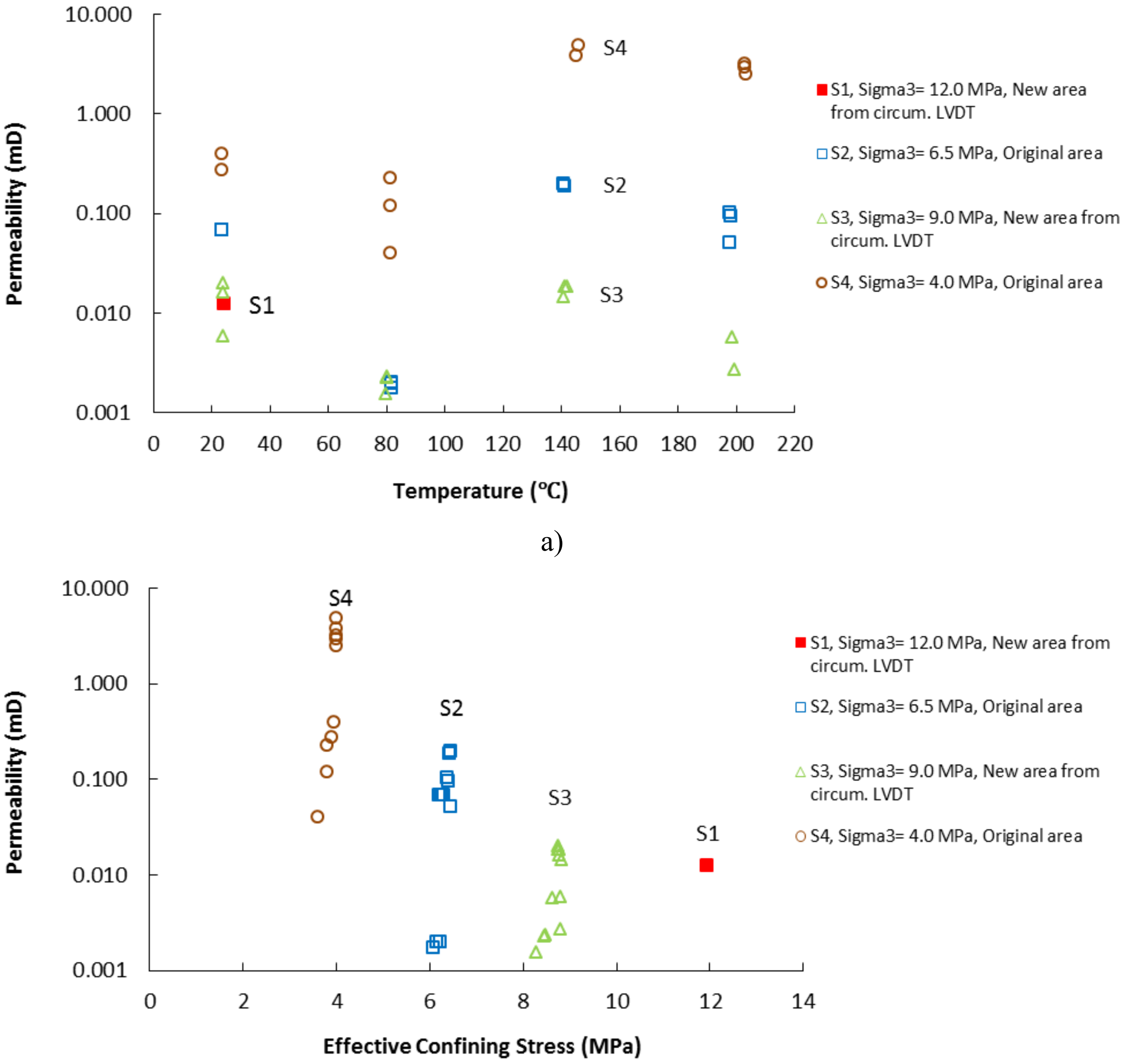

a)

b)

Figure 4.12 Variation of permeability of all specimens with: a) temperature; and b) effective stress

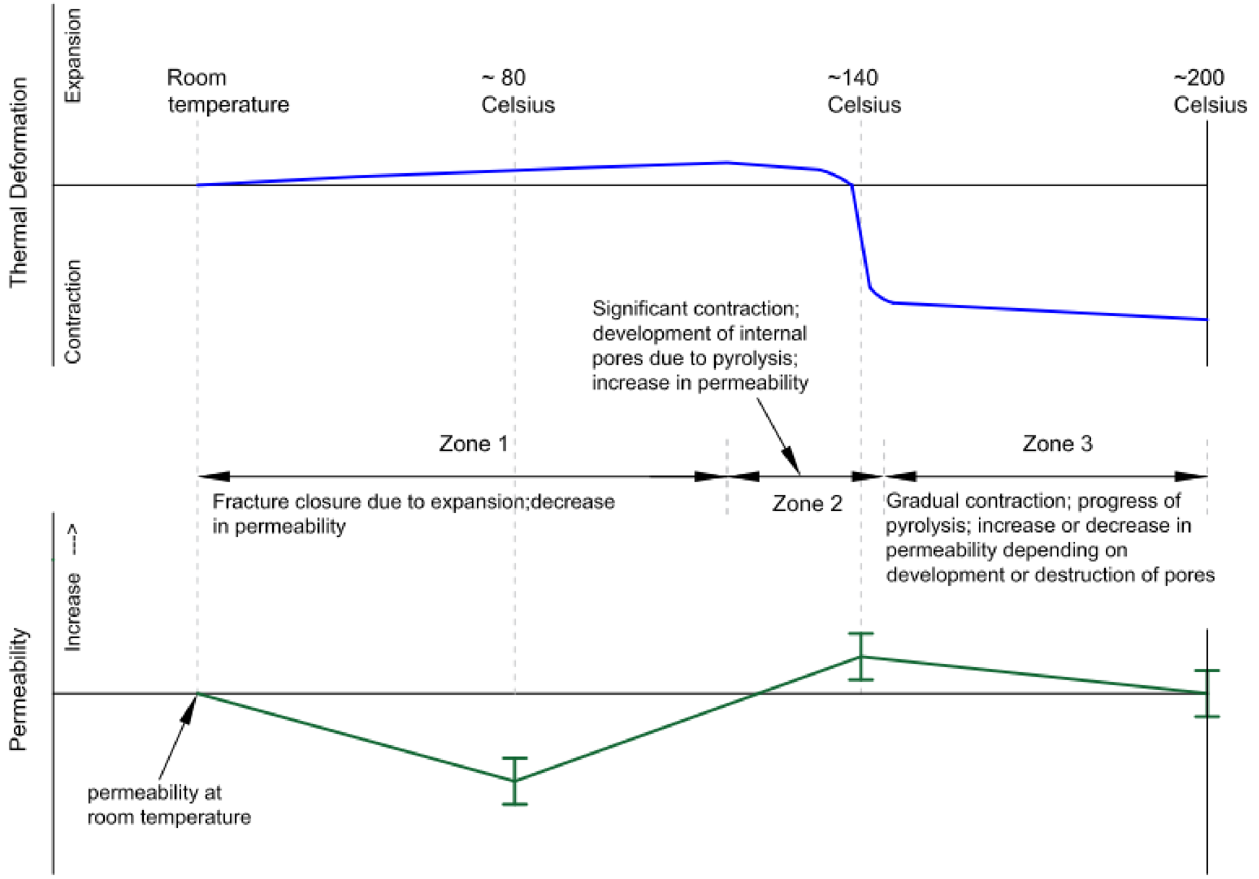

Figure 4.13 A qualitative representation of gas-permeability vs. thermal deformation of coal inferred from this experiments

4.4.7. Permeability evolution during progressive shearing

Permeability of S1 and S4 was measured during shearing. Table 4.3 provides details of each experiment. Permeability of S1 was measured at room temperature prior to shearing and during shearing (at axial strains of 0.52% and 1.39%). The shearing was done in a displacement-control mode. At any target shear strain, the ram pump was stopped without depressurizing it. After permeability test, pore pressure was released; shearing was resumed, and continued to the next target axial strain. Figure 4.14 shows permeability values versus axial strain for S1 and S4. As shearing proceeded (axial strain increased), permeability dramatically decreased. This could be interpreted as the effect of closure of initial fractures of the coal due to shearing. One would expect further shear, especially close to peak stress as well as in post-peak region, to increase permeability. In case of S1, this phenomenon did not happen. As it is seen from Figure 4.6, it was planned to measure permeability at other axial strains during shearing (2.58%, 3.68%, 4.57%) and after shearing; however, it was not possible to do so. Several differential pressures up to 1.035 MPa during shearing and 1.5 MPa after shearing were even tried, for which no significant flow occurred over a period of more than one day for each differential pressure. After disassembling the test, it was observed that failure mechanism was a combination of forming a wedge, and several inclined and horizontal cracks (along the bedding plane). None of the mentioned cracks had crossed the top end surface of S1. Cracking damage never reached to the top end surface. It was previously mentioned that nitrogen flow direction in this study was from top to bottom of sample. Shear deformation closed the initial cracks; hence, the progressive shear did not seem to increase permeability. Gas permeation through the matrix and microcracks of the top end surface probably needed much higher differential pressure. This pressure was not supplied to the specimen.

Permeability of S4 prior to shearing and after 2 MPa shear at room temperature (corresponding axial strain was 0.20%) were tested under various gas pressures (Figure 4.14). Permeability of S4 after shear decreased.

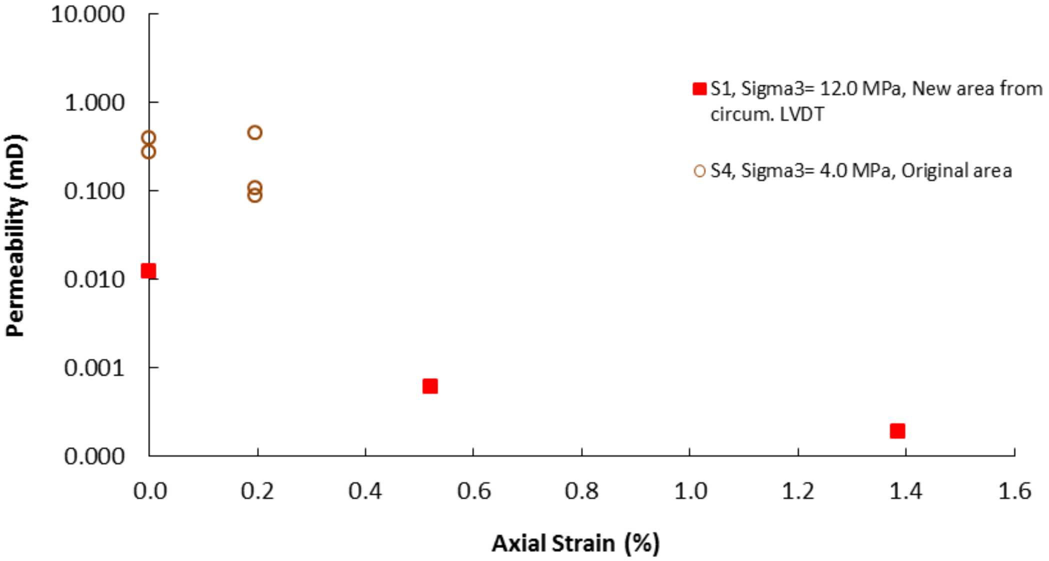

Figure 4.14 Permeability of S1 and S4 versus axial strain during shearing at room temperature

As it is seen Figure 4.14, the general trend of permeability with axial strain for the studied range was descending. Similar response was reported by other researchers. For example, Wang et al. (2013) tested water and CO_2 permeability of the Utah bituminous coal during progressive shearing and under an effective confining stress between 0.75 and 3 MPa. They also observed initial reduction of permeability; however, progressive shearing increased permeability by a few orders of magnitude near peak stress and post-peak.

4.5. Conclusions

Five cylindrical specimens of the Alberta coal tested in this study possessed cleats and bedding plane discontinuities. They were tested in a HPHT triaxial apparatus. The testing program included thermal deformation investigations, studying stress-strain and deformation characteristics at room temperature and 200 ^{o}C, and gas permeability measurements at various temperatures as well as during progressive shearing.

Thermal deformation was initially expansion that followed by contraction in both axial and lateral directions at about 140 ^{o}C. This temperature corresponds to occurrence of the thermo-chemical process of pyrolysis in which some gases were released from the coal matrix and resulted in contraction of the coal rock.

Specimens at 200 ^{o}C showed higher peak stresses and strains compared to the room temperature tests. Volumetric strain response of this coal, both at room and high temperature revealed that crack damage stress was equal to peak stress, that is, no reversal point in the volumetric strain plots were observed in pre-peak region. Instead, the reversal point was observed in the post-peak region.

Permeability of this coal was studied under various confining stresses, from 4 to 12 MPa, and temperatures, from room temperature to 200 ^{o}C. Permeability fluctuated with temperature. Reduction in permeability was notable at 80 ^{o}C, which was due to thermal expansion of the matrix and closure of initial fractures. Permeability evolution at higher temperature, especially around 140 ^{o}C and above was a combined response of thermal expansion and pyrolysis. Progressive shearing was observed to decrease permeability in the beginning of the stress-strain curve.

4.6. Acknowledgements

The authors would like to thank The Canadian Centre for Clean Coal/Carbon and Mineral Processing Technologies (C^5MPT) for providing financial support to this research program. Collaboration by the Sherritt Coal in supplying the coal blocks is also acknowledged.

4.7. References

Ahmed, T. (2006). Reservoir engineering handbook. Gulf Professional Publishing.

Akbarzadeh, H., & Chalaturnyk, R. J. (2014). Structural changes in coal at elevated temperature pertinent to underground coal gasification: A review. *International Journal of Coal Geology*, *131*, 126-146.

Arenillas, A., Rubiera, F., Pis, J. J., Cuesta, M. J., Iglesias, M. J., Jimenez, A., & Suarez-Ruiz, I. (2003). Thermal behaviour during the pyrolysis of low rank perhydrous coals. *Journal of Analytical and Applied Pyrolysis*, *68*, 371-385.

American Society for Testing and Materials. (2008). ASTM D4525-08 Standard Test Methods for Permeability of Rocks by Flowing Air. ASTM, USA.

American Society for Testing and Materials. (2013). ASTM D7012-13 Standard Test Methods for Compressive Strength and Elastic Moduli of Intact Rock Core Specimens under Varying States of Stress and Temperatures. ASTM, USA.

Buzzi, O., Sieffert, Y., Mendes, J., Liu, X., Giacomini, A., & Seedsman, R. (2014). Strength of an Australian coal under low confinement. *Rock Mechanics and Rock Engineering*, *47*(6), 2265-2270.

Dabbous, M. K., Reznik, A. A., Taber, J. J., & Fulton, P. F. (1974). The permeability of coal to gas and water. *Society of Petroleum Engineers Journal*, *14*(06), 563-572.

Elliott, G. M., & Brown, E. T. (1988). Laboratory measurement of the thermo-hydro-mechanical properties of rock. *Quarterly Journal of Engineering Geology and Hydrogeology*, *21*(4), 299-314.

Feng, Z. J., Zhao, Y. S., & Wan, Z. J. (2012). Experiment study of the thermal deformation of in-situ gas coal. *Rock Mechanics: Achievements and Ambitions-Proceedings of the 2nd ISRM International Young Scholars' Symposium on Rock Mechanics*, 103-108.

Gensterblum, Y., Ghanizadeh, A., & Krooss, B. M. (2014). Gas permeability measurements on Australian subbituminous coals: Fluid dynamic and poroelastic aspects. *Journal of Natural Gas Science and Engineering*, *19*, 202-214.

Gentzis, T., Deisman, N., & Chalaturnyk, R. J. (2007). Geomechanical properties and permeability of coals from the Foothills and Mountain regions of western Canada. *International Journal of Coal Geology*, *69*(3), 153-164.

Glass, R. E. (1984). The thermal and structural properties of a Hanna basin coal. *Journal of Energy Resources Technology*, *106*(2), 266-271.

Heuze, F. E. (1983). High-temperature mechanical, physical and thermal properties of granitic rocks-a review. *International Journal of Rock Mechanics and Mining Sciences & Geomechanics Abstracts, 20*(1), 3-10.

Li, Y., Tang, D., Xu, H., Meng, Y., & Li, J. (2014). Experimental research on coal permeability: The roles of effective stress and gas slippage. *Journal of Natural Gas Science and Engineering*, *21*, 481-488.

Liu, S., Zhang, S., Chen, F., Wang, C., & Liu, M. (2014). Variation of coal permeability under dehydrating and heating: A case study of Ulanqab lignite for underground coal gasification. *Energy & Fuels*, *28*(11), 6869-6876.

Luo, J. A., & Wang, L. (2011). High-temperature mechanical properties of mudstone in the process of underground coal gasification. *Rock Mechanics and Rock Engineering*, *44*(6), 749-754.

Martin, C. D., & Chandler, N. A. (1994). The progressive fracture of Lac du Bonnet granite. *International Journal of Rock Mechanics and Mining Sciences & Geomechanics Abstracts, 31*(6), 643-659.

Medhurst, T. P., & Brown, E. T. (1998). A study of the mechanical behaviour of coal for pillar design. *International Journal of Rock Mechanics and Mining Sciences*, *35*(8), 1087-1105.

National Institute of Standards and Technology (NIST). NIST Chemistry WebBook. (http://webbook.nist.gov/chemistry/, accessed Feb. 01, 2016).

Niu, S., Zhao, Y., & Hu, Y. (2014). Experimental investigation of the temperature and pore pressure effect on permeability of lignite under the in situ condition. *Transport in Porous Media*, *101*(1), 137-148.

Palchik, V. (2013). Is there link between the type of the volumetric strain curve and elastic constants, porosity, stress and strain characteristics?. *Rock mechanics and Rock Engineering*, *46*(2), 315-326.

Richter, D., & Simmons, G. (1974). Thermal expansion behavior of igneous rocks. *International Journal of Rock Mechanics and Mining Sciences & Geomechanics Abstracts, 11*(10), 403-411.

Shoemaker, H. D. (1976). Mechanical properties of the Pittsburgh coal at elevated temperatures. PhD Dissertation, West Virginia University.

Thorsness, C.B., Grens, E. A., & Sherwood, A. (1978). A one-dimensional model for in situ coal gasification. UCRL-52523, Lawrence Livermore, National Laboratory (LLNL) Report, Berkeley, California.

Thuro, K., Plinninger, R. J., Zah, S., & Schutz, S. (2001). Scale effects in rock strength properties. Part 1: Unconfined compressive test and Brazilian test. *EUROCK 2001: Rock Mechanics-A Challenge for Society*, 169-174.

Tuncay, E., & Hasancebi, N. (2009). The effect of length to diameter ratio of test specimens on the uniaxial compressive strength of rock. *Bulletin of engineering geology and the environment*, *68*(4), 491-497.

Wan, Z., Feng, Z., Zhao, Y., Zhang, Y., Li, G., & Zhou, C. (2011). Elastic modulus's evolution law of coal under high temperature and triaxial stress. *Journal of China Coal Society, 36*(10), 1736-1740.

Wang, S., Elsworth, D., & Liu, J. (2013). Permeability evolution during progressive deformation of intact coal and implications for instability in underground coal seams. *International Journal of Rock Mechanics and Mining Sciences*, *58*, 34-45.

Singer, J. M., & Tye, R. P. (1979). Thermal, mechanical, and physical properties of selected bituminous coals and cokes. Bureau of Mines Report RI 8364.

Somerton, W. H., Soylemezoglu, I. M., & Dudley, R. C. (1975). Effect of stress on permeability of coal. *International journal of Rock Mechanics and Mining Sciences & Geomechanics Abstracts, 12* (05), 129-145.

Zhao, Y., Qu, F., Wan, Z., Zhang, Y., Liang, W., & Meng, Q. (2010). Experimental investigation on correlation between permeability variation and pore structure during coal pyrolysis. *Transport in Porous Media, 82*(2), 401-412.

Chapter 5 Parametric Geomechanical Analyses of an Idealized Underground Coal Gasification Cavity[1]

5.1. Abstract

Although underground coal gasification (UCG) has been tested in many countries as an environmentally friendly technique for gasification of deep un-mineable coal seams in-situ, there are geomechanical risks during and post operation of a UCG. It is a fluid-thermal-chemical-mechanical process. Evolution of a cavity along with high temperature may result in fracturing and collapsing of formation adjacent to the gasification chamber as well as groundwater contamination. This paper presents results of a series of 3D coupled fluid-thermal-mechanical simulations of an example deep UCG site to investigate the evolution of an idealized cavity. The numerical simulation model included caprock on top, a layer of coal in the middle including a cubic cavity under syngas pressure and temperature, and underburden rock. Five scenarios were studied in order to investigate impacts of different operational conditions and material properties on the geomechanical response of the strata to the UCG activity. This study revealed that evolution of the cavity containing high temperature syngas resulted in large volumetric strain and change in pore pressure as well as increase in mean effective stress and mechanical failure of the strata around the cavity. Impacts of running a UCG plant under different operational pressures as well as using temperature-dependent elastic modulus and permeability for coal on the geomechanical response of the strata was also investigated.

Keywords: Cavity, Coupled Fluid-Thermal-Mechanical, Geomechanics, UCG, Underground Coal Gasification

---

[1] A version of this chapter has been published as:
Akbarzadeh, H., & Chalaturnyk, R.J. (2013). Coupled Fluid-Thermal-Mechanical Analyses of a Deep Underground Coal Gasification Cavity. Journal of Architecture and Civil Engineering, Quest Journals 1(1), 01-14.

5.2. Introduction

5.2.1. Advantages of UCG

The 2010 Survey of Energy Resources estimated world coal reserves at about 860 billion tonnes. Since the year 2000, global coal consumption has increased faster than any other fuel, at 4.9% per year. It is expected to increase by over 60% by the year 2030 (World Energy Council, 2010) which asks for more coal extraction. There are greater resources deep underground that if utilized can address the future additional demands but, based on current technology, are not economic to be mined. Underground coal gasification (UCG), as an environmentally friendly technique, can address the extra demands for coal consumption with gasification of deep un-mineable coal seams. The UCG requires substantially less capital expenses and a smaller CO_2 footprint compared to an equivalent surface gasifier (Burton et al., 2006).

5.2.2. UCG risks

Although the UCG has been trialed in many countries (World Energy Council, 2010), due to its coupled thermal-hydro-chemical-mechanical nature, there are geomechanical risks in any operation. Evolution of cavities with high temperature syngas, well over 1000 degrees Celsius, as well as change in pore fluid pressure may lead to fracturing and collapsing of formations adjacent to the gasification chamber. A shallow UCG plant may cause subsidence at the ground surface. Contamination of groundwater is another risk associated with the UCG projects.

5.2.3. Previous studies of UCG

Extensive laboratory, analytical, and numerical studies as well as field monitoring were done in order to optimize the UCG process and mitigate risks during and after gasification. Mechanical, thermal, and hydraulic properties of coals from different basins were investigated in laboratory (Dabbous et al., 1974; Glass, 1984; Zhao et al., 2015). A few coal block gasification experiments were conducted under laboratory conditions (Daggupati et al., 2010; Kostur and Kacur, 2008; Stanczyk et al., 2012; Yang, 2004).

Analytical models were developed for cavity growth prediction mainly based on the chemical process of gasification (Fausett, 1984; Jung, 1987; Sansgiry, 1990). Rate of syngas production, composition, and temperature as well as change in porosity and permeability of the coal seam due to gasification (which leads to formation of a cavity) has been studied via numerical simulations (Buscheck et al., 2009; Daggupati et al., 2010; Nourozieh et al., 2010; Sarraf Shirazi, 2012; Seifi et al., 2011; Yang, 2004).

Outcomes of field monitoring of several UCG trials were published (Bartel et al., 1976; Luo et al., 2008). Recently, the deepest UCG pilot test was successfully conducted at a depth of 1400 m in Swan Hills, Alberta, Canada (Swan Hills Synfuels, 2012).

UCG geomechanics of has two important aspects. First, geomechanical response of the strata to the coal gasification process can determine the level of risk or safety of the UCG operation. Second, failure, cracking, deformation, and in general geomechanical changes in coal and rock layers around the cavity will influence the chemical process of coal gasification by changing flow properties (porosity and permeability). Geomechanical simulations can provide the opportunity to predict the response of the coal seam and surrounding formations to the coal gasification and allow investigating the integrity of bounding seals at different time-steps and under different operational scenarios. To date, a few geomechanical simulations of the UCG process were published. Advani et al. (1976 & 1977) analyzed plane strain linear thermo-elastic finite element models of a simplified cavity (elliptical) containing high temperature and pressure to study stress changes around the cavity. Tan et al. (2008) utilized ANSYS software for plane strain finite element modeling of a UCG cavity including temperature-dependent thermal and mechanical properties for coal and rock layers. They applied high temperature to boundaries of the cavity, but no groundwater or syngas pressure. Vorobiev et al. (2008) conducted two-dimensional elastic finite element analysis of an idealized disc-shaped reservoir. They did element removal and observed stress redistribution and surface subsidence; however, no incorporations of pore pressure and temperature in the cavity was considered. Morris et al. (2009) used LDEC (Livermore Distinct Element Code) for three-dimensional simulation of a simplified UCG cavity. They removed any coal elements that became unstable by the excavation, under gravitational and an in-situ stress fields but without considerations for gasification temperature and groundwater or syngas pressure. They also studied the influence of coal cleat orientation and persistence on the cavity evolution. An integrated 3D UCG simulator capable of gasification and geomechanical simulations of the UCG was recently developed by the Lawrence Livermore National Laboratory (Nitao et al., 2011); however, this package is not commercially available.

5.2.4. Scope and objectives

Published geomechanical modeling of the UCG did not consider syngas pressure and temperature, and mechanical impacts together; hence, a set of 3D fluid-thermal-mechanical analyses may represent the field behavior more realistically. The main objective of this study was to investigate response of an example UCG site in a high in-situ stress condition (deep UCG) to the evolution of an idealized cubic cavity along with syngas pressure and temperature being applied to the cavity. A series of 3D fluid-thermal-mechanical simulations were conducted for five scenarios having different operational conditions and material properties.

5.3. Description of the simulation model

In this study, FLAC3D 4.00 of ITASCA was used. FLAC3D is a 3D explicit finite-difference program for modeling advanced geotechnical/geomechanical analyses of soil and rock media to calculate stress and deformation, fluid flow, heat conduction and convection using several built-in material models (Itasca Consulting Group Inc., 2009). The geometry of the simulation model, initial configuration, and material properties are explained in following sub-sections.

5.3.1. Geometry

The model studied in this paper included three geological units; a coal seam overlain by a layer of caprock and underlain with an underburden rock layer. Thicknesses of these layers from top to the bottom were 247, 6, and 247 m, respectively. The model dimensions in both X and Y directions were selected equal to 2000 m. The dimensions were chosen based on trying different sizes and in order to have the far boundaries unaffected by the cavity. A cubic cavity with the size of $6 \times 6 \times 6$ m, which extended the entire thickness of the coal seam, was considered.

Figure 5.1 shows one quarter of the model that was constructed in FLAC3D software in order to reduce the simulation runtime. As shown in Figure 5.1, a finer grid was adopted around the cavity to capture geomechanical changes more accurately however the grid became coarser farther away from the cavity. Any sensitivity analyses in regards to grid size and discretization scheme was beyond the scope of this study and was not performed. The total number of grid points and zones were 3751 and 2970, respectively. Also shown in Figure 5.1 are locations of four monitoring points on the perimeter of the cavity. Point A is the top center, B is the bottom center, C is the center point along the X-axis, and point D is the center point along the Y-axis of the cavity.

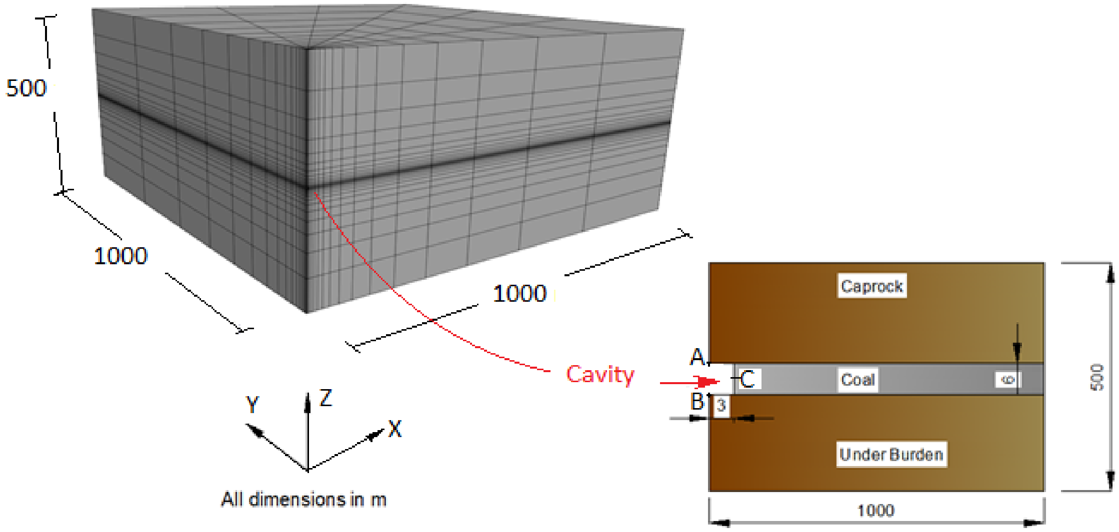

Figure 5.1 3D finite difference grid and the idealized cavity

5.3.2. Initial configurations and material properties

In the geomechanical simulations, the bottom of the model was fixed, the sides were selected as rollers and top of the caprock was assigned as a free boundary. High initial in-situ stress corresponding to a depth of 1400 m was assigned to the model such that total vertical stress in the middle of the coal seam was 31 MPa. Stress ratios for X and Y directions were chosen as unity. Initial hydrostatic pore pressure was assigned to the model such that pore pressure in the middle of the coal seam was 11.5 MPa. Initial temperature of formation was set equal to 60 ^{o}C.

The selected values for in-situ stress and pore pressure as well as formation temperature did not relate to any UCG project.

A set of input material properties was selected for the fluid-thermal-mechanical analyses as summarized in Table 5.1. These properties were chosen based on their corresponding ranges reported in literature but not intended to represent any particular UCG site. The rock layers were considered mechanically stronger but 10 times less porous than the coal; however, thermal conductivity or the rock materials was greater than the coal. It should be noted that the permeability used in FLAC3D is in fact a mobility coefficient and defined as the ratio of intrinsic permeability to fluid dynamic viscosity. Permeability of the coal and rock were selected as 1 and 0.1 millidarcy (mD), respectively. All strata were assumed homogeneous and isotropic, and the Mohr-Coulomb elastic perfectly plastic model was selected for mechanical analyses, for both coal and rock layers using the corresponding parameters shown in Table 5.1. Isotropic fluid flow and isotropic thermal flow was also considered for all layers.

After initializing the in-situ stresses, the cavity was excavated. To simulate the UCG process, an average temperature of 500 ºC was applied to the cavity boundaries. Syngas pressure in the range of 10 to 13 MPa was considered as a constant fluid pressure at the cavity boundaries. The reservoir pressure in this simulation was 11.5 MPa for which the steam saturation temperature is about 320 ^{o}C (American Society of Mechanical Engineers, 2009). Blocks of coal and rock in the vicinity of the cavity may experience temperatures above the steam saturation temperature; i.e., pore water will change phase from liquid water to steam. In a similar temperature and pressure condition in a real UCG site, there is a mix of other gases such as CH_4, CO, CO_2, and H_2, but this simulation assumed single-phase Darcy fluid flow. Any interactions between syngas, steam, and water as well as chemical reactions between syngas and coal were not included.

Table 5.1 Geomechanical, thermal, and fluid properties of coal and rock layers

Property	Coal	Rock
Elastic Modulus, E (MPa)	5000	30000
Poisson's Ratio, υ	0.3	0.3
Friction Angle, ϕ(°)	40	60
Cohesion, C (MPa)	10	35
Density ($\mathrm{kg/m^3}$)	1200	2500
Porosity (%)	0.0866	0.05
Permeability $\times 10^{-13}$ ($\mathrm{m^2/Pa.sec}$)	9.81	0.981
Thermal Conductivity, k ($\mathrm{W/m.°C}$)	0.3	2.5
Specific Heat, C_v ($\mathrm{J/kg.°C}$)	1400	1100
Coefficient of Linear Thermal Expansion, $\alpha_t \times 10^{-6}$ ($1/°C$)	9	15
Fluid Bulk Modulus (GPa)	1.5	1.5
Fluid Density ($\mathrm{kg/m^3}$)	1000	1000
Fluid Volumetric Thermal Expansion Coefficient, $3\alpha_f$ ($1/°C$) (@ P= 11.5 MPa, t= 100 °C)	0.734×10^{-3}	0.734×10^{-3}
Matrix Volumetric Thermal Expansion Coefficient, β ($1/°C$) (@ P= 11.5 MPa, t= 100 °C)	88.3×10^{-6}	79.5×10^{-6}

5.3.3. Coupled fluid-thermal-mechanical analyses

A UCG operation imposes significant geomechanical changes to the strata. Cavity evolution introduces mechanical deformation which, in turn, influences fluid pressure. Syngas extraction, while running the UCG plant at a pressure different from initial reservoir fluid pressure, causes mechanical deformation and alters in-situ stress condition. These are in compliance with Biot's three-dimensional theory of poroelasticity which states that a change in stress produces a change in fluid pressure or fluid volume in a porous medium; likewise, a change in fluid pressure or volume yields a change in the volume of a porous medium (Biot, 1941). The high temperature of gasification causes thermal stress and deformation, likewise thermally-induced pore pressure. All the aforementioned geomechanical perturbations happen simultaneously which requires a coupled fluid-thermal-mechanical analysis.

The fluid flow capability of FLAC3D is applicable to any problem involving single-phase Darcy flow of any type of fluid in a porous medium. It requires information regarding the variables; pore pressure, saturation, and three components of specific discharge vector. Thermal module of FLAC3D incorporates both conduction and convection models. Only conduction was included in this study. Variables involved in heat conduction in FLAC3D are temperature and three components of heat flux. Any of the fluid, thermal, mechanical modules can be run independently or coupled to others.

Formulation of coupled fluid-mechanical processes in FLAC3D is based on Biot's theory of poroelasticity. Variables in the coupled fluid-thermal-mechanical module are related through Darcy's law for fluid transport, balance laws (fluid mass balance equation, thermal energy balance equation, momentum balance equation), and a constitutive law relating changes in pore pressure to saturation, volumetric strains, and temperature (Itasca Consulting Group Inc., 2009). Material properties used in the coupled analyses of this study are provided in Table 5.1.

The fluid-thermal-mechanical constitutive law in FLAC3D has the general form of Equation 5.1. This Equation allows calculation of change in pore pressure due to temperature change and deformation of the saturated matrix.

$$\frac{\partial P}{\partial t} = M \left(\frac{\partial \zeta}{\partial t} - \alpha \frac{\partial \epsilon}{\partial t} + \beta \frac{\partial T}{\partial t}\right) \tag{5.1}$$

where ζ is the variation of fluid content, M is the Biot modulus, α is the Biot coefficient (equal to 1 for incompressible solid grains), ϵ is the volumetric strain, and β is the undrained volumetric thermal expansion coefficient. The Biot modulus is related to the fluid bulk modulus, K_f, and porosity, n, through Equation 5.2:

$$M = \frac{K_f}{n} \tag{5.2}$$

For an ideal porous material, β is related to the volumetric thermal expansion coefficients for the grains, $3\alpha_t$, and the fluid, $3\alpha_f$, through Equation 5.3:

$$\beta = 3\left[\alpha_t\left(\alpha - n\right) + \alpha_f n\right] \tag{5.3}$$

Equation 5.1 gives some insights about contributions of the three constituents on pore pressure change; namely fluid content in the pore space, deformation of the matrix, and temperature of the matrix. Based on Equation 5.1, adding more fluid to the pore space will increase pore pressure; likewise, increase in temperature will raise pore pressure. Volumetric strain has a reverse effect on pore pressure. If the matrix expands, pore pressure will drop and vice versa.

To perform a coupled fluid-thermal-mechanical simulation of a UCG cavity, the following steps were taken. The initial configuration was run for mechanical equilibrium, a cavity was created, and then a series of thermal, mechanical and fluid steps were followed until the intended simulation time was reached. Each step includes one thermal loop, followed by enough mechanical steps (to maintain quasi-static equilibrium) and sufficient flow loops which was again followed by enough mechanical steps after every flow step. It should be noted that the fluid time-step for these simulations was orders of magnitude smaller than the thermal time-step; hence, a mechanism was coded in FLAC3D in order to synchronize the fluid and thermal times by performing enough fluid loops per each thermal loop.

5.3.4. Description of five studied scenarios

The numerical simulations were performed on five different scenarios to investigate the impacts of various operational pressures and material properties on the geomechanical response of the cavity. The cavity temperature for all scenarios was 500 ℃. Information regarding the five scenarios is discussed in the following section and summarized in Table 5.2.

Table 5.2 Summary of five numerical simulation scenarios

Scenario	Cavity temperature (°C)	Syngas pressure (MPa)	Deviation in material properties from Table 5.1
1	500	11.5	-
2	500	10	-
3	500	10	Temperature-dependent elastic modulus for coal seam (as in Figure 5.2)
4	500	10	Temperature-dependent permeability for coal seam (as in Figure 5.3)
5	500	13	-

5.3.4.1. Scenario 1

This scenario used constant material properties as in Table 5.1. The syngas pressure for scenario 1 was selected as 11.5 MPa which is equal to the initial reservoir pressure at the middle of the coal seam. With that being said any changes in pore pressure after running the model are supposed to be due to thermally-induced pore pressure caused by the elevated temperature and/or mechanically-induced pore pressure because of perturbation caused by the cavity evolution.

5.3.4.2. Scenario 2

This scenario was the same as scenario 1, except syngas pressure that was 10 MPa, below initial pore pressure in the middle of the coal seam (which was 11.5 MPa). UCG practitioners prefer to operate the plant below initial reservoir pressure to prevent syngas diffusion to adjacent strata and instead, having water influx to the gasification chamber. This will reduce contaminant transport to groundwater.

5.3.4.3. Scenario 3

This scenario had similar specifications to scenario 1; except it used 10 MPa for syngas pressure and elastic modulus of the coal was assumed to be temperature-dependent. Like any mechanical properties of coal, elastic modulus of coal changes at elevated temperature. Change in elastic modulus of coal specimens from the Hanna Basin coal was studied by Glass (1984). He carried out triaxial experiments up to 250 ºC and uniaxial tests conducted in air at 350 ºC and 450 ºC, perpendicular and parallel to the bedding plane. Normalized elastic moduli of the Hanna Basin are plotted versus temperature in Figure 5.2. It can be seen in Figure 5.2 that there was an initial gain in elastic modulus at temperature of 80 ºC, in the direction parallel to the bedding plane. The normalized elastic modulus curves approached the abscissa at temperatures of about 350 ºC; however, in the direction normal to the bedding plane, a continuous decline of elastic modulus occurred during heating. The solid step-wise function in Figure 5.2 is the one adopted for this simulation. Elastic moduli of coal blocks were calculated as the multiplication of the initial elastic modulus of the blocks (as in Table 5.1) by the normalized values at the corresponding temperatures from the solid step-wise function in Figure 5.2.

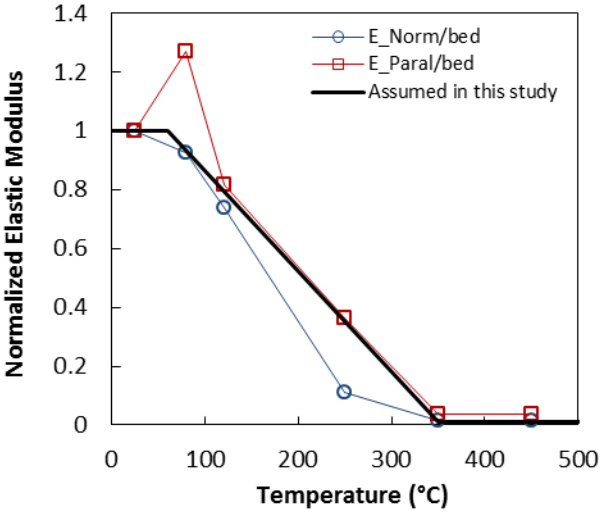

Figure 5.2 Normalized elastic modulus of the Hanna Basin coal versus temperature, normal and parallel to the bedding plane (Glass, 1984) as well as the assumed function used for scenario 3

5.3.4.4. Scenario 4

For this scenario, syngas pressure was 10 MPa and a temperature-dependent permeability was used for the coal. As a coal specimen is heated, its permeability increases. Thermal deformation and microcrack generation as well as release of volatile matters during heating of coal result in change in pore volume and permeability of the coal matrix. Thorsness et al. (1978) investigated change in permeability of the Wyodak coal specimens during drying and pyrolysis. Ratios of permeability of the Wyodak coal at elevated temperatures to their corresponding values at ambient temperature (which was 20 ºC) are plotted against temperature in Figure 5.3. Although the data points show an exponential trend, for the purpose of simplicity, a line was fitted to the initial linear part of the data points (temperature in the range of 60 to 500 ºC). The assumed line predicts normalized permeability equal to 1 and 125 at temperature of 60 and 500 ºC, respectively. Permeability of coal blocks in the heated area around the cavity was calculated as the multiplication of the initial permeability of the blocks (as in Table 5.1) by the normalized values at their corresponding temperatures.

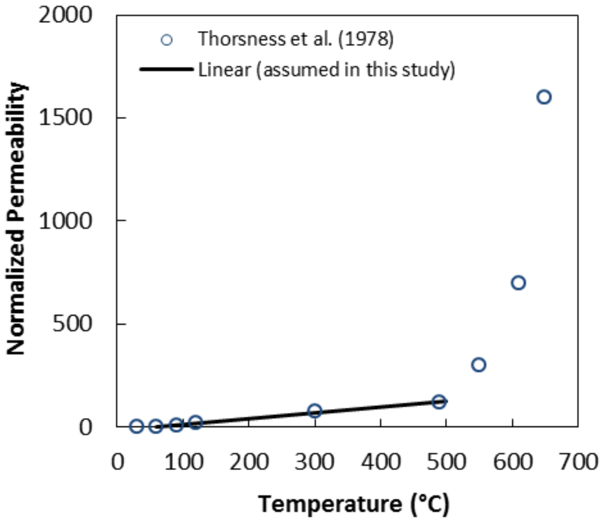

Figure 5.3 Normalized permeability of the Wyodak coal versus temperature (Thorsness et al., 1978) and the assumed function used for scenario 4

5.3.4.5. Scenario 5

In this scenario, everything was identical to scenario 1, except syngas pressure that was selected equal to 13 MPa; above the initial reservoir pressure. The intention for this scenario was to get some insights about how the geomechanical response would change if a UCG plan loses operation and exceeds the reservoir pressure. It is worth mentioning that the environmental influence of such a loss was not in the scope of this study.

5.4. Results and discussions

This section provides some geomechanical responses for all scenarios (Figure 5.4 to Figure 5.9) and discussions on the results. The geomechanical responses include changes in temperature and pore pressure, mean effective stress and volumetric strain along the middle of the coal seam as well as the base of the caprock. It should be noted that the coordinates for Figure 5.5 to Figure 5.9 were set on the center of the cavity. Displacements of four monitoring points on the perimeter of the cavity (points A, B, C, D; Figure 5.1) are shown in Figure 5.10.

5.4.1. Results of scenario 1

Figure 5.4 includes some of the observed changes in the strata after 182 days. Figure 5.4.a shows temperature contours. As seen in this figure, the temperature front extended more into the rock layers than in the coal seam. This is because the thermal conductivity of the rock was chosen greater than the coal seam (Table 5.1). The displacement contours presented in Figure 5.4.b show that larger deformation happened around the cavity. This is also in compliance with the volumetric strain contours shown in Figure 5.4.c. One important issue in underground activities such as UCG is maintaining caprock and bedrock integrity. Investigating the development of a plastic zone around the UCG reactor and potential failure of the caprock, bedrock, and the adjacent coal material is of significant importance. The materials in the plastic zone may undergo large deformation that can lead to failure or at least increase in porosity and permeability. The combination of thermal stresses induced by the high temperatures of coal gasification and mechanical perturbations caused by the cavity evolution were the reasons for strain localization and consequently formation of a plastic zone around the perimeter of the cavity, which is seen in Figure 5.4.d.

Figure 5.5 shows plots of changes in temperature, pore pressure, mean effective stress, and volumetric strain along the middle of the coal seam as well as the base of the caprock. Figure 5.5.a shows changes in temperature and pore pressure versus distance in the middle of the coal seam at different times; 1, 10, 30, and 182 days. With time, the temperature front moved farther from the cavity boundary which resulted in a decline of pore pressure. Similar behavior was observed in the base of the caprock (Figure 5.5.b). Mean effective stress and volumetric strain in the coal and caprock are shown in Figure 5.5.c and Figure 5.5.d, respectively. Initial mean effective stress along middle of the coal seam and base of the caprock was about 20 MPa which increased significantly due to the UCG activity such that after 182 days, maximum mean effective stresses along middle of the coal seam and base of the caprock were 64.6 and 162.0 MPa, respectively. The corresponding values for volumetric strain were 0.022 and 0.030, respectively.

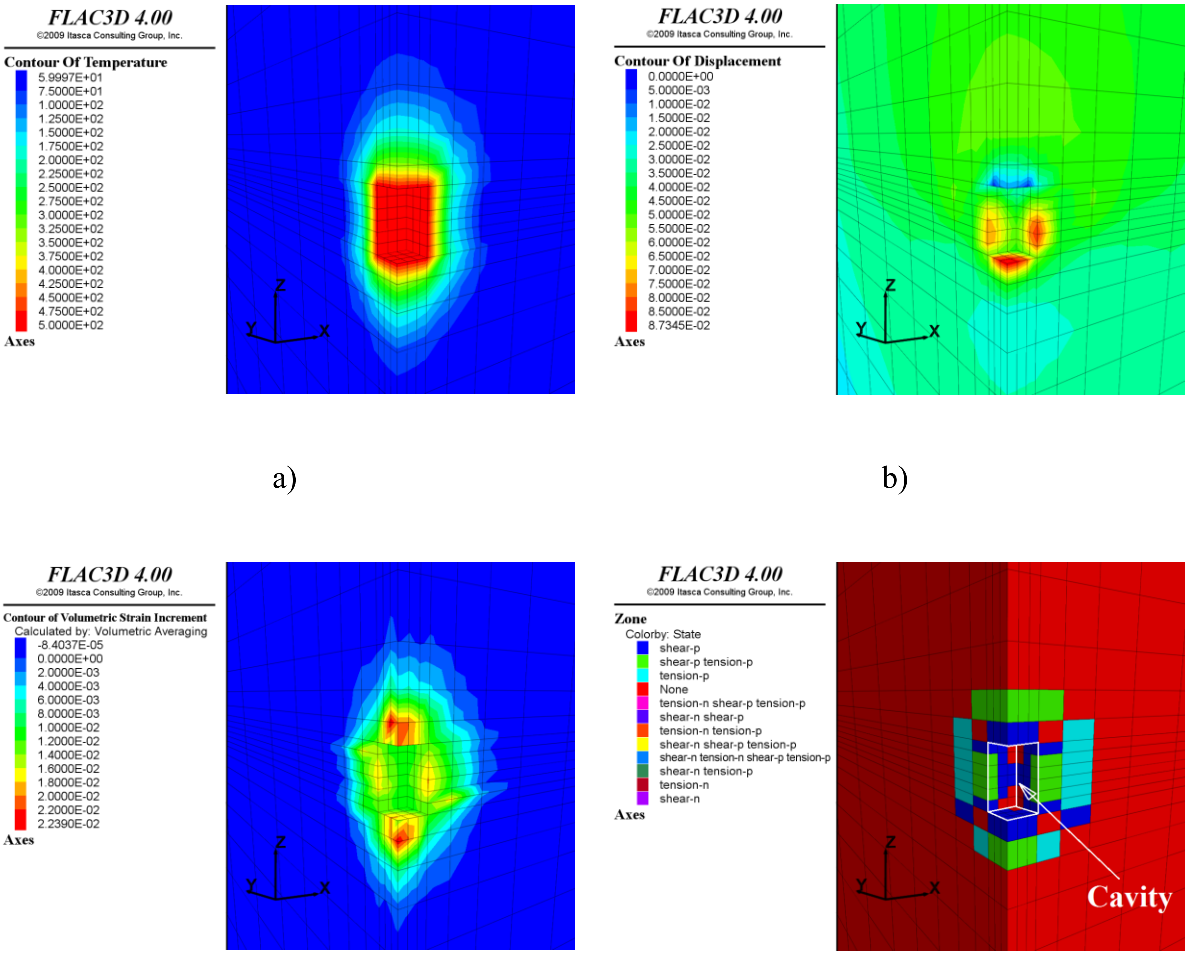

a) b)

c) d)

Figure 5.4 Contours from scenario 1 after 182 days: a) temperature (ºC); b) displacement (m); c) volumetric strain (fraction); and d) plastic zone (yielded state)

Based on Figure 5.5, it can be concluded that due to the cavity evolution and the high temperature of syngas, large volumetric strain happened around the cavity. The amount of observed volumetric strain in base of the caprock was greater than in middle of the coal seam. Because of the large deformation of the strata around the cavity, pore pressure in the coal and rock declined. Similar trend of pore pressure response was observed in the coal and caprock. At later times, either syngas diffused or water moved from farther points to the pore pressure decline area, which compensated pore pressure drops (Figure 5.5.a and Figure 5.5.b).

Besides large deformation of the strata around the cavity, mean effective stress in the coal and base of the caprock also increased. The base of the caprock experienced larger mean effective stress than the middle of the coal seam. The maximum mean effective stress in the base of the caprock occurred close to the top corner of the cavity. Moreover, it was found that the UCG influence on pore pressure profiles extended to a larger distance from the cavity (a few hundred meters) that that of temperature, mean effective stress, and volumetric strain profiles. This fact can be seen in Figure 5.5.a and Figure 5.5.b through Figure 5.9.a and Figure 5.9.b.

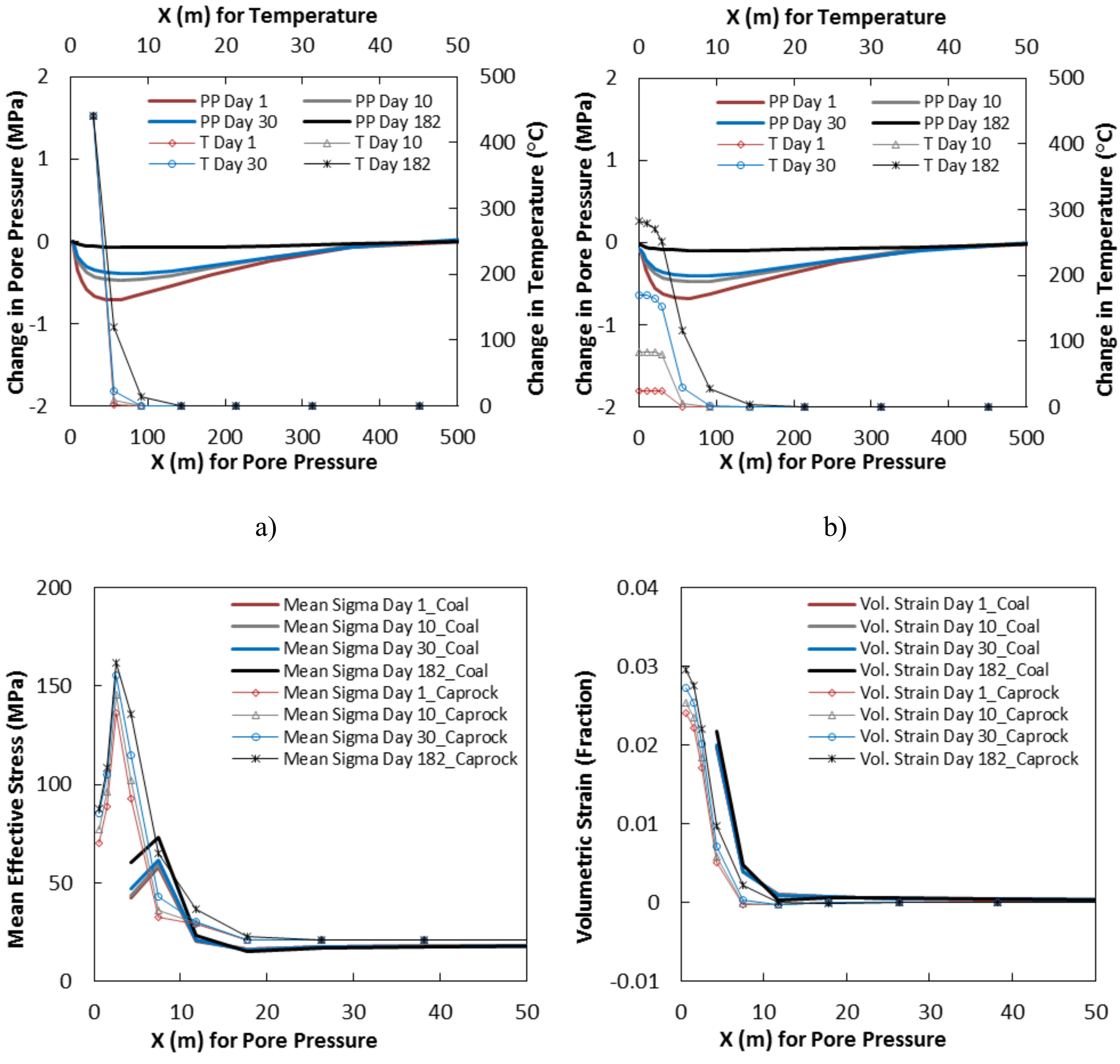

a)

b)

c)

d)

Figure 5.5 Results from scenario 1: a) change in pore pressure and temperature along middle of the coal seam; b) change in pore pressure and temperature along base of the caprock; c) mean effective stress along middle of the coal seam and base of the caprock; and d) volumetric strain along middle of the coal seam and base of the caprock

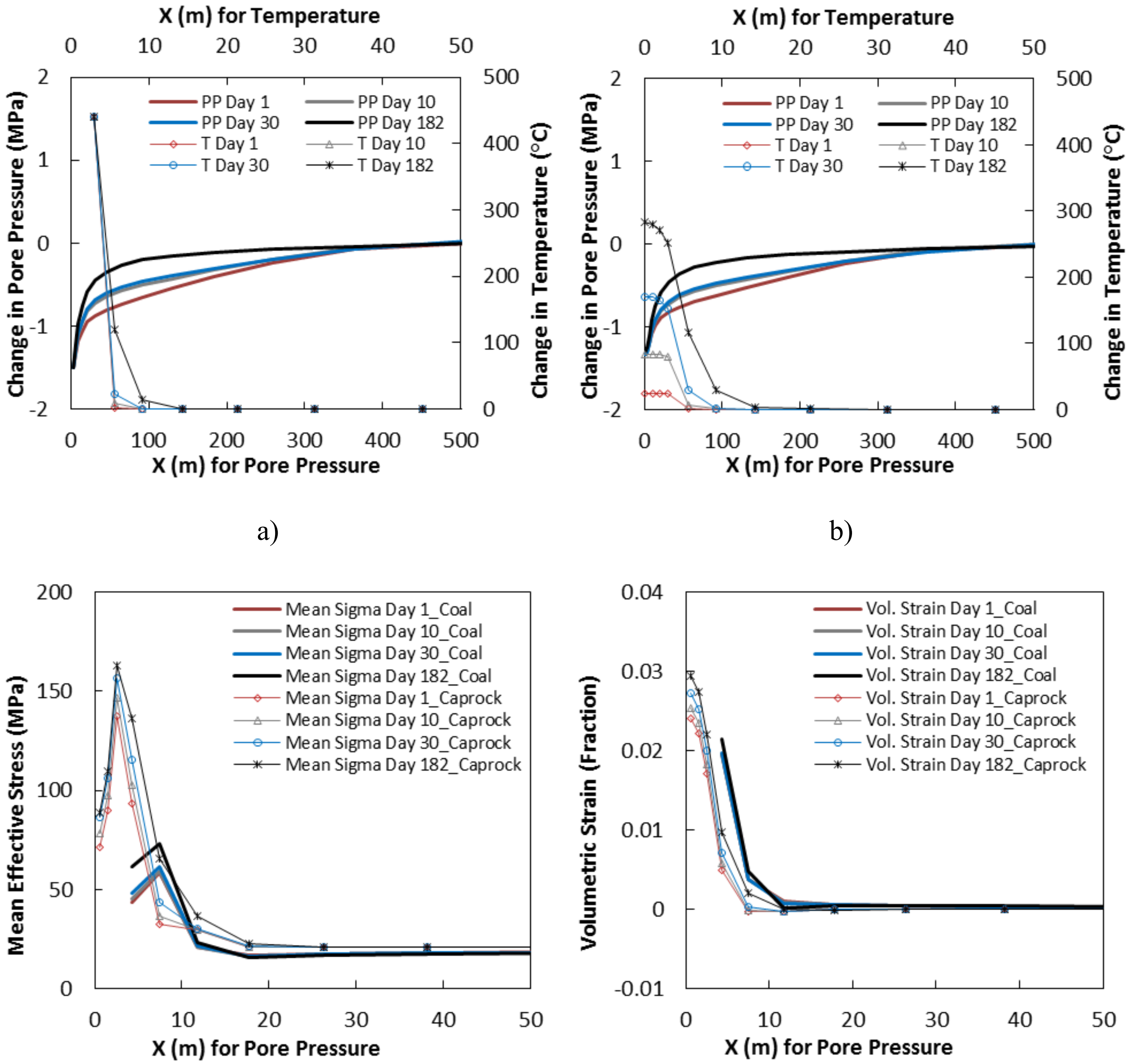

a)

b)

c)

d)

Figure 5.6 Results from scenario 2: a) change in pore pressure and temperature along middle of the coal seam; b) change in pore pressure and temperature along base of the caprock; c) mean effective stress along middle of the coal seam and base of the caprock; and d) volumetric strain along middle of the coal seam and base of the caprock

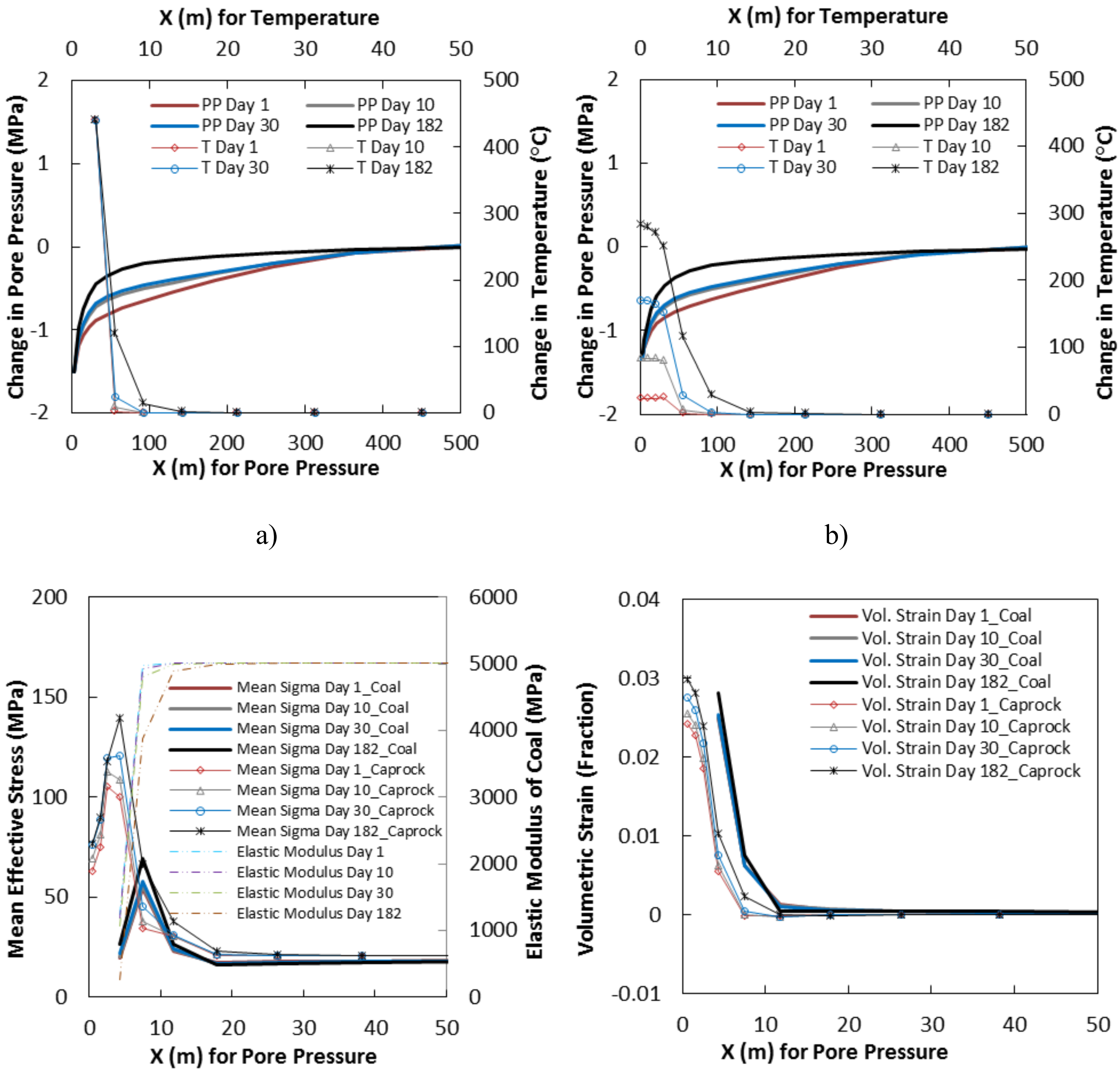

a) b)

c) d)

Figure 5.7 Results from scenario 3: a) change in pore pressure and temperature along middle of the coal seam; b) change in pore pressure and temperature along base of the caprock; c) mean effective stress and elastic modulus along middle of the coal seam as well as mean effective stress along base of the caprock; and d) volumetric strain along middle of the coal seam and base of the caprock

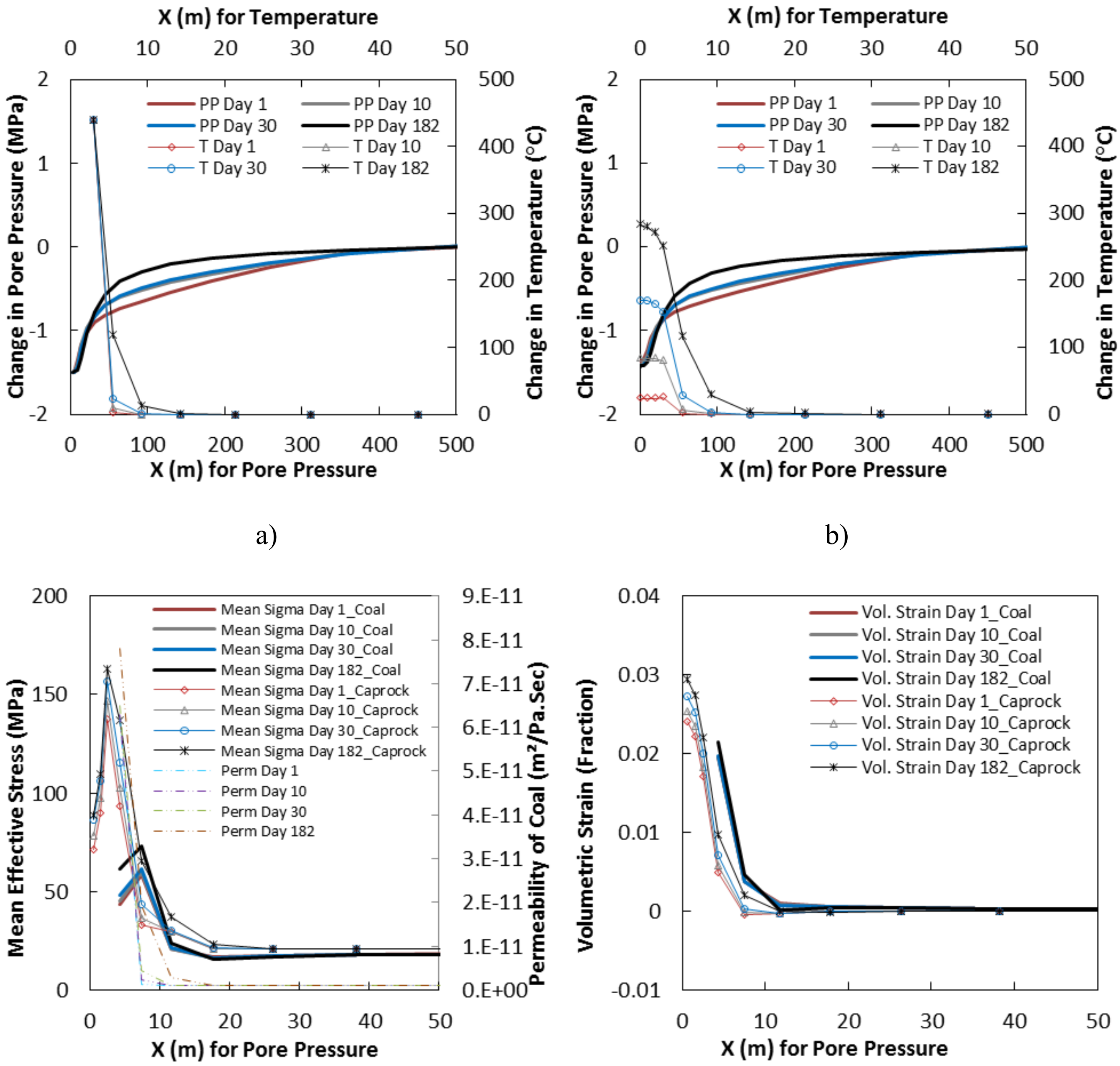

a)

b)

c)

d)

Figure 5.8 Results from scenario 4: a) change in pore pressure and temperature along middle of the coal seam; b) change in pore pressure and temperature along base of the caprock; c) mean effective stress and permeability along middle of the coal seam as well as mean effective stress along base of the caprock; and d) volumetric strain along middle of the coal seam and base of the caprock

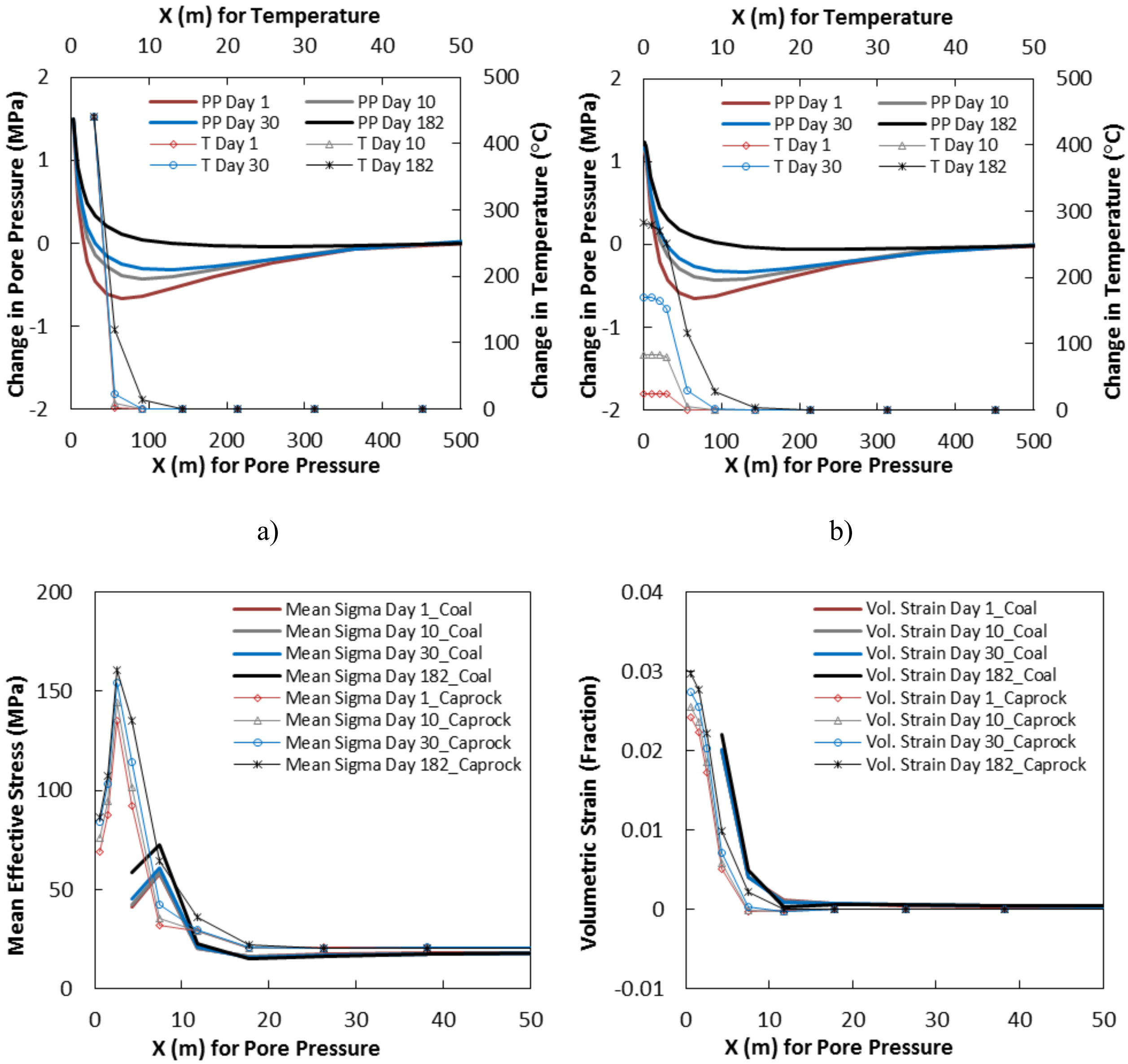

a)

b)

c)

d)

Figure 5.9 Results from scenario 5: a) change in pore pressure and temperature along middle of the coal seam; b) change in pore pressure and temperature along base of the caprock; c) mean effective stress along middle of the coal seam and base of the caprock; and d) volumetric strain along middle of the coal seam and base of the caprock

5.4.2. Impacts of syngas pressure on geomechanical response

For scenarios 1, 2 and 5, the value of syngas pressure was selected equal to, less than, and greater than the initial pore pressure. As seen in sub-sections a and b of Figure 5.5, Figure 5.6, and Figure 5.9, the base of the caprock and middle of the coal seam exhibited similar pore pressure responses despite the fact that permeability of the rock layers was one order of magnitude smaller than the coal seam. Regardless of the syngas pressure magnitude, in all cases, pore pressure dropped in early ages in the vicinity of the cavity and then increased over time. In scenario 1, which the syngas pressure was chosen equal to the initial pore pressure, after 182 days, pore pressure returned back to the initial pore pressure (Figure 5.5.a and b). In scenario 2, formation maintained the pressure difference between syngas and initial reservoir pressure (Figure 5.6.a and b). Although for scenario 5 the syngas pressure was selected above the initial reservoir pressure, in early ages and a few meters away from the cavity, pore pressure dropped. Later on, pore pressure increased.

The change in syngas pressure through scenarios 1, 2, and 5 did not show significant impacts on volumetric strain and mean effective stress in the coal and caprock. This study only considered thermal conduction; however, thermal convection was not included. As such, the change in syngas pressure did not create any influence on temperature plots.

5.4.3. Impacts of temperature-dependent coal elastic modulus on geomechanical response

The decline of elastic modulus of coal as a function of temperature for different simulation times are shown in Figure 5.7.c. In comparison to scenario 2, by considering temperature-dependent stiffness coal became softer around the cavity, which allowed more deformation and larger volumetric strain in the coal. However, smaller mean effective stress was observed in immediate vicinity of the cavity in both coal seam and caprock. This assumption did not result in any changes to the temperature plots.

5.4.4. Impacts of temperature-dependent coal permeability on geomechanical response

By this assumption, coal permeability exhibited up to two orders of magnitude changes in the vicinity of the cavity, where high temperature gradient existed (Figure 5.8.c). Initial permeability of the coal, just next to the cavity, was $9.81 \times 10^{-13}(\mathrm{m^2/Pa.sec})$ which after 182 days increased to $7.82 \times 10^{-11}(\mathrm{m^2/Pa.sec})$. It was observed that because of the enhanced coal permeability around the cavity, compared to scenario 2, pore pressure in the coal and base of the caprock rapidly reached a steady state condition. No changes were seen in the temperature front as thermal convection was not included in these simulations. This assumption did not create any noticeable changes to the volumetric strain and mean effective stress plots in the coal and rock.

5.4.5. Displacements of the monitoring points through scenarios 1 to 5

Displacements of the four monitoring points are plotted in Figure 5.10. In all scenarios, points A to D moved towards to center of the cavity which indicates that strata deformed towards the cavity. Each monitoring point had almost the same displacement throughout the scenarios except for scenario 3, which used temperature-dependent elastic modulus for coal. Since in scenario 3 coal stiffness declined in the vicinity of the cavity as a function of temperature, all monitoring points experienced larger displacements towards center of the cavity. Displacements of points A, B, C, and D in scenario 3 were -0.021, 0.093, -0.142, and -0.128 m, respectively.

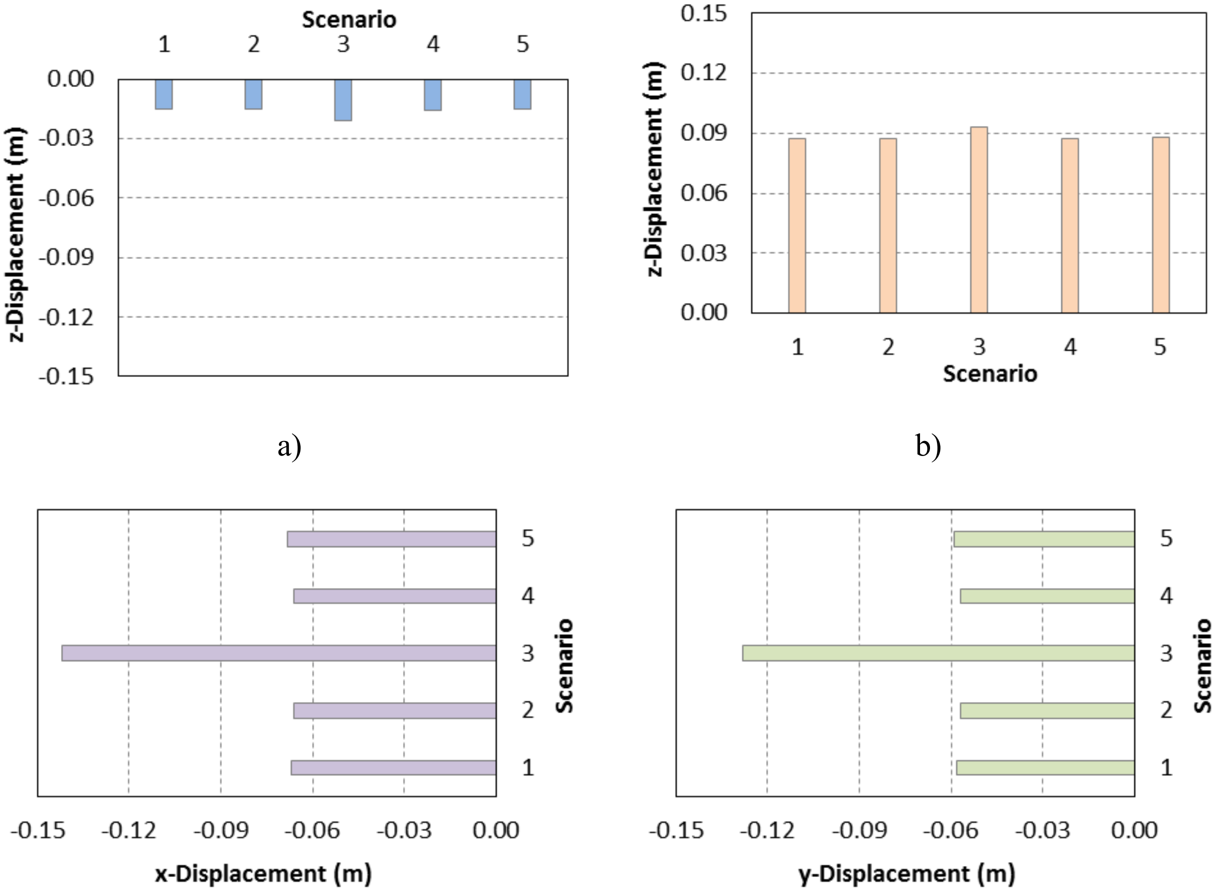

a)

b)

c)

d)

Figure 5.10 Displacements of the four monitoring points in different scenarios: a) point A; b) point B; c) point C; and d) point D

5.5. Summary and conclusions

To investigate the geomechanical response of an example deep UCG site to evolution of an idealized cubic cavity along with syngas pressure and temperature, a series of 3D coupled fluid-thermal-mechanical simulations were conducted in FLAC3D software. Five scenarios with different operational conditions and material properties were studied. The simulation model included caprock on top, a layer of coal in the middle including a fixed-size cavity under syngas pressure and high temperature, and underburden rock. Based on results obtained in this study, following conclusions were drawn:

- Due to cavity evolution and high temperature of syngas, large volumetric strain happened around the cavity.
- The base of the caprock experienced larger volumetric strain than the middle of the coal seam. Because of large deformation of strata around the cavity, pore pressure in the coal and rock dropped. At later times, pore pressure decline was compensated. Similar trends of pore pressure responses were observed in the coal and caprock.
- Mean effective stress in the coal and base of the caprock increased. The base of the caprock experienced larger mean effective stress than the middle of the coal seam.
- For the three assumptions for syngas pressure, pore pressure dropped in vicinity of the cavity in early ages and then increased over time.
- Change in syngas pressure did not show significant impacts on volumetric strain and mean effective stress in the coal and caprock.
- Using temperature-dependent elastic modulus for coal resulted in larger deformation and volumetric strain in the coal but smaller mean effective stress in both coal seam and caprock.
- Using temperature-dependent permeability for coal helped pore pressure in the coal and base of the caprock rapidly reach steady state conditions but no noticeable changes to volumetric strain and mean effective stress occurred.
- In all scenarios, the four monitoring points on the perimeter of the cavity moved towards the center of the cavity. This indicates that strata deformed towards the cavity. In the scenario with temperature-dependent elastic modulus for coal, all monitoring points experienced larger displacements towards center of the cavity.

5.6. Acknowledgements

The financial support for this study was provided by the Canadian Centre for Clean Coal/Carbon and Mineral Processing Technologies (C^5MPT).

5.7. References

Advani, S. H., Lin, Y. T., & Shuck, L. Z. (1977). Thermal and structural response evaluation for underground coal gasification. *Society of Petroleum Engineers Journal*, *17*(06), 413-422.

Advani, S. H., Shuck, L. Z., Lin, Y. T., & Chang, H. Y. (1976). Thermomechanics simulations associated with underground coal gasification. In *The 17th US Symposium on Rock Mechanics (USRMS)*. American Rock Mechanics Association.

American Society of Mechanical Engineers. (2009). ASME International Steam Tables for Industrial Use. Second Edition, American Society of Mechanical Engineers, New York.

Bartel, L. C., Beckham, L. W., & Reed, R. P. (1976). Instrumentation results from an in-situ coal gasification experiment. In *SPE Annual Fall Technical Conference and Exhibition*. Society of Petroleum Engineers.

Biot, M. A. (1941). General theory of three-dimensional consolidation. *Journal of Applied Physics*, *12*(2), 155-164.

Burton, E., Friedmann, J., & Upadhye, R. (2006). Best practices in underground coal gasification. Draft. US DOE contract no W-7405-Eng-48. Lawrence Livermore National Laboratory.

Buscheck, T. A., Hao, Y., Morris, J. P., & Burton, E. A. (2009). Thermal-hydrological sensitivity analysis of underground coal gasification. In *Proceedings of the 2009 International Pittsburgh Coal Conference, Pittsburgh, PA, USA* (Vol. 2023).

Dabbous, M. K., Reznik, A. A., Taber, J. J., & Fulton, P. F. (1974). The permeability of coal to gas and water. *Society of Petroleum Engineers Journal*, *14*(06), 563-572.

Daggupati, S., Mandapati, R. N., Mahajani, S. M., Ganesh, A., Mathur, D. K., Sharma, R. K., & Aghalayam, P. (2010). Laboratory studies on combustion cavity growth in lignite coal blocks in the context of underground coal gasification. *Energy*, *35*(6), 2374-2386.

Fausett, L.V. (1984). An analysis of mathematical models of underground coal gasification. PhD Dissertation, University of Wyoming.

Glass, R. E. (1984). The thermal and structural properties of a Hanna basin coal. *Journal of Energy Resources Technology*, *106*(2), 266-271.

Itasca Consulting Group Inc, (2009). FLAC3D User's Guide. Itasca Consulting Group Inc., Minneapolis, Minnesota.

Jung, K. S. (1987). Mathematical modeling of cavity growth during underground coal gasification. PhD Dissertation, University of Wyoming.

Kostur, K., & Kacur, J. (2008). The monitoring and control of underground coal gasification in laboratory conditions. *Acta Montanistica Slovaca*, *13*(1), 111-117.

Luo, X., Tan, Q., Luo, C., & Wang, Z. (2008). Microseismic monitoring of burn front in an underground coal gasification experiment. In *The 42nd US Rock Mechanics Symposium (USRMS)*. American Rock Mechanics Association.

Morris, J. P., Buscheck, T. A., & Hao, Y. (2009). Coupled geomechanical simulations of UCG cavity evolution. In *Proceedings of the 2009 International Pittsburgh Coal Conference, Pittsburgh PA*.

Nitao, J. J., Camp, D. W., Buscheck, T. A., White, J. A., Burton, G. C., Wagoner, J. L., & Chen, M. (2011). Progress on a new integrated 3-D UCG simulator and its initial application. In *International Pittsburgh Coal Conference* (pp. 1-13).

Nourozieh, H., Kariznovi, M., Chen, Z., & Abedi, J. (2010). Simulation study of underground coal gasification in Alberta reservoirs: Geological structure and process modeling. *Energy & Fuels*, *24*(6), 3540-3550.

Sansgiry, P. S. (1990). A numerical technique to track the growth of cavities in underground coal gasification. PhD Dissertation, University of Wyoming.

Sarraf Shirazi, A. (2012). CFD simulation of underground coal gasification. MSc Dissertation, University of Alberta.

Seifi, M., Chen, Z., & Abedi, J. (2011). Numerical simulation of underground coal gasification using the CRIP method. *The Canadian Journal of Chemical Engineering*, *89*(6), 1528-1535.

Stanczyk, K., Kapusta, K., Wiatowski, M., Swiadrowski, J., Smolinski, A., Rogut, J., & Kotyrba, A. (2012). Experimental simulation of hard coal underground gasification for hydrogen production. *Fuel*, *91*(1), 40-50.

Swan Hills Synfuels, (2012). Swan Hills in-situ coal gasification technology development; Final outcomes report. Swan Hills Synfuels, Alberta, Canada.

Tan, Q., Luo, X., & Li, S. (2008). Numerical modeling of thermal stress in a layered rock mass. In *The 42nd US Rock Mechanics Symposium (USRMS)*. American Rock Mechanics Association.

Thorsness, C. B., Grens, E. A., & Sherwood, A. (1978). A one-dimensional model for in situ coal gasification, UCRL-52523, Lawrence Livermore, National Laboratory (LLNL) Report, Berkeley, California.

Vorobiev, O. Y., Morris, J. P., Antoun, T. H., & Friedmann, S. J. (2008). Geomechanical simulations related to UCG activities. In *International Pittsburgh Coal Conference, Pittsburgh, PA*.

World Energy Council. (2010). Survey of energy resources. World Energy Council, London, UK.

Yang, L. (2004). Study on the model experiment and numerical simulation for underground coal gasification. *Fuel*, *83*(4), 573-584.

Zhao, Y., Qu, F., Wan, Z., Zhang, Y., Liang, W., & Meng, Q., (2010). Experimental investigation on correlation between permeability variation and pore structure during coal pyrolysis. *Transport in Porous Media, 82*(2), 401-412.

Chapter 6 A Numerical Modeling Workflow for Sequentially Coupled Reservoir and Geomechanical Simulation of Underground Coal Gasification[1]

6.1. Abstract

Underground coal gasification (UCG) has been identified as an environmentally friendly technique for gasification of deep un-mineable coal seams in-situ. This technology has the potential to be a clean and promising energy provider from coal seams with minimal greenhouse gas emission. UCG eliminates the presence of coal miners underground hence; it is believed to be a safer technique compared to deep coal mining methods. UCG includes drilling injection and production wells into the coal seam, igniting the coal, and injecting an oxygen-based mix to facilitate coal gasification. Produced syngas is extracted via the production well. Evolution of a cavity created from the gasification process along with high temperature as well as change in pore fluid pressure causes mechanical changes to the coal and surrounding formations. Therefore, simulation of the gasification process alone is not sufficient to represent this complex thermal-hydro-chemical-mechanical process. Instead, a coupled flow and geomechanical modeling can help better represent the process by allowing simultaneous observation of the syngas production, advancement of the gasification chamber, and the cavity growth. Adaptation of such a coupled simulation would aid in optimization of the UCG process while helping to control and mitigate the environmental risks caused by geomechanical failure and syngas loss to groundwater. This paper presents results of a sequentially coupled flow-geomechanical simulation of a three-dimensional (3D) UCG example using the numerical methodology devised in this study. The 3D model includes caprock on top, a coal seam in the middle, and another layer of rock underneath. Gasification modeling was conducted in the Computer Modelling Group Ltd. (CMG)'s Steam, Thermal, and Advanced processes Reservoir Simulator (STARS). Temperature and fluid pressure of each grid block as well as the cavity geometry, at the time-step level, were passed from the STARS to the geomechanical simulator i.e. the Fast Lagrangian Analysis of Continua in 3 Dimensions (FLAC3D) computer program (from the Itasca Consulting

---

[1] A version of this chapter has been published as:
Akbarzadeh, H., & Chalaturnyk, R. J. (2016). Sequentially coupled flow-geomechanical modeling of underground coal gasification for a three-dimensional problem. Mitigation and Adaptation Strategies for Global Change, 21(4), 577-594.

Group Inc.). Key features of the UCG process which were investigated herein include syngas flow rate, cavity growth, temperature and pressure profiles, porosity and permeability changes, and stress and deformation in the coal and rock layers. It was observed that the coal matrix deformed towards the cavity, displacement and additional stress happened, and some blocks in the coal and rock layers mechanically failed.

Keywords: Underground coal gasification (UCG), Pyrolysis, Gasification, Cavity, Geomechanics, Sequentially Coupled Modeling, Reservoir

6.2. Introduction

The 2010 Survey of Energy Resources estimated world coal reserves at about 860 billion tonnes (World Energy Council, 2010). Since 2000, global coal consumption has grown faster than any other fuel at 4.9% per year and is expected to rise by over 60% by 2030 (World Energy Council, 2010) which asks for more coal extraction. There are greater resources deep underground that can be a supplement to the proved reserves but, based on the current technology, are not economic to be mined. Underground coal gasification (UCG) is an alternative technique that can address the extra demands for coal consumption with the gasification of deep un-mineable coal seams, but with substantially less capital expenses and a smaller carbon dioxide (CO_2) footprint compared to the equivalent conventional surface gasifiers (Burton et al., 2006). More important is that UCG does not need the presence of coal miners underground which is of significant value form an occupational safety perspective. Since its introduction, UCG has been widely trialed. Figure 6.1 presents location of the UCG activities around the world.

Two main techniques are currently being used by industries for operation of the UCG. Linked Vertical Wells (LVW) requires drilling of vertical injection and production wells and a linkage between them. The newer technique is the Controlled Retraction Injection Point (CRIP) which provides more control over where the gasification takes place and allows access to deeper coal seams with far fewer wells being drilled from the surface (Couch, 2009). The CRIP needs one vertical well as producer and one horizontal well as injector. After sufficient amount of coal has been burnt away, the injection point retracts in upstream direction. Figure 6.2 shows the schematic of the LVW and the CRIP methods.

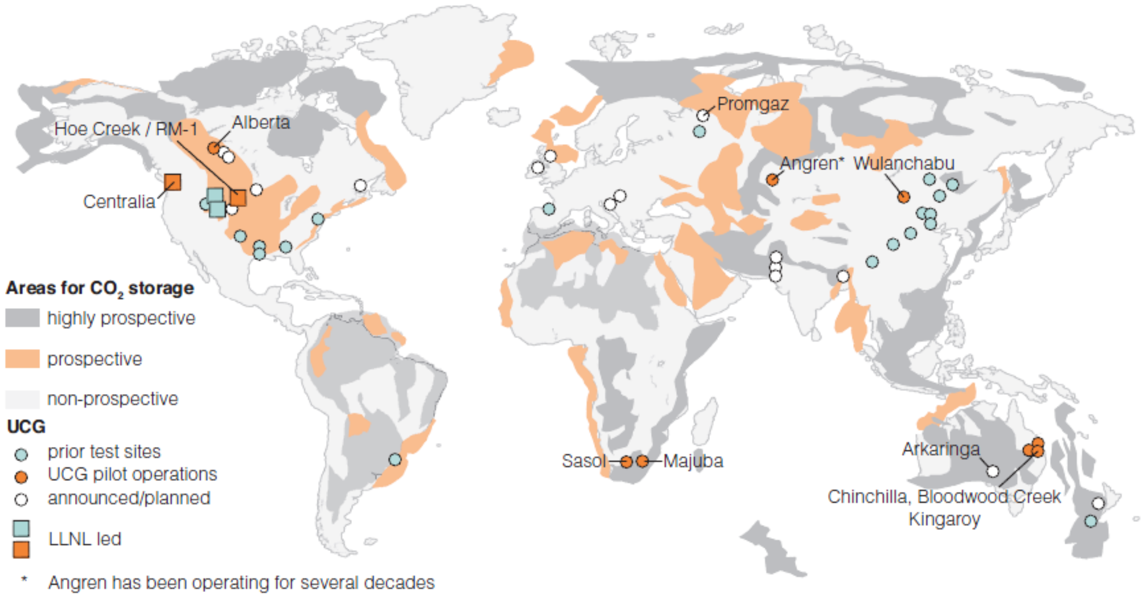

Figure 6.1 The UCG sites worldwide (Couch, 2009)

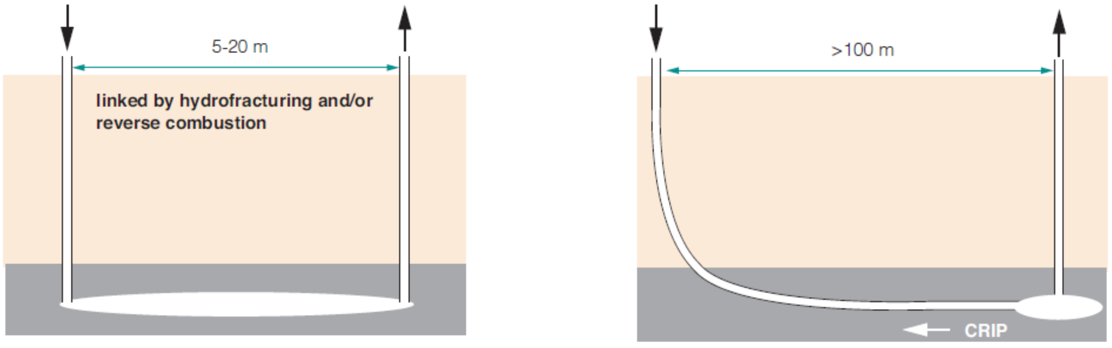

a)

b)

Figure 6.2 Schematics of the UCG process: a) linked vertical wells (LVW); and b) Controlled Retraction Injection Point (CRIP) (Couch, 2009)

Although the UCG has been tested and trialed in many countries across the world (Burton et al., 2006), because of the nature of the process, which is a coupled thermal-hydro-chemical-mechanical process, there are always geomechanical risks in a UCG operation. Evolution of the cavity along with high temperature well over 1000 degrees Celsius as well as change in pore fluid pressure may result in fracturing and collapsing of formation adjacent to the gasification chamber which will create an area of enhanced permeability and porosity around the cavity.

Subsidence of ground surface in a shallow UCG project and contamination of groundwater are the other risks associated with the UCG projects.

In order to optimize the UCG process and mitigate risks during and after gasification, extensive laboratory, analytical, and numerical studies as well as field monitoring have been done. Laboratory studies of mechanical, thermal and hydraulic properties of coals from different basins were performed (Dabbous et al., 1974; Glass, 1984; Zhao et al., 2010). A few coal gasification experimental set ups were utilized under laboratory conditions (Daggupati et al., 2010; Kostur and Kacur, 2008; Stanczyk et al., 2012; Yang, 2004).

Numerous analytical models were also developed for cavity growth prediction, mainly based on the chemical process of combustion (Fausett, 1984; Jung, 1987; Sansgiry, 1990). Rate of syngas production and its composition and temperature as well as change in porosity and permeability of the coal seam due to gasification (which leads to formation of a cavity) were the focus of numerical simulations (Buscheck et al., 2009; Daggupati et al., 2010; Nourozieh et al., 2010 ; Sarraf Shirazi, 2012; Seifi et al., 2011; Yang, 2004).

A few field monitoring results of the UCG trial sites were also published (Bartel et al., 1976; Luo et al., 2008). Recently, the world's deepest ever UCG pilot test was successfully conducted at a depth of 1400 m in Swan Hills, Alberta, Canada (Swan Hills Synfuels, 2012).

Literature has documented some geomechanical simulations of the UCG process as well. Advani et al. (1976 & 1977) analyzed plane strain linear thermo-elastic finite element models with an elliptical cavity within which high temperature and pressure was applied to investigate the tangential stress changes around the cavity. Vorobiev et al. (2008) performed two-dimensional finite element modeling of a disc-shaped reservoir. To simulate the UCG activities, they did element removal and observed stress redistribution and surface subsidence. The pressure and temperature in the cavity was set to zero and elastic material was assumed. Three-dimensional modeling of a UCG cavity was done by Morris et al. (2009) using LDEC (Livermore Distinct Element Code). They assumed a simplified cavity, then removed any coal elements became unstable by the excavation, under gravitational and an in-situ stress fields. They did not consider gasification temperature neither groundwater and syngas pressure. They also observed the influence of coal cleat orientation and persistence on cavity evolution. The

Lawrence Livermore National Laboratory recently developed a new integrated 3D UCG simulator which performs both gasification and geomechanics simulations (Nitao et al., 2011).

The UCG is a complex process and large scales experiments in laboratory, to replicate coal gasification and investigate its impact on geomechanics, are expensive and seem impractical. On the other hand, due to great depth of a gasification reactor, field monitoring of cavity growth, stress changes around the cavity, and spalling of coal and rock are also expensive. Coupled simulations can provide the opportunity to model coal gasification using the corresponding set of pyrolysis and gasification reactions as well as to predict mechanical response of the coal seam and surrounding formation which facilitates investigating caprock and bedrock integrity at different time-steps and under different operational conditions. Prior to running any UCG plant, an extensive coupled modeling could be performed in order to investigate effect of selection of different operational constraints (injection gas composition and its pressure and temperature, wells spacing, and the retraction pattern in the CRIP method) to oversee and mitigate geomechanical and environmental risks by preventing the catastrophic collapse of the gasification chamber which, in long run, may causes syngas loss to groundwater. To date, there have not been many publications on coupled UCG simulation using available commercial software.

6.3. Scope and objectives

The main objective of this study was to develop a numerical approach to conduct sequentially coupled 3D flow-geomechanical simulation of a UCG project using coal properties of the Swan Hills, Alberta, Canada with the aid of available commercial software.

6.4. Chemical reactions

In underground coal gasification, three main chemical processes occur; drying/vaporization, pyrolysis, and char gasification and combustion. Outside the gasification chamber, wherever temperature is above steam saturation temperature at pressure of that particular point, liquid water changes phase to steam. Depending on the pressure difference between the gasification chamber and surroundings, steam may stay in place or move to the chamber and participate in the chemical reactions. Pyrolysis is the process of releasing volatile matter by increasing coal temperature, which happens in the temperature range of 400-900 ^{o}C (Anthony and Howard, 1976). The main products of pyrolysis include char (which here is assumed to be carbon, C), methane (CH_4), carbon monoxide (CO), carbon dioxide (CO_2), and hydrogen (H_2) (Anthony and Howard, 1976) and to a lesser extent contaminant byproducts.

A series of chemical reactions with the corresponding reaction kinetics is usually used to represent and simulate the UCG process. Literature has documented these reactions but there are discrepancies in the literature on the UCG reactions and their kinetics. The majority of them have originated from surface coal gasification in atmospheric conditions and others were utilized for shallow UCG; hence, they have limitations in terms of pressure range. Kariznovi et al. (2013) summarized these reactions and modified their kinetics in order to match the Alberta deep UCG field data. This series of 10 reactions is provided below which were adopted for this study (Table 6.1). Reaction 6.1 was considered to represent the process of pyrolysis of the Alberta coal.

$$Dry\ Coal\ \rightarrow 4.63C +\ 0.43\ \mathrm{CO} + 0.12\mathrm{CO_2} + 0.79\mathrm{CH_4} + 0.18\mathrm{H_2}\quad \Delta \mathrm{H}^{o}_{298} = 0\ \ \mathrm{KJ/gmole}\ \ (6.1)$$

Kariznovi et al. (2013) also examined the influence of using different pyrolysis reaction kinetics on the product gas composition of the Alberta UCG simulation and concluded that the influence was not significant as the amount of gas produced in pyrolysis is much less than gasification. First order Arrhenius reaction rate (Equation 6.2) was used in this study with the temperature-dependent exponential rate constant of Equation 6.3. The corresponding pre-exponential factor (ε_o) and the activation energy (E) was chosen as 188.28 $\mathrm{KJ/gmole}$ and $1.00\ \times\ 10^{11}$, respectively (Kariznovi et al., 2013).

$$\frac{d\xi}{dt} = \ \varepsilon(\xi^{o} -\ \xi) \qquad (6.2)$$

where ξ is the volatile lost as a fraction of the original coal weight and ξ^{o} is the effective volatile content of the coal.

$$\varepsilon = \varepsilon_o \exp(-\frac{E}{RT}) \quad (6.3)$$

Reactions (6.4) to (6.10) with the corresponding activation energies and frequency factors mentioned in Table 6.1 represent the char reactions in the deep Alberta UCG (Kariznovi et al., 2013).

Table 6.1 Gasification reactions and kinetic parameters for the UCG in Alberta (Kariznovi et al., 2013)

Reaction no.	Reaction	Reaction name	Heat of reaction (KJ/gmole)	Activation energy (KJ/gmole)	Reaction frequency factor
(6.4)	$C + O_2 \rightarrow CO_2$	Coal combustion	-393	100	2.08×10^1
(6.5)	$C + CO_2 \rightarrow 2CO$	Boudouard	+172	249	6.57×10^6
(6.6)	$C + H_2O \rightarrow H_2 + CO$	Steam gasification	+131	156	1.87×10^4
(6.7)	$C + 2H_2 \rightarrow CH_4$	Hydrogen gasification	-75	200	1.81×10^3
(6.8)	$CO + \frac{1}{2}O_2 \rightarrow CO_2$	Carbon monoxide oxidation	-283	247	1.12×10^8
(6.9)	$CO + H_2O \rightarrow CO_2 + H_2$	Forward water shift	-41	12.6	1.73×10^0
(6.9)	$CO_2 + H_2 \rightarrow CO + H_2O$	Reverse water shift	+41	12.6	4.48×10^{-2}
(6.10)	$CH_4 + H_2O \rightarrow CO + 3H_2$	Forward methane steam reforming	+206	30	3.13×10^2
(6.10)	$CO + 3H_2 \rightarrow CH_4 + H_2O$	Reverse methane steam reforming	-206	30	4.00×10^3

6.5. Governing equations

In this study, STARS 2012 of the Computer Modelling Group Ltd. (CMG) was used for the gasification simulation. STARS (Steam, Thermal, and Advanced processes Reservoir Simulator) is a thermal, K-value compositional, chemical reaction and geomechanics reservoir simulator which is capable of modeling of recovery processes including thermal applications, steam and air injection, chemical and polymer flooding, dry and wet combustion, and many types of chemical additive processes using a wide range of grid and porosity models in both field and laboratory scales. STARS facilitates the simulation of in-situ processes by means of using a series of reactions between the various fluid and solid components in the reservoir (Computer Modelling Group Ltd., 2012).

In STARS, a series of conservation equations are solved; mass conservation equation for each flowing component, conservation equation for each solid component, and energy conservation equation for the entire system. In order to simulate a UCG process in STARS, a porous medium approach was used and hence, the organic part of coal (volatile matter and combustible solids) was assigned as initial solid concentration in the pore space (this approach was also adopted by Seifi et al., 2011). Solid concentration changes as pyrolysis and gasification proceeds. Chemical reactions are treated as the source/sink terms for each component (Computer Modelling Group, Ltd., 2012). Two main transport phenomena which occur in the UCG are heat and mass transfer. Heat transfer is done in the form of heat conduction and convection. Darcy's law is used for gas species flow. These equations are solved on each block using the Finite Difference Method.

Geomechanical simulation was performed with the aid of the Fast Lagrangian Analysis of Continua in 3 Dimensions (FLAC3D 4.00) computer program (from the Itasca Consulting Group Inc.). FLAC3D is a three-dimensional explicit finite-difference program for modeling advanced geotechnical analyses of soil and rock media to calculate stress and deformation, fluid flow, and heat conduction and convection using several built-in material models (Itasca Consulting Group Inc., 2009).

6.6. Flow-geomechanical coupling

Two major mechanisms dominate the UCG process which is flow of syngas and geomechanical changes. Flow of syngas occurs due to coal pyrolysis, gasification, and combustion of char. During this process, flow properties of coal such as permeability and fluid porosity change which is due to release of volatile matters and consumption of the organic part of the coal as a result of gasification and combustion. Fluid porosity of a grid block at each time-step depends on its initial void porosity and solid concentration (organic part of the coal) at the same time. When pyrolysis or gasification takes place, the amount of solid concentration decreases which will lead to an increase in fluid porosity. Equation 6.11 was used to calculate fluid porosity in STARS:

$$\emptyset_f = \emptyset_v \left(1 - \frac{C_s}{\rho_s}\right) \tag{6.11}$$

where $\emptyset_f$ and $\emptyset_v$ are fluid and void porosities, respectively and C_s and ρ_s are solid concentration (gmole per cubic meter of pore space) and solid density ($gmole\ /\ m^3$), respectively.

Geomechanical processes in the UCG deal with stress and strain in coal and rocks. Changes in temperature and pressure of the reservoir along with the cavity evolution alter stress and strain fields in the coal and surrounding formation which, in turn, will affect flow properties of the coal and rock layers above and below the coal seam.

Different coupling approaches used in reservoir engineering to couple flow and geomechanics have been discussed by Settari and Walters (2001). Fully coupled solutions solves two sets of corresponding equations for the two mechanisms at the same time which in the case of UCG, convergence poses a challenge because of significant changes in fluid porosity and permeability. Sequential coupling techniques have been utilized to overcome the computational challenges of fully coupled solutions. In sequential coupling of UCG, two levels of coupling can be considered. One is continuous updating of permeability during each time step in STARS because of change in fluid porosity of coal blocks in the gasification zone as a consequence of consumption of the organic part. The next level of coupling is updating permeability and fluid porosity of coal blocks as a result of geomechanical deformation. To perform the first level of coupling during each time step of flow calculation in STARS, permeability of each coal block needs to be updated using a relationship between permeability and fluid porosity. No experimental data were available for the Alberta coal which relates coal permeability to its fluid porosity during drying and pyrolysis/gasification. Relationship between permeability and porosity of the Wyodak coal during drying and pyrolysis was published by Thorsness et al. (1978) as in Equation 6.12:

$$\ln\left(\frac{K}{K_0}\right) = \alpha\,(\emptyset - \emptyset_0) \qquad \text{or} \qquad \frac{K}{K_0} = e^{\alpha\,(\emptyset - \emptyset_0)} \tag{6.12}$$

where K_0 and $\emptyset_0$ are initial permeability and fluid porosity of the coal and α has a value of approximately 12.

Permeability and porosity of samples from the Xing-Long-Zhuang Coal Mine in China was recently published by Zhao et al. (2010). This data was added to Thorsness et al. (1978) data and logarithm of permeability was plotted versus change in fluid porosity. A curve similar to Equation 6.12 was fitted to all data points (Figure 6.3) and α was estimated as 16.7. Equation 6.13 represents this updated relationship which was developed and used in this study.

$$\ln\left(\frac{K}{K_0}\right) = 16.7\,(\emptyset - \emptyset_0) \qquad \text{or} \qquad \frac{K}{K_0} = e^{16.7\,(\emptyset - \emptyset_0)} \tag{6.13}$$

Equation 6.13 was derived based on data available for these two types of coals and for the following conditions:

- Fluid porosity change: $\Delta\emptyset \leq 0.5$
- Temperature: $t \leq 650$ ℃
- Permeability: $K \leq 16$ Darcy

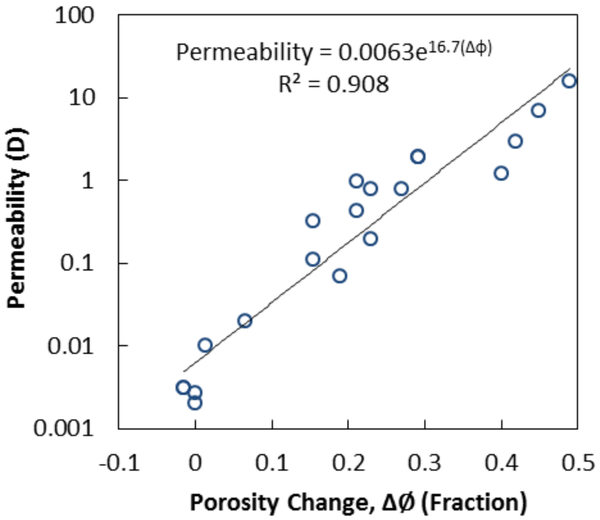

Figure 6.3 Permeability vs. change in fluid porosity during drying and pyrolysis based on data available for the Wyodak coal (Thorsness et al., 1978) and the Xing-Long-Zhuang coal (Zhao et al., 2010)

In this study, STARS 2012 was coupled with FLAC3D 4.00. Only the first level of coupling was conducted herein. Each time step in STARS was divided into sub-time-steps and continuous updating of permeability of coal blocks was done using Equation 6.13. In order to do the geomechanical calculation, at the time-step level, three sets of data were passed from STARS to FLAC3D; temperature, pressure, and the cavity geometry. This sequential coupling package was coded in FORTRAN and a LINUX script program. Figure 6.4 shows how the sequential coupling procedure works.

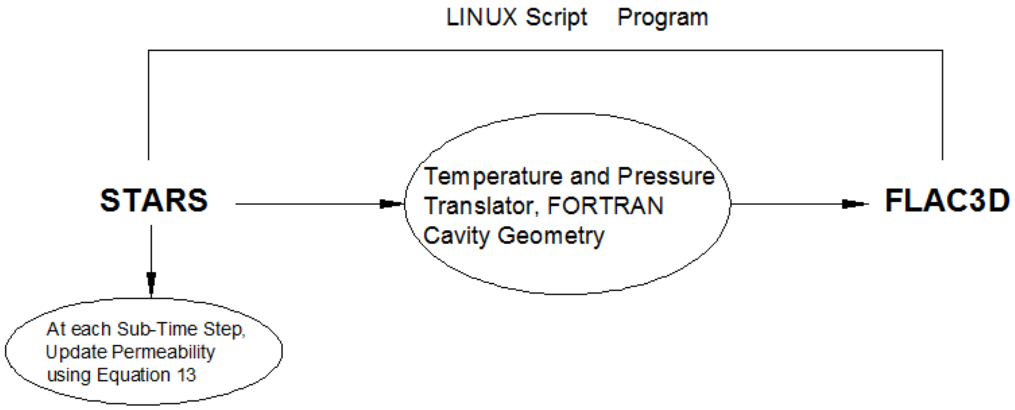

Figure 6.4 Flow-geomechanical sequential coupling algorithms

6.7. Simulation model

6.7.1. Geometry

The 3D model included three geological units; a coal seam overlain by a layer of caprock on top and underlain with an underburden rock layer (Figure 6.5.a). Thicknesses of these layers from top to the bottom are 50, 6, and 50 m, respectively. The model dimension in both x and y directions are 125 m. The coal seam of the Alberta UCG site has total thickness of 7 to 8 m with two partings and net thickness of about 6 m (Swan Hills Synfuels, 2012); hence, the coal layer thickness in this study was selected to be 6 m. The entire geometry was built in the geomechanical simulator; however, only a block with dimension of $25.0 \text{ m} \times 25.0 \text{ m} \times 6.0 \text{ m}$ from the central part of the coal seam was built in the flow simulator. The grid block size for the flow simulation was selected as $0.5 \text{ m} \times 0.5 \text{ m} \times 0.5 \text{ m}$. All boundaries in the flow model were considered as no-flow boundaries whereas in the geomechanical simulator, bottom of the model was fixed, sides were selected as rollers and top of the caprock was assigned free boundary. Initial in-situ stresses and pore pressure corresponding to a depth of 1400 m was applied to the model. The total number of grid blocks in the flow and geomechanical simulators was 30000 and 156800, respectively. No sensitivity analyses in regards to the grid size were conducted herein, since the main focus of this chapter was only on the development of the coupling workflow.

Figure 6.5.b shows a two-dimensional (2D) view of the gasification model at the middle of the model width, which includes the production and injection wells. The production well was extended from the surface to the third layer from the bottom of the coal seam and perforated at that layer. The injection well was placed in the same plane as the production well and was turned horizontally and extended up to a distance of 4.0 m from the production well. To simulate the CRIP process, the injection head was retracted two times for 2.5 m in the upstream direction. Four days of injection of equal molar mixture of steam and oxygen was considered for the first and third injection points; however, for the middle point, the injection time was two days. Also presented in Figure 6.5.b is the location of three monitoring points in the coal seam; points A, B, and C which were used to track temperature, pore pressure, stress and strain paths for 10 days of simulation time.

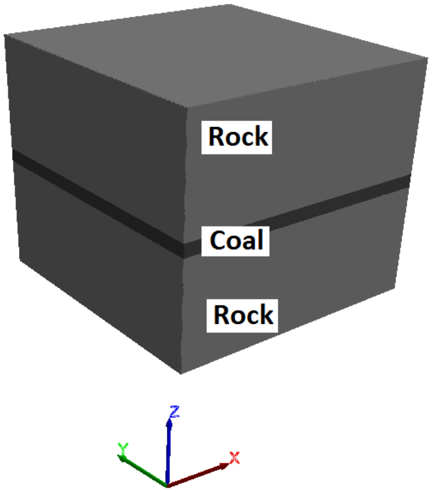

a)

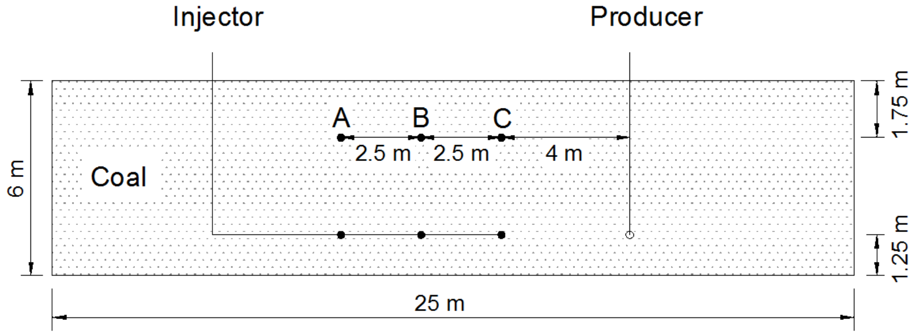

b)

Figure 6.5 Model geometry: a) 3D view; and b) vertical cross section of the gasification model at the plane of injection and production wells including monitoring points A, B, and C in the coal seam

6.7.2. Material properties

Coal properties used in this study were chosen to represent the Alberta deep UCG site at a depth of 1400 m but no actual site specific properties were available for this study. The coal is a high volatile B bituminous coal with average proximate analysis as shown in Table 6.2.

Table 6.3 represents initial reservoir properties and thermal properties of solids and fluids required for modeling in STARS. All thermal properties were assumed constant except the heat capacities of gas species that were calculated as a function of temperature using Equation 6.14 (Computer Modelling Group, Ltd., 2012) which corresponds to the ideal gas condition.

Table 6.2 Proximate analysis of coal of the Alberta UCG (Kariznovi et al., 2013; Swan Hills Synfuels, 2012)

Fixed carbon (%)	Volatile matter (%)	Ash (%)	Moisture (%)
55.6	30.4	9.2	4.8

Table 6.3 Initial Alberta UCG reservoir properties required for modeling in STARS (Kariznovi et al., 2013; Nourozieh et al., 2010; Seifi et al., 2011)

	Parameter	Value
Reservoir initial properties	Void porosity (coal and initial fluid) (fraction)	0.95
	Fluid porosity (fraction)	0.0866
	Absolute permeability (mD)	1
	Pressure (MPa)	11.5
	Temperature (ºC)	60
	Water saturation (fraction)	0.7
	Gas saturation (fraction)	0.3
	Initial fluid in the reservoir (-)	CH_4
	Coal density (kg/m^3)	1200
	Char density (kg/m^3)	1740
Solids and fluids thermal properties	Rock volumetric heat capacity (J/m^3. ºC)	3.0×10^6
	Rock thermal conductivity (J/m.day. ºC)	2.0×10^5
	Char heat capacity (J/gmole.ºC)	17
	Coal heat capacity (J/gmole.ºC)	17
	Solid thermal conductivity (J/m.day. ºC))	4.5×10^5
	Gas thermal conductivity (J/m.day. ºC)	4000
	Water thermal conductivity (J/m.day. ºC)	48384
	Water/steam densities, viscosities and enthalpies (-)	STARS defaults

$$C_p = CPG1 + CPG2 \times T + CPG3 \times T^2 + CPG4 \times T^3 \tag{6.14}$$

where C_p is heat capacity of gas and T is temperature in absolute degrees. Coefficients CPG1 to CPG4 are listed in Table 6.4.

Table 6.4 Coefficients for gas heat capacity correlation in Equation 6.14 (Computer Modelling Group Ltd., 2012)

Component	CPG1 (J/gmole °C)	CPG2 (J/gmole. °C)	CPG3 (J/gmole. °C)	CPG4 (J/gmole. °C)
O_2	28.106	-3.68×10^{-6}	1.75×10^{-5}	-1.07×10^{-8}
CO_2	19.795	7.34×10^{-2}	5.60×10^{-5}	1.72×10^{-8}
H_2	27.14	9.27×10^{-3}	-1.38×10^{-5}	7.65×10^{-9}
CO	30.869	-1.29×10^{-2}	2.79×10^{-5}	-1.28×10^{-8}
CH_4	19.251	5.21×10^{-2}	1.20×10^{-5}	-1.13×10^{-8}

STARS defaults were used for water/steam densities, viscosities and enthalpies. Rock thermal properties used in this study are shown in Table 6.5. The Mohr-Coulomb elastic perfectly plastic model was selected for geomechanical analyses of the coal and rock layers using a set of input parameters taken from literature as listed in Table 6.5. Although the gasification model used chemical reactions and coal properties reported for the Alberta UCG project, the properties chosen for the geomechanical model were selected from literature and not intended to represent the Alberta UCG site. The focus in this work was on the coupling work rather than any site-specific material properties.

Table 6.5 Geomechanical properties of coal and rock layers assumed in this study

	Parameter	Value
Coal geomechanical properties	Constitutive model	Mohr-Coulomb Elasto-Plastic
	Elastic modulus (MPa)	5000
	Poisson's ratio (-)	0.3
	Cohesion (MPa)	10
	Friction angle (Deg.)	40
	Biot's coefficient (-)	1
	Linear thermal expansion coefficient (1/^{o}C)	9×10^{-6}
Rock geomechanical properties	Constitutive model	Mohr-Coulomb Elasto-Plastic
	Elastic modulus (MPa)	30000
	Poisson's ratio (MPa)	0.3
	Cohesion (MPa)	35
	Friction angle (Deg.)	60
	Biot's coefficient (-)	1
	Linear thermal expansion coefficient (1/^{o}C)	15×10^{-6}
Rock thermal properties	Porosity (fraction)	0.05
	Absolute permeability (mD)	0.1
	Density (kg/m^3)	2500
	Rock volumetric heat capacity (J/m^3. ^{o}C)	3.0×10^6
	Rock thermal conductivity (J/m.day.^{o}C)	2.0×10^5

Another major coal property is relative permeability to gas and water which is mainly important where two phases of liquid water and gas exist; i.e., the region beyond the gasification chamber which there is mix of liquid water, steam, initial methane, or portion of syngas which diffused to this region. Gash et al. (1992) measured the relative permeability of the Fruitland Formation coal in New Mexico (Figure 6.6) which was used in this simulation

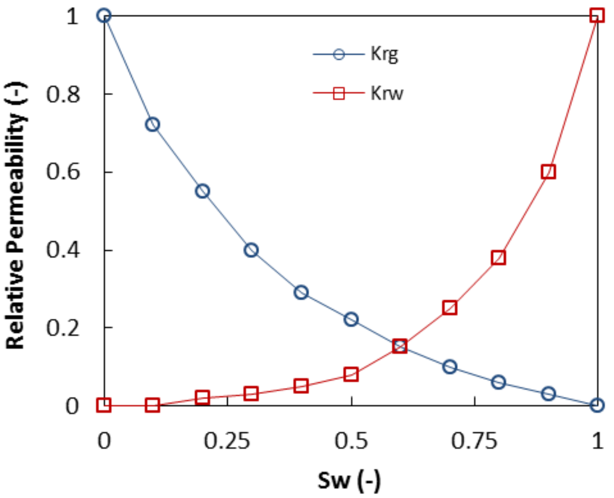

Figure 6.6 Relative permeability of the Fruitland formation coal in New Mexico to gas and water (Gash et al., 1992) used in this study

6.8. Results and discussion

6.8.1. Syngas production and cavity growth

The model was run only for 10 days of the process. Longer process time on a larger model is presented in Chapter 7. The injection point was retracted two times and because of that, three small cavities were formed. Gas species flow rates for the entire period of the process are shown in Figure 6.7. There are discrepancies in the literature with regards to injection fluid mix, temperature, pressure, and flow rate. Another important factor in CRIP is the distance between subsequent injection points. Optimum operation of the UCG is a function of the right selection of these factors according to properties of the particular coal, its reservoir pressure and depth, which influences syngas composition and flow rate. The gas composition shown in Figure 6.7 represents only one of the possible ways of operating within the Alberta UCG site and may not be the optimum way and, at this stage, does not intend to match measured field gas composition since the operation details required for this simulation were not available.

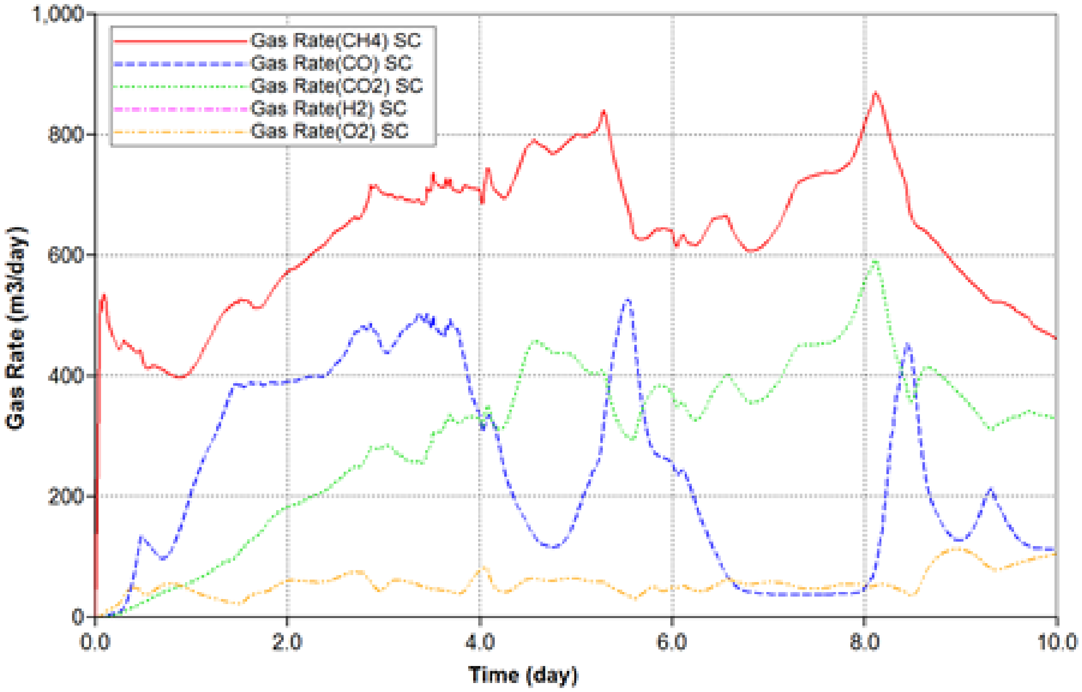

Figure 6.7 Flow rates of different gas species in the produced syngas in the first 10 days of the simulation

As pyrolysis and gasification proceeded, the temperature front expanded to adjacent blocks and hence, reservoir pressure changed. Temperature and pore pressure profiles of the reservoir after 10 days of simulation are shown in Figure 6.8.a and b, respectively. Although bottom-hole pressure for the producer well was set to 10 MPa, because of high temperature of the process and induced pore pressure change, only the area around the producer well was drained and farther from the producer well, pore pressure was about 12 MPa which is above the initial reservoir pressure (11.5 MPa). Based on the common practice in geomechanical simulation, boundaries should be selected far enough (in the order of hundreds of m) where activities of the gasification chamber does not cause any changes to temperature, pore pressure, and stress or displacement. Because of long runtime, only a core from the center of the cubic geometry was selected for gasification simulation; however, models in this range of size are usually considered by chemical engineering scientists working on coal gasification simulations (Nitao et al., 2011; Nourozieh et al., 2010; Seifi et al., 2011).

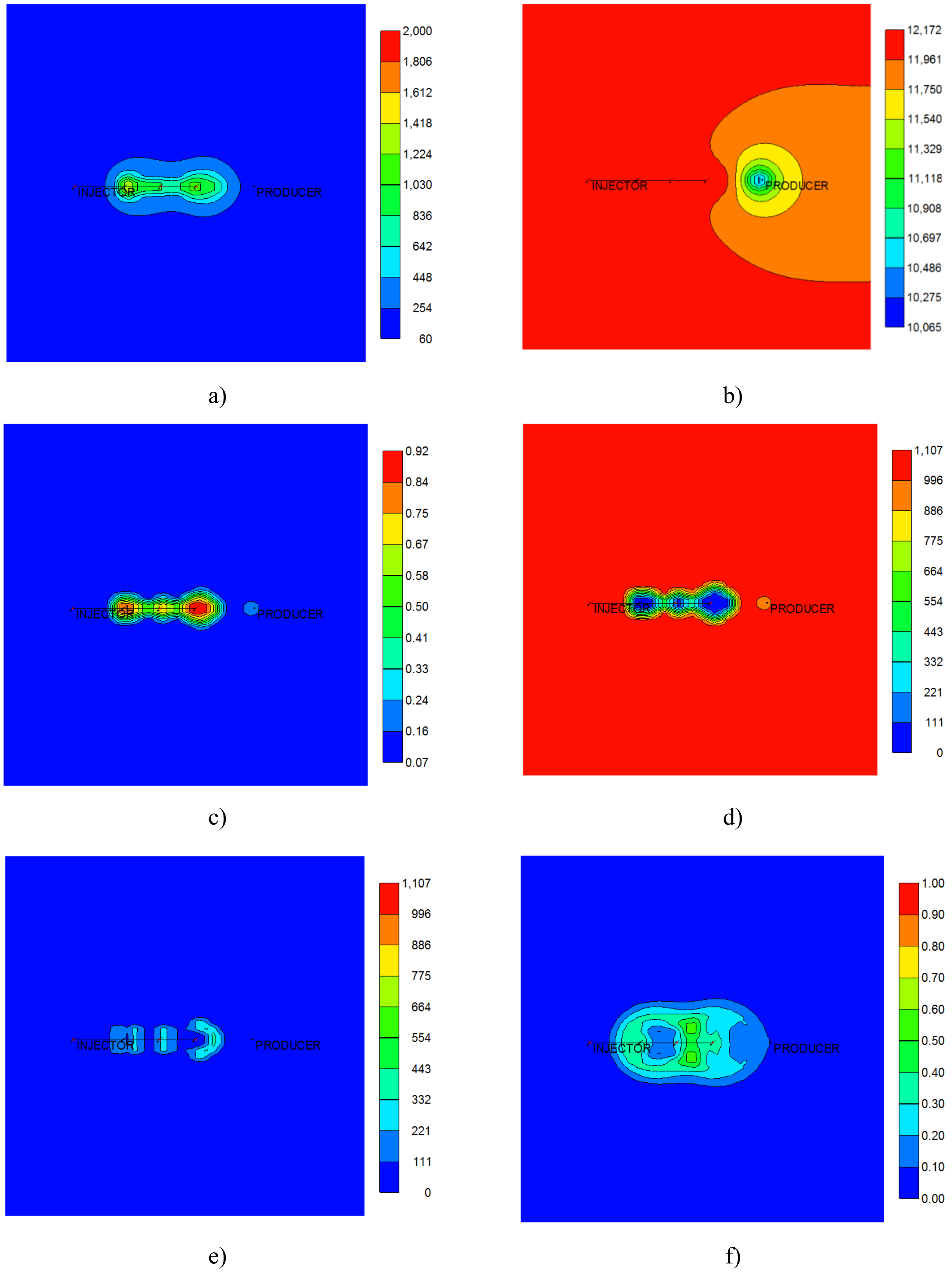

Figure 6.8 Different contours in the horizontal plane containing the injection and production wells after 10 days: a) temperature; b) pore pressure; c) fluid porosity; d) coal concentration; e) char concentration; and f) steam mole fraction

Another important objective of this simulation was to observe cavity growth and send its geometry to the geomechanical simulator every time-step. Comparing fluid porosity of coal, coal and char concentrations in Figure 6.8.c, d, and e, respectively, one can distinguish the cavity zone. A cavity was considered where fluid porosity was in the range of 60-95 % (this assumption was made by Seifi et al., 2011) and initial coal concentration is close to zero. It should be noted that outside the pyrolysis/gasification zone (either in the cavity or in fresh coal regions) char (C) concentration is zero. Based on these criteria, three small cavities can be seen in these plots.

Because of the high temperatures of the process, liquid water, which exists in the pore space, may change phase to steam. Around the gasifier, pore pressure is about 12 MPa for which the steam saturation temperature at this pressure is about 325 ^{o}C (American Society of Mechanical Engineers, 2009). Therefore, beyond the pyrolysis zone, superheated steam and/or compressed water exists. Another possible reason for having steam in this zone is diffusion of a portion of steam from the gasification chamber to surroundings. Farther from the gasifier, liquid water and mixture of other gases occupies coal pore space (Figure 6.8).

6.8.2. Geomechanical changes

Every six hours, temperature, pore pressure and cavity shape was passed to FLAC3D and the model was run to equilibrium. Stress field changed and deformation occurred. Figure 6.9 presents some geomechanical changes which occurred around the cavity in the vertical plane containing the injection and production wells after 10 days. Figure 6.9.a and b show volumetric strain and vertical displacement profiles, respectively. Deformation happened around the cavity and in fact, the coal matrix deformed and moved towards the cavity in all directions. Stress and strain localization is seen around the corners of the bigger cavity. Although the cavity is very small after 10 days, it is clear that at a later time in the process, the area around the cavity would undergo large deformations such that the coal porosity and permeability would be altered. This porosity and permeability alteration needs to be considered in updating coal porosity and permeability for gasification modeling in a fully and two-way coupled simulations. Contours of minimum principal stress (compressive stress is shown as negative) and shear stress are shown in Figure 6.9.c and d, respectively. As depicted in these figures, minimum principal stress and shear stress increased around the cavity and even influenced caprock and underburden rock layers.

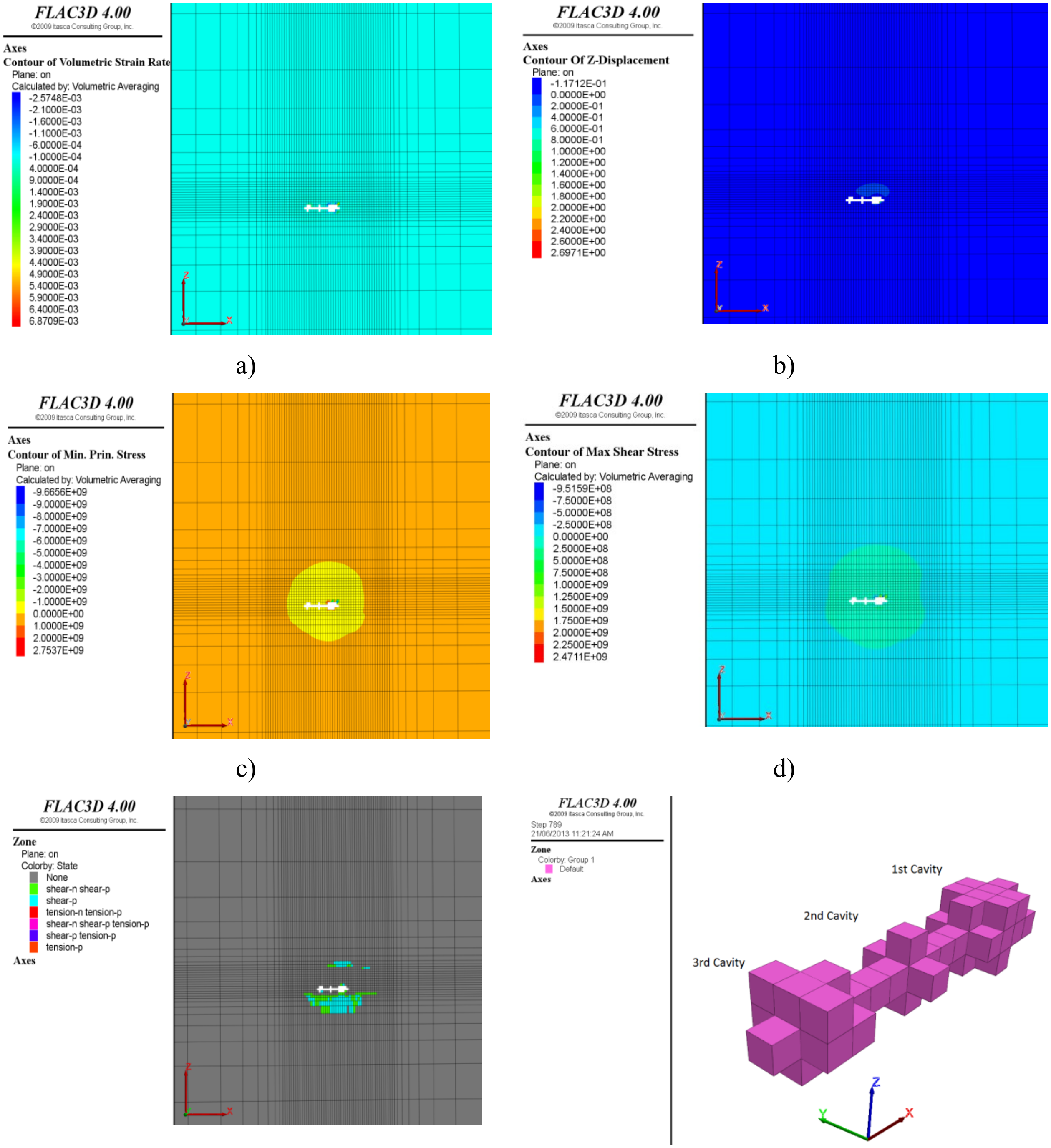

a)

b)

c)

d)

e)

f)

Figure 6.9 Geomechanical changes in the model at vertical plane the of injection and production wells after 10 days: a) volumetric strain; b) vertical displacement (m); c) minimum total principal stress (Pa); d) shear stress (Pa); e) failure state; and f) 3D geometry of cavities

The amount of changes at the cavity boundary was significant. As a consequence of the induced stress and deformation by UCG, some area around the cavity and even caprock and underburden rock mechanically failed which is shown in Figure 6.9.e. Colors except gray in this figure represent the failed zones. Since the injection points were set close to the bottom of the coal seam, high temperature concentration is closer to the underburden rock than the caprock hence, more failure happened in the underburden rock than the caprock. It is important to keep in mind that this condition may change (more failure may happen in caprock) if someone runs the simulation for a longer period (months or years) and creates a larger cavity. In the latter case, stress induced by element removal might be greater in caprock than underburden rock. Also included in Figure 6.9.f is the 3D geometry of the cavity at this time which its x-z view is seen in other sub-figures of Figure 6.9.

One way of tracking changes in any particular point in the coal reservoir is the history of changes over time. History plots of temperature, pore pressure, mean effective stress, and volumetric strain for the three monitoring points are presented in Figure 6.10. Point C is above the first injection point, points B is above the middle point, and point A is above the third injection point. With time, temperature increased at these points while pore pressure slightly oscillated around 12 MPa. Mean effective stress plots showed continuous ascending trends over the period. It was during operation in the second injection point that volumetric strain at all monitoring points dropped slightly to negative values (contraction happened) and during the third cavity evolution, it started to rapidly increase to positive values (expansion happened).

Other factors studied in this simulation were changes in mean effective stress and displacement of the caprock bottom. Mean effective stress profiles at different times at the caprock bottom is shown in Figure 6.11.a (in this figure, compressive stresses shown positive). As seen in Figure 6.11.a, as the process proceeded, mean effective stress increased above the reservoir. Maximum mean effective stress happened above the cavities areas and dropped sharply to the original stress far from the cavities. Figure 6.11.b shows plot of vertical displacement at the interface of caprock and coal seam for different times. Vertical displacement plots showed similar trend to the stress plots. The displacement values were positive which indicates upward movement (heave) at this level. Maximum displacement happened above the cavities.

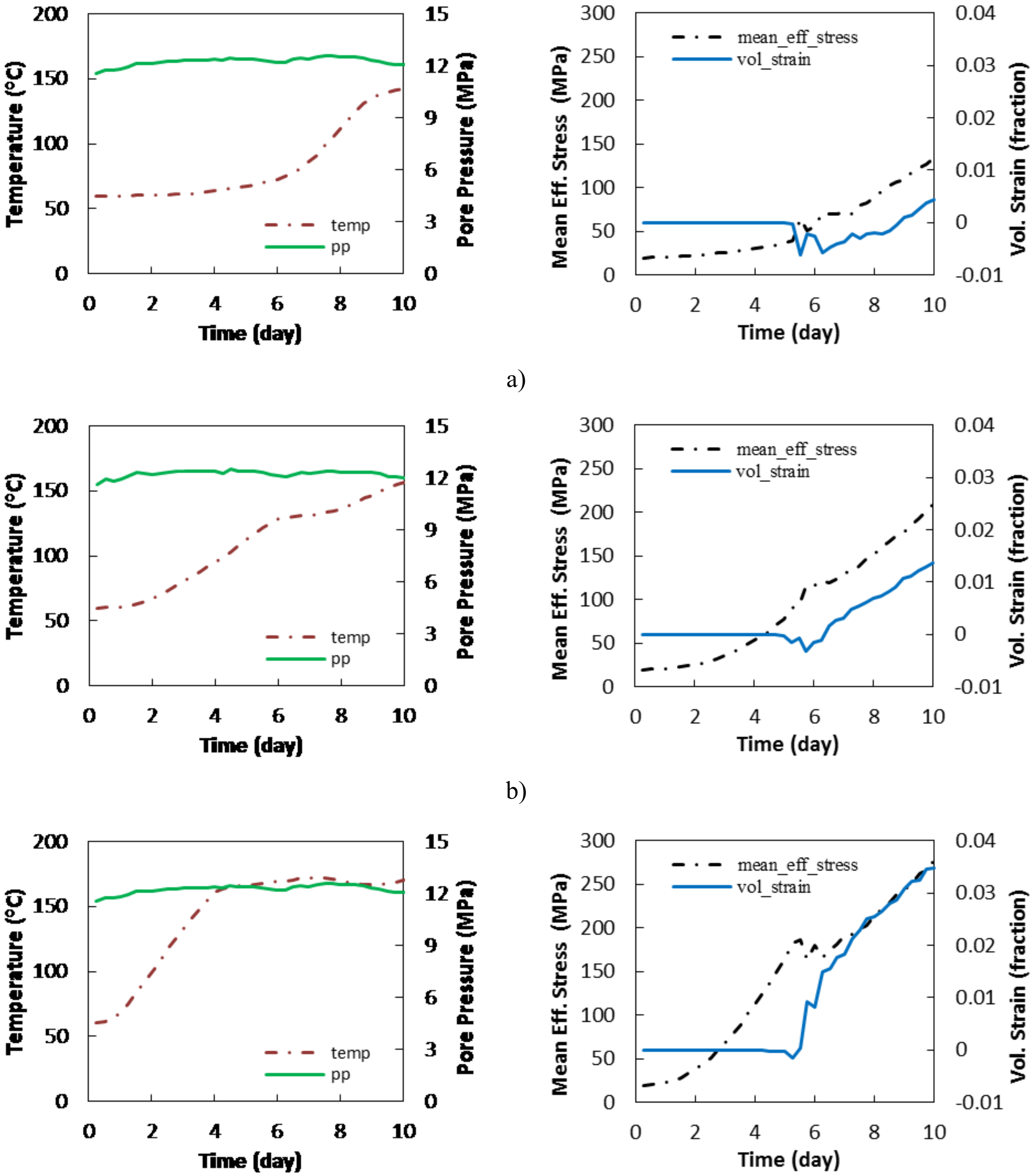

a)

b)

c)

Figure 6.10 History of temperature, pore pressure, mean effective stress and volumetric strain for monitoring points for 10 days of simulation time: a) point A; b) point B; and c) point C

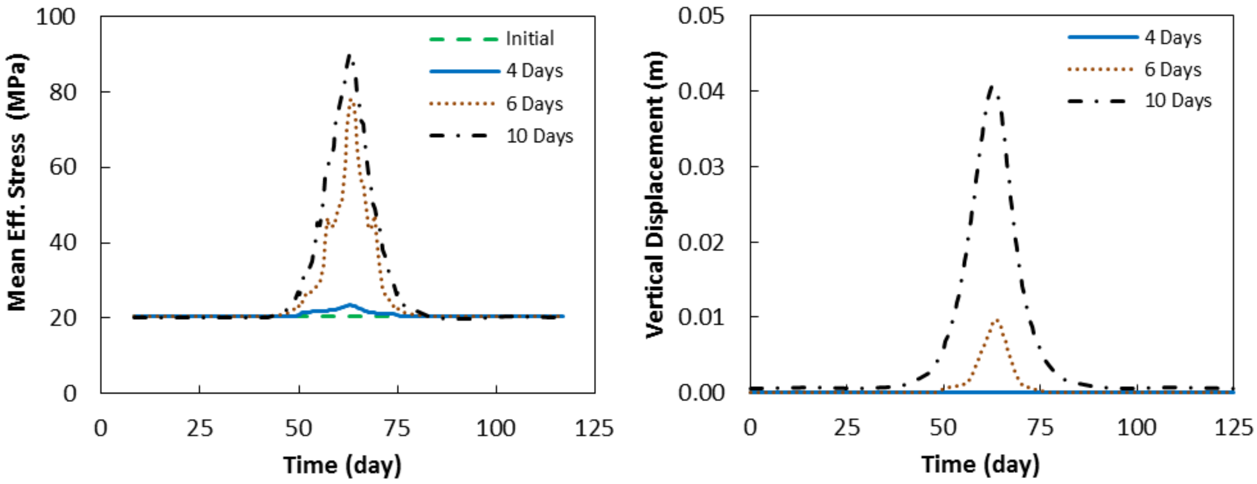

a) b)

Figure 6.11 a) Geomechanical changes at the caprock bottom: a) mean effective stress profile; and b) vertical displacement profile

6.9. Conclusions

Although the underground coal gasification is a promising and cleaner method for extraction of energy from coal seams with minimal greenhouse gas emission, there are several risks associated with its operation. Subsidence of the ground surface in a shallow UCG, uncontrolled collapse of the cavity, and contamination of the groundwater are the geomechanical and environmental risks within a UCG projects. The risks are closely related to the multi-disciplinary nature of the process. To properly address the geomechanical and environmental risks in a UCG project, the gasification mechanism and its interconnection to the geomechanical response of the strata need to be fully understood. This achievement can be made by performing a fully coupled thermal-hydro-chemical-mechanical analyses of any particular UCG site; however, such simulations require a tremendous number of material properties as well as extensive computational power. Sequentially coupled simulations can still provide some insight to the complex response of a UCG project with a reasonable number of material properties as well as an affordable computational power.

In this study, a numerical approach was devised in order to provide a platform to conduct sequentially coupled flow-geomechanical simulation of a UCG project using two commercial simulators. The simulation utilized a correlation between coal permeability and porosity during drying and pyrolysis which was modified in this study based on an existing correlation. The developed sequential coupling package in this study allows simultaneous observation of syngas production, advancement of gasification chamber, and cavity growth. By adopting this simulation strategy, one can set injection mixture composition as well as retraction of injection points (in CRIP method) and observe failure of the coal seam, caprock, and underburden rock, at any time during the process. Utilizing this methodology prior to running any particular UCG site and modeling different operational strategies can help find an optimum operational method without any catastrophic collapse of the gasification chamber which, in turn, minimizes the geomechanical and environmental risks at that particular site.

A 3D example was modeled utilizing the developed sequential coupling algorithm using Alberta coal properties. Based on this example, the following observations and conclusions can be drawn:

- Coal matrix deformed towards the cavity.
- Deformation and additional stress was observed in the caprock and underburden rock.
- Some area around the cavity and in the rock layers failed as a result of cavity evolution and elevated temperature.

6.10. Acknowledgements

The authors would like to thank The Canadian Centre for Clean Coal/Carbon and Mineral Processing Technologies (C^5MPT) for providing financial support for this research. Also contribution by Dr. Ranjender Gupta's research group at the University of Alberta is highly appreciated.

6.11. References

Advani, S. H., Lin, Y. T., & Shuck, L. Z. (1977). Thermal and structural response evaluation for underground coal gasification. *Society of Petroleum Engineers Journal*, *17*(06), 413-422.

Advani, S. H., Shuck, L. Z., Lin, Y. T., & Chang, H. Y. (1976). Thermomechanics simulations associated with underground coal gasification. In *The 17th US Symposium on Rock Mechanics (USRMS)*. American Rock Mechanics Association.

American Society of Mechanical Engineers. (2009). ASME International Steam Tables for Industrial Use. Second Edition, American Society of Mechanical Engineers, New York.

Anthony, D. B., & Howard, J. B. (1976). Coal devolatilization and hydrogastification. *AIChE Journal*, *22*(4), 625-656.

Bartel, L. C., Beard, S. G., Beckham, L. W., Reed, R. P., & Seavey, R. W. (1976). Instrumentation results from an in-situ coal gasification experiment. In *SPE Annual Fall Technical Conference and Exhibition*. Society of Petroleum Engineers.

Burton, E., Friedmann, J., & Upadhye, R. (2006). Best practices in underground coal gasification. Draft. US DOE contract no W-7405-Eng-48. Lawrence Livermore National Laboratory.

Buscheck, T. A., Hao, Y., Morris, J. P., & Burton, E. A. (2009). Thermal-hydrological sensitivity analysis of underground coal gasification. In *Proceedings of the 2009 International Pittsburgh Coal Conference, Pittsburgh, PA, USA* (Vol. 2023).

Computer Modelling Group Ltd. (2012). STARS User's Guide, 2012. Computer Modelling Group, Calgary, Alberta, Canada

Couch, G. R. (2009). Underground coal gasification. IEA Clean Coal Centre. International Energy Agency, London.

Dabbous, M. K., Reznik, A. A., Taber, J. J., & Fulton, P. F. (1974). The permeability of coal to gas and water. *Society of Petroleum Engineers Journal*, *14*(06), 563-572.

Daggupati, S., Mandapati, R. N., Mahajani, S. M., Ganesh, A., Mathur, D. K., Sharma, R. K., & Aghalayam, P. (2010). Laboratory studies on combustion cavity growth in lignite coal blocks in the context of underground coal gasification. *Energy*, *35*(6), 2374-2386.

Fausett, L.V. (1984). An analysis of mathematical models of underground coal gasification. PhD Dissertation, University of Wyoming.

Gash, B. W., Volz, R. F., Potter, G., & Corgan, J. M. (1992). The effects of cleat orientation and confining pressure on cleat porosity, permeability and relative permeability in coal. *Paper presented at the 1992 SCA Conference, paper number 9224.* 1992:1-14.

Glass, R. E. (1984). The thermal and structural properties of a Hanna basin coal. *Journal of Energy Resources Technology*, *106*(2), 266-271.

Itasca Consulting Group Inc. (2009). FLAC3D User's Guide. Itasca Consulting Group Inc., Minneapolis, Minnesota.

Jung, K. S. (1987). Mathematical modeling of cavity growth during underground coal gasification. PhD Dissertation, University of Wyoming.

Kariznovi, M., Nourozieh, H., Abedi, J., & Chen, Z. (2013). Simulation study and kinetic parameter estimation of underground coal gasification in Alberta reservoirs. *Chemical Engineering Research and Design*, *91*(3), 464-476.

Kostur, K., & Kacur, J. (2008). The monitoring and control of underground coal gasification in laboratory conditions. *Acta Montanistica Slovaca*, *13*(1), 111-117.

Luo, X., Tan, Q., Luo, C., & Wang, Z. (2008). Microseismic monitoring of burn front in an underground coal gasification experiment. In *The 42nd US Rock Mechanics Symposium (USRMS)*. American Rock Mechanics Association.

Morris, J. P., Buscheck, T. A., & Hao, Y. (2009). Coupled geomechanical simulations of UCG cavity evolution. In *Proceedings of the 2009 International Pittsburgh Coal Conference, Pittsburgh PA*.

Nitao, J. J., Camp, D. W., Buscheck, T. A., White, J. A., Burton, G. C., Wagoner, J. L., & Chen, M. (2011). Progress on a new integrated 3-D UCG simulator and its initial application. In *International Pittsburgh Coal Conference* (pp. 1-13).

Nourozieh, H., Kariznovi, M., Chen, Z., & Abedi, J. (2010). Simulation study of underground coal gasification in Alberta reservoirs: geological structure and process modeling. *Energy & Fuels*, *24*(6), 3540-3550.

Sansgiry, P. S. (1990). A numerical technique to track the growth of cavities in underground coal gasification. PhD Dissertation, University of Wyoming.

Sarraf Shirazi, A. (2012). CFD simulation of underground coal gasification. MSc Dissertation, University of Alberta.

Seifi, M., Chen, Z., & Abedi, J. (2011). Numerical simulation of underground coal gasification using the CRIP method. *The Canadian Journal of Chemical Engineering*, *89*(6), 1528-1535.

Settari, A., & Walters, D. A. (2001). Advances in coupled geomechanical and reservoir modeling with applications to reservoir compaction. *SPE Journal*, *6*(03), 334-342.

Stanczyk, K., Kapusta, K., Wiatowski, M., Swiadrowski, J., Smolinski, A., Rogut, J., & Kotyrba, A. (2012). Experimental simulation of hard coal underground gasification for hydrogen production. *Fuel*, *91*(1), 40-50.

Swan Hills Synfuels. (2012). Swan Hills in-situ coal gasification technology development; Final outcomes report. Swan Hills Synfuels, Alberta, Canada.

Thorsness, C. B., Grens, E. A., & Sherwood, A. (1978). A one-dimensional model for in situ coal gasification, UCRL-52523, Lawrence Livermore, National Laboratory (LLNL) Report, Berkeley, California.

Vorobiev, O. Y., Morris, J. P., Antoun, T. H., & Friedmann, S. J. (2008). Geomechanical simulations related to UCG activities. In *International Pittsburgh Coal Conference, Pittsburgh, PA*.

World Energy Council, (2010). 2010 survey of energy resources. World Energy Council, London, UK.

Yang, L. (2004). Study on the model experiment and numerical simulation for underground coal gasification. *Fuel*, *83*(4), 573-584.

Zhao, Y., Qu, F., Wan, Z., Zhang, Y., Liang, W., & Meng, Q. (2010). Experimental investigation on correlation between permeability variation and pore structure during coal pyrolysis. *Transport in Porous Media, 82*(2), 401-412.

Chapter 7 Sequentially Coupled Reservoir and Geomechanical Simulation of Underground Coal Gasification in Alberta[1]

7.1. Abstract

Underground Coal Gasification (UCG) is an in-situ technology for extraction of energy from otherwise un-minable coal seams. As coal is gasified, high temperature is generated and cavities are formed. Hence, the UCG imposes significant geomechanical changes to strata. The province of Alberta, Canada recently operated a deep UCG demonstration project, at a depth of 1400 m. The demonstration project successfully produced methane, hydrogen, and other gases. This study aimed at conducting a sequentially coupled coal gasification and geomechanical simulation to study effects of the Alberta UCG on the coal seam and bounding seal system. A mechanical earth model was built for the test site utilizing geological layers reported for the site and under anisotropic in-situ stress magnitudes and orientations, particular to the Western Canadian Sedimentary basin. Ten chemical reactions along with their kinetics were implemented in a reservoir simulator. The Controlled Retraction Injection Point (CRIP) method was studied, in which four gasification chambers were simulated. The product gas compositions, over a period of 60 days, were in good agreement with the syngas composition measured at the demonstration project. By utilizing the coupling workflow, complex three-dimensional (3D) geometry of the UCG cavities as well as temperature and pore pressure, were passed along from the gasification module to a geomechanical simulator. This allowed simultaneous observation of geomechanical response of the strata as the gasification process advanced, syngas produced, and cavities developed.

Keywords Underground Coal Gasification (UCG), Coupled Simulation, Geomechanics, Cavity, Alberta

---

[1] A version of this chapter will be submitted for journal publication as:
Akbarzadeh, H., & Chalaturnyk, R.J. (201x). Coupled reservoir and geomechanical simulation for a deep underground coal gasification project.

7.2. Introduction

Coal is currently the world's second largest source of primary energy (after oil) and accounting for about 40% of global electricity production (World Energy Council, 2013). In the province of Alberta, Canada, coal supplied 52% of the province's electricity in both 2012 and 2013 (Government of Alberta, 2014). The Alberta's coal reserves and resources were estimated at 33.2 and 2000 billion tonnes, respectively (Alberta Energy Regulator, AER, 2014). It is predicted that energy generated by the Alberta' coal resources can be more than three times of the oilsands; however, much of these coal resources are currently un-minable (Richardson and Singh, 2012).

The major concern about coal-fired power plants is greenhouse gas (GHG) emission. The 2035 outlook of Canada's energy future highlights that any coal facilities built after July 1st 2015 should be equipped with carbon capture and storage (CCS) technology in order to be permitted to operate (National Energy Board, 2013). An alternative method for extracting coal energy from Alberta coal seams, with less GHG emissions could be Underground Coal Gasification (UCG). Recently, a UCG demonstration facility was constructed and successfully tested in a deep coal seam (depth of 1400 m) near Swan Hills, Alberta (Swan Hills Synfuels, 2012).

The produced gas in a UCG plant mainly contains H_2, CH_4, CO, CO_2, and small amount of some contaminants. The syngas can be combusted for power generation; liquefied to fuels, separated into methane and hydrogen for petrochemical use (Couch, 2009). A UCG operation generally includes a system of injector and producer wells. There are several operational techniques for the UCG explained elsewhere (e.g., Burton et al., 2006; Couch, 2009). The Controlled Retraction Injection Point (CRIP) method, in particular, is suitable for deep coal seams. In this method, after igniting the coal at a point near a vertical producer well, an oxygen-based mixture is provided downhole via a horizontal in-seam injector well to maintain the gasification process. The injection point is retracted in the upstream direction after some coal has been gasified. During a UCG operation, temperature may increase over 1000 ºC, coal turns into ash, cavities are developed while cavity walls and rock layers may spall into the void areas. On the other hand, groundwater might be contaminated (Burton et al., 2006; Couch, 2009; Sury et al., 2004a; Sury et al., 2004b). Porosity and permeability of coal and rock formations in the disturbed zone are compromised. The later will, in turn, influence the chemical process of coal gasification. In conclusion, the UCG represents a coupled hydro-thermo-chemical-mechanical process. Conducting coupled modeling can help investigate effect of different UCG operational scenarios while minimizing the geomechanical and environmental risks.

Extensive coal gasification simulations of UCG have been conducted to study syngas flow rate and composition, temperature, porosity, permeability, and syngas heating value, etc. In these studies, a series of chemical reactions were implemented in either a Computational Fluid Dynamics (CFD) based software (e.g., Sarraf Shirazi et al., 2013; Zogala and Janoszek, 2015) or a reservoir engineering simulator (e.g., Nourozieh et al., 2010; Seifi et al., 2011). Khan et al. (2015) recently reviewed underground coal gasification modeling works. Several geomechanical models of UCG process have also been published (e.g., Advani et al., 1976 & 1977; Akbarzadeh and Chalaturnyk, 2013; Laouafa et al., 2014; Morris et al., 2009; Tan et al., 2008; Vorobiev et al., 2008). In these works, simplified geometries were usually assumed for the UCG cavities; with or without syngas pressure and temperature. The Lawrence Livermore National Laboratory (LLNL) developed a couplde UCG simulator (Camp et al., 2012; Nitao et al., 2011); however, this package is not commercially available. Akbarzadeh and Chalaturnyk (2016) accomplished a numerical modeling workflow for UCG to couple two commercial software; a gasification simulator to a geomechanical modeller. To date, there has not been any published coupled gasification-geomechanical simulation of the Alberta deep UCG test.

7.3. Scope and objectives

The objective of this study was to investigate potential geomechanical impacts of the Alberta deep UCG by means of performing 3D coupled gasification-geomechanical simulation utilizing publically available information regarding geology of the site, in-situ stresses, and material properties.

7.4. Model descriptions

7.4.1. Geology

The site under study is located in the Western Canadian Sedimentary Basin, WCSB (Figure 7.1), near the town of Swan Hills, Alberta, Canada. A simplified 3D geological model was built for the site based on information reported by Swan Hills Synfuels (2012), a vertical section of which is shown in Figure 7.2.a. Swan Hills Synfuels (2012) stated that during drilling the horizontal injector well, no faults were observed; hence, this study did not consider any fault in the geomechanical simulations. The geological strata, from the ground surface downwards include: 795.5 m of sandstones, siltstones, and shales from the Paskapoo, Scollard, and Wapiti groups; 500 m of the Lea Park and Colorado shales; immediate overburden which is 101.5 m thick; Medicine River coal seam; and underburden rock. The Lea Park and Colorado shales are supposed to be the major caprock which plays reservoir containment role (Swan Hills Synfuels, 2012). The immediate overburden includes 13 m thick Viking sandstone, 8.5 m Joli Fou shale, and 80 m Mannville interbedded layers. The underburden rock belongs to the Mannville interbedded layers which includes sandstones, siltstones, and mudstones. The Medicine River coal seam belongs to the Upper Mannville formation. It exists at a depth of about 1400 m. It is moderately to poorly cleated and is 7.2 to 7.9 m thick. The coal seam contains two claystone partings. The partings share 8 to 19% in total thickness of the coal seam (Swan Hills Synfuels, 2012). This study assumed one single layer of coal with a net thickness of 6 m.

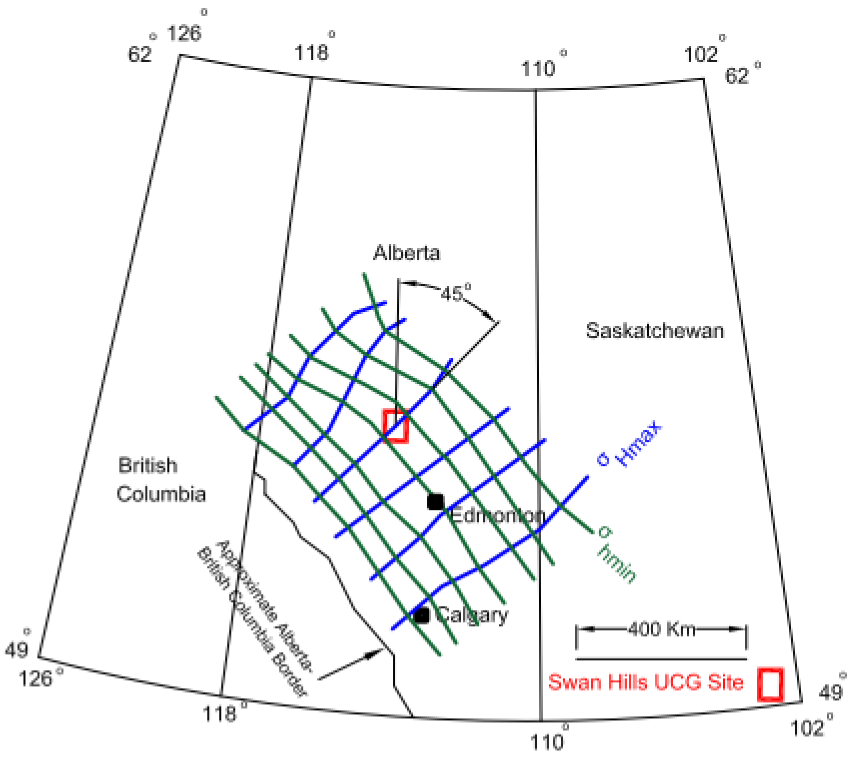

Figure 7.1 In-situ horizontal stress trajectory map of the WCSB (modified from Bell and Grasby, 2012) and placement of the Swan Hills UCG site

*Note: The red symbol which represents the site is not set to the scale of the map.

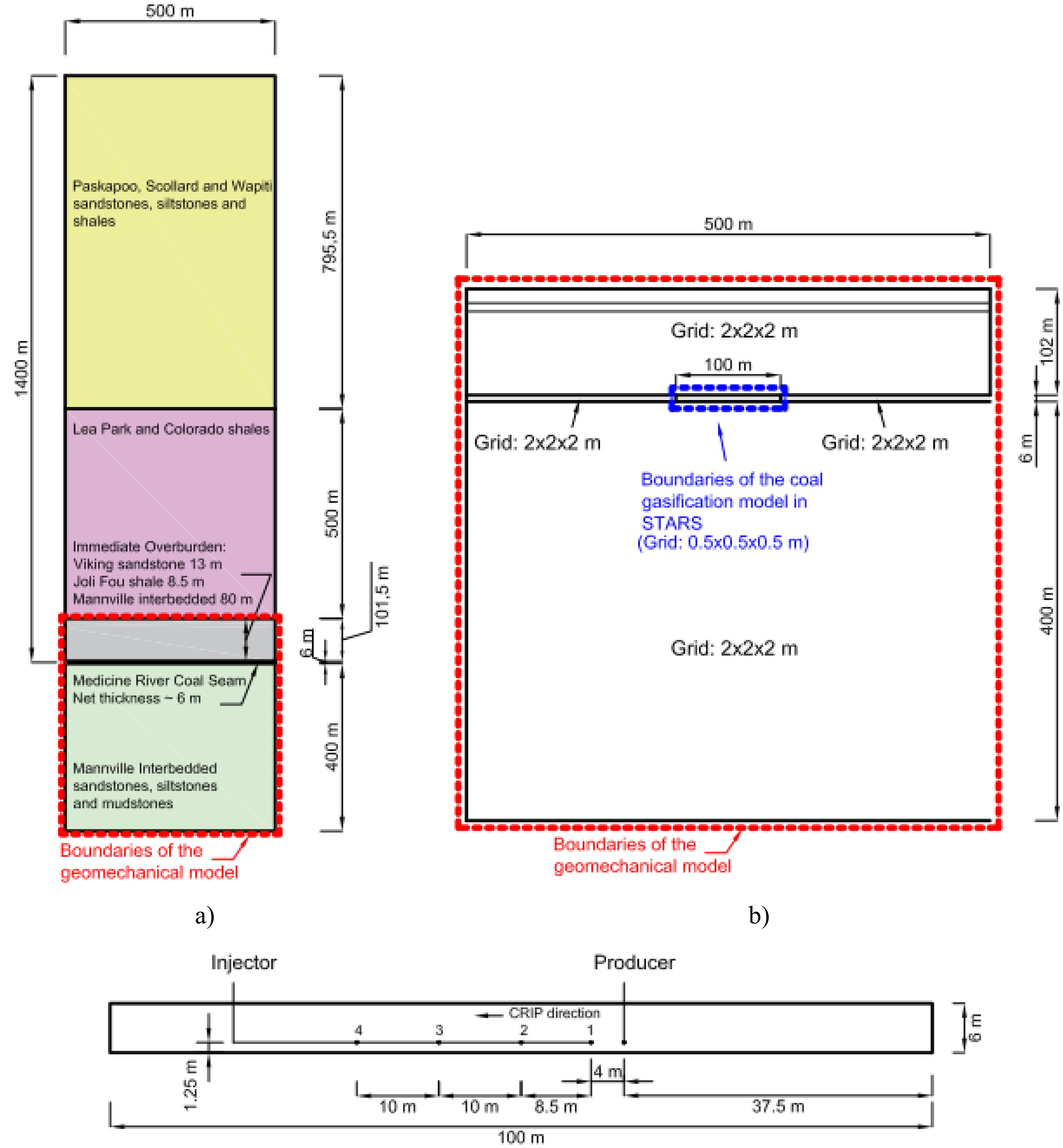

a)

b)

c)

Figure 7.2 a) A simplified geology built for the geomechanical model of the Swan Hills UCG site (modified from Swan Hills Synfuels, 2012); b) geometry and mesh size for the coal gasification and geomechanical models; and c) geometry of the gasification model and details of a single linear CRIP

7.4.2. In-situ stresses

Figure 7.1 also shows placement of the Swan Hills UCG site in regards to σ_{hmin} and σ_{Hmax} stress trajectories of the WCSB. The site is located is the S-N direction with the producer well sitting in the northern part. The injector well is positioned in the southern side and turns to horizontal within the coal seam and extends all the way up to the north, very close to the producer well. If one assumes X-axis in the S-N direction, σ_{Hmax} would be compressional stress acting in the NE-SW direction. Using the same justification, σ_{hmin} would be compressional stress acting in the NW-SE. The other principal stress is overburden stress (σ_{v}) which is vertical.

To define a complete in-situ stress state, principal stresses magnitudes were calculated using a study by Hawkes et al. (2005). As shown in Figure 7.3.a, the UCG site under study is positioned in the region 3 (close to border with the region 8) of the Albert Basin zoning map for the lower bound of σ_{hmin} developed by Hawkes et al. (2005). For the region 3, vertical stress gradient was 23.8 kPa/m. Gradient of σ_{hmin} was interpreted 17.0 kPa/m for depths from 250 to some 750 m and 12.9 kPa/m thereafter to a depth of 3000 m (Figure 7.3.b). Hawkes et al. (2005) interpreted the gradient of 12.9 kPa/m from depleted reservoirs; hence, the actual initial gradient in those regions might be greater than this value. Despite this limitation and because this is the only data available to this research program, it was used in this work. Since there is a normal stress regime in the region, σ_{Hmax} would have a value between σ_{hmin} and σ_{v}. In this study, σ_{Hmax} was assumed equal to the average of σ_{hmin} and σ_{v}.

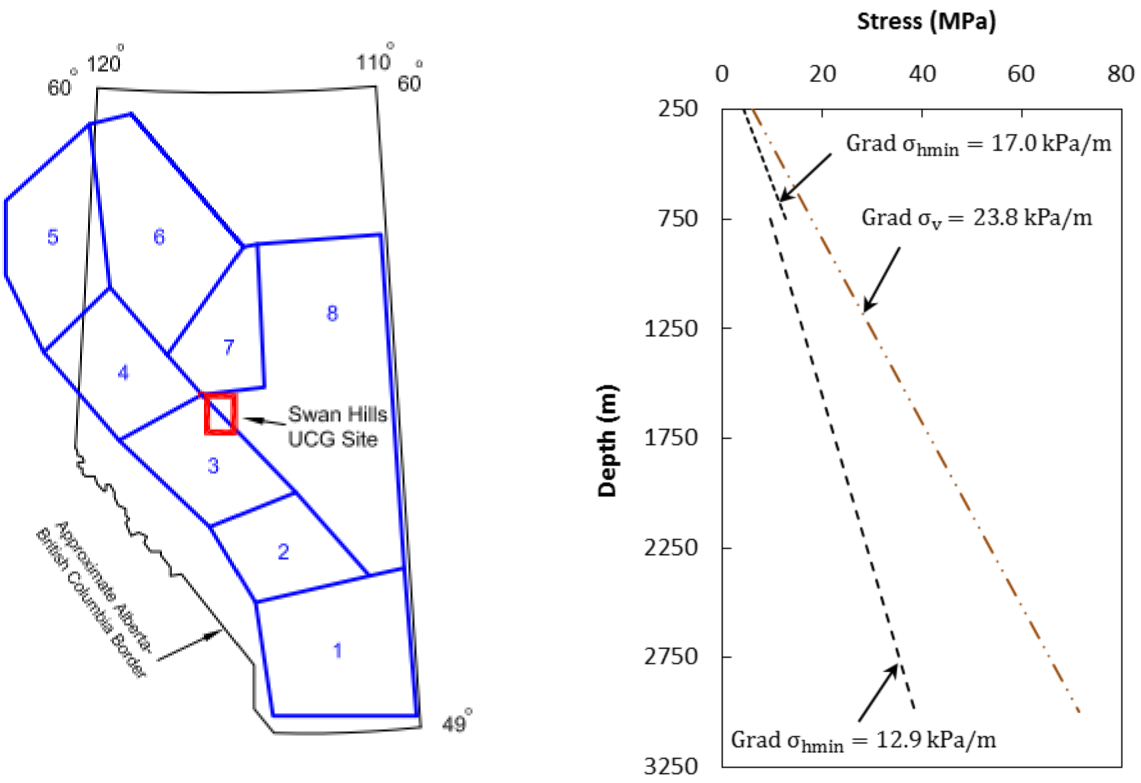

a) b)

Figure 7.3 a) Placement of the Swan Hills UCG site in zone 3 of the Alberta Basin zoning map for lower bound of σ_{hmin} (modified from Hawkes et al., 2005); and b) principal stress gradients for the zone 3

*Note: The red symbol which represents the site is not set to the scale of the map.

7.4.3. Coal gasification modeling

The coal gasification simulation was performed utilizing STARS 2012 (Computer Modelling Group Ltd., 2012).

7.4.3.1. Three-dimensional model

A 3D block with dimension of 100 m × 100 m × 6 m from the central part of the coal seam of Figure 7.2.b was built in STARS. Grid block size for the gasification simulation was selected as 0.5 m × 0.5 m × 0.5 m. This model had 480,000 grid blocks. All boundaries in the model were considered as no-flow boundaries. Figure 7.2.c shows a vertical cross section from the middle of the model width, which includes the injector and producer wells. The producer well was extended from the surface to the third layer from the bottom of the coal seam and perforated at that layer. The injector well was placed at the same plane as the production well and was turned horizontally and extended up to a distance of 4.0 m from the producer well. This location is the first injection point (Figure 7.2.c). To simulate a single linear CRIP process, the injection point was retracted three times in the upstream direction; for 8.5 m, 10 m, and 10 m, respectively (Figure 7.2.c). Injection times at points 1 to 4 were 5 days, 17 days, 15 days, and 23 days, respectively (total time = 60 days). Equal molar mixture of steam and oxygen was selected as the injection agent.

7.4.3.2. Chemical reactions and a porous media approach

Previously, ten chemical reactions and kinetics were calibrated for the Alberta deep UCG project (Kariznovi et al. 2013; Nourozieh et al., 2010). These reactions which are as listed in Table 7.1 were utilized in this study. First order Arrhenius reaction rate (Equation 7.11) was used for all reactions.

$$r_k = \frac{d\xi}{dt} = \varepsilon(\xi^o - \xi) \tag{7.11}$$

where:

$r_k = \frac{d\xi}{dt}$: rate of reaction k,

ξ^o: initial volatile content as a fraction of original coal weight,

ξ: current volatile content as a fraction of original coal weight, and

ε: temperature-dependent rate constant as defined in Equation 7.12.

$$\varepsilon = \varepsilon_o \exp(-\frac{E}{RT}) \tag{7.12}$$

where:

ε_o: reaction frequency factor,

E: activation energy,

R: gas constant, and

T: temperature.

Table 7.1 Chemical reactions and their kinetic parameters for the Alberta UCG (Kariznovi et al. 2013; Nourozieh et al., 2010)

No.	Reaction	Enthalpy (kJ/gmole)	E (kJ/gmole)	ε_o
(7.1)	$\text{Dry Coal} \rightarrow 4.63\text{C} + 0.43\,\text{CO} + 0.12\text{CO}_2 + 0.79\text{CH}_4 + 0.18\text{H}_2$	0	188.28	1.00×10^{11}
(7.2)	$\text{C} + \text{O}_2 \rightarrow \text{CO}_2$	-393	100	2.08×10^{1}
(7.3)	$\text{C} + \text{CO}_2 \rightarrow 2\text{CO}$	+172	249	6.57×10^{6}
(7.4)	$\text{C} + \text{H}_2\text{O} \rightarrow \text{H}_2 + \text{CO}$	+131	156	1.87×10^{4}
(7.5)	$\text{C} + 2\text{H}_2 \rightarrow \text{CH}_4$	-75	200	1.81×10^{3}
(7.6)	$\text{CO} + \frac{1}{2}\text{O}_2 \rightarrow \text{CO}_2$	-283	247	1.12×10^{8}
(7.7)	$\text{CO} + \text{H}_2\text{O} \rightarrow \text{CO}_2 + \text{H}_2$	-41	12.6	1.73×10^{0}
(7.8)	$\text{CO}_2 + \text{H}_2 \rightarrow \text{CO} + \text{H}_2\text{O}$	+41	12.6	4.48×10^{-2}
(7.9)	$\text{CH}_4 + \text{H}_2\text{O} \rightarrow \text{CO} + 3\text{H}_2$	+206	30	3.13×10^{2}
(7.10)	$\text{CO} + 3\text{H}_2 \rightarrow \text{CH}_4 + \text{H}_2\text{O}$	-206	30	4.00×10^{3}

Other researchers (Nourozieh et al., 2010; Seifi et al., 2011) utilized a porous medium approach to simulate coal gasification in STARS. The same methodology was implemented in this study. In this approach, the organic part of coal was assigned as initial solid concentration in pore space. Ratio of void volume (combined volume of water, gas, solid) to gross volume of a grid block is defined as void porosity ($\emptyset_\text{v}$). Void porosity varies if pore pressure and/or temperature in the block change, as defined by Equation 7.13 (Computer Modelling Group Ltd., 2012).

$$\emptyset_v = \emptyset_0\,[1 + a(p - p_0) - \beta_t(T - T_0)] \tag{7.13}$$

where:

$\emptyset_0$: void porosity at initial pressure and temperature,

a: coal compressibility,

p_0, p: initial and current pore pressure, respectively,

β: volumetric thermal expansion coefficient of coal, and

T_0, T: initial and current temperature.

Fluid porosity ($\emptyset_f$) is equal to the ratio of fluid volume (water, gas) to gross volume of the block. It is function of both the void porosity and solid concentration in the void space as defined by Equation 7.14 (Computer Modelling Group Ltd., 2012). Fluid porosity changes during heating, pyrolysis, gasification, and or combustion. This could occur as a consequence of a physical phenomenon (temperature and/or pore pressure change) that alters void porosity. It could also be a result of reduction of solid concentration in void space that happens during pyrolysis, gasification, and combustion. The resultant value of fluid porosity is calculated using Equation 7.14.

$$\emptyset_f = \emptyset_v \left(1 - \frac{C_s}{\rho_s}\right) \tag{7.14}$$

where:

C_s: mole concentration of solid component in void space, and

ρ_s: molar density of solid component.

7.4.3.3. Governing equations

Mass conservation equations for each flowing/solid components as well as energy conservation equation were solved for any grid block in STARS using the Finite Difference Method. Heat transfer was done in the form of heat conduction and convection. Darcy's law was used for convective gas flow. Any effects of adsorption/diffusion as well as water influx to/from adjacent formations were neglected in this study. No heat loss to/from adjacent formations to the model domain was also considered.

The mass conservation equation for flowing components in a grid block with volume V has the form of Equation 7.15 (Computer Modelling Group Ltd., 2012). The left side of this equation represents the rate of change of accumulation of flowing components; however, the right side is a summation of rate of inflow from adjacent regions and rate of addition from source/sink terms. The first term on the right side of this equation accounts for convective flow. Mass transfer by chemical reactions is denoted by the second term. The last term on the right side represents injection/production of water/gas by wells.

$$V\frac{\partial}{\partial t}\left[\emptyset_f\left(\rho_w S_w w_i + \rho_g S_g y_i\right)\right] =$$
$$\sum_{k=1}^{n_f}\left[T_w \rho_w w_i \Delta\Phi_w + T_g \rho_g y_i \Delta\Phi_g\right] + V\sum_{k=1}^{n_r}(s'_{ki} - s_{ki})r_k + (\rho_w q_{wk} w_i + \rho_g q_{gk} y_i) \qquad (7.15)$$

where:

ρ_w, ρ_g: water and gas density, respectively,

S_w, S_g: water and gas saturation, respectively,

w_i, y_i: mole fraction of water and gas, respectively,

n_f: number of neighboring regions or grid block faces,

n_r: number of reactions,

T_w, T_g: transmissibility of water and gas, respectively, as in Equation 7.16

$\Delta\Phi_w, \Delta\Phi_g$: fluid potential difference for water and gas, respectively,

s_{ki}, s'_{ki}: reactant and product stoichiometric coefficients of component *i* in reaction *k*, respectively,

r_k: rate of reaction *k*, and

q_{wk}, q_{gk}: injection/production flow rate of water and gas, respectively, in layer *k* of well.

$$T = (A/\Delta l)(k/\mu) \qquad (7.16)$$

where:

A: cross sectional area,
Δl: distance between neighboring nodes,
k: effective permeability (to water/gas), and
μ: viscosity of water/gas.

Equation 7.17 defines the mass conservation equation for solid components in a grid block with volume V (Computer Modelling Group Ltd., 2012). The left side of the equation represents an accumulation term for solid components whereas the right side accounts for mass transfer caused by chemical reactions. In our modeling, the solid components included initial coal (Dry Coal) and char which was assumed to be pure carbon (C), as in Table 7.1.

$$V \frac{\partial}{\partial t}[\emptyset_v C_i] = V \sum_{k=1}^{n_r} (s'_{ki} - s_{ki}) r_k \tag{7.17}$$

where C_i is mole concentration of solid component *i* in void space.

The energy conservation equation could be simplified as shown in Equation 7.18 (Computer Modelling Group Ltd., 2012). The left side refers to rate of change of accumulation term for energy. The first and second terms on the right side define energy transfer by convection and conduction, respectively. Well source/sink term for energy is the third term. The fourth term describes the reaction source/sink term for energy.

$$\begin{aligned} V \frac{\partial}{\partial t}\left[\emptyset_f\left(\rho_w S_w U_w + \rho_g S_g U_g\right) + \emptyset_v c_s U_s + (1 - \emptyset_v) U_r\right] = \\ \sum_{k=1}^{n_f}\left[T_w \rho_w H_w \Delta\Phi_w + T_g \rho_g H_g \Delta\Phi_g\right] + \sum_{k=1}^{n_f} K_T \Delta T + \left(\rho_w q_{wk} H_w + \rho_g q_{gk} H_g\right) + \\ V \sum_{k=1}^{n_r} H_{rk} r_k \end{aligned} \tag{7.18}$$

where:
U_w, U_g: internal energy of water and gas, respectively,
U_s, U_r: internal energy of solid component and rock (inorganic or ash), respectively,
H_w, H_g: enthalpy of water and gas, respectively,

K: thermal conductivity,

ΔT: temperature change, and

H_{rk}: enthalpy of reaction k.

7.4.3.4. Material properties

The coal rank is high volatile B bituminous which contains 55.6% fixed carbon, 30.4% volatile matter, 9.2% ash, and 4.8% moisture (Kariznovi et al. 2013; Nourozieh et al. 2010; Swan Hills Synfuels, 2012). Initial material properties are summarized in Table 7.2. Except gas heat capacities, other thermal properties were selected constant (see Chapter 6). No gas-water relative permeability was available for the coal under study; hence, experimental data by Gash et al. (1992) was used (Figure 7.4).

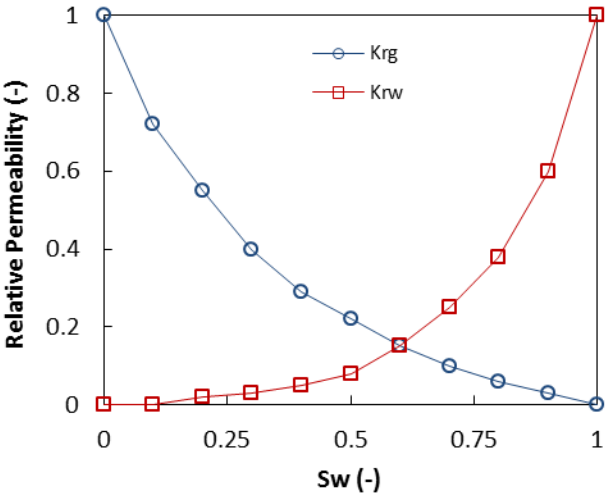

Figure 7.4 Relative permeability of the Fruitland formation coal of New Mexico to gas and water (Gash et al., 1992)

Table 7.2 Initial properties for the gasification model (Kariznovi et al. 2013; Nourozieh et al. 2010; Seifi et al., 2011)

Parameter	Value
Void porosity (fraction)	0.95
Fluid porosity (fraction)	0.0866
Absolute permeability (mD)	1
Pressure (MPa)	11.5
Temperature (°C)	60
Water saturation (fraction)	0.7
Gas saturation (fraction)	0.3
Initial fluid (-)	CH_4
Coal density (kg/m^3)	1200
Char density (kg/m^3)	1740
Rock volumetric heat capacity (J/m^3. °C)	3.0×10^6
Rock thermal conductivity (J/m.day.°C)	2.0×10^5
Char heat capacity (J/gmole.°C)	17
Coal heat capacity (J/gmole.°C)	17
Solid thermal conductivity (J/m.day.°C)	4.5×10^5
Gas thermal conductivity (J/m.day.°C)	4000
Water thermal conductivity (J/m.day.°C)	48384
Water/steam densities, viscosities and enthalpies (-)	STARS defaults

7.4.4. Geomechanical modeling

The 3D model of Figure 7.2.b was simulated in FLAC3D (Itasca Consulting Group Inc., 2009).

7.4.4.1. Three-dimensional model

The model dimensions in both x and y directions were 500 m. The model included 400 m underburden, coal seam, and 102 m (instead of 101.5 m, for the purpose of simplicity) of the immediate overburden. The common part between STARS and FLAC3D had a grid dimension of $0.5\text{ m} \times 0.5\text{ m} \times 0.5\text{ m}$ which included 480,000 grid blocks. The rest of the geomechanical model had a grid dimension of $2\text{ m} \times 2\text{ m} \times 2\text{ m}$. The entire geomechanical model included

16,347,500 grid blocks. Geomechanical constraints in the model were such that the bottom face was fixed against z-direction movements, the sides and the top faces of the model were assigned stress boundaries.

7.4.4.2. Governing equations

The momentum balance law was solved in FLAC3D together with the compatibility equation and a constitutive law in order to calculate stress/deformation and to assess mechanical failure of the strata. During a time-step, incremental stress rate derived from the momentum balance equation and incremental strain rate was governed by an elasto-plastic constitutive law.

The momentum balance law (equation of motion) in FLAC3D has the form of Equation 7.19 (Itasca Consulting Group Inc., 2009). In the case of static equilibrium of the medium, the acceleration term ($\frac{\partial \mathrm{v_i}}{\partial \mathrm{t}}$) is zero and the momentum balance law reduces to the partial differential equations of equilibrium.

$$\sigma_{ij,j} + \rho b_i = \rho \frac{dv_i}{dt} \tag{7.19}$$

where:

$\sigma_{ij,j}$: divergence of stress tensor,

ρ: density of medium,

b_i: body force per unit mass, and

$\frac{dv_i}{dt}$: material derivative of velocity (v).

The compatibility equation relates strain rate and velocity gradient for a continuum. If particles of the medium under study move with velocity (v), components of the strain rate tensor (ξ_{ij}) occurred during an infinitesimal time dt is determined by Equation 7.20 (Itasca Consulting Group Inc., 2009).

$$\xi_{ij} = \frac{1}{2}(v_{i,j} + v_{j,i}) \tag{7.20}$$

The constitutive laws in FLAC3D are generally given in the form of Equation 7.21 (Itasca Consulting Group Inc., 2009). This study utilized the Mohr-Coulomb elastic-perfectly-plastic constitutive law.

$$\sigma_{ij} + \alpha \frac{\partial P}{\partial t} \delta_{ij} = H_{ij}(\sigma_{ij}, \xi_{ij} - {\xi_{ij}}^{T}, \kappa) \tag{7.21}$$

where:

σ_{ij}: stress rate tensor,

α: Biot's coefficient,

P: pore pressure,

δ_{ij}: Kronecker delta,

H_{ij}: given material function,

${\xi_{ij}}^{T}$: thermal strain rate tensor, as in Equation 7.22, and

κ: a parameter that is function of history of loading.

$${\xi_{ij}}^{T} = \alpha_t \frac{\partial T}{\partial t} \delta_{ij} \tag{7.22}$$

where:

α_t: linear thermal expansion coefficient, and

T: temperature.

Note that pore pressure and temperature terms in Equation 7.21 were imported form STARS into FLAC3D for particular time-steps by means of a coupling interface. After updating temperature, pore pressure, and cavity geometry, the model was brought to static equilibrium. This altered stress and displacement fields in the geomechanical model.

7.4.4.3. Material properties

The geomechanical properties of different layers used in this work are summarized in Table 7.3. For rock layers, the properties were taken from other studies in the region (e.g., Nygaard, 2010) which included the same formation, at a depth close to that of the Swan Hills UCG site. Coal properties were taken from Gentzis (2009) and Gentzis et al. (2008). Cohesion and friction angle for the coal was calculated based on the experiments presented in Chapter 4. Permeability of the Mannville coal from several other locations in Alberta was studied by Gentzis et al. (2008) which showed that the Mannville coal has a permeability of less than one millidarcy (mD) at a depth similar to that of the Swan Hills site. In another study, Gentzis (2009) reviewed and analyzed geomechanical properties of the Mannville coal from several locations in Alberta. From one of the wells that he studied, the Mannville coal was at a depth of about 1370 m and had a Young's modulus of 1330 MPa to 4320 MPa with a mean value of 2100 MPa; hence, this average value was selected for the coal in this study. All the aforementioned material properties were taken as temperature-independent. The reason for that was the universal lack of a temperature-dependent constitutive model for coal.

Table 7.3 Geomechanical properties of different formations

Parameter	Viking sandstone	Joli Fou shale	Mannville interbedded layers	Coal seam
Elastic modulus (MPa)	12200	8500	10700	2100
Poisson's ratio (-)	0.25	0.30	0.30	0.22
Cohesion (MPa)	10.1	8.5	10.1	7.8 [a]
Friction angle (Deg.)	39	20	39	30.9 [a]
Tensile strength (MPa)	3.3	2.8	3.3	13.0 [b]
Biot's coefficient (-)	1	1	1	1
Linear thermal expansion coefficient (1/°C)	15×10^{-6} [c]	15×10^{-6} [c]	15×10^{-6} [c]	9×10^{-6} [c]
Reference	(Nygaard, 2010)	(Nygaard, 2010)	(Nygaard, 2010)	Gentzis (2009)

[a] From the experimental data presented in Chapter 4
[b] Calculated: cohesion/ tan(friction angle)
[c] Assumed

7.4.5. Sequential gasification and geomechanical coupling approach in UCG

The current study utilized a sequential coupling workflow of Figure 7.5 that was developed by Akbarzadeh and Chalaturnyk (2016). They integrated the coal gasification capability of STARS 2012 with geomechanical modeling in FLAC3D 4.00. Based on their work, two levels of coupling can be considered for the UCG. Level one is done for each sub-time step within STARS which includes updating permeability as a function of porosity. At a time step, which is greater than the internal sub-time step in STARS, temperature and pore pressure as well as geometry of the cavities are sent to FLAC3D. The level two updates permeability and fluid porosity as functions of deformation and/or stress changes computed by FLAC3D.

Ideally, a set of experimental data was needed to correlate permeability of the coal under study to its porosity; at gasification temperatures (level one). Another set of experimental data was required to correlate permeability/porosity of the coal to geomechanical deformations/stresses (level two). No such experimental data was available for the Alberta coal; neither for the level one, nor for the level two. Equation 7.23 which was reported by Akbarzadeh and Chalaturnyk (2014) was utilized for the level one coupling in current study. The level two coupling was not conducted herein.

$$\frac{K}{K_0} = e^{16.7\,(\emptyset-\emptyset_0)} \tag{7.23}$$

where K_0 and $\emptyset_0$ are initial permeability and fluid porosity of coal; K and $\emptyset$ are permeability and fluid porosity of coal after the thermo-chemical changes.

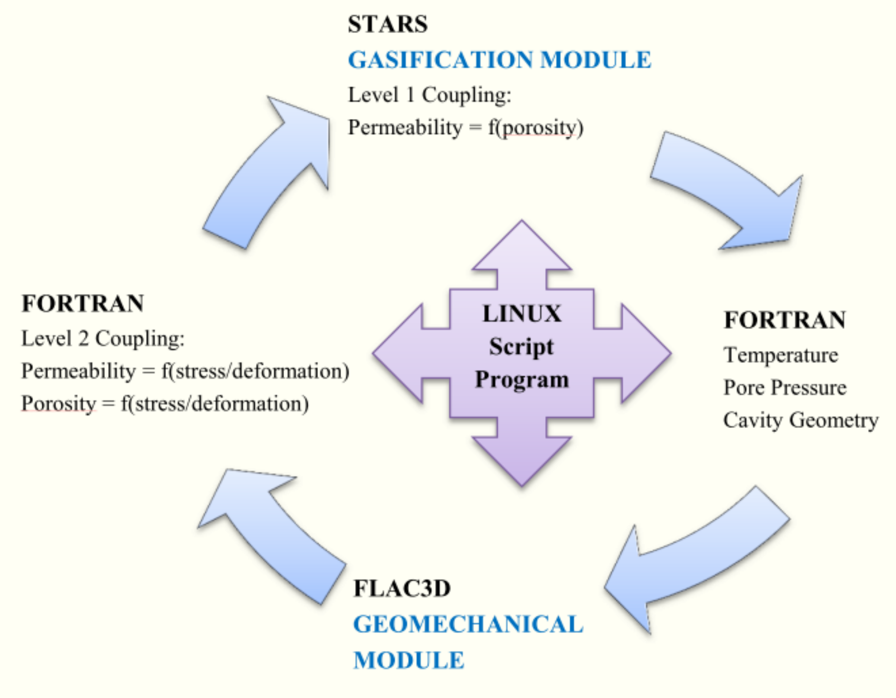

Figure 7.5 A workflow for coupled modeling of the UCG (Akbarzadeh and Chalaturnyk, 2016)

7.5. Simulation results and discussion

7.5.1. Syngas production and cavity growth

The gasification model was run for 60 days, injecting at four different points to represent the linear CRIP process. Total syngas and its species flow rates (corresponding to a standard condition) are presented in Figure 7.6.a. Four humps are observed in this figure which indicates four CRIP scenarios. Syngas flow rate steadily increased as the UCG proceeded. Cumulative gas volumes are depicted in Figure 7.6.b. Over the 60-day process time, this simulation produced 42.5% CH_4, 36.1% CO_2, 11.6% H_2, 4.9% O_2, 4.5% CO, and 0.4% H_2O. This gas composition is very close to the field measurements by Swan Hills Synfuels (2012) reported in Table 7.4. Nonetheless, it is not reasonable to compare the syngas flow rate of this study with the pilot test flow rate, if any available, since the flow rate is function of the model size as well as operational factors (e.g., injection pressure and temperature, CRIP schedule, and so on).

Figure 7.7.a represents temperature profiles along the length of the reservoir in the horizontal plane of the wellbores; initial temperature as well as temperature profiles in the end of each CRIP. The CRIPs were performed in the upstream direction, hence, the temperature profiles moved towards the left in Figure 7.7.a.

Table 7.4 Syngas compositions from this study vs. field measurements by the Swan Hills Synfuels (2012)

Cumulative gas (%) in 60 days	CH_4	CO_2	H_2	O_2	CO	H_2O	C_2^+
This study	42.5	36.1	11.6	4.9	4.5	0.4	-
Swan Hills Synfuels (2012)	37	41	15	-	5	-	2

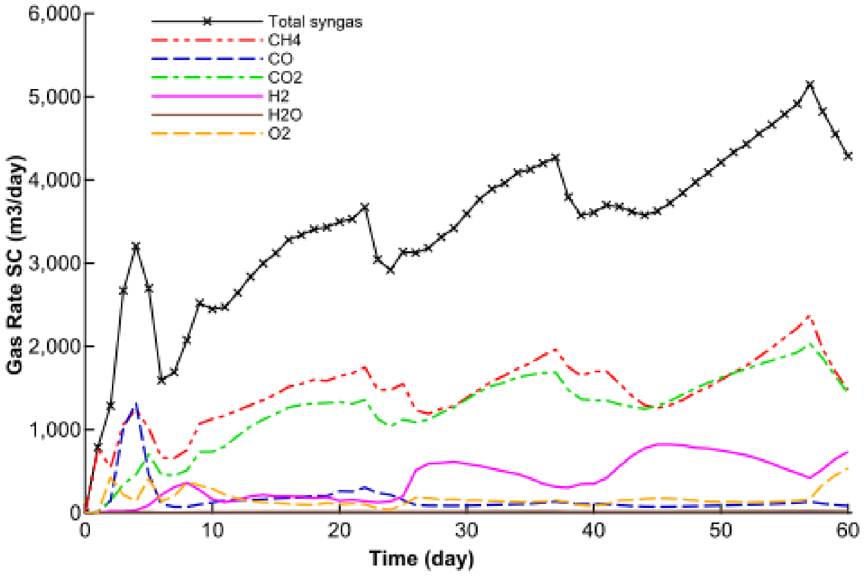

a)

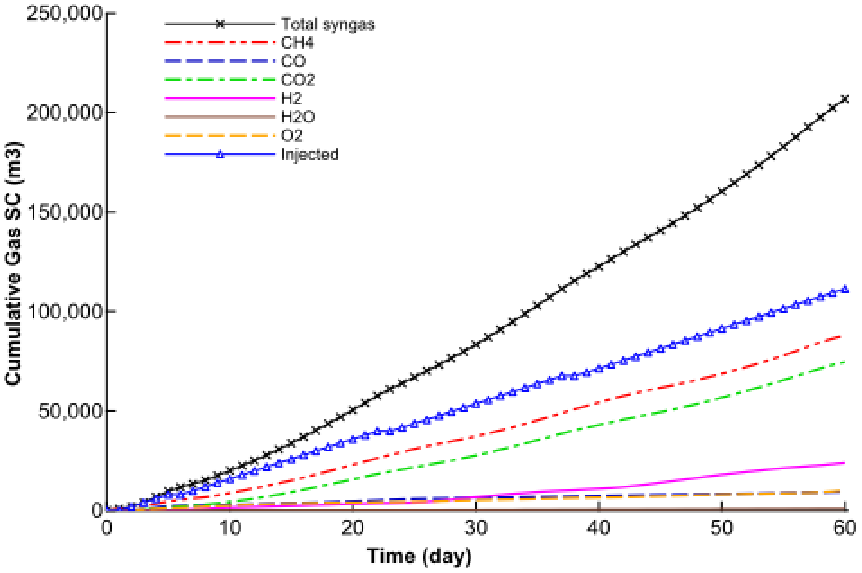

b)

Figure 7.6 Syngas composition over a 60-day period: a) syngas and species flow rates; and b) cumulative production of syngas and species as well as cumulative injected gas

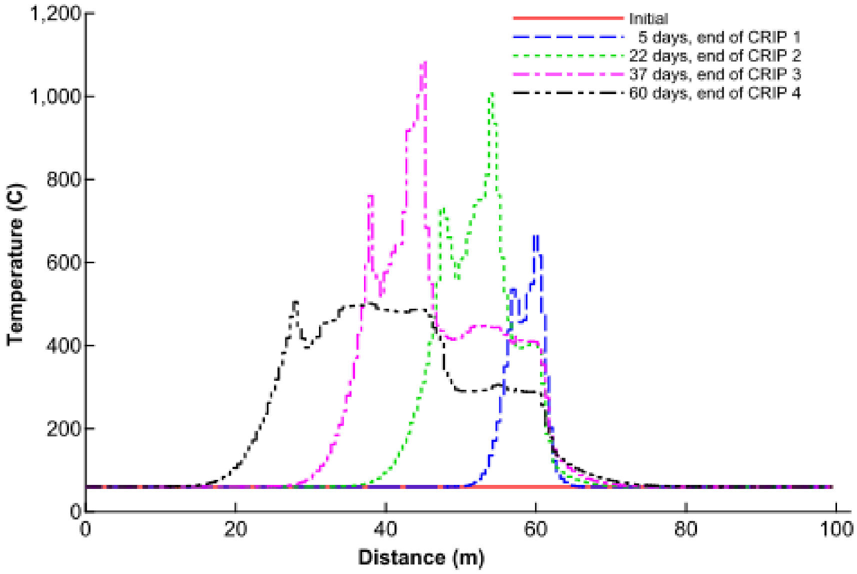

a)

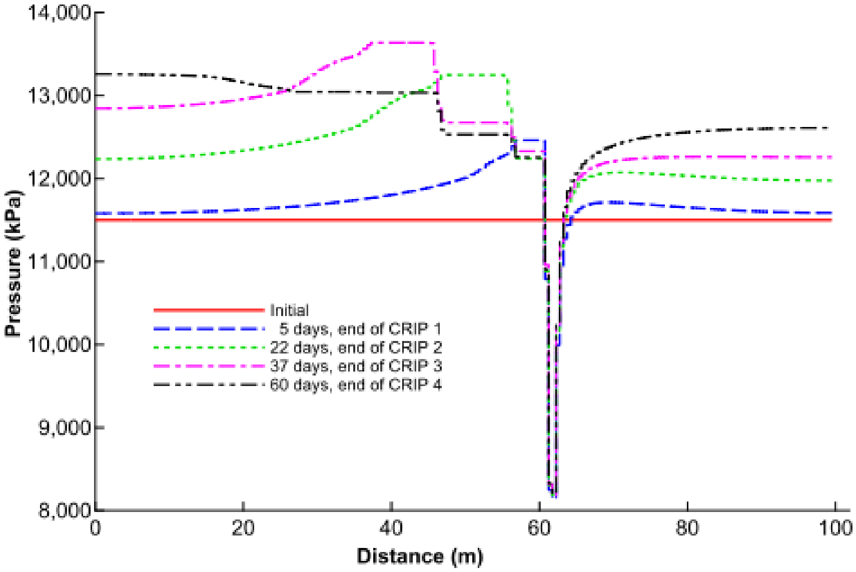

b)

Figure 7.7 a) Temperature; and b) pore pressure variations in a horizontal plane including the injection points and tip of the producer well

At the same time, pore pressure started to build up in the reservoir (Figure 7.7.b). Unlike temperature, pore pressure affected a much larger area around any injection point. By the end of the 2nd CRIP, pore pressure rise was already observed in the entire reservoir length. Figure 7.8 also confirms the same observation on a horizontal plane containing the wellbores. The conclusion is that to have the far pressure boundaries not affected by the UCG activities, they need to be set much farther. Such a model would require a huge computational power. This is what reservoir/chemical engineering researchers studying the UCG would need to resolve to get more reliable results from larger models, once computational power is no longer an issue. Published literature dealt with models with relatively small geometries along with fine meshes (e.g., Camp et al., 2012; Nourozieh et al., 2010; Seifi et al., 2011; Zogala and Janoszek, 2015). In the current study, the model dimensions in X and Y directions were selected 100 meters, having a 0.5 meter mesh dimension in all directions. Despite having 480,000 grid blocks, boundaries of the model were still affected by the pore pressure build up.

Figure 7.9 shows how concentrations of different gas species changed as coal gasification/combustion proceeded. Initially, methane existed in the coal seam which, after 60 days, CH_4 concentration in vicinity of the gasification chambers dropped whereas other species formed. Gas permeation to the un-gasified coal occurred which resulted in spread of other species to regions farther than those the temperature front advanced to.

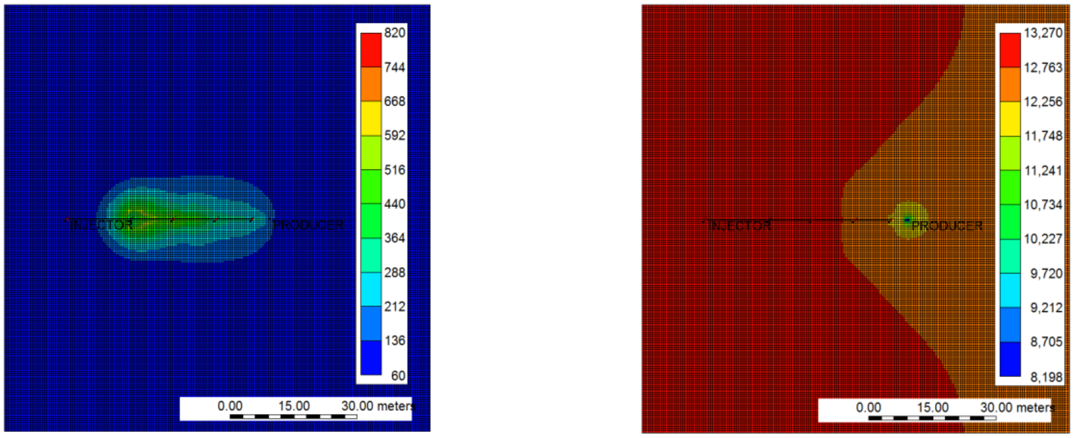

a)

b)

Figure 7.8 a) Temperature (°C); and b) pore pressure contours (kPa) after 60 days in a horizontal plane including the injector and producer wells

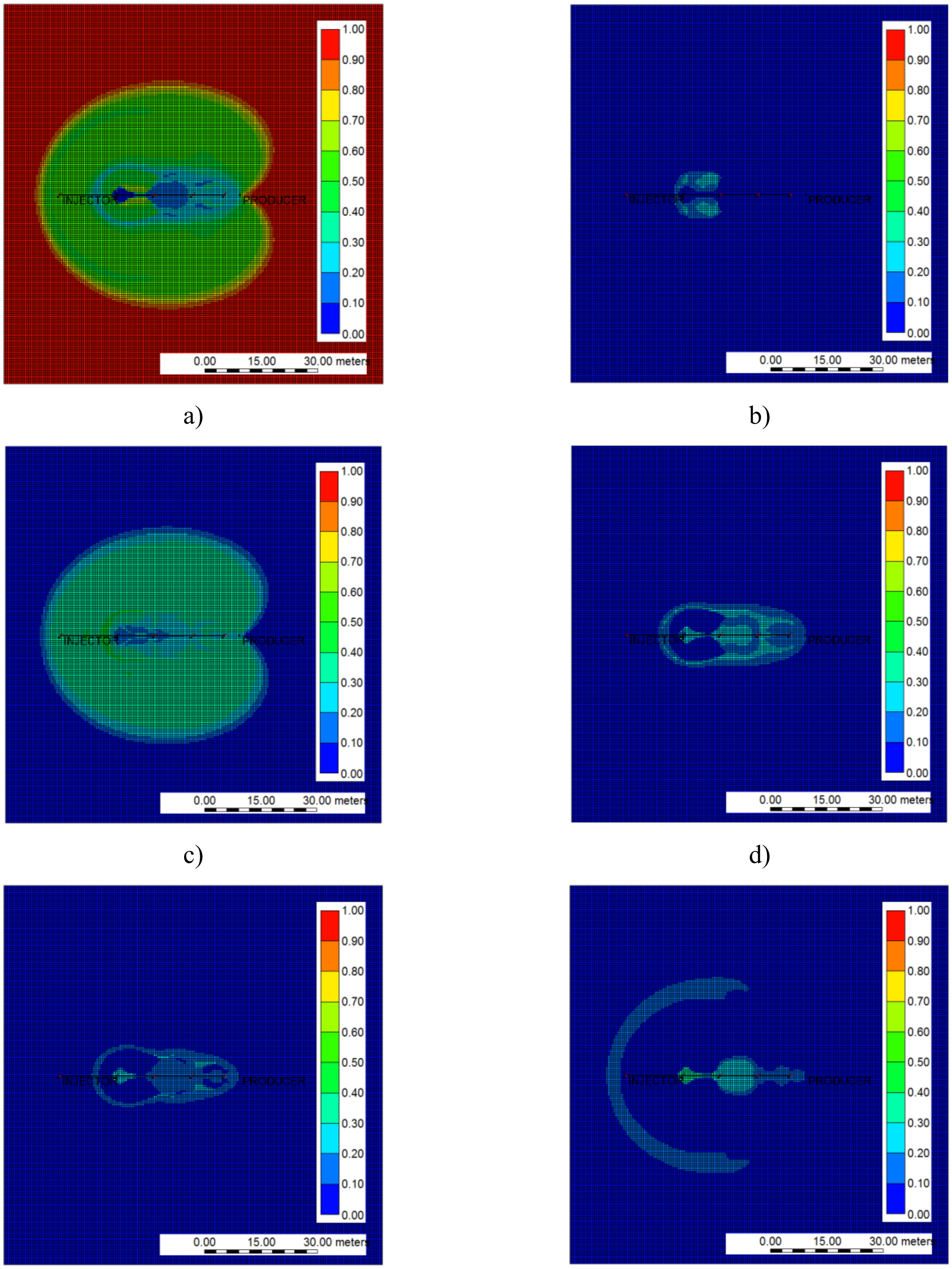

a)

b)

c)

d)

e)

f)

Figure 7.9 Concentrations of different gas species after 60 days in a horizontal plane including the wellbores: a) CH_4; b) CO; c) CO_2; d) H_2; e) H_2O; and f) O_2

As shown in Figure 7.10.a, four porosity contours formed around the injection points; ranging from 0.07 to 0.94. It is worth noting that injection time at each CRIP point was a trade-off between gasifying as much coal as possible and preventing a breakthrough to the producer well. Concentration of carbon and initial coal are presented in Figure 7.10.b and c, respectively. Figure 7.10.d shows porosity plot on a vertical plane including the wellbores.

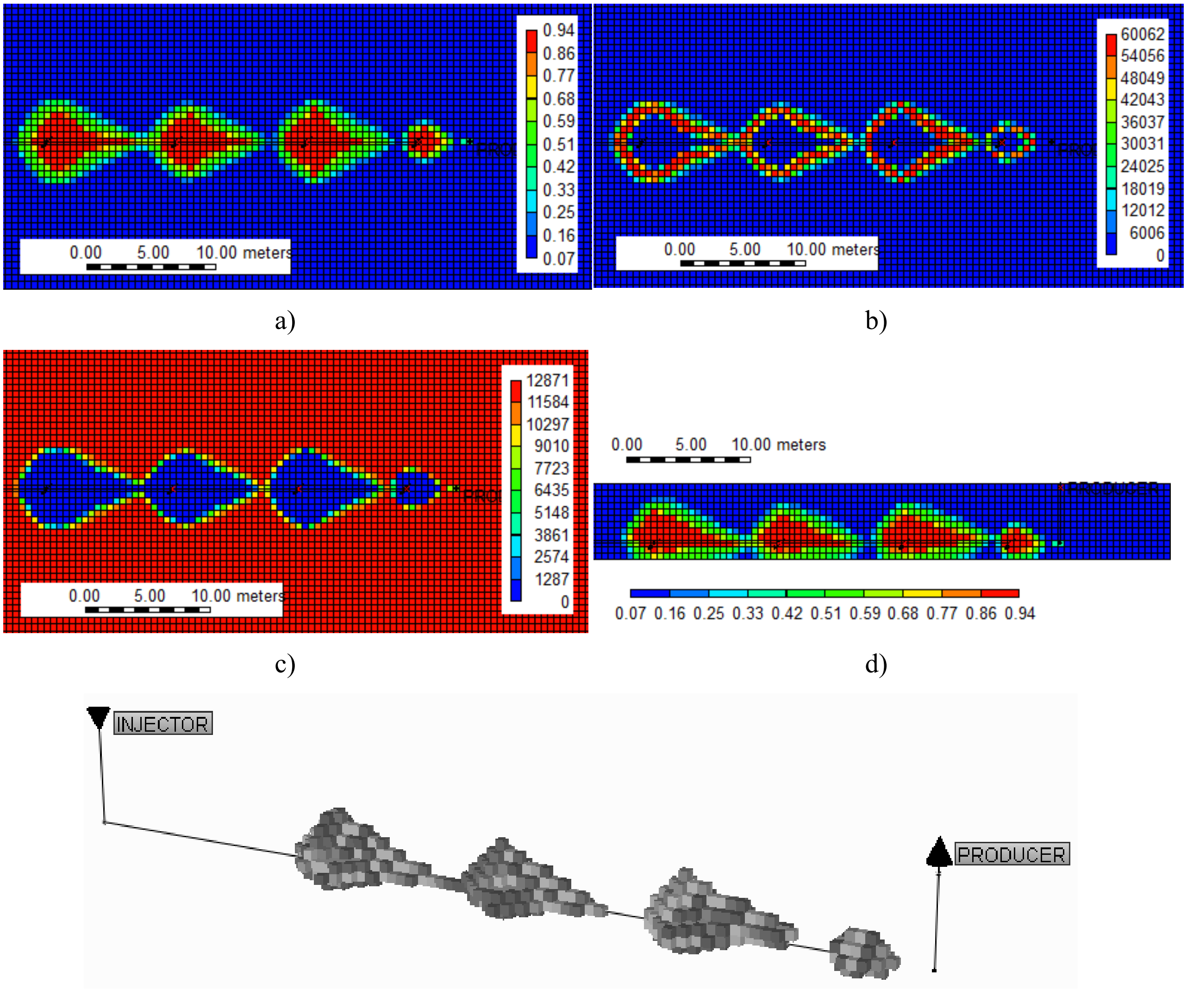

a)

b)

c)

d)

e)

Figure 7.10 Outputs from the coal gasification model after 60 days: a) fluid porosity (fraction); b) carbon concentration (gmole/m^3); c) coal concentration (gmole/m^3); at a horizontal plane including the wells; d) fluid porosity (fraction) at a vertical plane including the wells; and e) a 3D view of the four cavities

By comparing Figure 7.10.a through d, four cavities can be identified. A cavity was considered to exist where porosity was above 60%, concentration of the initial coal dropped significantly, and char (carbon) concentration was near zero. Based on the above criteria, four tear-drop shaped cavities were observed. The cavities grew laterally around the CRIP locations with apices pointing towards the producer well. A three-dimensional view of the cavities is provided in Figure 7.10.e. The idea of assuming grid blocks having porosity of 60% and above as a cavity needs further research to verify at what porosity coal loses its structural stability and/or turns to ash and/or spalls down.

One may use a similar approach to that of the single linear CRIP simulated in this work, and run multiple linear CRIPs in order to simulate a commercial-scale operation, if there is enough computational power. In such a case, coal pillars left between the cavities may help reduce instability of the cavities as well as displacement of rock layers.

7.5.2. Geomechanical effects on the strata

After initializing the in-situ stresses, initial temperature and pore pressure, the model was run for equilibrium. Every 10 days, three sets of data were passed along from STARS to FLAC3D; temperature, pore pressure, and cavity geometry. Then, the model was run until equilibrium was achieved. Due to the significant number of grid blocks in the model, it took eleven days to run it using a high-performance computer. Sharing data in a shorter interval was ideal but it would extensively increase the run time.

As a result of the UCG process, significant geomechanical effects were observed in the strata. Large stress and strain occurred in the perimeter of the cavities.

It was previously mentioned that maximum and minimum horizontal stresses apply at 45^{o} angles to the X and Y axes of the model. If we do stress transformation for the XYZ coordinate system, initial shear stress in the XY plane and for middle of the coal seam thickness would be about 3.8 MPa. Figure 7.11.a shows that maximum shear stress after 60 days, when four cavities have been formed, has increased to about 140 MPa. This indicates significant shear stress localization around the cavities. Significant volumetric strain was also observed in the cavities' surroundings (Figure 7.11.b).

Stress concentration induced mechanical failure in the cavities' perimeters. Figure 7.12.a shows failure zones after 60 days, in a vertical plane including the cavities centerline. Failure zones in a horizontal plane including the wellbores are shown in Figure 7.12.b. These failure zones may spall into the cavities which, in turn, might affect the chemical process of gasification. If the failure zones extend to the overburden, cracks could form which would act as potential pathways for gas leakage to the strata and groundwater.

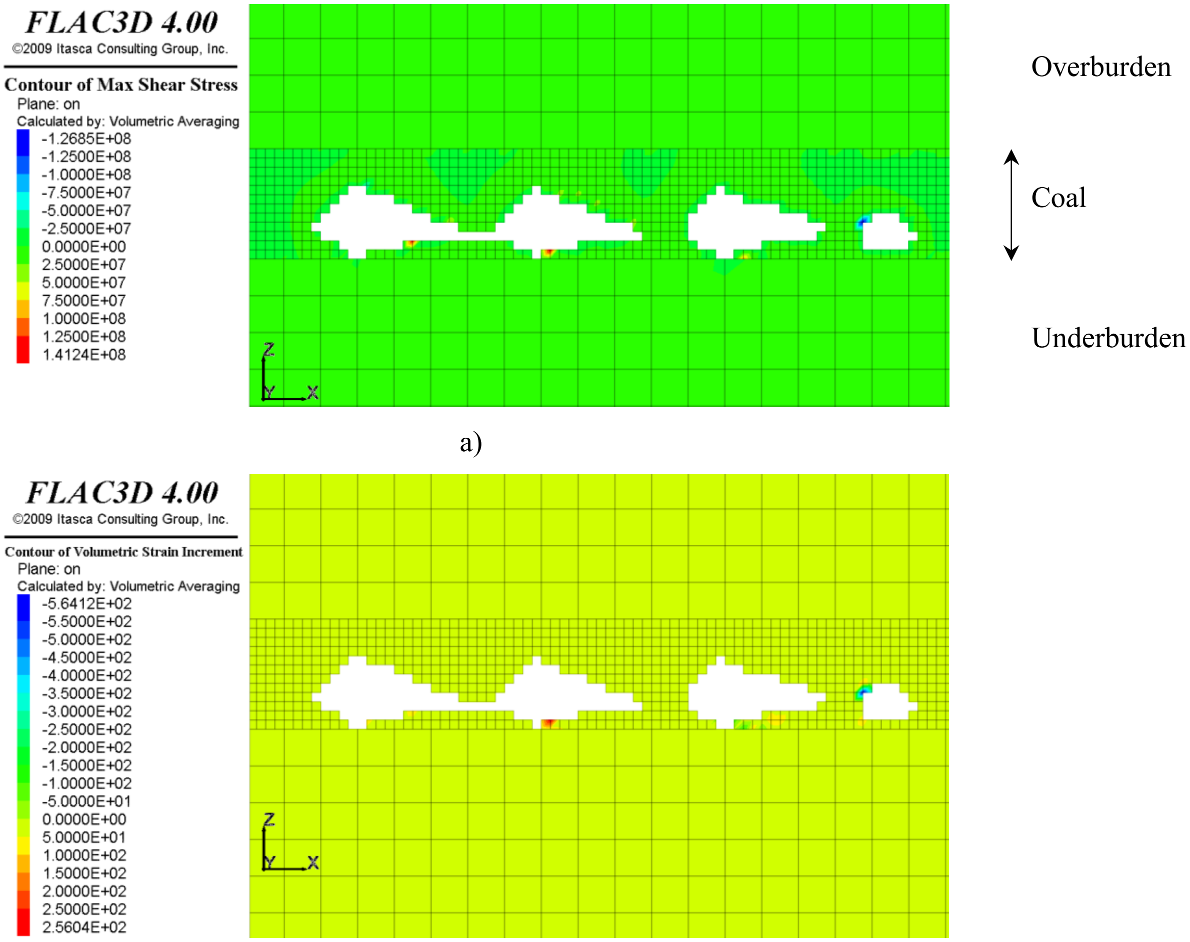

a)

b)

Figure 7.11 a) Maximum shear stress (Pa); and b) volumetric strain increment (fraction); after 60 days in a vertical plane crossing the cavities centerline and containing the wellbores

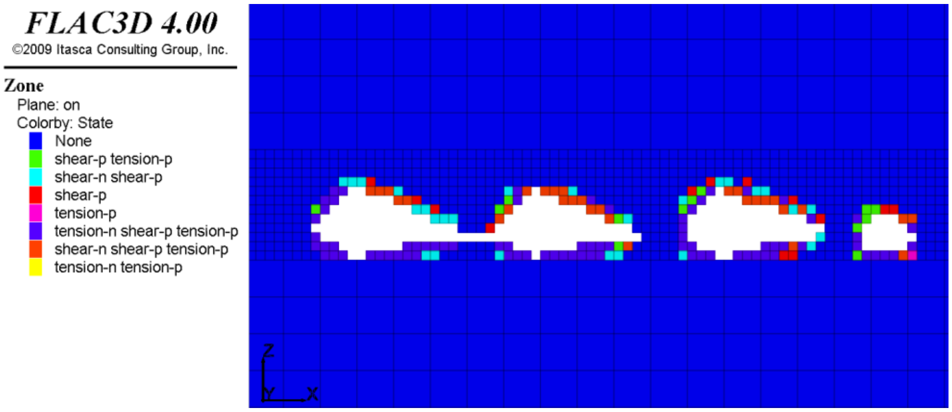

a)

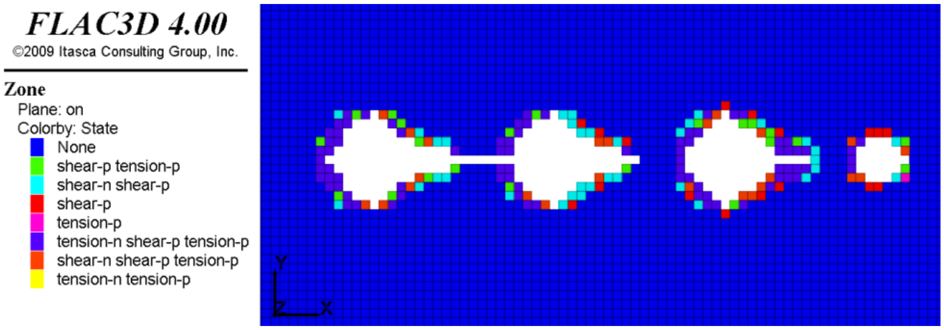

b)

Figure 7.12 Failure zones around the cavities after 60 days: a) in a vertical plane crossing the cavities centerline; and b) in a horizontal plane including the wellbores

Very large deformation happened in the coal seam. As depicted in Figure 7.13, areas around the cavity deformed towards the cavities. Older cavities exhibited significant displacement as the CRIP proceeded to newer locations.

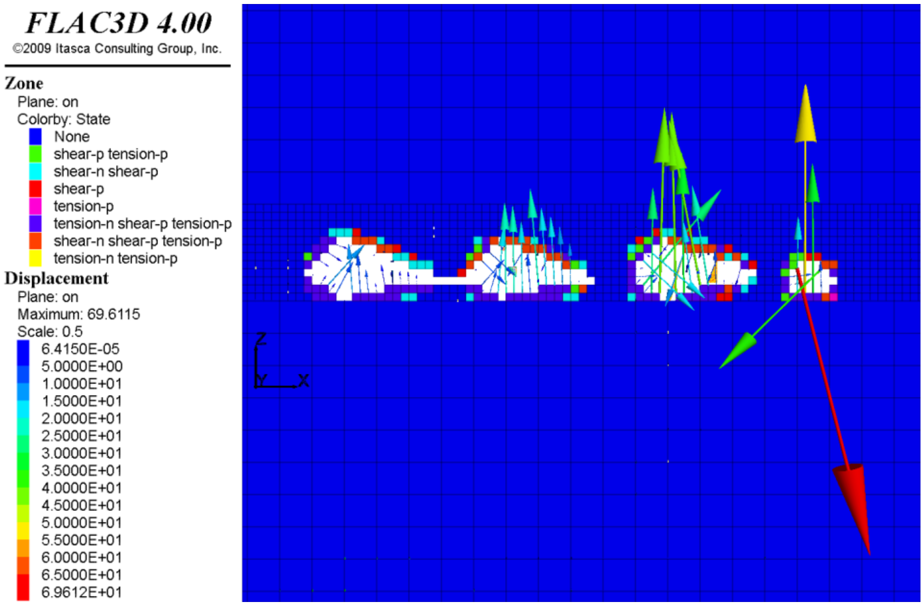

Figure 7.13 Displacement vectors showing large deformation of coal seam towards the cavities at a vertical plane crossing the cavities centerline and containing the wellbores

Histories of mean effective stress and volumetric strain in the bottom of the immediate overburden were monitored. As the gasification proceeded, mean effective stress in the bottom of the overburden increased from about 14 MPa to 18.5 MPa; however, it dropped slightly outside the reservoir area (Figure 7.14.a). At the same time, compressional volumetric strain concentration was observed above the gasification chamber.

The coal seam and the overburden moved upward. The area above the gasification chamber locally deformed more than the side areas. The maximum z-displacement at the interface between the coal and the overburden was 0.32 m. The entire overburden deformed almost uniformly such that z-displacement at top of the model was about 0.31 m (Figure 7.14.b). This indicates that in a large UCG operation, uplift may occur at the ground surface.

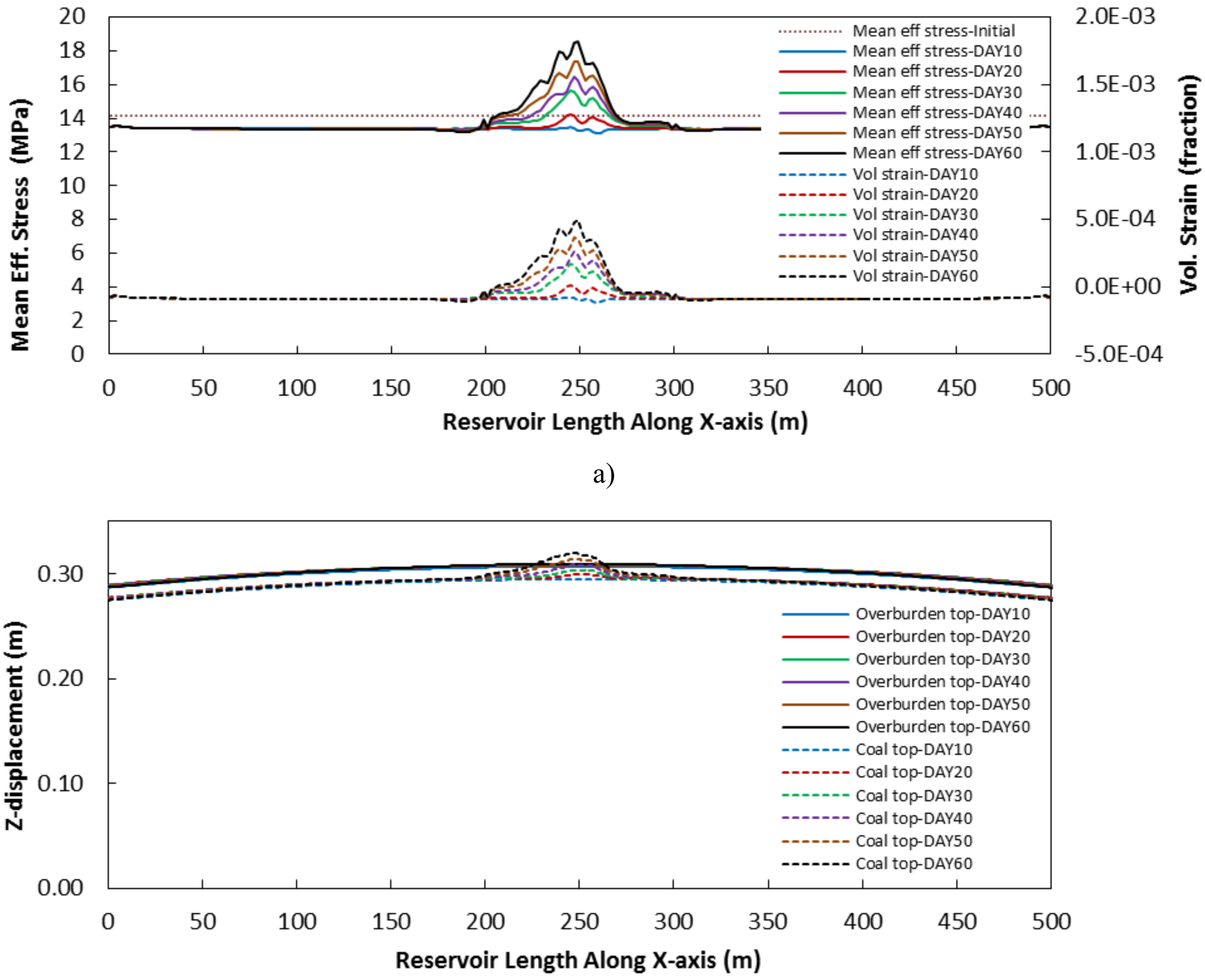

a)

b)

Figure 7.14 a) Mean effective stress and volumetric strain in bottom of the immediate overburden; and b) z-displacement above the coal seam and top of the model

7.1. Conclusions

This study conducted a sequentially coupled coal gasification geomechanical simulation for the Alberta deep UCG project. The coupled analysis allowed simultaneous observation of geomechanical effects on strata as the gasification front advanced and cavities evolved over a 2-month period, and under the linear CRIP operational method. Syngas compositions from this study were in a good agreement with the field measurements. The coal seam and overburden rock deformed upward. Deformation of overburden rock at the surface of the model was nearly uniform. The coal seam, in the area above the gasification chambers, experienced significant displacements and stresses. Cavity walls underwent large displacement towards the interior of the cavities. Perturbations caused by the UCG activities combined with the anisotropic in-situ maximum and minimum horizontal stresses acting at 45 degree angles to the model resulted in mechanical failure in the cavities perimeters.

The presented geomechanical effects of the Alberta UCG in this study pertain only to the CRIP operational method and the selected material properties for the site.

7.2. Acknowledgements

The authors are thankful to The Canadian Centre for Clean Coal/Carbon and Mineral Processing Technologies (C^5MPT) for financial support of this research program.

7.3. References

Advani, S. H., Lin, Y. T., & Shuck, L. Z. (1977). Thermal and structural response evaluation for underground coal gasification. *Society of Petroleum Engineers Journal*, *17*(06), 413-422.

Advani, S. H., Shuck, L. Z., Lin, Y. T., & Chang, H. Y. (1976). Thermomechanics simulations associated with underground coal gasification. In *The 17th US Symposium on Rock Mechanics (USRMS)*. American Rock Mechanics Association.

Akbarzadeh, H., & Chalaturnyk, R. J. (2013). Coupled fluid-thermal-mechanical analyses of a deep underground coal gasification cavity. *Journal of Architecture and Civil Engineering, Quest Journals 1*(1), 01-14.

Akbarzadeh, H., & Chalaturnyk, R. J. (2014). Structural changes in coal at elevated temperature pertinent to underground coal gasification: A review. *International Journal of Coal Geology*, *131*, 126-146.

Akbarzadeh, H., & Chalaturnyk, R. J. (2016). Sequentially coupled flow-geomechanical modeling of underground coal gasification for a three-dimensional problem. *Mitigation and Adaptation Strategies for Global Change*, 21(4), 577-594.

Alberta Energy Regulator (AER). (2014). ST98-2014: Alberta's Energy Reserves 2013 and Supply/Demand Outlook 2014-2023. (http://www.aer.ca/data-and-publications/statistical-reports/st98, accessed Oct. 08, 2014).

Bell, J. S., & Grasby, S. E. (2012). The stress regime of the Western Canadian sedimentary basin. *Geofluids*, *12*(2), 150-165.

Burton, E., Friedmann, J., & Upadhye, R. (2006). Best practices in underground coal gasification. Draft. US DOE contract no W-7405-Eng-48. Lawrence Livermore National Laboratory.

Camp, D.W., Nitao, J. J., White, J. A., Burton, G. C., Reid, C., Friedmann, J. (2012). A fully integrated 3-D multi-physics UCG simulator applied to UCG field tests. A presentation at the 2nd IEA Underground Coal Gasification Network Workshop, Banff, Alberta, Canada.

Computer Modelling Group Ltd. (2012). STARS User's Guide, 2012. Computer Modelling Group, Calgary, Alberta, Canada

Couch, G. R. (2009). Underground coal gasification. IEA Clean Coal Centre. International Energy Agency, London.

Gash, B. W., Volz, R. F., Potter, G., & Corgan, J. M. (1992). The effects of cleat orientation and confining pressure on cleat porosity, permeability and relative permeability in coal. Paper presented at the 1992 SCA Conference, paper number 9224. 1992:1-14.

Gentzis, T. (2009). Review of mannville coal geomechanical properties: Application to coalbed methane drilling in the Central Alberta Plains, Canada. *Energy Sources, Part A: Recovery, Utilization, and Environmental Effects*, *32*(4), 355-369.

Gentzis, T., Goodarzi, F., Cheung, F. K., & Laggoun-Defarge, F. (2008). Coalbed methane producibility from the Mannville coals in Alberta, Canada: A comparison of two areas. *International Journal of Coal Geology*, *74*(3), 237-249.

Government of Alberta. (2014). Government of Alberta 2013-2014 Energy Annual Report. (http://www.energy.alberta.ca/About_Us/1001.asp, accessed Oct. 08, 2014).

Hawkes, C. D., Bachu, S., Haug, K., & Thompson, A. W. (2005). Analysis of in-situ stress regime in the Alberta Basin, Canada, for performance assessment of CO_2 geological sequestration sites. In *Proceedings of the fourth annual conference on carbon capture and sequestration DOE/NETL.*

Itasca Consulting Group Inc, (2009). FLAC3D User's Guide. Itasca Consulting Group Inc., Minneapolis, Minnesota.

Kariznovi, M., Nourozieh, H., Abedi, J., & Chen, Z. (2013). Simulation study and kinetic parameter estimation of underground coal gasification in Alberta reservoirs. *Chemical Engineering Research and Design*, *91*(3), 464-476.

Khan, M. M., Mmbaga, J. P., Shirazi, A. S., Liu, Q., & Gupta, R. (2015). Modelling underground coal gasification-A review. *Energies*, *8*(11), 12603-12668.

Laouafa, F., Farret, R., Vidal-Gilbert, S., & Kazmierczak, J. B. (2014). Overview and modeling of mechanical and thermomechanical impact of underground coal gasification exploitation. *Mitigation and Adaptation Strategies for Global Change*, 1-30.

Morris, J. P., Buscheck, T. A., & Hao, Y. (2009). Coupled geomechanical simulations of UCG cavity evolution. In *Proceedings of the 2009 International Pittsburgh Coal Conference, Pittsburgh PA*.

National Energy Board. (2013). Canada's Energy Future 2013 - Energy Supply and Demand Projections to 2035 (http://www.neb-one.gc.ca/clf-nsi/rnrgynfmtn/nrgyrprt/nrgyftr/2013/nrgftr2013-eng.html, accessed Oct. 08, 2014).

Nitao, J. J., Camp, D. W., Buscheck, T. A., White, J. A., Burton, G. C., Wagoner, J. L., & Chen, M. (2011). Progress on a new integrated 3-D UCG simulator and its initial application. In *International Pittsburgh Coal Conference* (pp. 1-13).

Nourozieh, H., Kariznovi, M., Chen, Z., & Abedi, J. (2010). Simulation study of underground coal gasification in Alberta reservoirs: Geological structure and process modeling. *Energy & Fuels*, *24*(6), 3540-3550.

Nygaard, R. (2010). Geomechanical Analysis: Wabamun area CO_2 sequestration project (WASP). *Energy and Environmental Systems Group (EES), University of Calgary*.

Richardson, R. J., & Singh, S. (2012). Prospects for underground coal gasification in Alberta, Canada. *Proceedings of the ICE-Energy, 165*(3), 125-136.

Sarraf Shirazi, A., Karimipour, S., & Gupta, R. (2013). Numerical simulation and evaluation of cavity growth in in situ coal gasification. *Industrial & Engineering Chemistry Research*, *52*(33), 11712-11722.

Seifi, M., Chen, Z., & Abedi, J. (2011). Numerical simulation of underground coal gasification using the CRIP method. *The Canadian Journal of Chemical Engineering*, *89*(6), 1528-1535.

Sury, M., White, M., Kirton, J., Carr, P., Woodbridge, R., Mostade, M., Chappell, R., Hartwell, D., Hunt, D., & Rendell, N. (2004a). Review of environmental issues of underground coal gasification-best practice guide: United Kingdom Department of Trade and Industry Report No. COAL R273. DTI/Pub URN 04/1881.

Sury, M., White, M., Kirton, J., Carr, P., Woodbridge, R., Mostade, M., Chappell, R., Hartwell, D., Hunt, D., & Rendell N. (2004b). Review of environmental issues of underground coal gasification: United Kingdom Department of Trade and Industry. Report No. COAL R272. DTI/Pub URN 04/1880.

Swan Hills Synfuels. (2012). Swan Hills in-situ coal gasification technology development; final outcomes report. Swan Hills Synfuels, Alberta, Canada.

Tan, Q., Luo, X., & Li, S. (2008). Numerical modeling of thermal stress in a layered rock mass. In *The 42nd US Rock Mechanics Symposium (USRMS)*. American Rock Mechanics Association.

Vorobiev, O. Y., Morris, J. P., Antoun, T. H., & Friedmann, S. J. (2008). Geomechanical simulations related to UCG activities. In *International Pittsburgh Coal Conference, Pittsburgh, PA*.

World Energy Council. (2013). World Energy Resources: 2013 Survey. (https://www.worldenergy.org/publications/2013/world-energy-resources-2013-survey/, accessed Nov. 27, 2015).

Zogala, A., & Janoszek, T. (2015). CFD simulations of influence of steam in gasification agent on parameters of UCG process. *Journal of Sustainable Mining*, *14*(1), 2-11.

Chapter 8 Conclusions and Recommendations

8.1. Summary

The objectives of the accomplished research were to investigate coal properties at elevated temperature as well as conducting coupled simulations of underground coal gasification.

An inter-disciplinary study was conducted in Chapter 3 to investigate the impact of elevated temperatures on thermal, transport, and mechanical properties of coal of different ranks, from various locations. The properties investigated included: weight loss, thermal deformation, microcrack generation, transport properties, as well as strength and stiffness.

Chapter 4 provided results of High-Pressure High-Temperature (HPHT) triaxial experiments on a fractured coal from Alberta. The properties measured included: thermal deformation, stress-strain, elastic properties, and permeability to N_2 gas as well as permeability evolution during progressive shearing.

Parametric geomechanical analyses of an idealized UCG cavity was conducted with the aid of FLAC3D (of ITASCA) in Chapter 5 to understand impacts of syngas pressures (less than, equal to, or greater than in-situ pore pressure) as well as coal material properties (constant or temperature-dependent) on thermally-induced pore pressure along with deformation and stresses around the cavity.

A numerical modeling workflow was devised in Chapter 6 in order to sequentially couple coal gasification modeling in STARS (from the Computer Modelling Group Ltd., CMG) with geomechanical modeling in FLAC3D, for an example 3D problem.

The coupling workflow of Chapter 6 was applied to a reservoir scale modeling of the Swan Hills, Alberta UCG project, as provided in Chapter 7.

8.2. Conclusions

Major conclusions from this research study are:

- Coal exhibits a unique response to high temperature due to its organic nature as well as inherent fracture network. Coal loses its weight under elevated temperature because of thermo-chemical decomposition. Thermal deformation of coal is different from other rock types. Initially coal expands (positive thermal expansion coefficient). At certain temperature thermo-chemical decomposition begins; hence, coal undergoes compressional deformation (negative thermal expansion coefficient). In general, pore volume, aperture, porosity, and permeability of coal increase with temperature although fluctuations were observed. Elastic and shear moduli of coal under heating may initially stay unchanged or increase, but after exceeding a threshold temperature they degrade drastically. Both moduli exhibit dependence on loading direction with regard to the bedding plane, loading rate, and specimen size. However the effect of anisotropy vanishes at elevated temperature.
- The specimens from the Genesee coal mine, Alberta, initially exhibited expansion under heating. It was then followed by a collapse in both axial and lateral directions at about 140 °C. This temperature corresponds to the occurrence of the thermo-chemical process of pyrolysis. Specimens at 200 °C showed higher peak strengths and strains compared to the room temperature tests. Volumetric strain response of this coal, both at room and high temperature revealed that the crack damage stress was equal to the peak stress; that is, no reversal point in the volumetric strain plots were observed in pre-peak region. Instead, the reversal point was observed in post-peak region. Permeability of this coal fluctuated with temperature and effective confining stress. Reduction in permeability measurements was notable at 80 °C, which was due to thermal expansion of the matrix and closure of initial fractures. Permeability evolution at higher temperature, especially around 140 °C and

above was a complex response of thermal expansion and pyrolysis. Progressive shear resulted in reduction of permeability in the beginning of stress-strain curve.

- The parametric study of Chapter 5 revealed that due to cavity evolution and high temperature of syngas, large volumetric strain happened around the cavity. This large deformation, in turn, dropped pore pressure in the coal and rock as one may expect based on Biot's theory of poroelasticity. The high temperature increased mean effective stress in strata. Using temperature-dependent elastic modulus for coal resulted in larger deformation and volumetric strain in the strata though less increase in mean effective stress. Using temperature-dependent permeability for coal helped pore pressure in the strata rapidly reach steady state conditions. The change in syngas pressure in the studied range did not show significant impacts on volumetric strain and mean effective stress in the strata.
- The numerical coupling workflow developed in Chapter 6 consists of two levels of coupling. Level one is continuous updating of permeability during each sub-time-step in gasification module due to devolatilization and reduced concentration of organic matters. At a time-step level, three sets of information are passed along to the geomechanical module; temperature and pore pressure as well as cavity geometry. The second level of coupling is updating permeability and porosity of coal as a result of geomechanical changes. This coupling workflow facilitates simultaneous observation of temperature front movement, syngas production, cavity growth, as well as stresses, deformations, and mechanical failure of strata.
- The sequentially coupled simulation of the Alberta UCG project utilized a geological section reported for the site and under in-situ stress field, particular to the Western Canadian Sedimentary basin. Ten chemical reactions along with their reaction kinetics were implemented in the gasification simulation. Produced syngas compositions were in a good agreement with the field measurements utilizing the linear CRIP operational method. The sequentially coupled analysis allowed simultaneous observation of geomechanical effects on strata as gasification front advanced and cavities evolved over a 2-month period. The coal seam and overburden rock deformed upward. Deformation of

overburden rock at the surface of the model was nearly uniform. The coal seam, in areas above the gasification chambers, experienced displacement and stress concentrations. The coal seam adjacent to the gasification chambers experienced significant deformation towards the interior of the 3D tear-drop shape cavities. Perturbations caused by the UCG activities combined with the anisotropic in-situ horizontal stresses acting at 45 degree angles to the model resulted in mechanical failure in the zones surrounding the cavities.

8.3. Recommendations for future research

Further research in the area of reservoir-geomechanics of the UCG is recommended as follows:

8.3.1. Experimental research

- Design and employment of a HPHT (600 ^{o}C and potentially higher) triaxial device with capabilities of measuring porosity, permeability, stress-strain with accurate deformation measurement can provide information required for the level two coupling. Currently, porosity is mainly measured in a porosimeter. It is recommended to add gas porosity measurement capability to the same triaxial set up, which may utilize an inert gas and work based on the Boyle-Mariotte law.
- Measurement of pyrolysis gas compositions as well as deriving reaction kinetics of the Alberta coal under effect of confining stress would be a significant advancement in this field.
- An appropriate constitutive geomechanical model for coal under high-pressure high-temperature is very important, in particular for the CRIP method, to properly study formation response as the gasification chamber moves to different locations.

8.3.2. Simulation research

- Conducting level two coupling will better represent the UCG process.

- Very large gasification models are recommended to obviate the issue of pore pressure boundary effects.
- Inclusion of caprock and underburden rock layers in gasification models may help better understand response of the bounding seal system to the gasification process.
- Further numerical tuning is needed regarding material balance error in coal gasification modeling. This will become more important, in particular, when the level two coupling is performed.
- Implementation of the negative thermal expansion coefficient of coal, a fracture rock, and under elevated temperature in geomechanical modeling could provide a better representation of coal seam response to the UCG.
- Utilizing more accurate magnitudes of in-situ stresses and material properties in a two-way sequential coupling while considering all the above-mentioned recommendations can better represent the Alberta UCG.
- A two-way coupled UCG model for Alberta needs to be calibrated against field measurements.

References

Advani, S. H., Lin, Y. T., & Shuck, L. Z. (1977). Thermal and structural response evaluation for underground coal gasification. *Society of Petroleum Engineers Journal*, *17*(06), 413-422.

Advani, S. H., Shuck, L. Z., Lin, Y. T., & Chang, H. Y. (1976). Thermomechanics simulations associated with underground coal gasification. In *The 17th US Symposium on Rock Mechanics (USRMS)*. American Rock Mechanics Association.

Ahmed, T. (2006). Reservoir engineering handbook. Gulf Professional Publishing.

Aiman, W. R., Ganow, H. C., & Thorsness, C. B. (1980). Hoe Creek II revisited: boundaries of the gasification zone. *Combustion Science and Technology*, *23*(3-4), 125-130.

Akbarzadeh, H., & Chalaturnyk, R. J. (2013). Coupled Fluid-Thermal-Mechanical Analyses of a Deep Underground Coal Gasification Cavity. *Journal of Architecture and Civil Engineering, Quest Journals, 1*(1), 01-14.

Akbarzadeh, H., & Chalaturnyk, R. J. (2014). Structural changes in coal at elevated temperature pertinent to underground coal gasification: A review. *International Journal of Coal Geology*, *131*, 126-146.

Akbarzadeh, H., & Chalaturnyk, R. J. (2016). Sequentially coupled flow-geomechanical modeling of underground coal gasification for a three-dimensional problem. *Mitigation and Adaptation Strategies for Global Change*, 21(4), 577-594.

Alberta Energy Regulator (AER). (2014). ST98-2014: Alberta's Energy Reserves 2013 and Supply/Demand Outlook 2014-2023. (http://www.aer.ca/data-and-publications/statistical-reports/st98, accessed Oct. 08, 2014).

American Society for Testing and Materials. (2013). ASTM D7012-13 Standard Test Methods for Compressive Strength and Elastic Moduli of Intact Rock Core Specimens under Varying States of Stress and Temperatures. ASTM, USA.

American Society for Testing and Materials. (2012). ASTM D388-12 Standard Classification of Coals by Rank. ASTM, USA.

American Society for Testing and Materials. (2008). ASTM D4525-08 Standard Test Methods for Permeability of Rocks by Flowing Air. ASTM, USA.

American Society of Mechanical Engineers. (2009). ASME International Steam Tables for Industrial Use. Second Edition, American Society of Mechanical Engineers, New York.

Anthony, D. B., & Howard, J. B. (1976). Coal devolatilization and hydrogastification. *AIChE Journal*, *22*(4), 625-656.

Arenillas, A., Rubiera, F., & Pis, J. J. (1999). Simultaneous thermogravimetric–mass spectrometric study on the pyrolysis behaviour of different rank coals. *Journal of Analytical and Applied Pyrolysis*, *50*(1), 31-46.

Arenillas, A., Rubiera, F., Pis, J. J., Cuesta, M. J., Iglesias, M. J., Jimenez, A., & Suarez-Ruiz, I. (2003). Thermal behaviour during the pyrolysis of low rank perhydrous coals. *Journal of Analytical and Applied Pyrolysis*, *68*, 371-385.

Avid, B., Purevsuren, B., Born, M., Dugarjav, J., Davaajav, Y., & Tuvshinjargal, A. (2002). Pyrolysis and TG analysis of Shivee Ovoo coal from Mongolia. *Journal of Thermal Analysis and Calorimetry*, *68*(3), 877-885.

Balek, V., & de Koranyi, A. (1990). Diagnostics of structural alterations in coal: Porosity changes with pyrolysis temperature. *Fuel*, *69*(12), 1502-1506.

Bangham, D., & Franklin, R.E. (1946). Thermal expansion of coals and carbonised coals. *Transactions of the Faraday Society, 42*, B289-294.

Bartel, L. C., Beard, S. G., Beckham, L. W., Reed, R. P., & Seavey, R. W. (1976). Instrumentation results from an in-situ coal gasification experiment. In *SPE Annual Fall Technical Conference and Exhibition*. Society of Petroleum Engineers.

Bell, J. S., & Grasby, S. E. (2012). The stress regime of the Western Canadian sedimentary basin. *Geofluids*, *12*(2), 150-165.

Biot, M. A. (1941). General theory of three-dimensional consolidation. *Journal of Applied Physics*, *12*(2), 155-164.

Brandenburg, C. F., Reed, R. P., Boyd, R. M., Northrop, D. A., & Jennings, J. W. (1975). Interpretation of chemical and physical measurements from an in situ coal gasification experiment. In *SPE Annual Fall Technical Conference and Exhibition*. Society of Petroleum Engineers.

Burton, E., Friedmann, J., & Upadhye, R. (2006). Best practices in underground coal gasification. Draft. US DOE contract no W-7405-Eng-48. Lawrence Livermore National Laboratory.

Buscheck, T. A., Hao, Y., Morris, J. P., & Burton, E. A. (2009). Thermal-hydrological sensitivity analysis of underground coal gasification. In *Proceedings of the 2009 International Pittsburgh Coal Conference, Pittsburgh, PA, USA* (Vol. 2023).

Buzzi, O., Sieffert, Y., Mendes, J., Liu, X., Giacomini, A., & Seedsman, R. (2014). Strength of an Australian coal under low confinement. *Rock Mechanics and Rock Engineering*, *47*(6), 2265-2270.

Camp, D. W., Nitao, J. J., White, J. A., Burton, G. C., Reid, C., Friedmann, J. (2012). A fully integrated 3-D multi-physics UCG simulator applied to UCG field tests. A presentation at the 2nd IEA Underground Coal Gasification Network Workshop, Banff, Alberta, Canada.

Computer Modelling Group Ltd. (2012). STARS User's Guide, 2012. Computer Modelling Group, Calgary, Alberta, Canada

Cooke, S. D., & Oliver, R. L. (1983). Ground water quality at the Hanna underground coal gasification experimental sites, Hanna, Wyoming: data base and summary. *US Department of Energy/Associated Western Universities, Inc. Under cooperative, contract (DE-AC07–76ET10723).*

Couch, G. R. (2009). Underground coal gasification. IEA Clean Coal Centre. International Energy Agency, London.

Dabbous, M. K., Reznik, A. A., Taber, J. J., & Fulton, P. F. (1974). The permeability of coal to gas and water. *Society of Petroleum Engineers Journal*, *14*(06), 563-572.

Daggupati, S., Mandapati, R. N., Mahajani, S. M., Ganesh, A., Mathur, D. K., Sharma, R. K., & Aghalayam, P. (2010). Laboratory studies on combustion cavity growth in lignite coal blocks in the context of underground coal gasification. *Energy*, *35*(6), 2374-2386.

Daggupati, S., Mandapati, R. N., Mahajani, S. M., Ganesh, A., Sapru, R. K., Sharma, R. K., & Aghalayam, P. (2011). Laboratory studies on cavity growth and product gas composition in the context of underground coal gasification. *Energy*, *36*(3), 1776-1784.

de Koranyi, A., & Balek, V. (1985). Structural changes in coals during pyrolysis. *Thermochimica Acta*, *93*, 737-740.

De la Puente, G., Iglesias, M. J., Fuente, E., & Pis, J. J. (1998). Changes in the structure of coals of different rank due to oxidation-effects on pyrolysis behaviour. *Journal of Analytical and Applied Pyrolysis*, *47*(1), 33-42.

Elbeyli, I., Piskin, S., & Sutcu, H. (2004). Pyrolysis kinetics of Turkish bituminous coals by thermal analysis. *Turkish Journal of Engineering* and *Environmental* Sciences*, 28*, 233-239.

Elliott, G. M., & Brown, E. T. (1988). Laboratory measurement of the thermo-hydro-mechanical properties of rock. *Quarterly Journal of Engineering Geology and Hydrogeology*, *21*(4), 299-314.

Fausett, L. V. (1984). An analysis of mathematical models of underground coal gasification. PhD Dissertation, University of Wyoming.

Feng, Z. J., Zhao, Y. S., & Wan, Z. J. (2012). Experiment study of the thermal deformation of in-situ gas coal. *Rock Mechanics: Achievements and Ambitions-Proceedings of the 2nd ISRM International Young Scholars' Symposium on Rock Mechanics*, 103-108.

Gash, B. W., Volz, R. F., Potter, G., & Corgan, J. M. (1992). The effects of cleat orientation and confining pressure on cleat porosity, permeability and relative permeability in coal. Paper presented at the 1992 SCA Conference, paper number 9224. 1992:1-14.

Gensterblum, Y., Ghanizadeh, A., & Krooss, B. M. (2014). Gas permeability measurements on Australian subbituminous coals: Fluid dynamic and poroelastic aspects. *Journal of Natural Gas Science and Engineering*, *19*, 202-214.

Gentzis, T. (2009). Review of Mannville coal geomechanical properties: Application to coalbed methane drilling in the Central Alberta Plains, Canada. *Energy Sources, Part A: Recovery, Utilization, and Environmental Effects*, *32*(4), 355-369.

Gentzis, T., Deisman, N., & Chalaturnyk, R. J. (2007). Geomechanical properties and permeability of coals from the Foothills and Mountain regions of western Canada. *International Journal of Coal Geology*, *69*(3), 153-164.

Gentzis, T., Goodarzi, F., Cheung, F. K., & Laggoun-Défarge, F. (2008). Coalbed methane producibility from the Mannville coals in Alberta, Canada: A comparison of two areas. *International Journal of Coal Geology*, *74*(3), 237-249.

Ghabezloo, S. (2013). Effect of porosity on the thermal expansion coefficient of porous materials. *In Poromechanics V@ ASCE 2013. Proceedings of the Fifth Biot Conference on Poromechanics*, 1857-1866.

Glass, R. E. (1984). The thermal and structural properties of a Hanna basin coal. *Journal of Energy Resources Technology*, *106*(2), 266-271.

Government of Alberta. (2014). Government of Alberta 2013-2014 Energy Annual Report. (http://www.energy.alberta.ca/About_Us/1001.asp, accessed Oct. 08, 2014).

Hawkes, C. D., Bachu, S., Haug, K., & Thompson, A. W. (2005). Analysis of in-situ stress regime in the Alberta Basin, Canada, for performance assessment of CO_2 geological sequestration sites. In *Proceedings of the fourth annual conference on carbon capture and sequestration DOE/NETL.*

Hill, J. O., Ma, S., & Heng, S. (1989). Thermal analysis of Australian coals-A short review. *Journal of Thermal Analysis*, *35*(6), 2009-2024.

Heuze, F. E. (1983). High-temperature mechanical, physical and thermal properties of granitic rocks-a review. *International Journal of Rock Mechanics and Mining Sciences & Geomechanics Abstracts, 20*(1), 3-10.

http://en.wikipedia.org/wiki/Coal#Types (accessed May 02, 2014)

http://en.wikipedia.org/wiki/Wyodak_Mine (accessed May 02, 2014)

Itasca Consulting Group Inc, (2009). FLAC3D User's Guide. Itasca Consulting Group Inc., Minneapolis, Minnesota.

Jung, K. S. (1987). Mathematical modeling of cavity growth during underground coal gasification. PhD Dissertation, University of Wyoming.

Kapusta, K., Stanczyk, K., Wiatowski, M., & Checko, J. (2013). Environmental aspects of a field-scale underground coal gasification trial in a shallow coal seam at the Experimental Mine Barbara in Poland. *Fuel, 113*, 196-208.

Kariznovi, M., Nourozieh, H., Abedi, J., & Chen, Z. (2013). Simulation study and kinetic parameter estimation of underground coal gasification in Alberta reservoirs. *Chemical Engineering Research and Design*, *91*(3), 464-476.

Khan, M. M., Mmbaga, J. P., Shirazi, A. S., Liu, Q., & Gupta, R. (2015). Modelling underground coal gasification-a review. *Energies*, *8*(11), 12603-12668.

Kostur, K., & Kacur, J. (2008). The monitoring and control of underground coal gasification in laboratory conditions. *Acta Montanistica Slovaca*, *13*(1), 111-117.

Kotyrba, A., Kortas, L., & Stanczyk, K. (2015). Imaging the underground coal gasification zone with microgravity surveys. *Acta Geophysica, 63*(3), 634-651.

Krzesinska, M., Szeluga, U., Czajkowska, S., Muszynski, J., Zachariasz, J., Pusz, S., Kwiecinska, B., Koszorek, A., & Pilawa, B. (2009). The thermal decomposition studies of three Polish bituminous coking coals and their blends. *International Journal of Coal Geology, 77*(3), 350-355.

Laouafa, F., Farret, R., Vidal-Gilbert, S., & Kazmierczak, J. B. (2014). Overview and modeling of mechanical and thermomechanical impact of underground coal gasification exploitation. *Mitigation and Adaptation Strategies for Global Change*, 1-30.

Li, Y., Tang, D., Xu, H., Meng, Y., & Li, J. (2014). Experimental research on coal permeability: The roles of effective stress and gas slippage. *Journal of Natural Gas Science and Engineering*, *21*, 481-488.

Linc Energy. (2015). (http://www.lincenergy.com, accessed Nov. 26, 2015)

Liu, S., Zhang, S., Chen, F., Wang, C., & Liu, M. (2014). Variation of coal permeability under dehydrating and heating: a case study of Ulanqab lignite for underground coal gasification. *Energy & Fuels*, *28*(11), 6869-6876.

Long, Q.M., Wen, G. C., Zou, Y. H., & Zhao, X. S. (2009). Experimental study on gas permeability by adsorption under 3D-stress. *Journal of Coal Science & Engineering (China) 15*(2), 148-151.

Lu, T., Laman, G., xxxx. A preliminary comparison of coal Classification and processing between Canada and China (http://www.tetratech.com/pdfs/66/Coal_Classification_CMP2012_Ting_Lu.pdf, accessed May 02, 2014*)*

Luo, J. A., & Wang, L. (2011). High-temperature mechanical properties of mudstone in the process of underground coal gasification. *Rock Mechanics and Rock Engineering, 44*(6), 749-754.

Luo, X., Tan, Q., Luo, C., & Wang, Z. (2008). Microseismic monitoring of burn front in an underground coal gasification experiment. In *The 42nd US Rock Mechanics Symposium (USRMS)*. American Rock Mechanics Association.

Minister of Justice. (2012). Reduction of Carbon Dioxide Emissions from Coal-fired Generation of Electricity Regulations (SOR/2012-167) (http://laws.justice.gc.ca/eng/regulations/SOR-2012-167/, accessed Oct. 14, 2014).

Martin, C. D., & Chandler, N. A. (1994). The progressive fracture of Lac du Bonnet granite. *International Journal of Rock Mechanics and Mining Sciences & Geomechanics Abstracts, 31*(6), 643-659.

Medhurst, T. P., & Brown, E. T. (1998). A study of the mechanical behaviour of coal for pillar design. *International Journal of Rock Mechanics and Mining Sciences*, *35*(8), 1087-1105.

Morris, J. P., Buscheck, T. A., & Hao, Y. (2009). Coupled geomechanical simulations of UCG cavity evolution. In *Proceedings of the 2009 International Pittsburgh Coal Conference, Pittsburgh PA*.

National Energy Board. (2013). Canada's Energy Future 2013 - Energy Supply and Demand Projections to 2035 (http://www.neb-one.gc.ca/clf-nsi/rnrgynfmtn/nrgyrprt/nrgyftr/2013/nrgftr2013-eng.html, accessed Oct. 08, 2014).

National Institute of Standards and Technology (NIST). NIST Chemistry WebBook. (http://webbook.nist.gov/chemistry/, accessed Feb. 01, 2016).

Nitao, J. J., Camp, D. W., Buscheck, T. A., White, J. A., Burton, G. C., Wagoner, J. L., & Chen, M. (2011). Progress on a new integrated 3-D UCG simulator and its initial application. In *International Pittsburgh Coal Conference* (pp. 1-13).

Niu, S., Zhao, Y., & Hu, Y. (2014). Experimental investigation of the temperature and pore pressure effect on permeability of lignite under the in situ condition. *Transport in Porous Media*, *101*(1), 137-148.

Northrop, D. A., Beard, S. G., Bartel, L. C., Beckham, L. W., & Hommert, P. J. (1977). Instrumentation for in situ coal gasification: an assessment of techniques evaluated on the Hanna II experiment (No. SAND-77-1072). Sandia Labs., Albuquerque, N. Mex. (USA).

Nourozieh, H., Kariznovi, M., Chen, Z., & Abedi, J. (2010). Simulation study of underground coal gasification in Alberta reservoirs: geological structure and process modeling. *Energy & Fuels*, *24*(6), 3540-3550.

Nygaard, R. (2010). Geomechanical Analysis: Wabamun area CO_2 sequestration project (WASP). *Energy and Environmental Systems Group (EES), University of Calgary*.

Ohtomo, Y., Ijiri, A., Ikegawa, Y., Tsutsumi, M., Imachi, H., Uramoto, G. I., ... & Inagaki, F. (2013). Biological CO_2 conversion to acetate in subsurface coal-sand formation using a high-pressure reactor system. *Frontiers in Microbiology, 4*, 1-17.

Palchik, V. (2013). Is there link between the type of the volumetric strain curve and elastic constants, porosity, stress and strain characteristics?. *Rock mechanics and Rock Engineering*, *46*(2), 315-326.

Perera, M. S. A., Ranjith, P. G., Choi, S. K., & Airey, D. (2012). Investigation of temperature effect on permeability of naturally fractured black coal for carbon dioxide movement: An experimental and numerical study. *Fuel*, *94*, 596-605.

Podder, J., Hossain, T., & Mannan, K. M. (1995). An investigation into the thermal behaviour of Bangladeshi coals. *Thermochimica Acta*, *255*, 221-226.

Qu, H., Liu, J., Chen, Z., Wang, J., Pan, Z., Connell, L., & Elsworth, D. (2012). Complex evolution of coal permeability during CO_2 injection under variable temperatures. *International Journal of Greenhouse Gas Control*, *9*, 281-293.

Richardson, R. J., & Singh, S. (2012). Prospects for underground coal gasification in Alberta, Canada. *Proceedings of the ICE-Energy, 165*(3), 125-136.

Richter, D., & Simmons, G. (1974). Thermal expansion behavior of igneous rocks. *International Journal of Rock Mechanics and Mining Sciences & Geomechanics Abstracts, 11*(10), 403-411.

Rotaru, A. (2012). Thermal analysis and kinetic study of Petroşani bituminous coal from Romania in comparison with a sample of Ural bituminous coal. *Journal of Thermal Analysis and Calorimetry, 110*(3), 1283-1291.

Sansgiry, P. S. (1990). A numerical technique to track the growth of cavities in underground coal gasification. PhD Dissertation, University of Wyoming.

Sarraf Shirazi, A. (2012). CFD simulation of underground coal gasification. MSc Dissertation, University of Alberta.

Sarraf Shirazi, A., Karimipour, S., & Gupta, R. (2013). Numerical simulation and evaluation of cavity growth in in situ coal gasification. *Industrial & Engineering Chemistry Research*, *52*(33), 11712-11722.

Schrider, L. A., & Jennings, J. W. (1974). An underground coal gasification experiment, Hanna, Wyoming. In *Fall Meeting of the Society of Petroleum Engineers of AIME*. Society of Petroleum Engineers.

Seifi, M., Chen, Z., & Abedi, J. (2011). Numerical simulation of underground coal gasification using the CRIP method. *The Canadian Journal of Chemical Engineering*, *89*(6), 1528-1535.

Seo, D. K., Park, S. S., Kim, Y. T., Hwang, J., & Yu, T. U. (2011). Study of coal pyrolysis by thermo-gravimetric analysis (TGA) and concentration measurements of the evolved species. *Journal of Analytical and Applied Pyrolysis*, *92*(1), 209-216.

Settari, A., & Walters, D. A. (2001). Advances in coupled geomechanical and reservoir modeling with applications to reservoir compaction. *SPE Journal*, *6*(03), 334-342.

Shoemaker, H. D. (1976). Mechanical properties of the Pittsburgh coal at elevated temperatures. PhD Dissertation, West Virginia University.

Singer, J. M., & Tye, R. P., (1979). Thermal, mechanical, and physical properties of selected bituminous coals and cokes. Bureau of Mines Report RI 8364.

Somerton, W. H., Soylemezoglu, I. M., & Dudley, R. C. (1975). Effect of stress on permeability of coal. *International journal of Rock Mechanics and Mining Sciences & Geomechanics Abstracts, 12* (05), 129-145.

Sonibare, O. O., Ehinola, O. A., Egashira, R., & KeanGiap, L. (2005). An investigation into the thermal decomposition of Nigerian coal. *Journal of Applied Sciences 5*, 104-107.

Speight, J. G. (2005). Handbook of Coal Analysis. John Wiley & Sons.

Stanczyk, K., Smolinski, A., Kapusta, K., Wiatowski, M., Swiadrowski, J., Kotyrba, A., & Rogut, J. (2010). Dynamic experimental simulation of hydrogen oriented underground gasification of lignite. *Fuel, 89*, 3307-3314.

Stanczyk, K., Howaniec, N., Smolinski, A., Swiadrowski, J., Kapusta, K., Wiatowski, M., Grabowski, J., & Rogut, J. (2011). Gasification of lignite and hard coal with air and oxygen enriched air in a pilot scale ex situ reactor for underground gasification. *Fuel, 90*, 1953-1962.

Stanczyk, K., Kapusta, K., Wiatowski, M., Swiadrowski, J., Smolinski, A., Rogut, J., & Kotyrba, A. (2012). Experimental simulation of hard coal underground gasification for hydrogen production. *Fuel*, *91*(1), 40-50.

Su, F., Nakanowataru, T., Itakura, K., Ohga, K., & Deguchi, G. (2013). Evaluation of structural changes in the coal specimen heating process and UCG model experiments for developing efficient UCG systems. *Energies, 6*, 2386-2406.

Sury, M., White, M., Kirton, J., Carr, P., Woodbridge, R., Mostade, M., Chappell, R., Hartwell, D., Hunt, D., & Rendell, N. (2004a). Review of environmental issues of underground coal gasification-best practice guide: United Kingdom Department of Trade and Industry Report No. COAL R273. DTI/Pub URN 04/1881.

Sury, M., White, M., Kirton, J., Carr, P., Woodbridge, R., Mostade, M., Chappell, R., Hartwell, D., Hunt, D., & Rendell N. (2004b). Review of environmental issues of underground coal gasification: United Kingdom Department of Trade and Industry. Report No. COAL R272. DTI/Pub URN 04/1880.

Swan Hills Synfuels. (2012). Swan Hills in-situ coal gasification technology development; final outcomes report. Swan Hills Synfuels, Alberta, Canada.

Tan, Q., Luo, X., & Li, S. (2008). Numerical modeling of thermal stress in a layered rock mass. In *The 42nd US Rock Mechanics Symposium (USRMS)*. American Rock Mechanics Association.

Thimons, E. D., & Kissell, F. N. (1973). Diffusion of methane through coal. *Fuel*, *52*(4), 274-280.

Thorsness, C. B., Grens, E. A., & Sherwood, A. (1978). A one-dimensional model for in situ coal gasification. UCRL-52523, Lawrence Livermore, National Laboratory (LLNL) Report, Berkeley, California.

Thuro, K., Plinninger, R. J., Zah, S., & Schutz, S. (2001). Scale effects in rock strength properties. Part 1: Unconfined compressive test and Brazilian test. *EUROCK 2001: Rock Mechanics-A Challenge for Society*, 169-174.

Tuncay, E., & Hasancebi, N. (2009). The effect of length to diameter ratio of test specimens on the uniaxial compressive strength of rock. *Bulletin of engineering geology and the environment*, *68*(4), 491-497.

UCG Association. (2014). http://www.ucgassociation.org (accessed May 02, 2014)

Vorobiev, O. Y., Morris, J. P., Antoun, T. H., & Friedmann, S. J. (2008). Geomechanical simulations related to UCG activities. In *International Pittsburgh Coal Conference, Pittsburgh, PA*.

Wan, Z., Feng, Z., Zhao, Y., Zhang, Y., Li, G., & Zhou, C., (2011). Elastic modulus's evolution law of coal under high temperature and triaxial stress. *Journal of China Coal Society, 36*(10), 1736-1740.

Wang, J., Du, J., Chang, L., & Xie, K. (2010). Study on the structure and pyrolysis characteristics of Chinese western coals. *Fuel Processing Technology, 91*(4), 430-433.

Wang, S., Elsworth, D., & Liu, J. (2013). Permeability evolution during progressive deformation of intact coal and implications for instability in underground coal seams. *International Journal of Rock Mechanics and Mining Sciences*, *58*, 34-45.

Wang, C., He, M., Zhang, X., Liu, Z., & Zhao, T. (2013). Temperature influence on macro-mechanics parameter of intact coal sample containing original gas from Baijiao Coal Mine in China. *International Journal of Mining Science and Technology, 23*(4), 597-602.

Wang, G. X., Wang, Z. T., Feng, B., Rudolph, V., & Liao, J. L. (2009). Semi-industrial tests on enhanced underground coal gasification at Zhong-Liang-Shan coal mine. *Asia-Pacific Journal of Chemical Engineering, 4*(5), 771-779.

Wiatowski, M., Stanczyk, K., Swiadrowski, J., Kapusta, K., Cybulski, K., Krause, E., Grabowski, J., Rogut, J., Howaniec, N. & Smolinski, A. (2012). Semi-technical underground coal gasification (UCG) using the shaft method in Experimental Mine "Barbara". *Fuel*, *99*, 170-179.

World Energy Council. (2010). 2010 survey of energy resources. World Energy Council, London, UK.

World Energy Council. (2013). World Energy Resources: 2013 Survey. (https://www.worldenergy.org/publications/2013/world-energy-resources-2013-survey/, accessed Nov. 27, 2015).

Xu, R., Li, H., Guo, C., & Hou, Q. (2014). The mechanisms of gas generation during coal deformation: Preliminary observations. *Fuel, 117*, 326-330.

Yang, L. (2004). Study on the model experiment and numerical simulation for underground coal gasification. *Fuel*, *83*(4), 573-584.

Yao, Y., & Liu, D. (2012). Comparison of low-field NMR and mercury intrusion porosimetry in characterizing pore size distributions of coals. *Fuel, 95*, 152-158.

Yao, Y., Liu, D., Che, Y., Tang, D., Tang, S., & Huang, W. (2009). Non-destructive characterization of coal samples from China using microfocus X-ray computed tomography. *International Journal of Coal Geology, 80*(2), 113-123.

Yin, G., Jiang, C., Wang, J. G., & Xu, J. (2013). Combined effect of stress, pore pressure and temperature on methane permeability in anthracite coal: An experimental study. *Transport in Porous Media, 100*(1), 1-16.

Youngberg, A. D., Sinks, D. J., Craig, G. N., Ethridge, F. G., & Burns, L. K. (1983). Postburn evaluation for Hanna II, Phases 2 and 3 underground coal gasification experiments, Hanna, Wyoming. United States Office of Scientific and Technical Information, Technical Information Center. Under cooperative contract (DE-FC21-83FE60177).

Yu, Y., Liang, W., Hu, Y., & Meng, Q. (2012). Study of micro-pores development in lean coal with temperature. *International Journal of Rock Mechanics & Mining Sciences, 51*, 91-96.

Zhao, Y., Qu, F., Wan, Z., Zhang, Y., Liang, W., & Meng, Q., (2010). Experimental investigation on correlation between permeability variation and pore structure during coal pyrolysis. *Transport in Porous Media, 82*(2), 401-412.

Zogala, A., & Janoszek, T. (2015). CFD simulations of influence of steam in gasification agent on parameters of UCG process. *Journal of Sustainable Mining*, *14*(1), 2-11.

Zou, M., Wei, C., Zhang, M., Shen, J., Chen, Y., & Qi, Y. (2013). Classifying coal pores and estimating reservoir parameters by nuclear magnetic resonance and mercury intrusion porosimetry. *Energy & Fuels, 27*(7), 3699-3708.